

## **General Disclaimer**

### **One or more of the Following Statements may affect this Document**

- This document has been reproduced from the best copy furnished by the organizational source. It is being released in the interest of making available as much information as possible.
- This document may contain data, which exceeds the sheet parameters. It was furnished in this condition by the organizational source and is the best copy available.
- This document may contain tone-on-tone or color graphs, charts and/or pictures, which have been reproduced in black and white.
- This document is paginated as submitted by the original source.
- Portions of this document are not fully legible due to the historical nature of some of the material. However, it is the best reproduction available from the original submission.

# COLLEGE OF EARTH AND MINERAL SCIENCES



(E84-10057) COMBINED USE OF REMOTE SENSING AND SEISMIC OBSERVATIONS TO INFER GEOLOGICALLY RECENT CRUSTAL DEFORMATION, ACTIVE FAULTING, AND STRESS FIELDS Final Technical Report, 1 May 1980 - (Pennsylvania G3/43

N84-15628

Unclas 00057

FINAL TECHNICAL REPORT

COMBINED USE OF REMOTE SENSING AND SEISMIC OBSERVATIONS  
TO INFER GEOLOGICALLY RECENT CRUSTAL DEFORMATION,  
ACTIVE FAULTING, AND STRESS FIELDS

Grant No. NAG 5-49

May 1, 1980 - November 30, 1982

Shelton S. Alexander  
Principal Investigator  
Department of Geosciences  
Geophysics Graduate Program  
403 Deike Building  
University Park, PA 16802

**The Pennsylvania  
State University  
University Park,  
Pennsylvania**



FINAL TECHNICAL REPORT

COMBINED USE OF REMOTE SENSING AND SEISMIC OBSERVATIONS TO INFER  
GEOLOGICALLY RECENT CRUSTAL DEFORMATION, ACTIVE FAULTING, AND STRESS FIELDS

Grant No. NAG 5-49

May 1, 1980 - November 30, 1982

**Original photography may be purchased  
from EOS Data Center  
Sioux Falls, SD 57198**

Shelton S. Alexander  
Principal Investigator  
Department of Geosciences  
Geophysics Graduate Program  
403 Deike Building  
University Park, PA 16802

## TABLE OF CONTENTS

### SECTION

- I. SUMMARY
- II. RECENT FAULTING IN CALIFORNIA EXAMINED FROM REMOTELY SENSED DATA AND SEISMICITY
- III. UTILITY OF DIGITALLY MERGED SEASAT-A SAR, LANDSAT MSS, AND MAGNETIC FIELD DATA SETS FOR MAPPING LITHOLOGY AND STRUCTURE IN A VEGETATED TERRAIN

SECTION I

SUMMARY

## SUMMARY

The principal objectives of this investigation were:

- (a) to assess the usefulness of combined analysis of LANDSAT imagery and high-quality digital seismic data from existing and new global networks of seismic stations (principally SRO) to infer geologically recent crustal deformation, active faulting, and stress fields;
- (b) to determine the most effective combinations of LANDSAT MSS channels and digital analysis of them that delineate and enhance tectonic features in several different types of active source regions;
- (c) to determine the extent and nature of the surface expression on LANDSAT images of major earthquakes;
- (d) to search for discernible precursory changes in LANDSAT images prior to these major earthquakes;
- (e) to develop a software package to implement these analysis techniques for routine application by users without background in remote sensing.

One new and potentially important data source emerged (SEASAT Synthetic Aperture Radar (SAR)) that was incorporated into the analysis. SAR imagery has the advantages over LANDSAT and other visible-infrared imagery that (1) it is sensitive to surface rock and soil texture, spatial contrast, and near-surface moisture content and (2) that it penetrates clouds and vegetation, a significant factor in a number of active earthquake zones. Inasmuch as one of our very preliminary findings was that known geologically-recent active faults appear to be more sharply defined (higher spatial contrast) on LANDSAT imagery than older or inactive ones in the same region, the SEASAT (SAR) imagery was especially helpful in identifying which faults have been active in tectonic regions where little ground-based data was available. Another important question was whether SAR and LANDSAT digital imagery could be combined to yield improved definition of active tectonic features. Therefore, SEASAT radar imagery was included in the analysis in regions for which it was available (North America primarily). In selected areas comparison with conventional side-looking radar data was also made.

This grant is a continuation of Grant NCC5-12 that has been reported upon previously. The appendices give the details of the results of this portion of the investigation. They are summarized as follows:

### RECENT FAULTING IN CALIFORNIA EXAMINED FROM REMOTELY SENSED DATA AND SEISMICITY

Landsat imagery and seismicity data were analyzed to determine the usefulness of remotely sensed data for identifying the locations of the most earthquake prone areas in seismically active regions. Characteristic traits were determined for earthquakes associated with strike-slip motion in Central California and the area surrounding the Salton Sea using only remotely sensed data. These results were compared to a pattern recognition study that used

ground-based data in the same areas. All the important diagnostic characteristics determined from the ground-based study were observable on the imagery. The mapped lineaments are orientated in several dominant directions. One direction is the same as the trend of the San Andreas fault, the major strike-slip fault in this region. The other directions differ from area to area and may reflect the stresses of earlier geologic processes. The pattern of lineament orientations is significantly different across the major San Andreas fault zone in Central California and the Salton Sea areas. A third area, where the left-lateral Garlock fault intersects the right-lateral San Andreas fault, was investigated to test the results. It was possible to distinguish between areas dominated by dip-slip faulting and strike-slip faulting in this area.

UTILITY OF DIGITALLY MERGED SEASAT-A SAR, LANDSAT MSS, AND  
MAGNETIC FIELD DATA SETS FOR MAPPING LITHOLOGY  
AND STRUCTURE IN A VEGETATED TERRAIN

Remotely sensed data from each part of the electromagnetic spectrum contains potentially different and independent information about the Earth's surface and subsurface. Interpretation of these different data sets, together with conventional geophysical and geological information, is greatly facilitated by merging all the data sets such that each (spatial) resolution element has associated with it an n-dimensional vector composed of information from each of the n data sets. In this study, Landsat MSS, Seasat-A Synthetic Aperture Radar (SAR), and magnetic field data from the South Mountain area west of Gettysburg, Pennsylvania, were registered to match each other in spatial position, and merged. Pattern recognition techniques were then applied to the composite data set to determine its utility in recognizing different rock types and structures in vegetated terrain around South Mountain. The SAR imagery was filtered in order to reduce its directional dependence. Principal components analysis was used to decrease the dimensionality of the entire data set. A texture algorithm was then applied to the first two principal axes, and later to the third axis, in order to enhance various geologic features. Next, the contribution of each data set and texture measure to the separability of rock type classes in the training area was evaluated. A classification of the entire study area was then done using the enhanced data that contributed the most to the separability of classes.

The texture measures were found to emphasize the geologic information in the data and thus increase the separability of the rock type classes. The best classification was obtained when texture measures from each of the first three principal component axes were merged with the magnetic field data. About 40% of the area was classified as having the same rock types as the geologic map showed. The confusion of rock type classes was due to the large amount of variance within each class when compared to the between-group variance. The variance is thought to originate from three sources; registration errors, the heavy vegetation cover, and systematic noise in the SAR data.

A test of the correlation between SAR tone and texture, Landsat tone and texture, and magnetic field data, revealed no tone or texture measures

linking any two of these original data sets.

The magnetic field data showed a 60% correlation with the surface geology of the area, and about 20% was correlatable with the known subsurface geology. In contrast, the satellite data was related only to the surface characteristics. Thus, the merged data set contained mainly surface information, but had a small component of subsurface information.



SECTION II

RECENT FAULTING IN CALIFORNIA EXAMINED FROM  
REMOTELY SENSED DATA AND SEISMICITY

The Pennsylvania State University  
The Graduate School  
Department of Geosciences

Recent Faulting in California Examined From  
Remotely Sensed Data and Seismicity

A Paper in  
Geophysics

by

Barbara Jeanette Lee

Submitted in Partial Fulfillment  
of the Requirements  
for the Degree of

Master of Science

August 1980

The signatories below indicate that they have read and approved the paper of Barbara Jeanette Lee.

Date of Signature:

\_\_\_\_\_

\_\_\_\_\_  
Shelton S. Alexander, Professor  
of Geophysics, Chairman of the  
Geophysics Program, Advisor

\_\_\_\_\_

\_\_\_\_\_  
Benjamin F. Howell, Jr.,  
Professor of Geophysics

\_\_\_\_\_

\_\_\_\_\_  
Lawrence M. Cathles, Associate  
Professor of Geosciences

ABSTRACT

Landsat imagery and seismicity data were analyzed to determine the usefulness of remotely sensed data for identifying the locations of the most earthquake prone areas in seismically active regions. Characteristic traits were determined for earthquakes associated with strike-slip motion in Central California and the area surrounding the Salton Sea using only remotely sensed data. These results were compared to a pattern recognition study that used ground-based data in the same areas. All the important diagnostic characteristics determined from the ground-based study were observable on the imagery. The mapped lineaments are oriented in several dominant directions. One direction is the same as the trend of the San Andreas fault, the major strike-slip fault in this region. The other directions differ from area to area and may reflect the stresses of earlier geologic processes. The pattern of lineament orientations is significantly different across the major San Andreas fault zone in Central California and the Salton Sea areas. A third area, where the left-lateral Garlock fault intersects the right-lateral San Andreas fault, was investigated to test the results. It was possible to distinguish between areas dominated by dip-slip faulting and strike-slip faulting in this area.

Table of Contents

Abstract.....	iii
Table of Contents.....	iv
List of Tables.....	v
List of Figures.....	vi
Acknowledgements.....	ix
Geologic History.....	1
Previous Investigations.....	10
Statement of the Problem.....	19
Procedures.....	20
Observations and Analysis.....	26
Discussion.....	71
Summary and Conclusions.....	76
Suggestions for Future Analyses.....	80
References.....	83
Appendix.....	85

List of Tables

1. Characteristics of larger earthquakes associated with dip-slip movement as determined by Briggs et al (1977).....	12
2. Summary of characteristic traits for dip-slip type earthquakes from Briggs et al (1977).....	13
3. Characteristics of larger earthquakes associated with strike-slip movement as determined by Briggs et al (1977).....	14
4. Summary of characteristic traits for strike-slip type earthquakes from Briggs et al (1977).....	16
5. Analyzed Landsat imagery.....	20
6. Seismicity data.....	25
7. Characteristics of events near the Salton Sea.....	55
8. Characteristics of events between Monterey and San Francisco.....	60

List of Figures

1.	Location map of California showing the major faults and areas investigated in this study.....	2
2a.	Geologic map of Southern California.....	3
2b.	Explanation of geologic maps shown in Figure 2a and Figure 3.....	4
3.	Geologic map of Central California.....	8
4.	Locations of dangerous areas for large dip-slip and strike-slip type earthquakes as determined by Briggs et al (1977).....	17
5a.	Comparison of image interpretations (Central California region).....	21
5b.	Comparison of image interpretations (Salton Sea region).....	22
6.	Permanent stations of the Southern California Seismic Network.....	24
7a.	Imagery of the Salton Sea.....	27
7b.	Imagery of the Salton Sea and mapped lineaments...	28
8a.	Imagery of Central California.....	29
8b.	Imagery of Central California and mapped lineaments.....	30
9a.	Base map of the Salton Sea region.....	31
9b.	Earthquakes of magnitude greater than 5 from 1932-1979 in Salton Sea region S1 and associated focal mechanisms.....	32
9c.	Earthquakes of magnitude greater than 5 from 1932-1979 in Salton Sea region S2 and associated focal mechanisms.....	33
9d.	Earthquakes of magnitude greater than 5 from 1932-1979 in Salton Sea region S3 and associated focal mechanisms.....	34
9e.	Earthquakes of magnitude greater than 5 from 1932-1979 in Salton Sea region S4 and associated focal mechanisms.....	35

10a.	Base map of Central California.....	36
10b.	Earthquakes of magnitude greater than 5 from 1963-1976 between Monterey and San Francisco (Central California region M1) and associated focal mechanisms.....	37
10c.	Earthquakes of magnitude greater than 5 from 1963-1976 between Monterey and San Francisco (Central California region M2) and associated focal mechanisms.....	38
10d.	Earthquakes of magnitude greater than 5 from 1963-1976 between Monterey and San Francisco (Central California region M3) and associated focal mechanisms.....	39
11.	Rose diagrams of lineaments SW of San Andreas fault in the Salton Sea region.....	41
12.	Rose diagrams of lineaments NE of San Andreas fault in the Salton Sea region.....	42
13a.	Mapped lineaments and seismicity (1975, all magnitudes) in Salton Sea region S1.....	43
13b.	Mapped lineaments and seismicity (1979, $m < 2$ ) in Salton Sea region S1.....	44
13c.	Mapped lineaments and seismicity (1979, $m \geq 2$ ) in Salton Sea region S1.....	45
13d.	Mapped lineaments and seismicity (1975, all magnitudes) in Salton Sea region S2.....	46
13e.	Mapped lineaments and seismicity (1975, all magnitudes) in Salton Sea region S3.....	47
13f.	Mapped lineaments and seismicity (1979, $m < 2$ ) in Salton Sea region S3.....	48
13g.	Mapped lineaments and seismicity (1979, $m \geq 2$ ) in Salton Sea region S3.....	49
13h.	Mapped lineaments and seismicity (1975, all magnitudes) in Salton Sea region S4.....	50
13i.	Mapped lineaments and seismicity (1979, $m < 2$ ) in Salton Sea region S4.....	51
13j.	Mapped lineaments and seismicity (1979, $m \geq 2$ ) in Salton Sea region S4.....	52



14.	Rose diagrams of lineaments NE of San Andreas fault in Central California.....	57
15.	Rose diagrams of lineaments SW of San Andreas fault in Central California.....	58
16.	Mapped lineaments and seismicity (1972, all magnitudes) in Central California region M1.....	59
17.	Mapped lineaments in Nevada.....	61
18.	Rose diagrams of lineaments mapped in Nevada.....	62
19a.	Mapped lineaments and seismicity (1932-79, $m > 5$ ) near Los Angeles.....	64
19b.	Mapped lineaments and seismicity (1972, $m \geq 2$ ) near Los Angeles.....	65
19c.	Mapped lineaments and seismicity (1979, $m \geq 2$ ) near Los Angeles.....	66
20.	Rose diagrams of lineaments NE of San Andreas fault near Los Angeles.....	67
21.	Rose diagrams of lineaments SW of San Andreas fault near Los Angeles.....	68
22a.	Grid and characteristic traits in the area near Los Angeles.....	69
22b.	Interpretation of lineaments and seismicity in the area near Los Angeles.....	70
23.	Orientations of stress ellipsoids and the fault motion associated with each stress condition.....	72
24.	Orientations of stress axes in California.....	72
25.	Rose diagrams showing rotations of lineaments across the San Andreas fault.....	74

Acknowledgements

The author expresses appreciation to her advisor, Dr. Shelton S. Alexander, for his suggestions and guidance throughout this project. In addition, the discussions and imagery interpretations from Carolyn Petrus were most helpful.

Computer facilities were made available by the Computation Center of The Pennsylvania State University. This project was funded through NASA Cooperative Agreement No. NCC 5-12.

## Geologic History

The two major areas of interest for this study are the Salton Trough region and the area between Monterey and San Francisco in California. These areas are divided into several natural provinces each with unique geologic histories (see Figure 1).

The Salton Trough region lies mainly in the Colorado Desert province. It is bordered on the west by the Peninsular Range province, on the east by the Mojave Desert, and on the north by the Transverse Ranges [Jahns, 1954]. A generalized geologic map of the Salton Sea region is shown in Figure 2. The Salton Trough is a linear and narrow depression approximately 1400 km in length [Sharp, 1972]. It formed in Pliocene or Miocene epoch by active right-lateral strike-slip faulting in the San Andreas fault system and is an extension of the Gulf of California physiographic province. This region experiences the highest level of seismicity along the San Andreas system.

The Colorado Desert is at the delta of the Colorado River. The Salton Sea lies within this natural province and was most recently filled when the Colorado River burst levees between 1905 and 1907. The low-lying depression is a former basin filled with mid-late Cenozoic sediments. Most of these rocks are alluvial-fan and lacustrine deposits and some are shallow marine

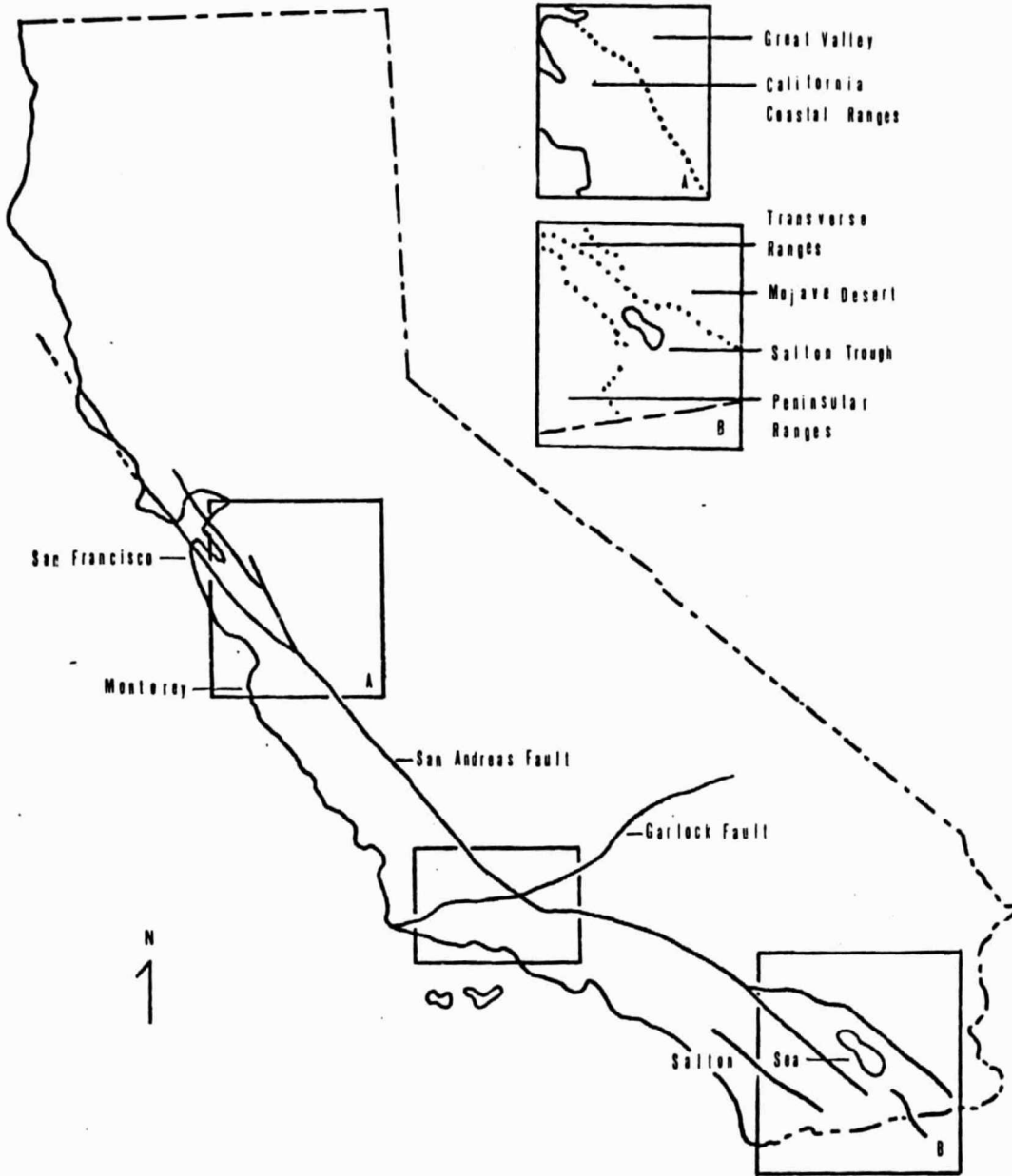
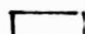

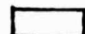

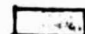






Figure 1. Location map of California showing the major faults and areas investigated in this study. The boundaries of the natural physiographic provinces within the two major areas of interest are shown in the upper right corner.


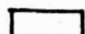


Figure 2a. Geologic map of Southern California [redrawn from U.S.G.S. Map I-512, 1966].  
See Figure 2b for explanation.

SEDIMENTARY AND VOLCANIC ROCKS

-  Cenozoic nonmarine (continental) sedimentary rocks and alluvial deposits
-  Cenozoic marine sedimentary rocks
-  Cenozoic volcanic rocks
-  Late Mesozoic (latest Jurassic and Cretaceous) shelf and slope sedimentary rocks
-  Late Mesozoic (latest Jurassic and Cretaceous) eugeosynclinal rocks of the Franciscan Formation
-  Mesozoic sedimentary and volcanic rocks older than the Nevadan orogeny; in places strongly metamorphosed
-  Paleozoic sedimentary and volcanic rocks; in places strongly metamorphosed; includes some late Precambrian sedimentary rocks in Great Basin
-  Precambrian rocks of all types including coarse-grained intrusives
-  Pre-Cenozoic metamorphic rocks of unknown age

INTRUSIVE IGNEOUS ROCKS

-  Granitic rocks chiefly of Mesozoic age
-  Ultramafic rocks chiefly of Mesozoic age

— Contact

≡... Fault, dotted where concealed; includes low-angle faults; arrows indicate direction of movement on strike-slip faults

Figure 2b. Explanation of geologic maps shown in Figure 2a and Figure 3.

deposits of Eocene age from the Gulf of California. There is a thick section of fine- to very coarse-grained, non-marine strata made up of late Cenozoic volcanics, in addition to igneous and metamorphic rocks of pre-Cenozoic age. Faults bound the province and cut rocks as young as Quarternary. Subparallel breaks of the San Andreas fault zone are found on the northeast edge. The western edge of the province is bounded by the Elsinore, San Jacinto, and other major northwest-trending faults.

The Peninsular Range also has northwest trending topography. Several relatively high mountain ranges are located in this province and the coastal plain has several marine terraces. The Paleozoic and Mesozoic rocks are igneous, metasedimentary, and metavolcanic. The igneous rocks are associated with the great California batholith. There was another period of volcanism and deposition of non-marine sedimentary rocks in the mid-late Cenozoic era. The sedimentary sections are folded along west-northwest and north-northwest trending axes with ridges made of rocks resembling the Franciscan Formation. There is evidence that the faults were active during the Cenozoic era.

The most extensive province is the Mojave Desert. It is bounded on the north by the left-lateral Garlock fault and on the southwest by the right-lateral San Andreas fault. Within the province there are folds trending north to

northwest, steeply dipping faults, and some major thrust faults of middle Jurassic to late Cretaceous age. The structural features of late Cenozoic age are open folds, low angle thrust faults, and steeply dipping faults that trend northwest and show some evidence of recent movement. Indications of igneous activity in the province include pre-Cambrian and Mesozoic plutonic rocks, pre-Cenozoic volcanic and metavolcanic rocks, and Cenozoic hypabyssal intrusive rocks. There are severely deformed and metamorphosed sedimentary rocks, sections of metamorphosed Paleozoic rocks, and some sedimentary, metasedimentary, and metavolcanic rocks of Mesozoic age. Basin formation from the middle Miocene epoch to the present is indicated by young fluvial deposits and lacustrine sedimentation.

Elongated mountain ranges, valleys, chains of hills, and broad basins are major features in the Transverse Ranges. The structures trend east to west. There are some steeply dipping strike-slip faults, but most faults in this province are reverse faults. The San Andreas and San Jacinto faults cross the eastern part of the province. The Paleozoic and pre-Cambrian rocks are metamorphosed sedimentary and volcanic units. There was an orogeny in the late Mesozoic era causing widespread plutonic intrusion. Large basins are filled with marine and non-marine sedimentary rocks of the Tertiary period. Another orogeny in



the mid-Pleistocene epoch caused intense folding and uplift as reflected in the scarps seen in the present topography of the province.

The area between Monterey and San Francisco lies mainly in the Central California Coastal Ranges (see Figure 3 for generalized geologic map). To the east is the Great Valley province which shows very little seismic activity [Richter, 1958].

The California Coastal Ranges lie between the Mendocino and Murray fracture zones and experience moderate to high seismicity. The basement complex is made of metamorphosed sedimentary rocks and volcanics. The granitic plutonic rocks are exposed along the San Andreas fault and to the west [Taliaferro, 1941]. Rocks of the Franciscan Formation (shallow marine clastics and chemical and organic sediments) later filled the sinking geosynclinal basin. During the Mesozoic era there were periods of uplift, intense folding, sedimentation, and volcanism. During the Eocene epoch there were thrust faulting and vertical movement along the San Andreas fault. Miocene sedimentation was followed by another period of uplifting, folding, and downwarping. This continued into the Pliocene and Pleistocene epochs. These thrust faults are the en echelon faults now observed.



Figure 3. Geologic map of Central California [redrawn from U.S.G.S. Map I-512, 1965].  
See Figure 2b for explanation.

Movement along the San Andreas fault has been in excess of 300 km of right-lateral slip during the last 8 or 10 million years [Sylvester and Crowell, 1979]. Between 38 and 29 million years ago the North American and Pacific plates converged and a transform boundary was created. Faulting, subsidence, uplifting, and volcanic activity began as a result of the plate interactions. The modern San Andreas fault became the major transform boundary between the Pacific and North American plates about 4 million years ago. Faults of the present San Andreas system include the main branch of the San Andreas, the San Jacinto fault, and the Elsinore fault. Each of these right-lateral faults shows displacement of the order of 30 km.

### Previous Investigations

Ground-based geologic observations were used to determine characteristic traits of the most earthquake prone and the least earthquake prone areas in Nevada and California [Briggs et al, 1977]. The pattern recognition algorithm that they used could distinguish among earthquakes characteristic of the San Andreas fault system, Basin and Range province type earthquakes, and places within these active regions where the epicenters of strong earthquakes are unlikely to occur. Briggs et al used earthquake epicenters of magnitude 6.0 or greater for their study.

The algorithm used for pattern recognition is described in an earlier paper where it was used to predict strong earthquake epicenters in California [Gelfand et al, 1976]. A pattern is defined as "a suite of traits that characterizes a group of objects and distinguishes this group of objects from another group" [Briggs et al, 1977]. Their studies were undertaken to forecast epicentral locations in space, but not in time, and to investigate earthquake processes. Because our understanding of earthquake processes is incomplete, it is not possible to fully describe the epicentral locations or to include all of the important source-related properties. Therefore, to describe epicentral locations, they chose to include characteristics that were common to  $\geq 65$  percent of G1 objects (locations that are earthquake

epicenter prone) and  $\leq 10$  percent of G2 objects (locations that are not earthquake epicenter prone).

They searched combinations of one, two, and three properties from answers to a list of 45 geologic and geomorphic questions to identify the characteristic traits. These questions were based on recent ground-based studies of the California-Nevada region and data from standard geologic and tectonic maps. All points were reclassified as D (dangerous) or N (non-dangerous, safe) depending on the number of traits they possessed characteristic of G1 objects or G2 objects. All of the characteristic traits were combinations of two or more properties. They found it was possible to discriminate between dangerous zones of dip-slip type and strike-slip type events.

Earthquakes with dip-slip displacement are characteristic of the Basin and Range province of Nevada. Briggs et al used a set of 28 locations near epicenters and 160 other points to determine the combination of traits that are characteristic of earthquake prone versus more stable areas associated with significant vertical fault movement. (Table 1 is a summary of the characteristics of larger earthquakes associated with dip-slip movement. The values indicate the limits characterizing areas with dangerous traits. Safe traits correspond to the areas falling outside those limits.) They found 89 percent of G1 (earth-

quake prone) locations were recognized as dangerous and 90 percent of G2 (not earthquake prone) locations were recognized as safe.

Table 1. Characteristics of larger earthquakes associated with dip-slip movement as determined by Briggs et al (1977)

High elevation	>7000' within 15 km
Large local variations in elevation	>2000' within 15 km
Dip-slip faults nearby	<40 km
Numerous faults	>5 within 25 km
Geothermal activity	<50 km
Absence of nearby strike-slip faults	>40 km
Earthquake $6.0 > M > 5.0$	<30 km
Major branch of San Andreas	>75 km
Body of water (oceans, lakes)	>10 km
Mélange outcrop	>30 km
Spreading center (divergence zones)	>300 km
Two or more lineaments	<40 km
Lineament intersection	>30 km

The dangerous areas are characterized by high elevation, large local variations in elevation, nearby dip-slip faults, numerous faults and parallel lineaments, geothermal activity, and an absence of nearby major strike-slip faults. They suggest these characteristics are consistent with a model proposed by Scholz et al (1971) in which warm, melted remnants of the Farallon plate rise under Nevada. This would cause uplifting and dip-slip faulting that would explain why the intrusions there still retain some heat and have observable thermal anomalies. The safe areas are regions with lower elevation, absence of geothermal activity, and

Table 2. Summary of characteristic traits for dip-slip type earthquakes from Briggs et al (1977)

Dangerous traits:

1. Region of considerable uplift with closely-spaced, extended linear features, but not faulted to an extreme degree
2. Hot water circulation associated with regions that have undergone uplift and block faulting for time periods on the order of  $10^6$  years
3. Same characteristics as in trait 2, plus nearby topographic relief that directs or concentrates drainage to geothermal areas
4. Areas free from lineament intersections and far from spreading centers
5. Areas with nearby major dip-slip faults, moderate fault density, and absence of mélangé
6. Same characteristics as in trait 5, plus an absence of surface bodies of water
7. Same characteristics as in trait 5, plus closely-spaced, nonintersecting lineaments
8. Moderately faulted regions with geothermal activity and an absence of smaller earthquakes
9. Areas with geothermal activity, absence of a major strike-slip fault and an absence of mélangé

Safe traits:

- 1.. Areas where uplift and block faulting have not occurred
2. Areas with low lineament density and no recent normal faulting
3. Absence of large-scale dip-slip features in areas with no indication of recent movement on smaller faults
4. Areas with low fault density and absence of geologically recent normal faulting or dip-slip activity
5. Absence of geothermal activity in undersaturated, dilatant regions

absence of major dip-slip faults. The combination of characteristics that were determined to define dangerous and safe traits are summarized in Table 2.

San Andreas type earthquakes are associated with strike-slip movement. Learning in Briggs et al's study was based on 26 locations near epicenters and 162 other points to determine the combinations of dangerous versus safe characteristic traits. (Table 3 is a summary of the characteristics of larger earthquakes associated with strike-slip movement. The values indicate the limits characterizing areas with dangerous traits; safe traits correspond to the areas falling outside those limits.) They found 77 percent of G1 (locations that are earthquake epicenter prone) were recognized as dangerous and 90 percent of G2 (locations that are not earthquake epicenter prone) were recognized as safe from large strike-slip earthquakes.

Table 3. Characteristics of larger earthquakes associated with strike-slip movement as determined by Briggs et al (1977)

Major branch of San Andreas	<75 km
Intersections of lineaments	<40 km
Longer, active strike-slip faults	<30 km
Major normal or reverse faults	>40 km
Major strike-slip fault	<40 km
Historically active major fault	<20 km
Volcanism	<40 km
Mélange outcrop	<30 km
Spreading center	<300 km
Nearest lineament	<20 km



Areas with longer, active strike-slip faults, numerous lineament intersections, and absence of vertical faults are considered dangerous regions for large events associated with strike-slip motion. The San Andreas fault system is a major transform fault between the North American and Pacific plates. At this boundary, transcurrent motion occurs along the linear features. Safe areas are characterized by an absence of active major strike-slip faults and an absence of lineament intersections. In the study region, safe areas are situated in those parts of California and Nevada not associated with the San Andreas fault, areas of aseismic creep, or areas not under stress. The combination of characteristics that were determined to define dangerous and safe traits are summarized in Table 4.

Briggs et al found most dip-slip events were located in Western Nevada and most strike-slip events were located along the San Andreas fault. Both types of faulting occur where the east-west trending Garlock fault intersects the San Andreas fault (see Figure 4).

The stability of their algorithm was also tested. They found that additional questions used in the analysis resulted in the same conclusions. A control experiment was devised in which the first half of the earthquake catalogue was used to predict the locations of the other half. The algorithm's prediction success was approximately 16 out of

Table 4. Summary of characteristic traits for strike-slip type earthquakes from Briggs et al (1977)

Dangerous traits:

1. Areas along the transform fault that have been historically or currently active
2. Faulted areas with an absence of compression or tension and where there are no bends in the fault
3. Lineament intersections in areas along the transform fault
4. Recent strike-slip faulting, absence of dip-slip faulting

Safe traits:

1. Stable areas with no major faulting at present or in recent geologic history
2. Absence of mélangé in areas away from the plate boundary
3. Areas away from the transform fault with an absence of recent volcanism
4. Regions located away from a spreading center that are not located near a major strike-slip fault

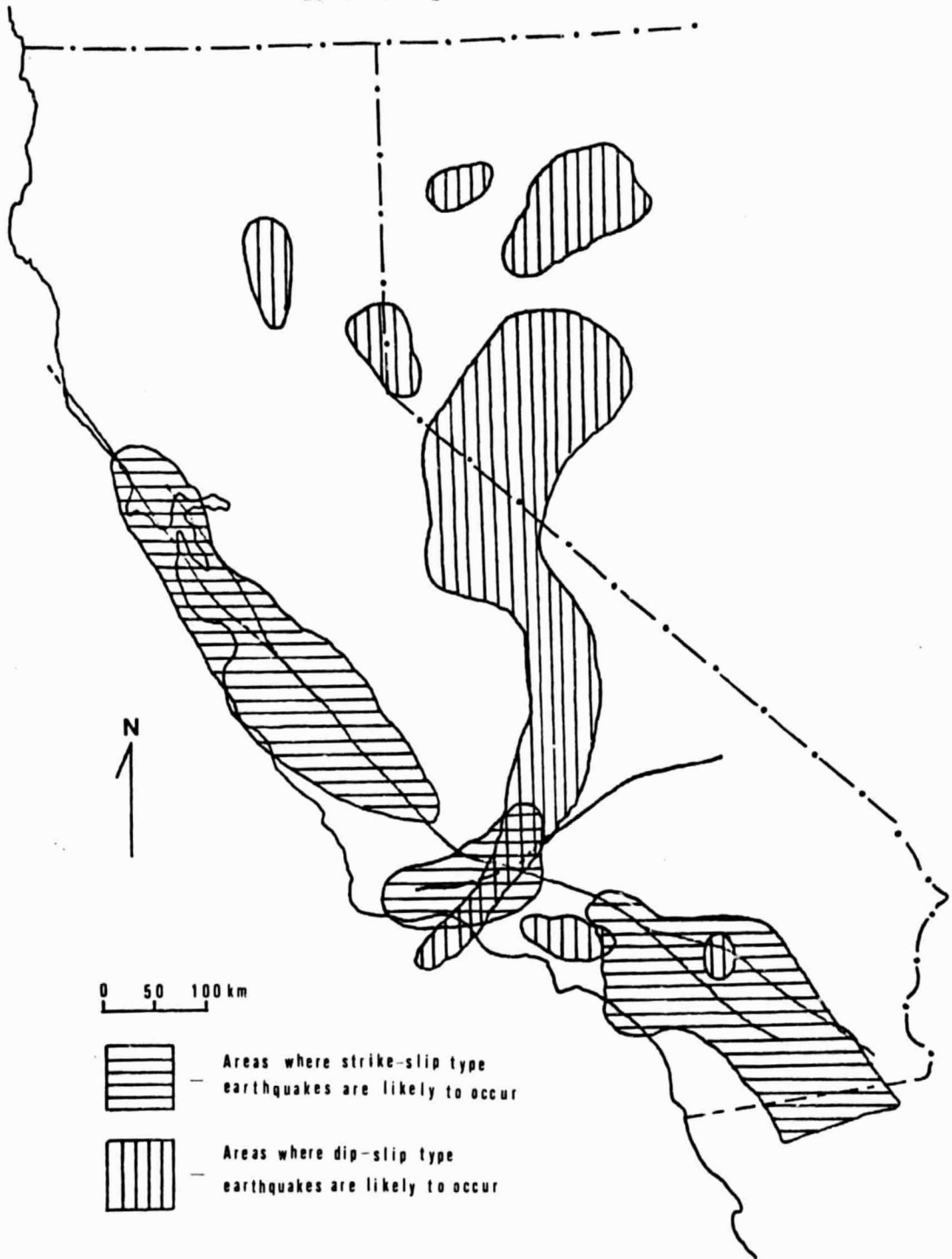


Figure 4. Locations of dangerous areas for large dip-slip and strike-slip type earthquakes as determined by Briggs et al (1977). The San Andreas and Garlock faults are shown in red. [Redrawn from Figures 2 and 3, Geol. Soc. of Amer. Bull., v.88, pages 161-173.]

20 events.

Briggs et al's study outlines a procedure for locating areas of significant earthquake activity and areas without significant activity within a major seismic province. They used ground-based data that had been collected by many researchers over several decades. This method would not be feasible in seismic areas that have had few or no previous ground-based investigations. For these areas it is suggested that remote sensing techniques may be used to gather analogous diagnostic data. The regional trends and smaller features could easily be observed as can most of the significant diagnostic characteristics discussed earlier. The remotely sensed data are expected to further supplement those areas with extensive ground-based data. Remotely sensed data (e.g., Landsat) can provide complete coverage of the earth's land masses. For Landsat, the same ground scene is repeated every 18 days which would allow an observer to study the longer term changes that may be associated with large earthquakes. It also provides an economical means of comparing geologically recent spatial features to crustal stress conditions inferred from earthquake focal mechanisms. This study is concerned with evaluating these possible joint applications of remote sensing and seismic observations.

### Statement of the Problem

The objective of this study is to compare data observed on Landsat imagery with the characteristic traits which define seismically active areas determined by Briggs et al's (1977) ground-based pattern recognition investigation. The same areas are examined in both studies and a similar set of criteria are used. This study is a preliminary determination, based on visual analysis, of the usefulness of remotely sensed data in earthquake investigations. If the important characteristics can be observed using these data, a more quantified analysis could be developed to be used in seismically active areas where little ground-based data have been collected. To be useful, the observations must define characteristics which distinguish among areas where strike-slip type earthquakes, dip-slip type earthquakes, and no large earthquakes are likely to occur. Features that describe more geologically recent structures will be emphasized in the analysis. Observations will be discussed in terms of regional tectonics. Finally, a procedure will be outlined for investigating other seismically active areas.

### Procedures

Visual analysis of Landsat satellite images were used to identify the locations of distinct lineaments and other geologic features. (Table 5 is a list of the analyzed images.) For this study, lineaments are defined as any linear surface expressions that are geologic, geomorphic, or topographic, and faults refer to those lineaments which are known to be associated with vertical or horizontal movement. Features used in the image interpretation include: fault valleys, saddles, narrow troughs and ridges, scarps, steep mountain fronts, changes in rock type and/or texture, offset streams, and sag ponds.

Table 5. Analyzed Landsat imagery (all in color)

Location	Identification	Date
Salton Sea	E-2120-17382	May 22, 1975
Monterey-San Francisco	E-1002-18134	July 25, 1972
Monterey	E-1057-18172	Sept. 18, 1972
Garlock (Los Angeles)	E-1018-18010	Aug. 10, 1972
Nevada	E-1072-17592	Oct. 3, 1972

Another observer (geologist), in addition to the author, interpreted the imagery. This gave further corroboration of the locations and dominant orientations of the observable lineaments. Rose diagrams (see Figures 5a and 5b) were constructed for the sets of data for both observers, and the dominant orientations agree in almost all cases.

ORIGINAL PAGE IS  
OF POOR QUALITY

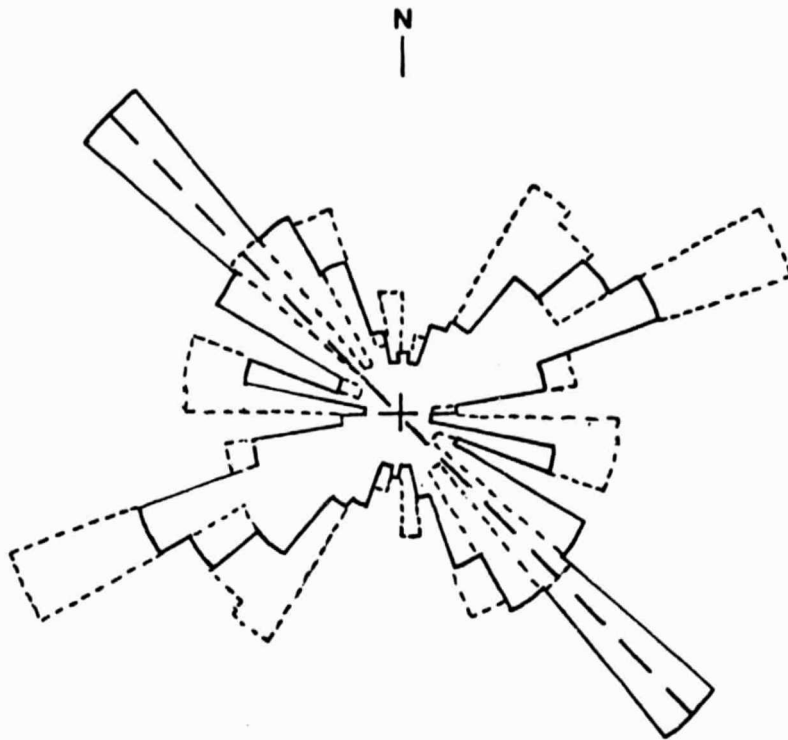


Figure 5a. Comparison of image interpretations. The solid lines represent the orientations of the lineaments mapped by the author in the Central California region. The small dotted lines represent the interpretation of another observer on the same imagery. The rose diagrams were constructed from length data. The large dotted line (N45°W) represents the trend of the San Andreas fault in this area.

ORIGINAL PAGE IS  
OF POOR QUALITY

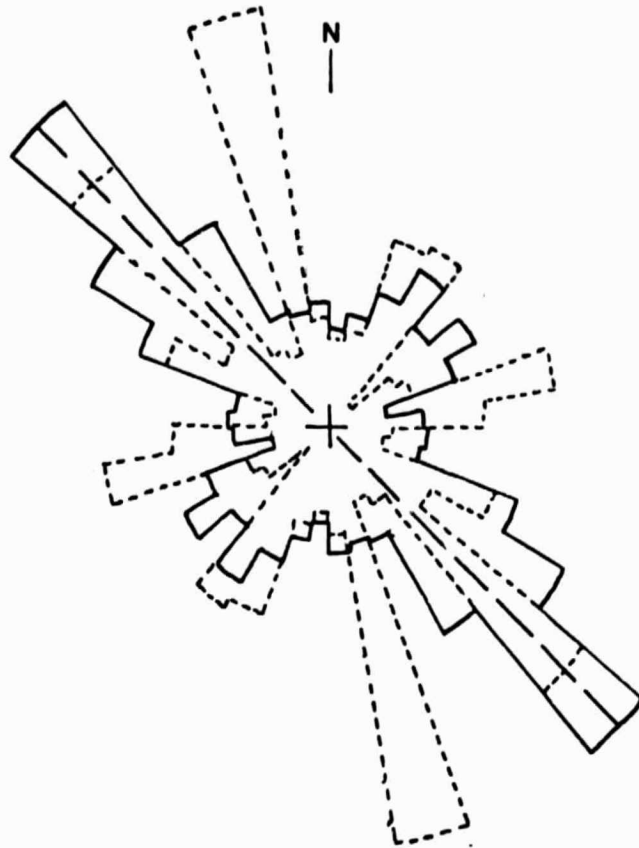


Figure 5b. Comparison of image interpretations. The solid lines represent the orientations of the lineaments mapped by the author in the Salton Sea region. The small dotted lines represent the interpretation of another observer on the same imagery. The rose diagrams were constructed from length data. The large dotted line ( $N45^{\circ}W$ ) represents the trend of the San Andreas fault in this area.



Agricultural effects and cloud cover were the major problems in interpreting the images. Digital analysis of the data should be considered for more detailed future analysis.

The recent seismicity of each region was plotted at the same scale as the imagery. This was done to compare the lineaments to the zones of greater current activity. The seismicity data are contained on two computer tapes. Data for the seismicity of the world for 1963-1976 are contained on Tape EPTP76. These data were used for the epicenter plots of Central California. The data sources listed include: BRK, ERL, and GS. Southern California seismicity data for 1932-1979 are listed on Tape CALSEI. This tape was used to plot the seismicity of the Salton Sea region and the Los Angeles area. Since 1973, the relative epicentral location error is within 4 km due to the dense seismic network in Southern California (see Figure 6). Much of the 1979 data in Southern California is accurate to within 2.5 to 1 km [Johnson, 1979]. Both sets of data were searched for location and magnitude before being plotted. Wolfplot graphics routines were used to plot the data on a Tektronix 4662 plotter. Where possible, the data were plotted for the year the images were taken, for 1979, and for the events with magnitudes greater than 5 from 1932 to 1979 (see Table 6).

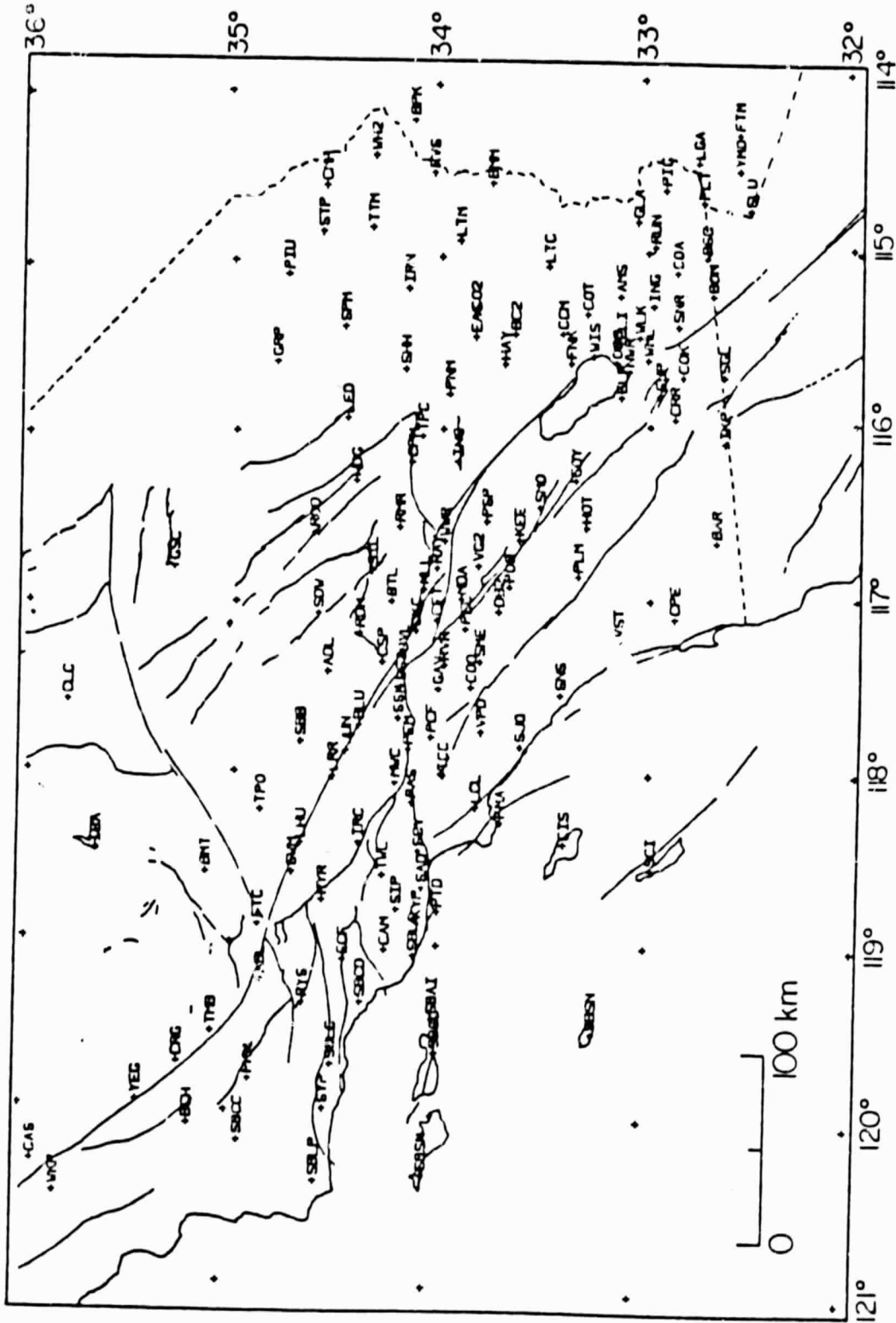


Figure 6. Permanent stations of the Southern California Seismic Network [Johnson, 1979]

Table 6. Seismicity data

Location	Lat ( $^{\circ}$ N)	Long ( $^{\circ}$ W)	Source	Date	Mag.
Garlock (Los Angeles)	34-35	117-120	Tape CALSEI	1972	$\geq 2$
Garlock (Los Angeles)	34-35	117-120	Tape CALSEI	1932-79	$\geq 5$
Garlock (Los Angeles)	34-35	117-120	Tape CALSEI	1979	$\geq 2$
Monterey- San Francisco	36-38	120-122	Tape EPTP76	1972	$\geq 0$
Monterey- San Francisco	36-38	120-122	Tape EPTP76	1963-76	$\geq 5$
Salton Sea	32-35	115-117	Tape CALSEI	1975	$\geq 0$
Salton Sea	32-35	115-117	Tape CALSEI	1979	$< 2$
Salton Sea	32-35	115-117	Tape CALSEI	1979	$\geq 2$
Salton Sea	32-35	115-117	Tape CALSEI	1932-79	$\geq 5$

### Observations and Analysis

The imagery of the Salton Sea region and the area between Monterey and San Francisco are presented in Figures 7a and 8a, respectively. The imagery of these two regions, with the lineaments mapped, are presented in Figures 7b and 8b. Both major study areas have been seismically active and are associated with strike-slip fault movements. (Figures 9a-9e and 10a-10d show some of the larger earthquakes of the two regions and indicate the associated focal mechanisms.) The questions used to analyze the data are listed in the Appendix.

An image of Nevada and an image of the area around Los Angeles were also interpreted. The Nevada image was used to compare the characteristics of a region with dip-slip faults (the Basin and Range province) with the characteristics of the strike-slip faulted regions in the major study areas. The Los Angeles image included the intersection of the Garlock fault and the San Andreas fault where both dip-slip faulting and strike-slip faulting are known to occur. This area was chosen to test the results of the study by finding distinguishing combinations of characteristic traits associated with the two types of faulting.

The San Andreas fault trends approximately N45°W in the Salton Sea region. On the southwest side of the fault

ORIGINAL PAGE IS  
OF POOR QUALITY



Figure 7a. Imagery of the Salton Sea

ORIGINAL PAGE IS  
OF POOR QUALITY



Figure 7b. Imagery of the Salton Sea and mapped lineaments

ORIGINAL PAGE IS  
OF POOR QUALITY



Figure 8a. Imagery of Central California

ORIGINAL PAGE IS  
OF POOR QUALITY.



Figure 8b. Imagery of Central California and mapped lineaments



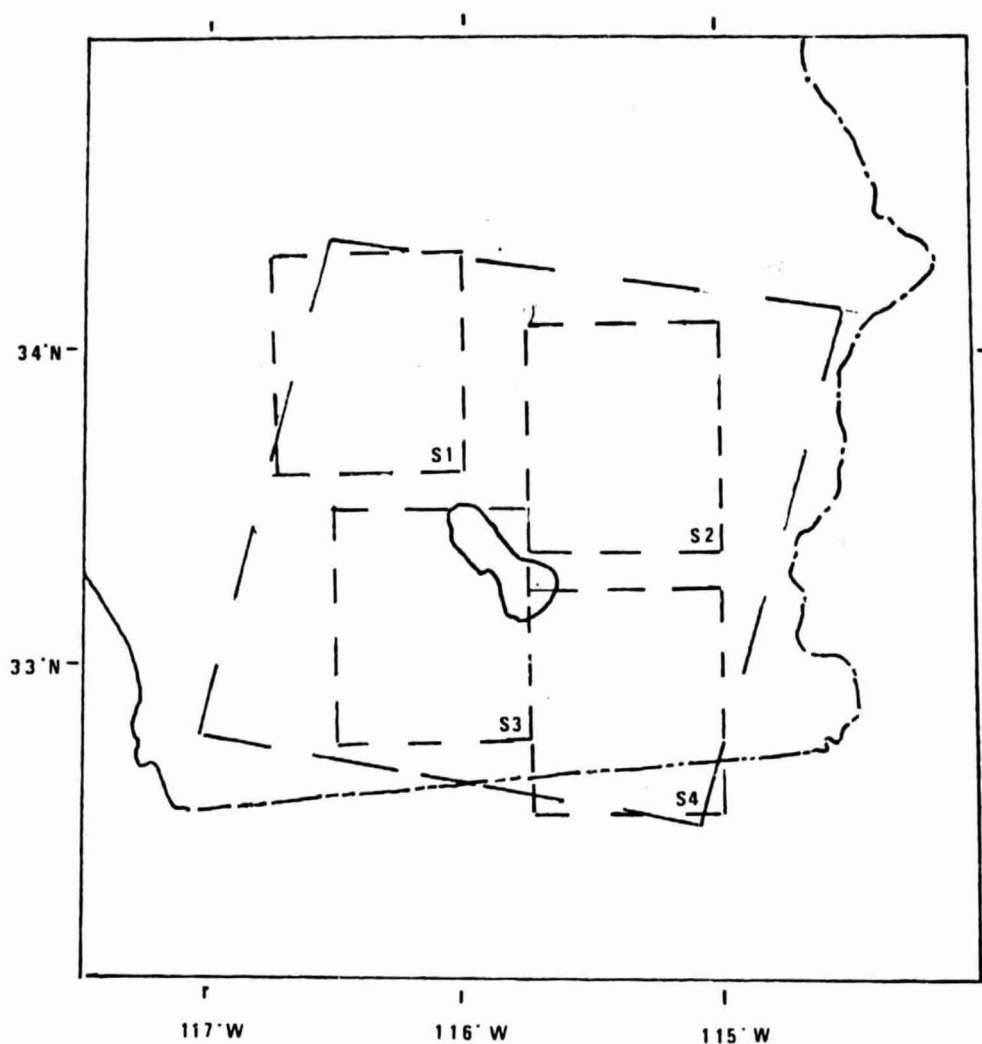


Figure 9a. Base map of the Salton Sea region. The large dashed line shows the region in the Landsat imagery. S1, S2, S3, and S4 are the areas shown in Figures 9b-e and Figures 13a-j. (scale of figures: 1 cm = 5 km)

Symbols used in Figures 9b-9e:

- ★ Earthquake epicenter of magnitude  $\geq 5$
- ⊙ Earthquake epicenter of magnitude  $\geq 5$  (test point)
- ⊕ Earthquake epicenter (test point)
- Test point
- ★ Spreading center

(SS) Strike-slip focal mechanism

(DS) Dip-slip focal mechanism

(T) Thrust focal mechanism

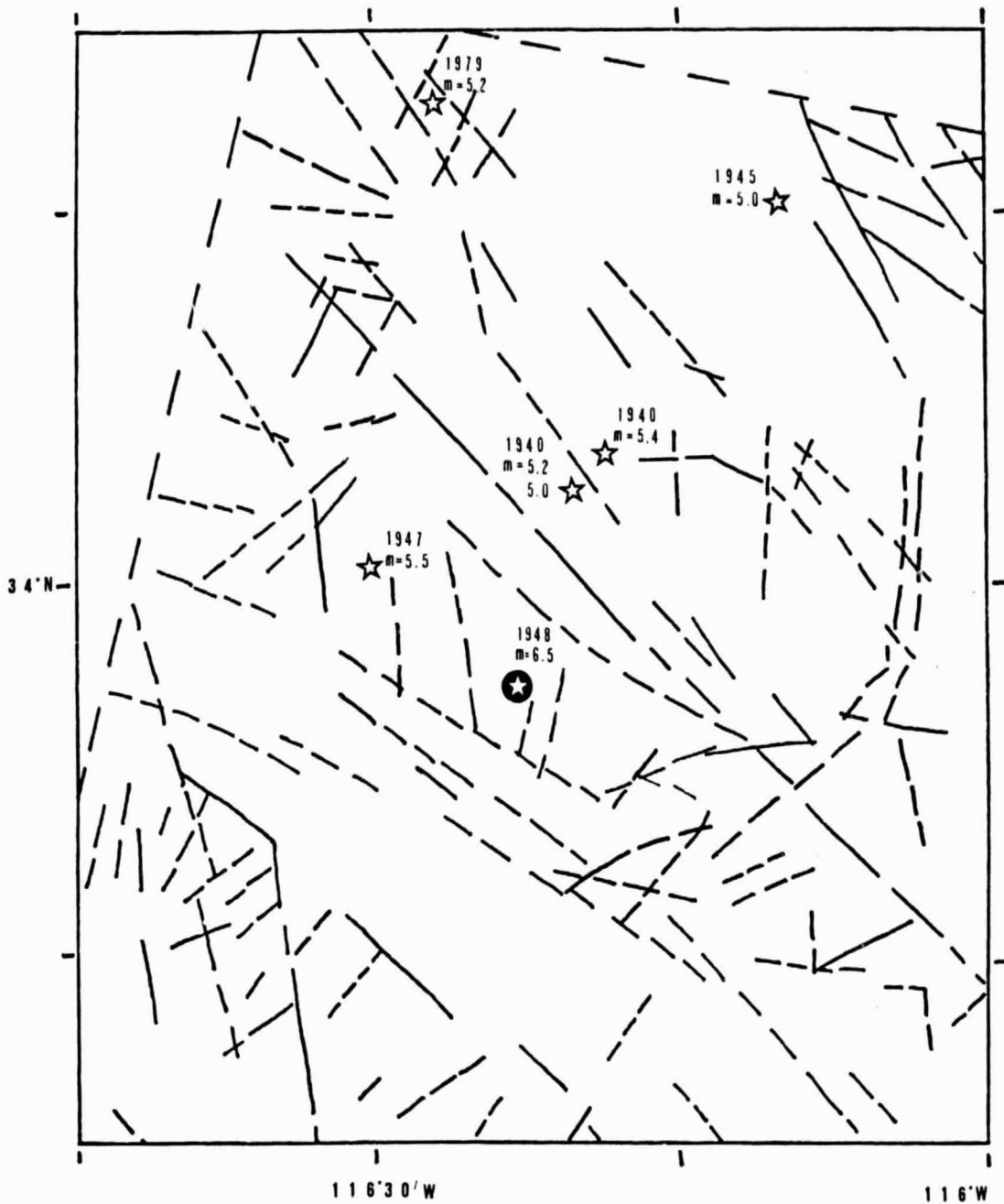


Figure 9b. Earthquakes of magnitude greater than 5 from 1932-1979 in Salton Sea region S1 and associated focal mechanisms.

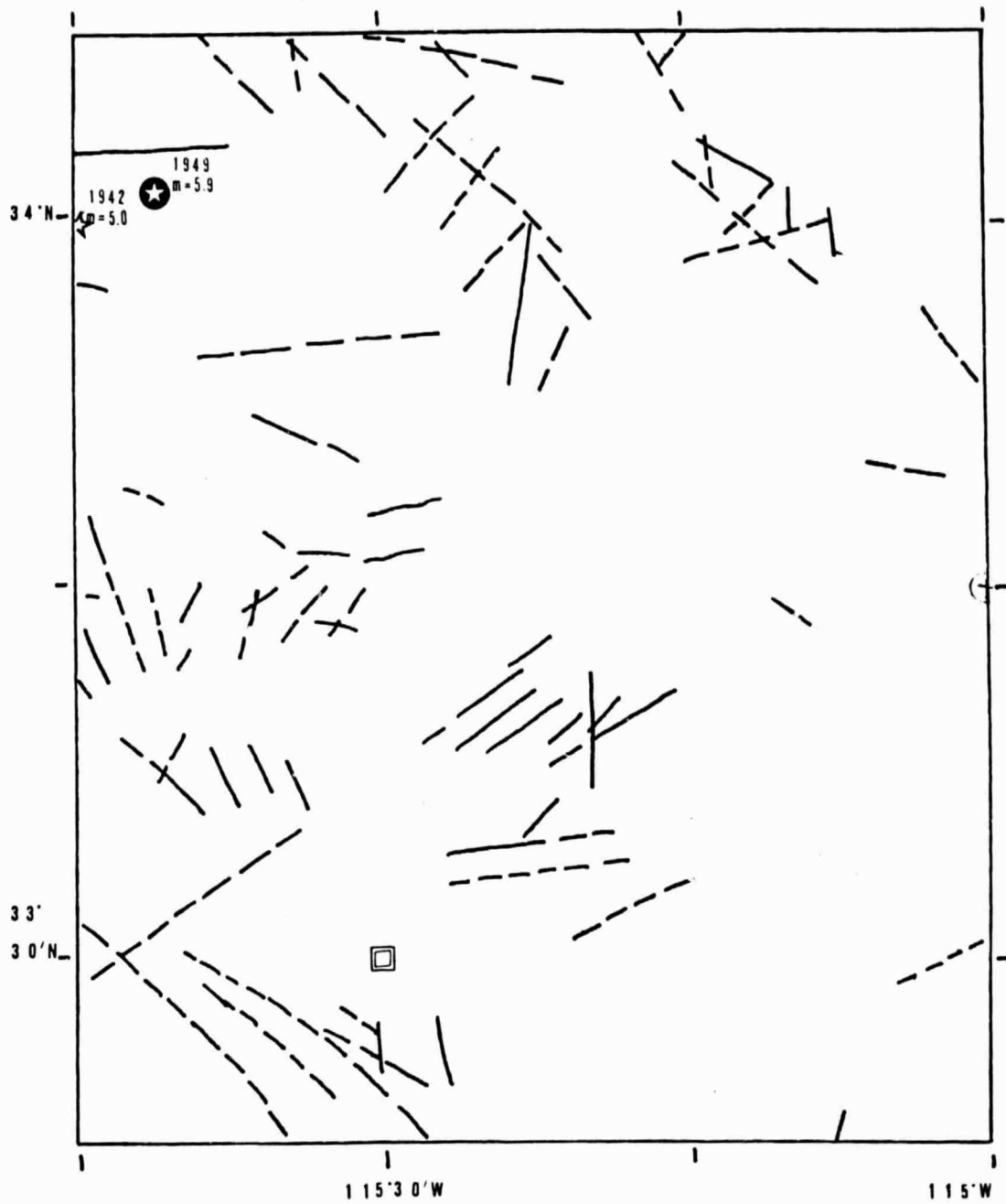


Figure 9c. Earthquakes of magnitude greater than 5 from 1932-1979 in Salton Sea region S2 and associated focal mechanisms.

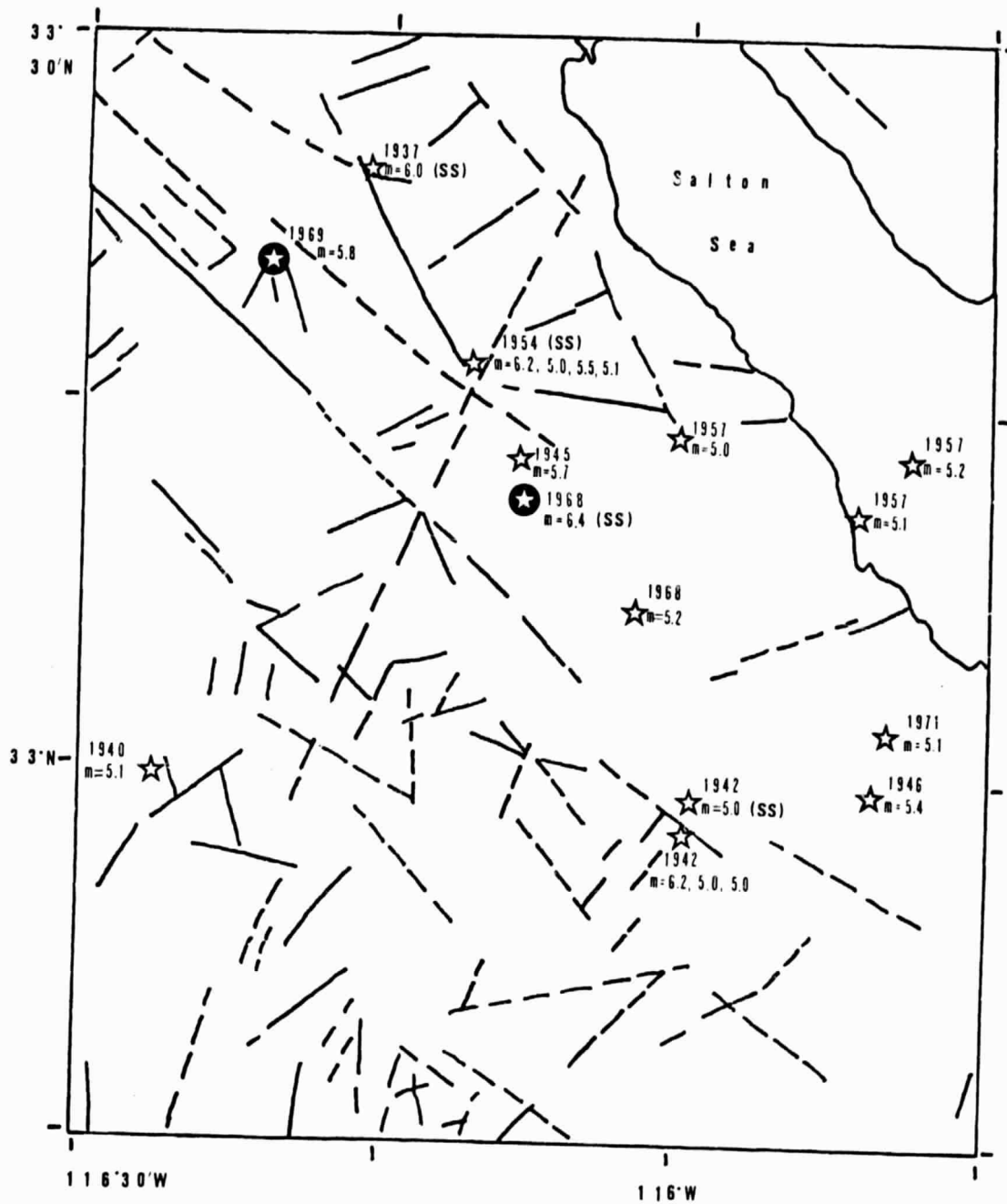


Figure 9d. Earthquakes of magnitude greater than 5 from 1932-1979 in Salton Sea region S3 and associated focal mechanisms.

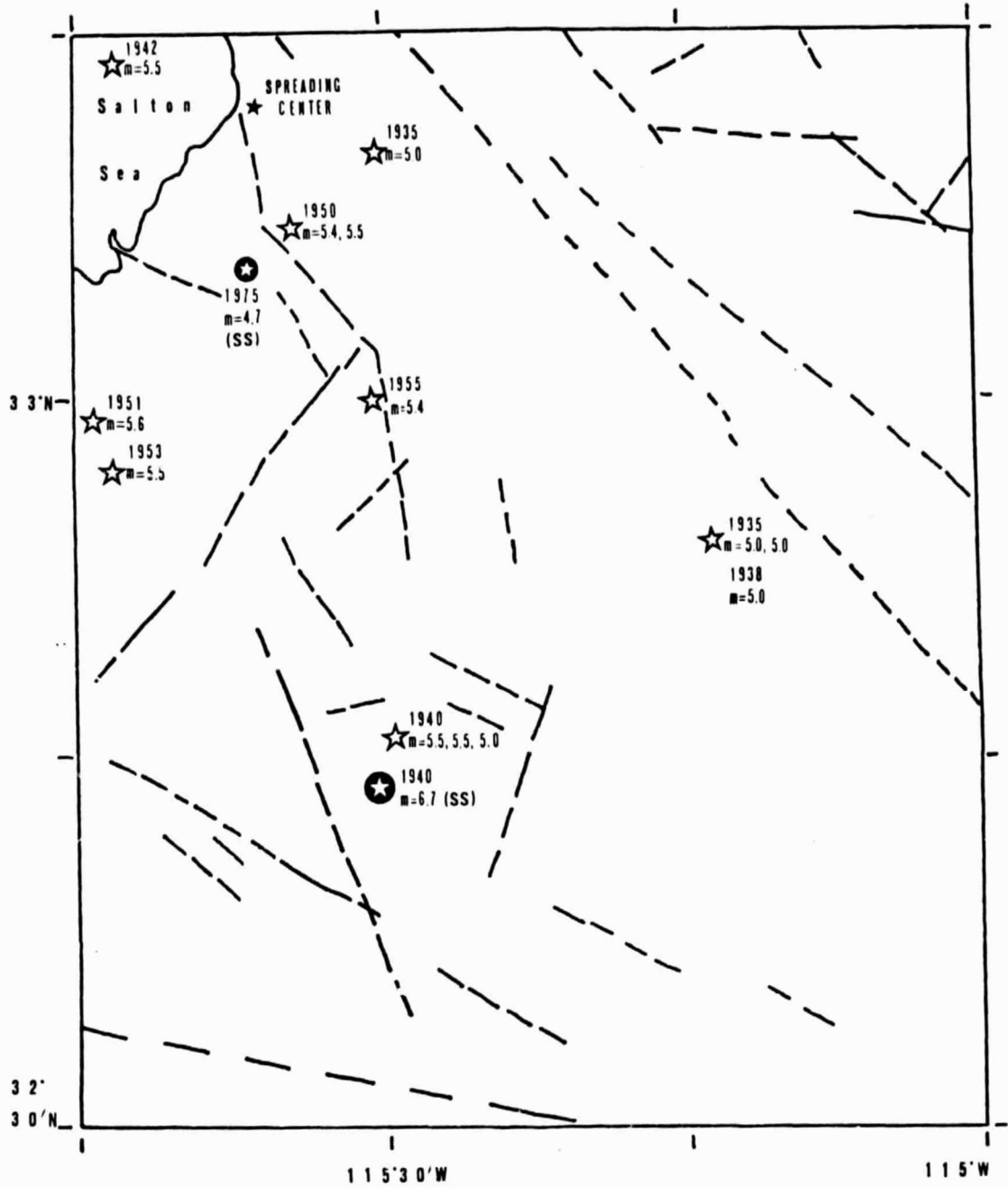


Figure 9e. Earthquakes of magnitude greater than 5 from 1932-1979 in Salton Sea region S4 and associated focal mechanisms.

ORIGINAL PAGE IS  
OF POOR QUALITY

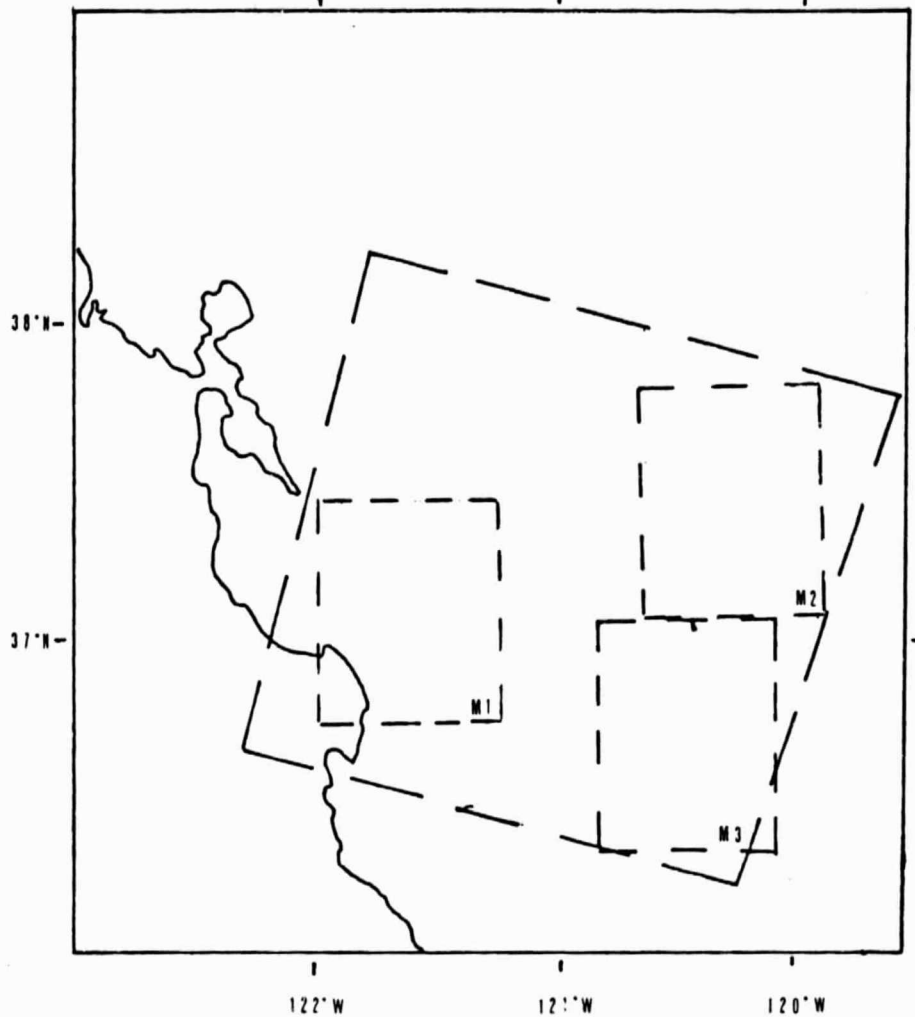


Figure 10a. Base map of Central California. The large dashed line shows the region in the Landsat imagery. M1, M2, and M3 are the areas shown in Figures 10b-d and Figure 16. (scale of figures: 1 cm = 5 km)

Symbols used in Figures 10b-10d:

- ☆ Earthquake epicenter of magnitude  $\geq 5$
- ⊛ Earthquake epicenter of magnitude  $\geq 5$  (test point)
- ⊙ Earthquake epicenter (test point)
- Test point

(SS) Strike-slip focal mechanism

(DS) Dip-slip focal mechanism

(T) Thrust focal mechanism

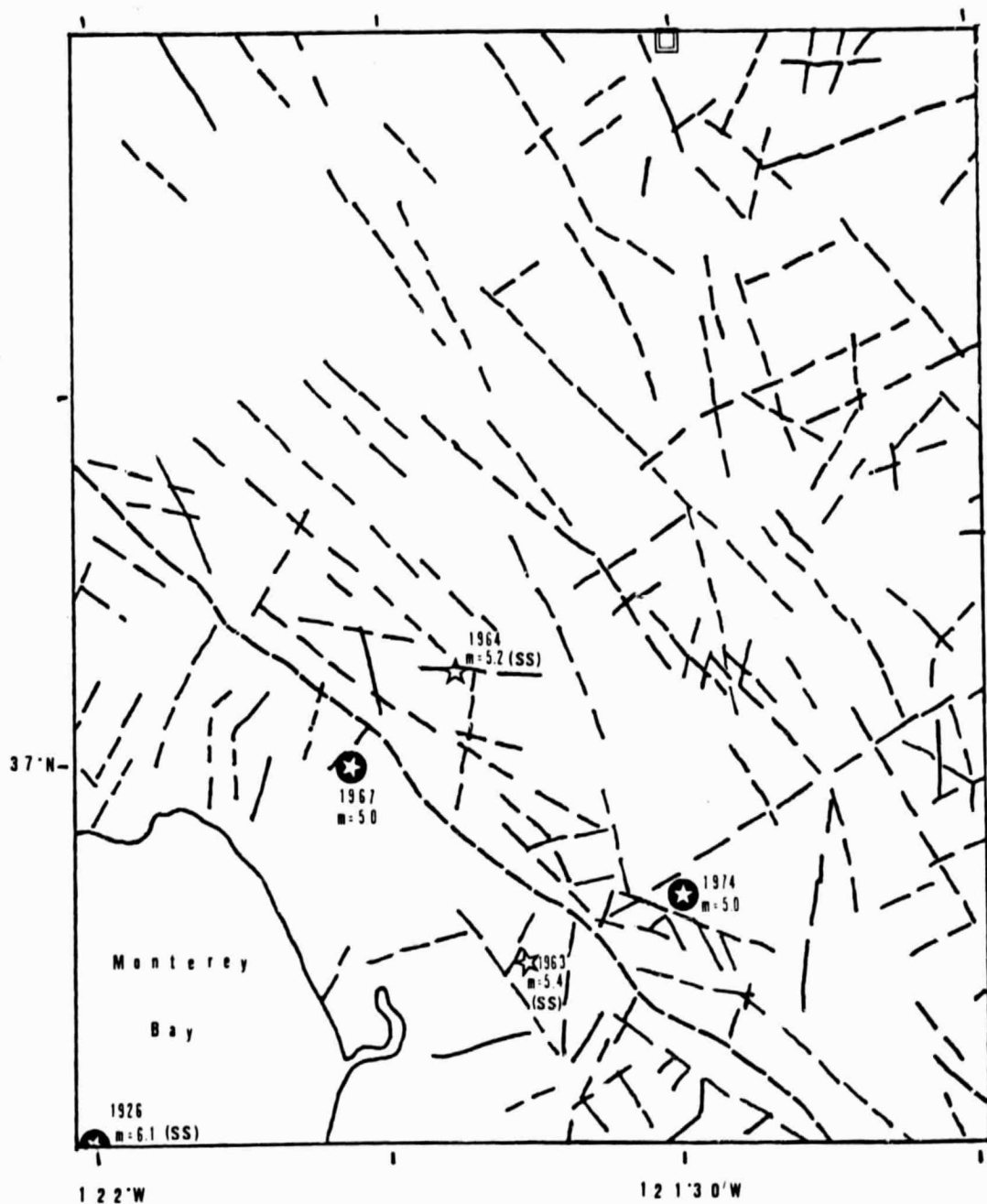


Figure 10b. Earthquakes of magnitude greater than 5 from 1963-1976 between Monterey and San Francisco (Central California region M1) and associated focal mechanisms.

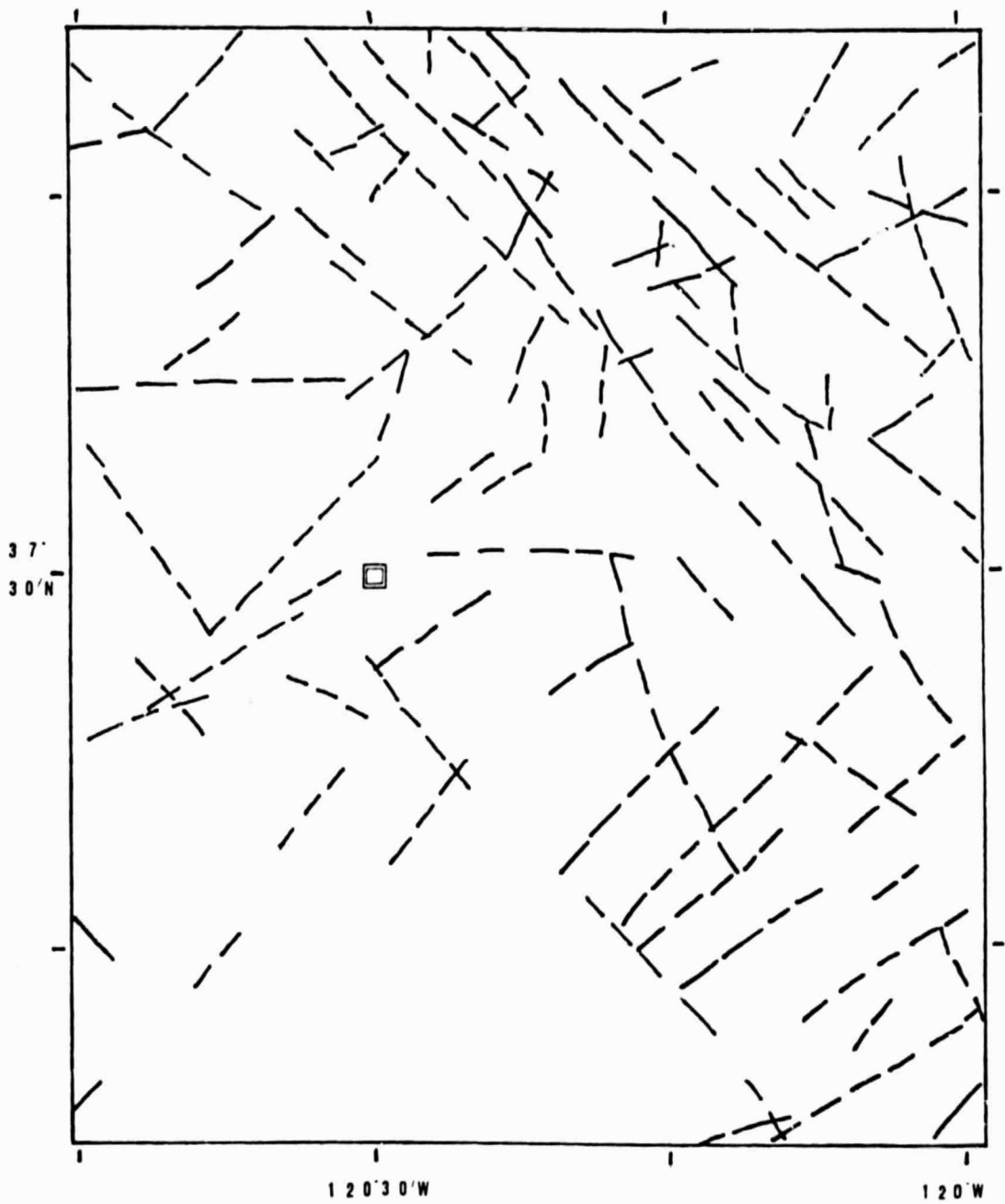


Figure 10c. Earthquakes of magnitude greater than 5 from 1963-1976 between Monterey and San Francisco (Central California region M2) and associated focal mechanisms.



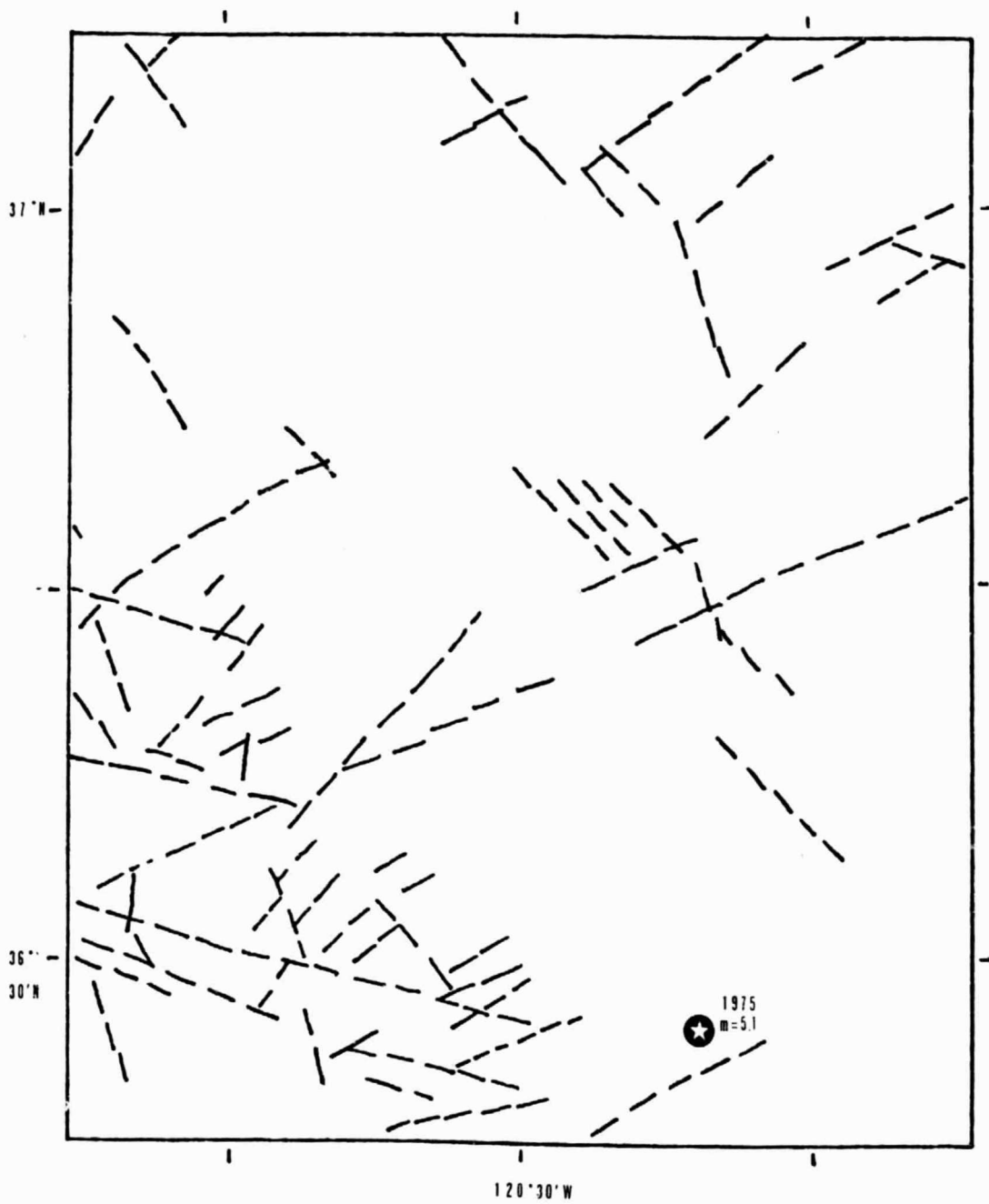


Figure 10d. Earthquakes of magnitude greater than 5 from 1963-1976 between Monterey and San Francisco (Central California region M3) and associated focal mechanisms.

there are two sets of lineaments (see Figure 11). One set trending from  $N40^{\circ}W$  to  $N70^{\circ}W$  reflects the orientation of the faults of the San Andreas system in this area. Another set ranges from  $N10^{\circ}E$  to  $N70^{\circ}E$ .

On the northeast side of the San Andreas fault there are two major orientations and two minor orientations of the lineaments that are prominent (see Figure 12). The two major trends are from  $N30^{\circ}W$  to  $N50^{\circ}W$  and from  $N30^{\circ}E$  to  $N40^{\circ}E$ . The first reflects the trend of the San Andreas fault as does one set of lineaments southwest of the fault. The minor orientations range from  $0^{\circ}N$  to  $N10^{\circ}E$  and from  $N50^{\circ}E$  to  $N60^{\circ}E$ .

The zones of activity in the Salton Sea region are concentrated mostly south of the Salton Sea along the Imperial, San Jacinto, and Coyote Creek faults and in the area where the San Andreas fault begins to splay into the other faults. Little activity is observed in the Mojave Desert area to the northeast. Figures 13a-13j show the lineaments mapped by the author and the locations of seismic activity. The seismic data for this region were extensive. As shown on these figures, the mapped lineaments are concentrated in the same locations as the greatest seismic activity. The more recent events are associated with the more prominent lineaments on the satellite imagery. For example, the lineaments on and near the 1968 (Borrogo

ORIGINAL PAGE IS  
OF POOR QUALITY

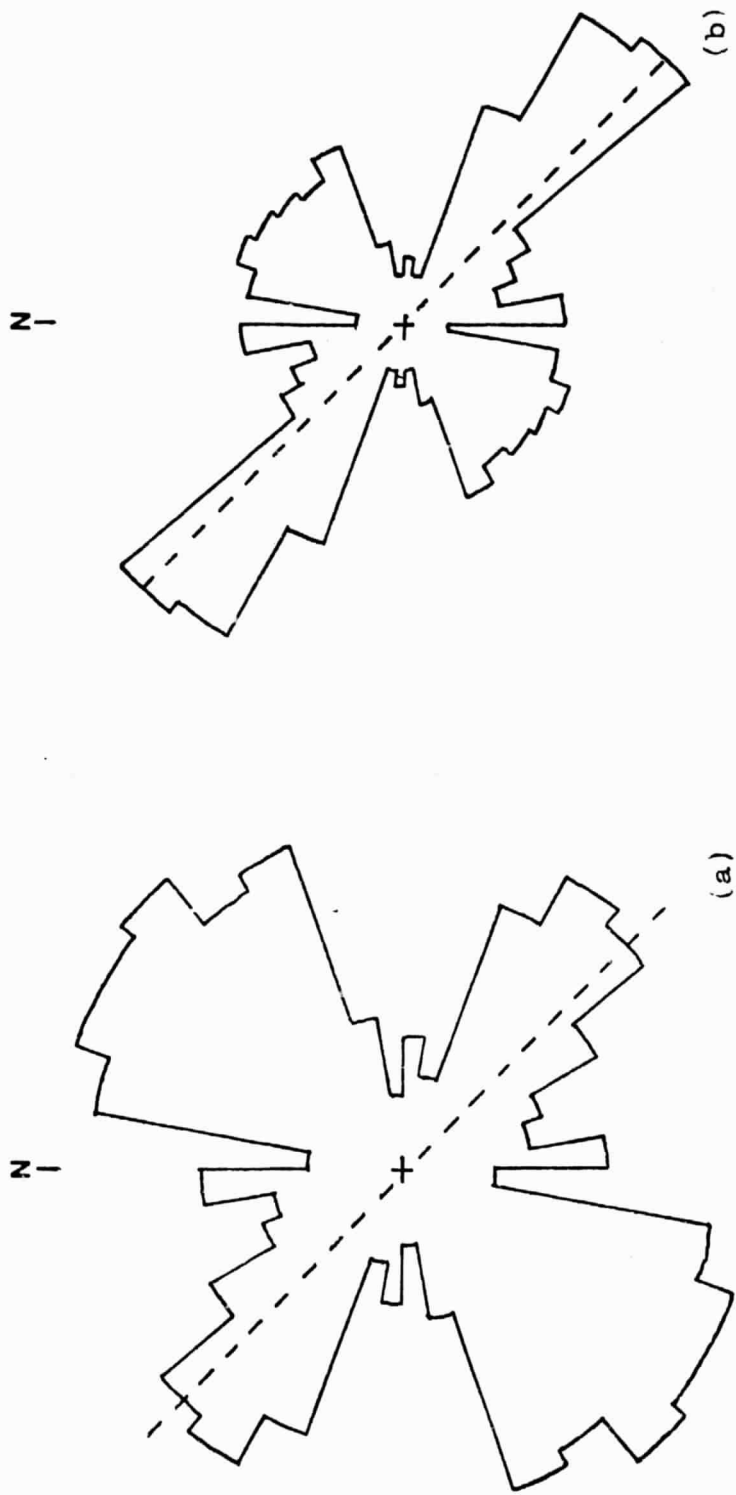


Figure 11. Rose diagrams of lineaments SW of the San Andreas fault (dashed line) in the Salton Sea region. (a) frequency (1"=1340 km) (b) length (1"=10 lineaments).

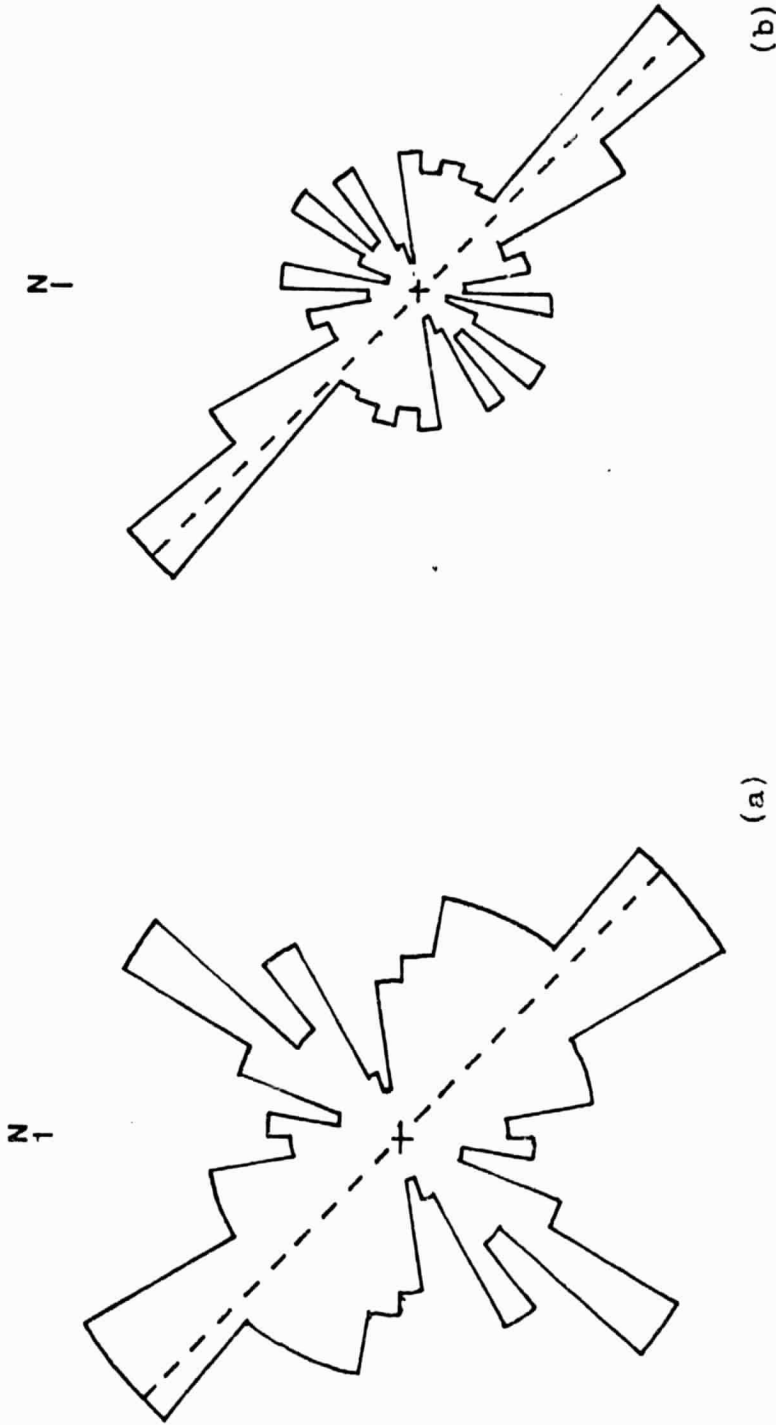


Figure 12. Rose diagrams of lineaments NE of the San Andreas fault (dashed line) in the Salton Sea region. (a) frequency (1"=1155 km) (b) length (1"=8.5 lineaments).

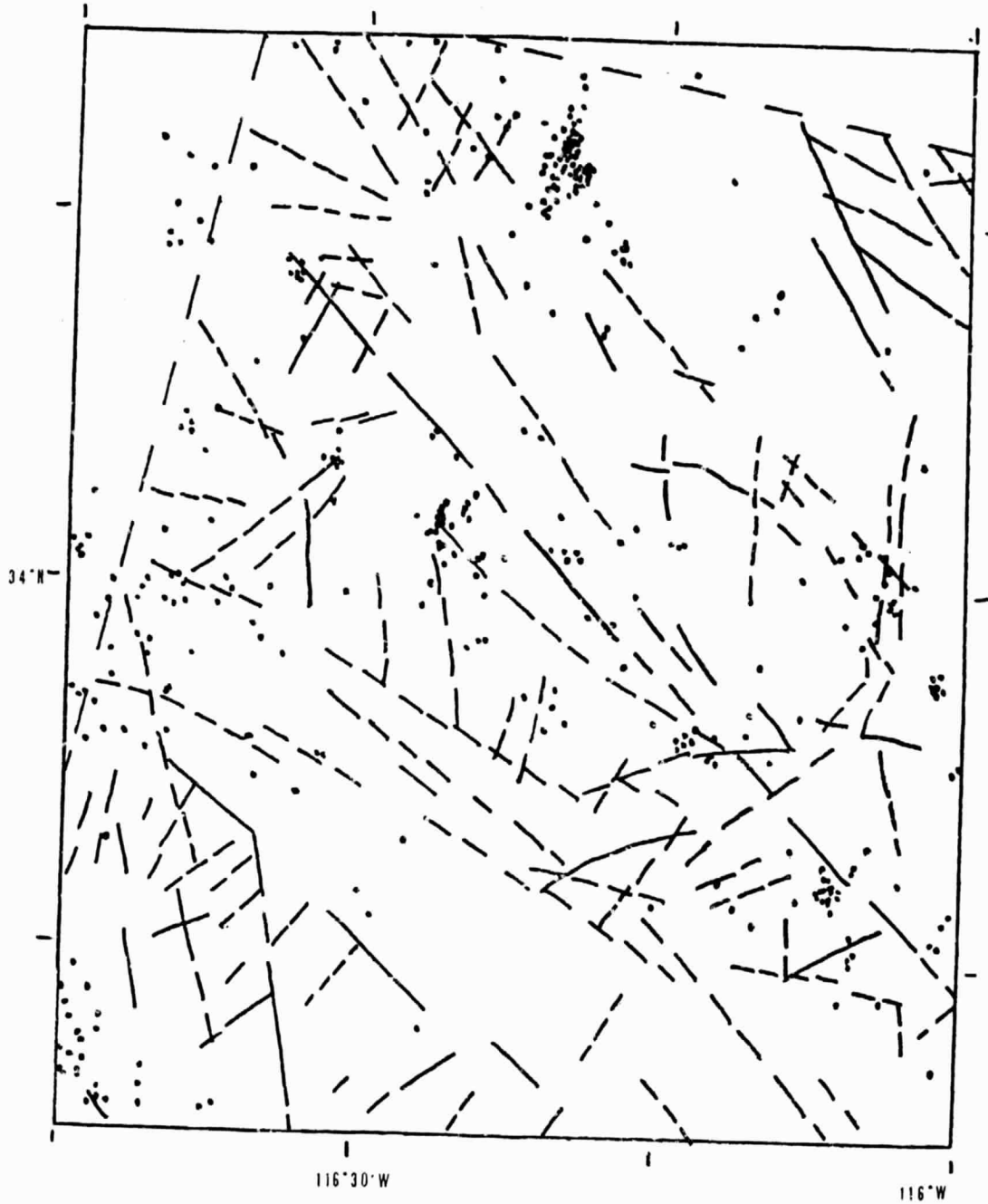


Figure 13a. Mapped lineaments and seismicity in Salton Sea region S1. The red dots represent locations of 1975 events of all magnitudes.

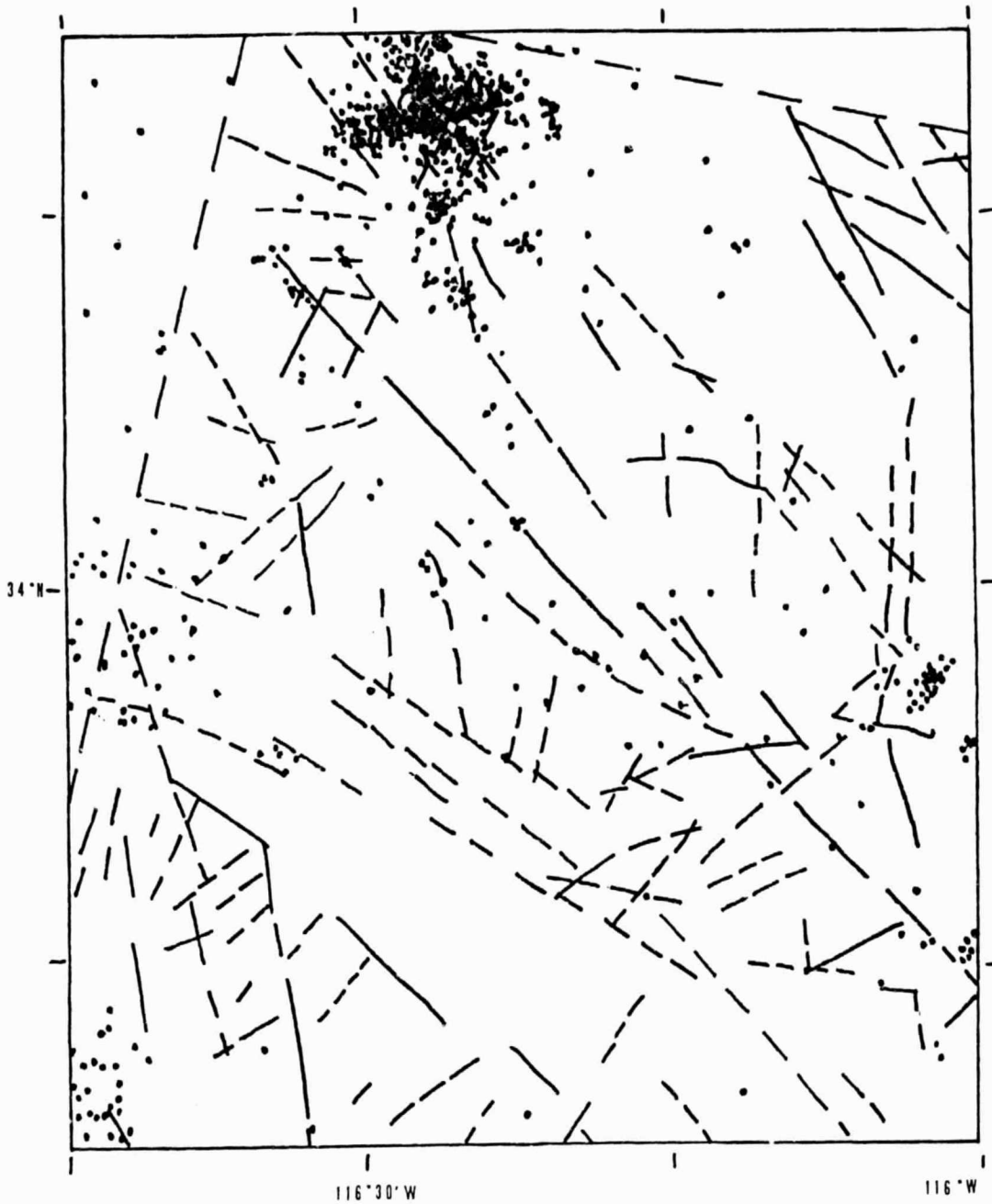


Figure 13b. Mapped lineaments and seismicity in Salton Sea region S1. The red dots represent locations of 1979 events of magnitude less than 2.

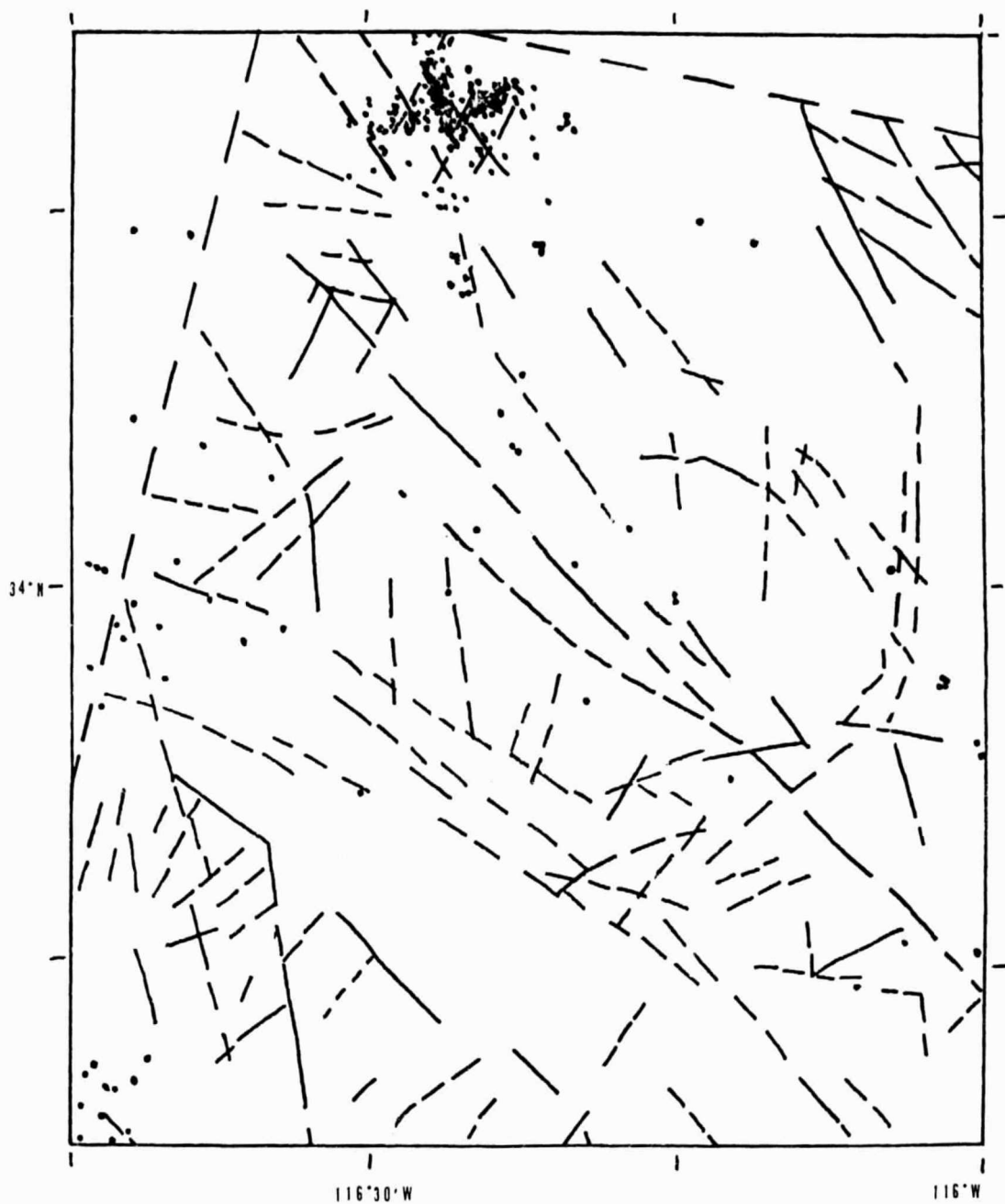


Figure 13c. Mapped lineaments and seismicity in Salton Sea region S1. The red dots represent locations of 1979 events of magnitude greater than or equal to 2.

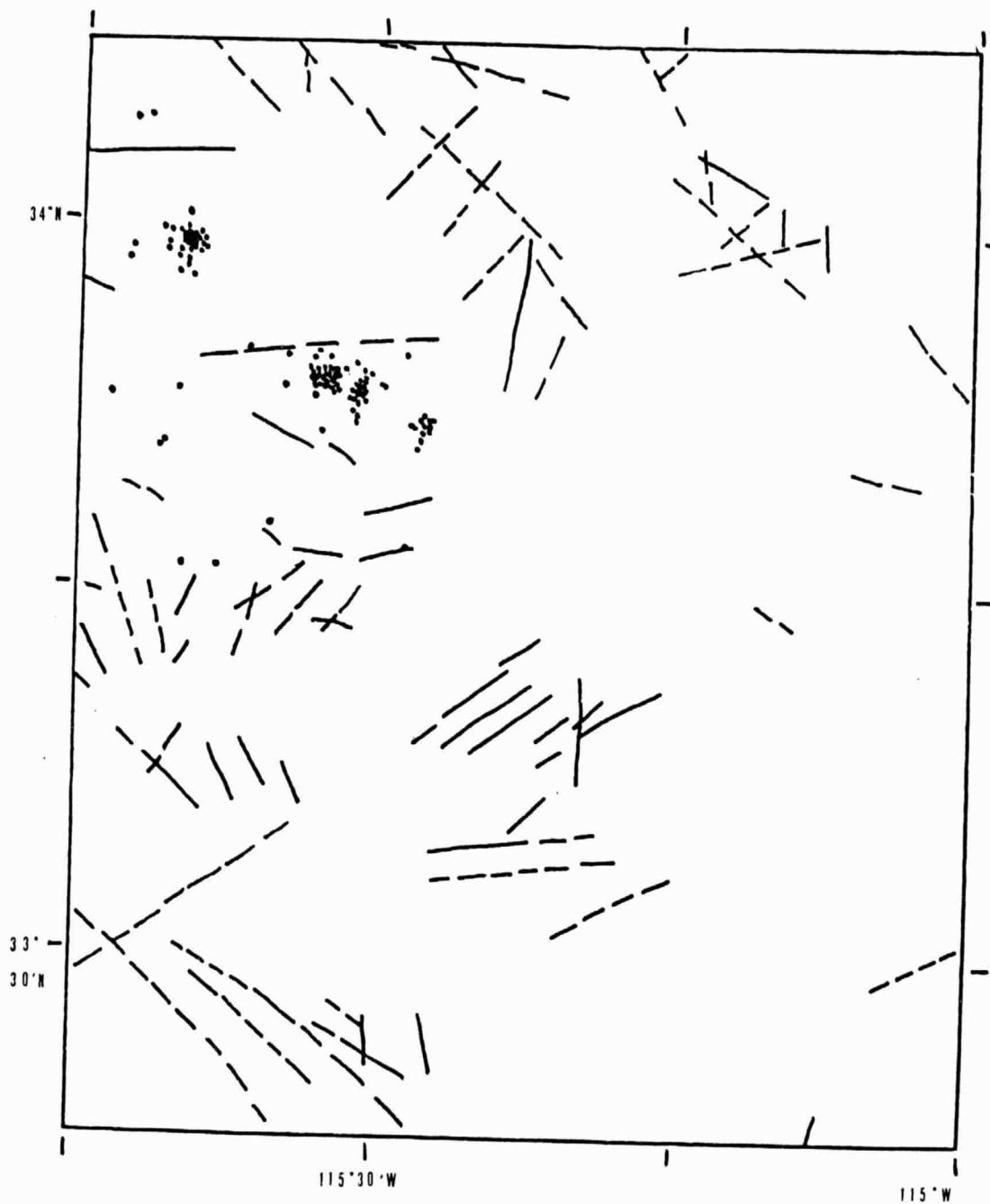


Figure 13d. Mapped lineaments and seismicity in Salton Sea region S2. This is the more stable Mojave Desert region. The red dots represent locations of events of all magnitudes which occurred in 1975.



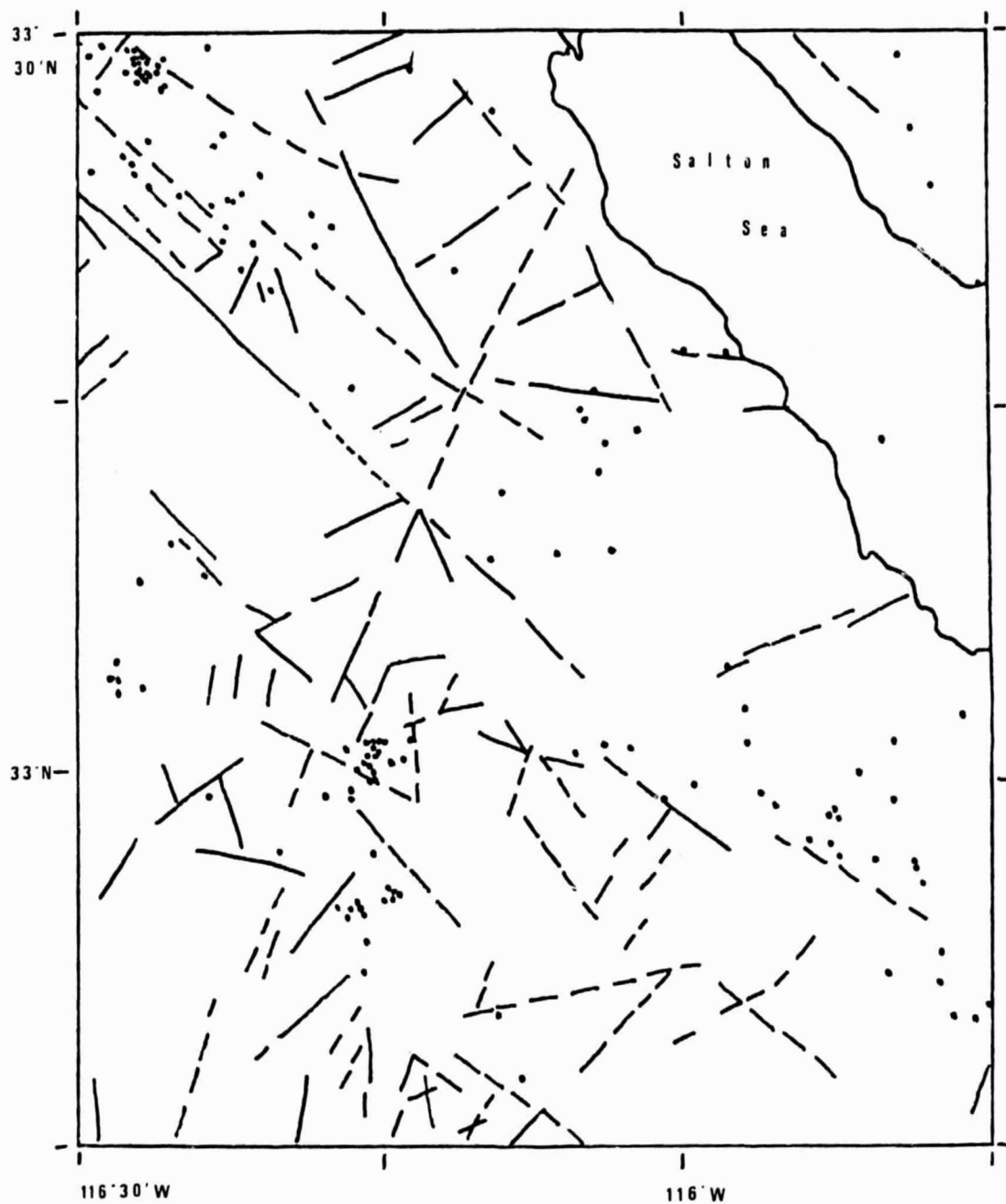


Figure 13e. Mapped lineaments and seismicity in Salton Sea region S3. The red dots represent locations of 1975 events of all magnitudes.

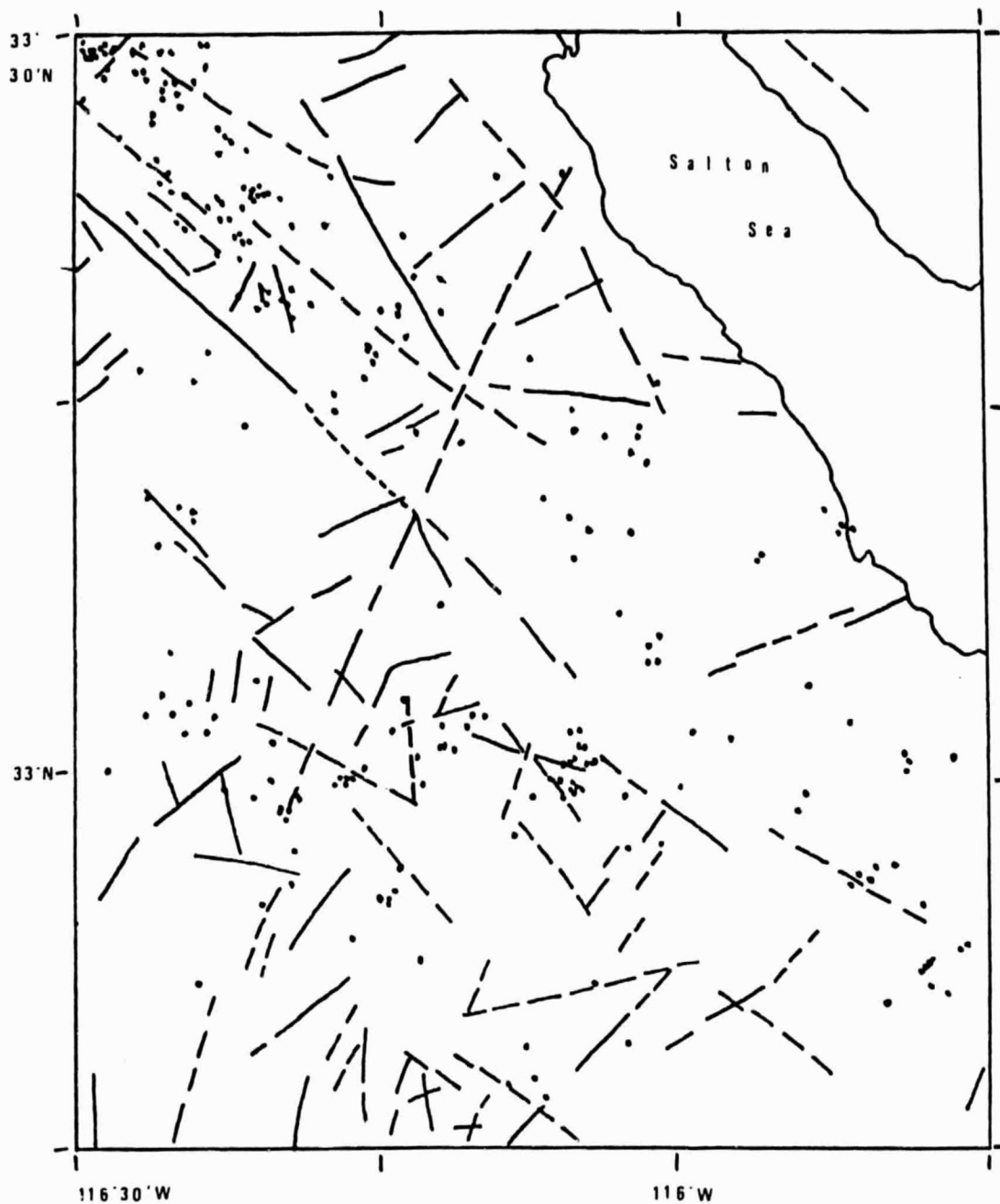


Figure 13f. Mapped lineaments and seismicity in Salton Sea region S3. The red dots represent locations of 1979 events of magnitude less than 2.

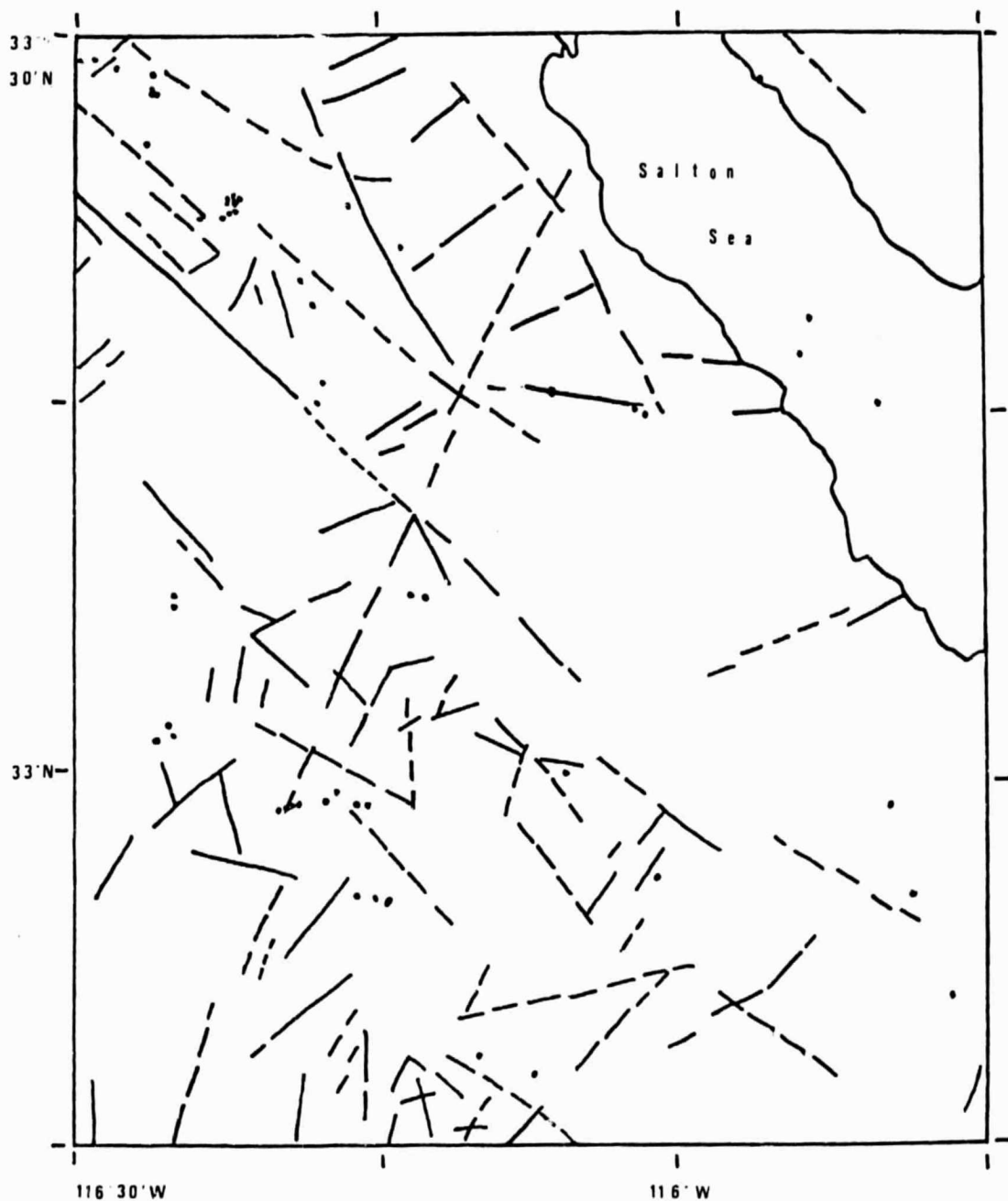


Figure 13g. Mapped lineaments and seismicity in Salton Sea region S3. The red dots represent locations of 1979 events of magnitude greater than or equal to 2.

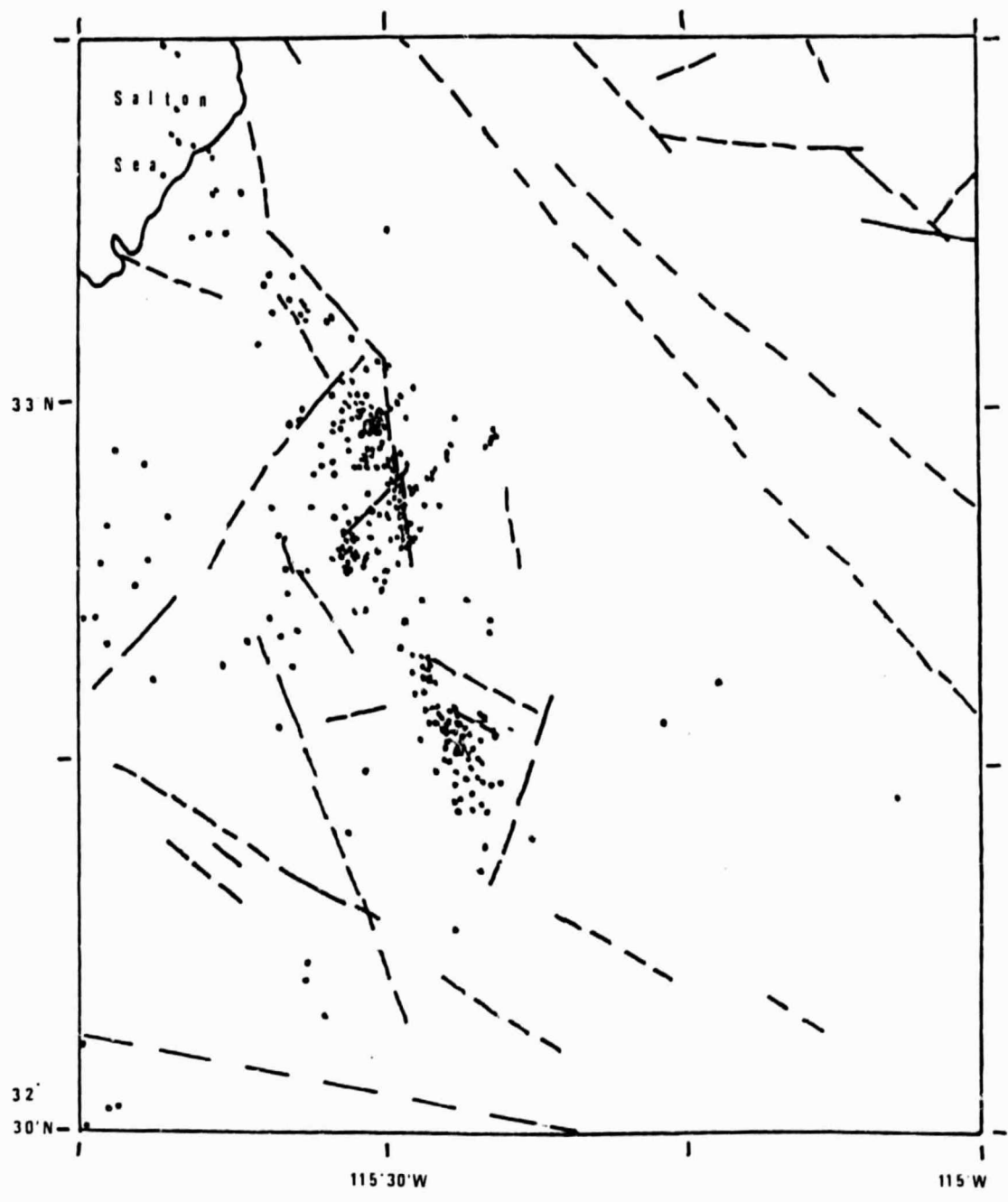


Figure 13h. Mapped lineaments and seismicity in Salton Sea region S4. The red dots represent locations of 1975 events of all magnitudes.

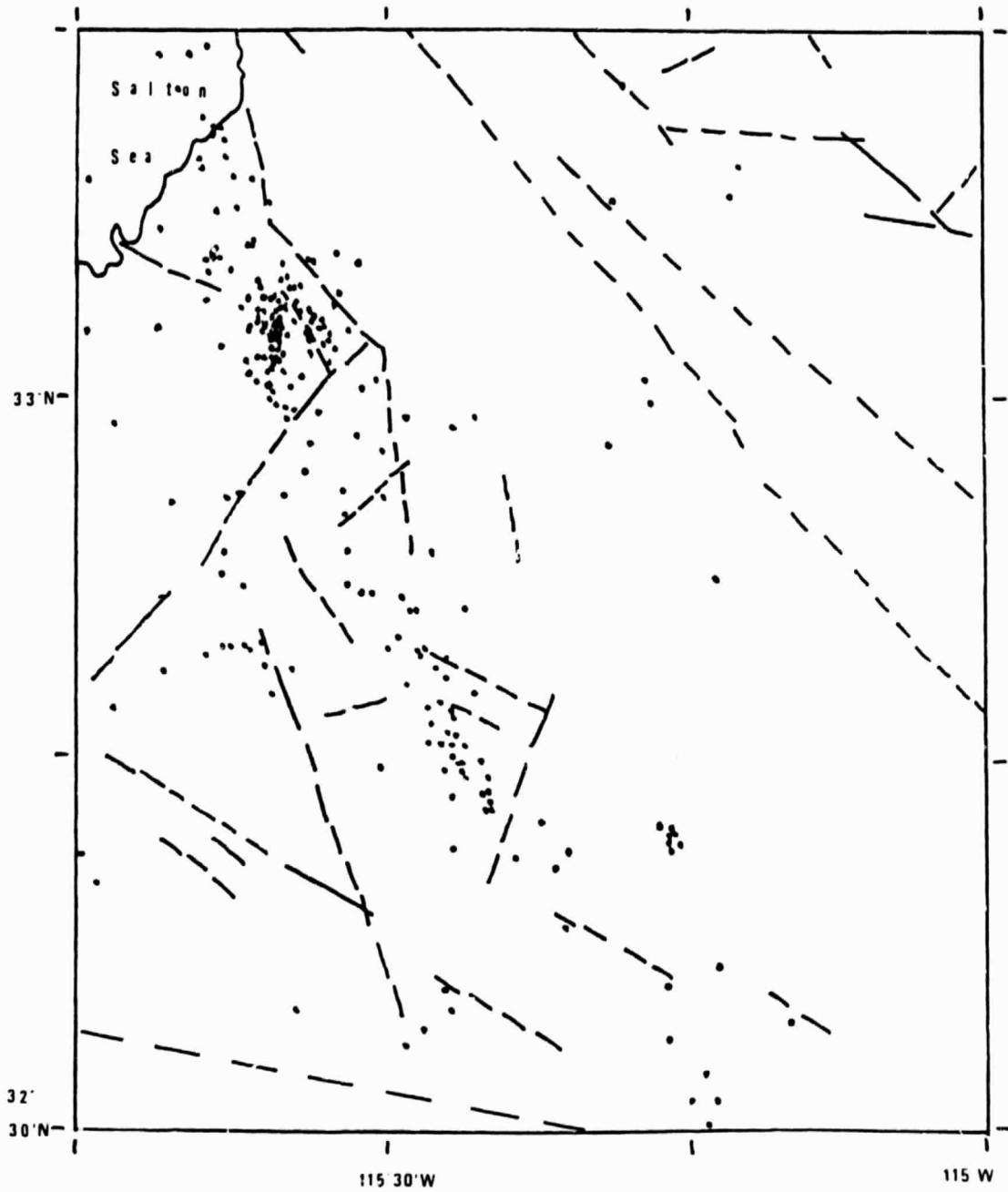


Figure 131. Mapped lineaments and seismicity in Salton Sea region S4. The red dots represent locations of 1979 events of magnitude less than 2.

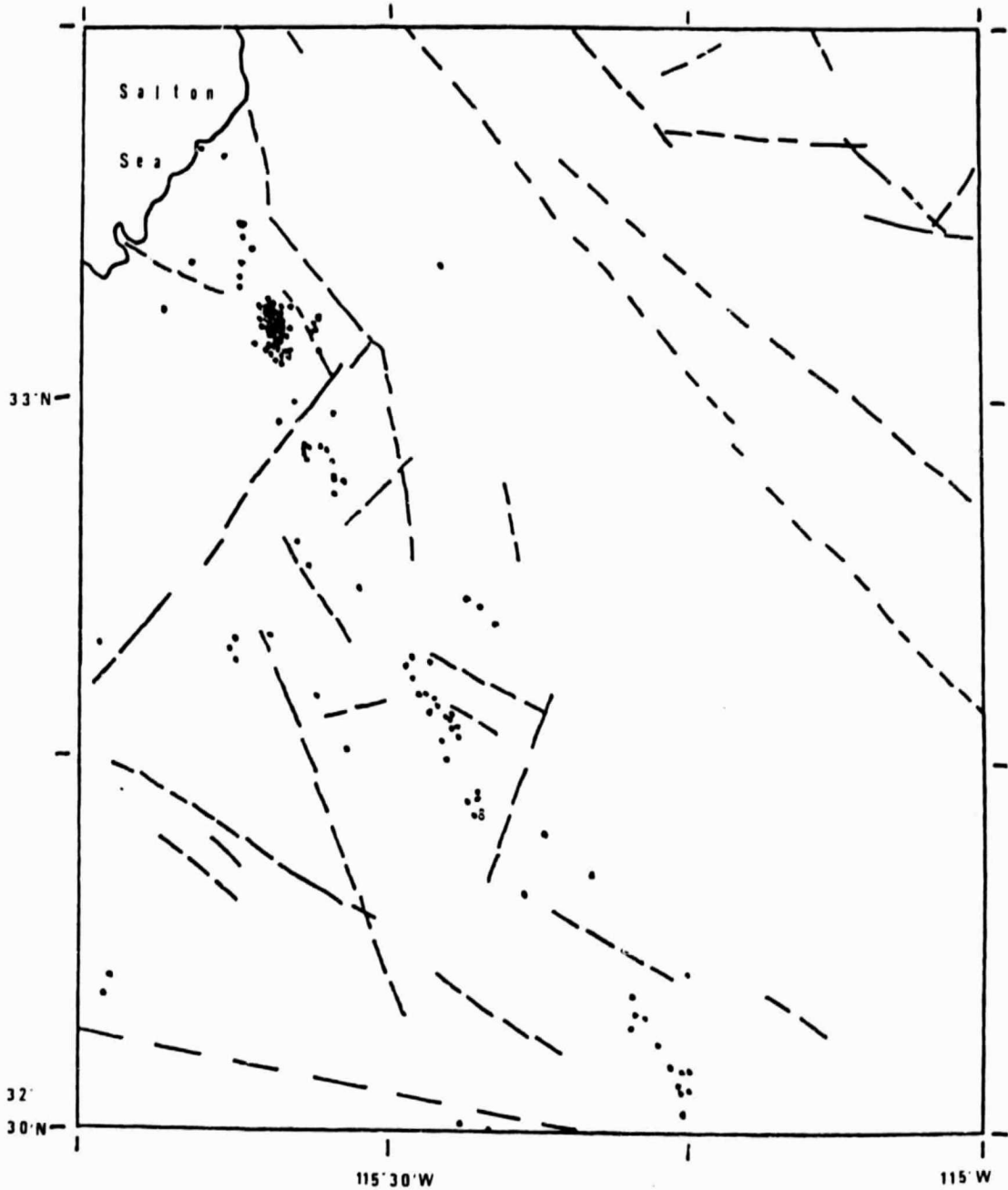
ORIGINAL PAGE IS  
OF POOR QUALITY

Figure 13j. Mapped lineaments and seismicity in Salton Sea region S4. The red dots represent locations of 1979 events of magnitude greater than or equal to 2.

Mt.), 1969 (Coyote Mt.), and 1975 (Brawley) earthquakes are very prominent (refer to Figures 7b, 9d, and 9e). The features easily identifying these lineaments are a sharp visual contrast in environments across the lineaments and offset streams. These lineaments include the Coyote Creek, San Jacinto, Superstition Hills, and Imperial faults where there were observations of lateral surface displacement. Although this study involves only a visual study of the images, it is apparent that further enhancement of the digital images and the addition of radar imagery will increase the distinction of the more recent geological features. The most recent features are less likely to be blurred or suppressed by agricultural, cultural, and erosional factors. It appears that the preferential association of seismic events with the lineaments is independent of the magnitude of the events. This was expected to be true since the majority of smaller magnitude events occur in the same locations as the stronger earthquakes. Only two plotted events occurred in the Mojave Desert area where no lineaments are mapped and those events were of magnitude less than 2.

Six epicentral locations and two locations where no strong earthquakes are known to have occurred were used to examine the characteristics of strike-slip events near the Salton Sea. The six epicentral locations were chosen to

represent different areas of significant seismic activity. The other test points were chosen to sample the less active areas. Table 7 is a list of the locations, nearby epicenters, and the more important characteristics of these areas. The importance of a combination of traits is shown from these data. Although some characteristics of the inactive locations are the same as in an epicentral location, the overall patterns are distinguishable. Current seismic activity, lineament intersections, and numerous lineaments characterize most epicentral locations. One test point in the stable area has had no large earthquakes and the other test point in a less active region has had fewer earthquakes than most of the test points in seismically active locations. Both of these points have fewer lineaments and lineament intersections than the more active regions. Areas with numerous lineaments and lineament intersections where evidence of recent active faulting is observed are inferred to be likely sites of future events. The test points that are at epicentral locations are within 5 km of a mapped lineament and an average of 6.7 km from a lineament intersection. In this region the distance to the Salton Sea and the distance to known spreading centers appear to be insignificant. All locations in the investigation were the same relative distance from these features. It may be important that the points lie within 50 km of the San Andreas fault zone, however.



Table 7. Characteristics of events near the Salton Sea

Latitude (°N)	33.083	33.113	33.343	33.933	34.017	32.753	33.250	33.500
Longitude (°W)	115.600	116.037	116.346	116.383	115.683	115.500	115.000	115.500
Date of event	1975	1968	1969	1948	1949	1940	---	---
Magnitude	4.7	6.4	5.8	6.5	5.9	6.7	---	---
Relief	low	moderate	sharp	moderate	sharp	low	sharp	moderate
Distance to spreading center (km)								
(lat 33.2°N, long 115.6°W)								
Number of earthquakes (1932-1979) magnitude >5 within 50 km	12	48	78	115	90	52	80	35
Distance to San Andreas (km)	18	17	11	9	4	11	0	5
Distance to Salton Sea (km)	20	50	50	10	40	35	60	15
Number of lineaments within 25 km	10	18	25	55	60	45	75	25
Number of parallel lineaments within 25 km	11	45	47	46	30	17	4	23
Number of lineament intersections within 25 km	8	13	20	19	20	7	0	10
Distance to nearest lineament (km)	4	19	19	21	10	3	0	4
Distance to nearest lineament intersection (km)	2	4	0	1	4	3	10	5
	3	8	0	5	15	9	30	5

The San Andreas fault trends approximately  $N45^{\circ}W$  from Monterey to San Francisco. On the northeast side of the fault there are two major trends and two minor trends of the mapped lineaments (see Figure 14). The major orientations range from  $N40^{\circ}E$  to  $N70^{\circ}E$  and from  $N40^{\circ}W$  to  $N50^{\circ}W$ . The minor orientations range from  $N20^{\circ}E$  to  $N30^{\circ}E$  and from  $N70^{\circ}W$  to  $N80^{\circ}W$ . On the southwest side of the fault there are two trends observed (see Figure 15). These range from  $N30^{\circ}E$  to  $N70^{\circ}E$  and from  $N30^{\circ}W$  to  $N40^{\circ}W$ .

A less complete catalogue of seismicity was used for the Central California area. The activity is concentrated around the San Andreas fault. Figure 16 shows the lineaments mapped by the author and the related seismicity.

Five locations were chosen for the analysis of this region. Three of these are epicentral locations and two are located in areas less seismically active. A summary of the data is listed in Table 8. These data agree with the conclusions from the Salton Sea data. The main characteristics of strike-slip events are the nearness of the San Andreas fault (<50 km), numerous nearby lineaments and lineament intersections, and active faulting.

An image of an area in Nevada where events are associated with dip-slip movement was interpreted (see Figure 17). The trends of the lineaments are oriented in one major direction from  $0^{\circ}N$  to  $N30^{\circ}E$  (see Figure 18).

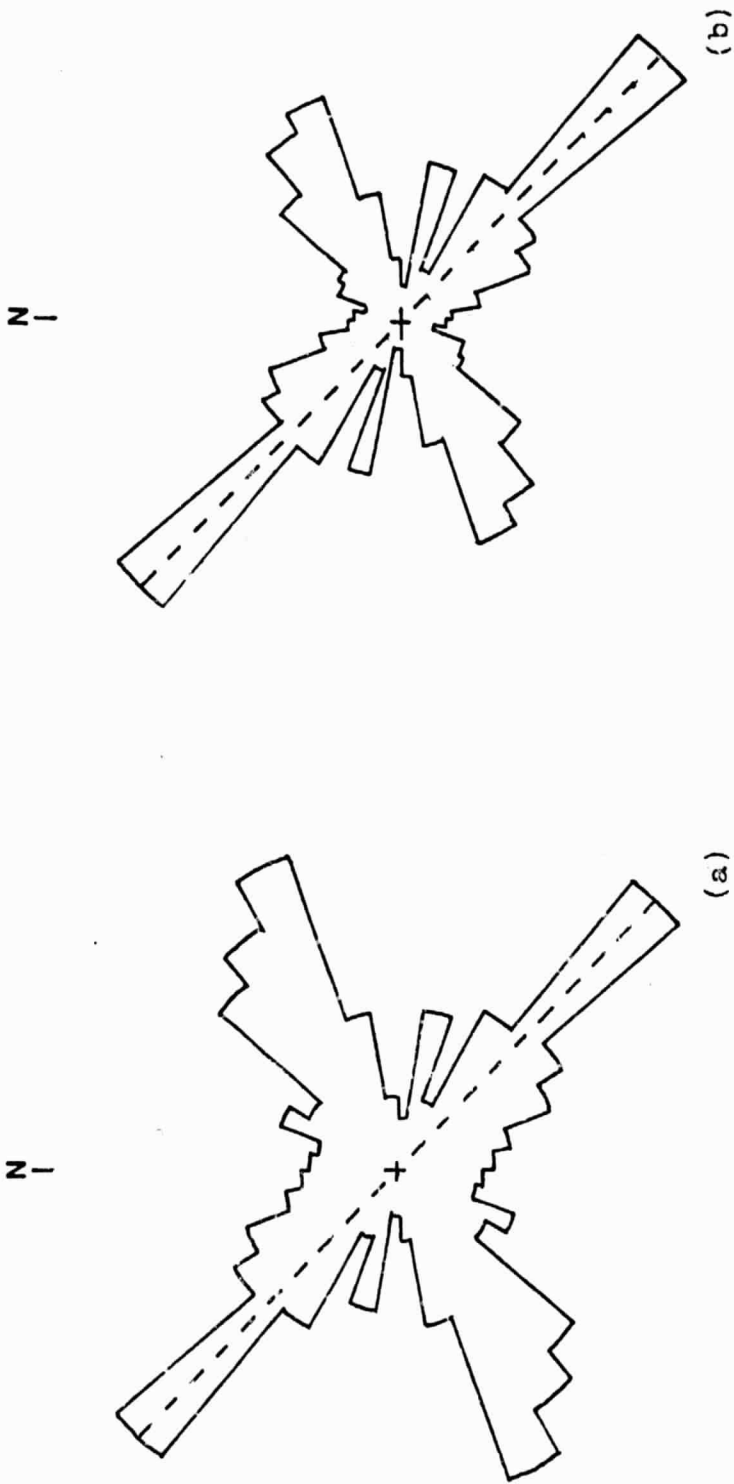


Figure 14. Rose diagrams of lineaments NE of the San Andreas fault (dashed line) in Central California. (a) frequency (1"=30.5 lineaments), (b) length (1"=37.45 km)

ORIGINAL PAGE IS  
OF POOR QUALITY

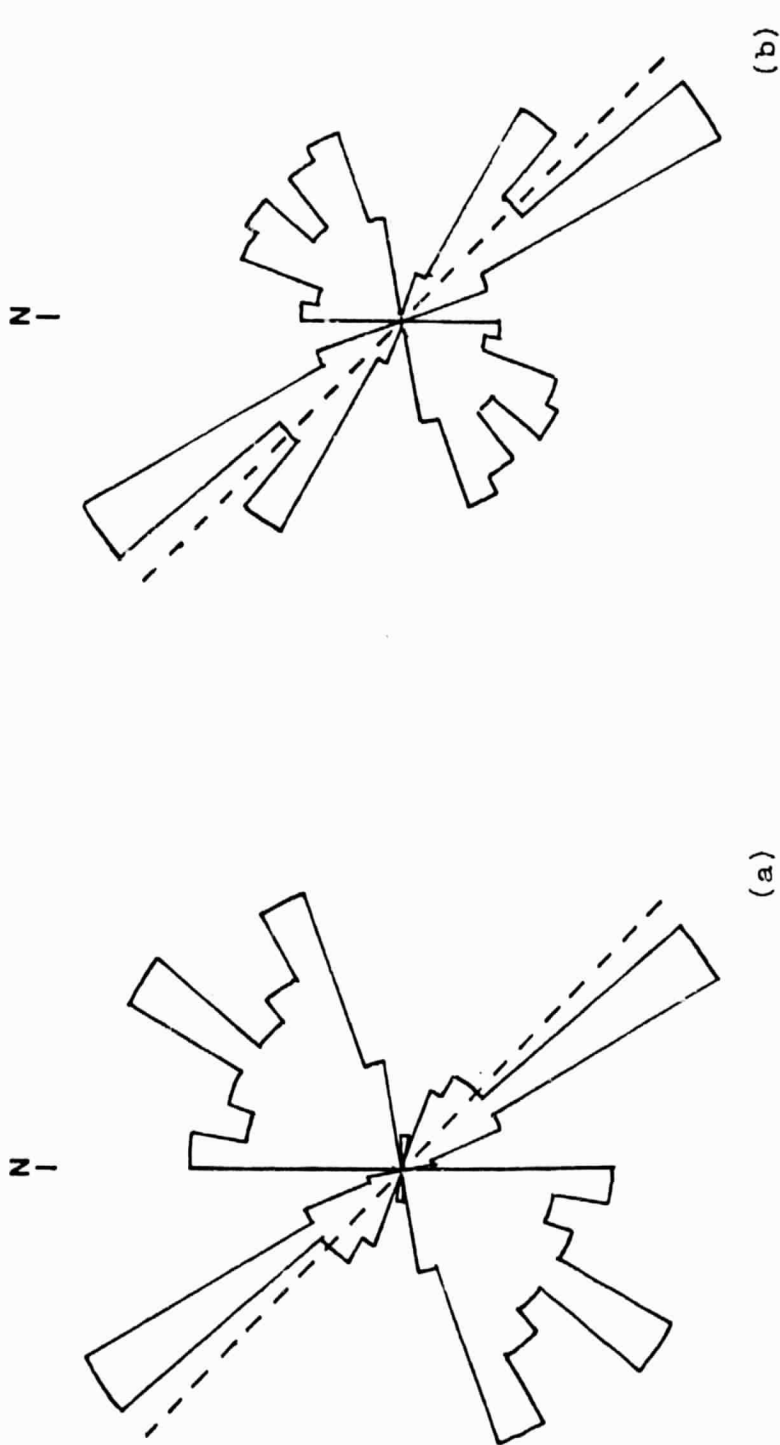


Figure 15. Rose diagrams of lineaments SW of the San Andreas fault, (dashed line) in Central California. (a) frequency (1"=7 lineaments), (b) length (1"=630 km)

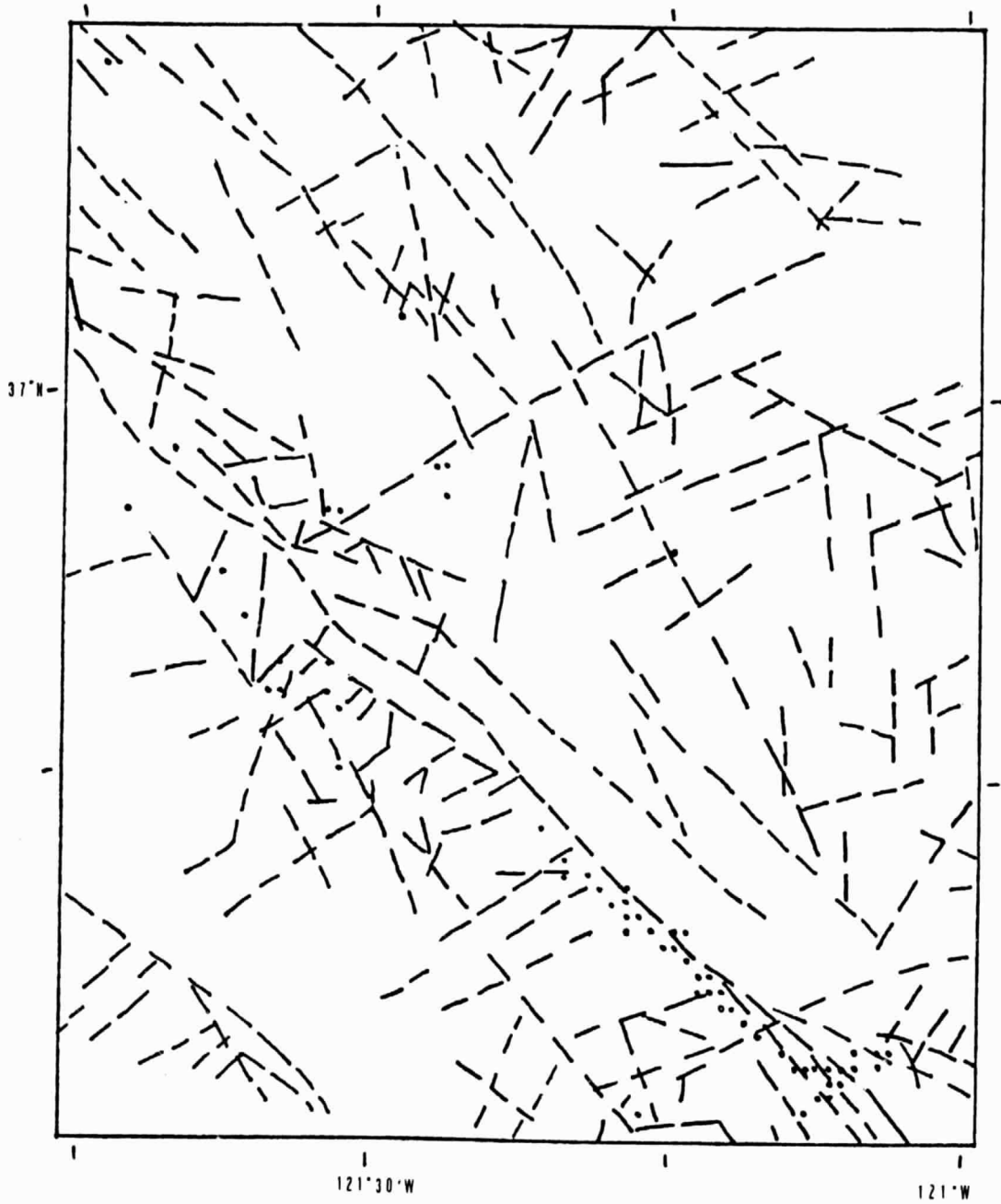


Figure 16. Mapped lineaments and seismicity in Central California region M1. The red dots represent locations of events which occurred in 1972.

Table 8. Characteristics of events between Monterey and San Francisco

Latitude (°N)	37.000	36.458	36.912	37.500	37.500
Longitude (°W)	121.780	120.345	121.497	120.500	121.500
Date of event	1967	1975	1974	---	---
Magnitude	5.0	5.1	5.0	---	---
Relief	sharp	moderate	moderate	low-	low-
Distance to spreading center (km) (lat 40.5°N, long 126.6°W)	300	-sharp 300	-sharp 300	moderate 300	moderate 300
Number of earthquakes (1963-1976) magnitude >5 within 50 km	4	1	4	0	0
Distance to San Andreas (km)	5	35	7	115	55
Distance to Pacific Ocean (km)	8	120	25	135	65
Number of lineaments within 25 km	48	>14	78	24	41
Number of parallel lineaments within 25 km	20	>9	15	11	18
Number of lineament intersections within 25 km	21	>8	43	6	11
Distance to nearest lineament (km)	2	3	0	1	0
Distance to nearest lineament intersection (km)	5	10	0	6	6

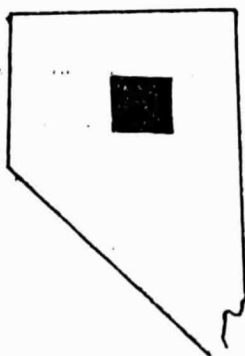
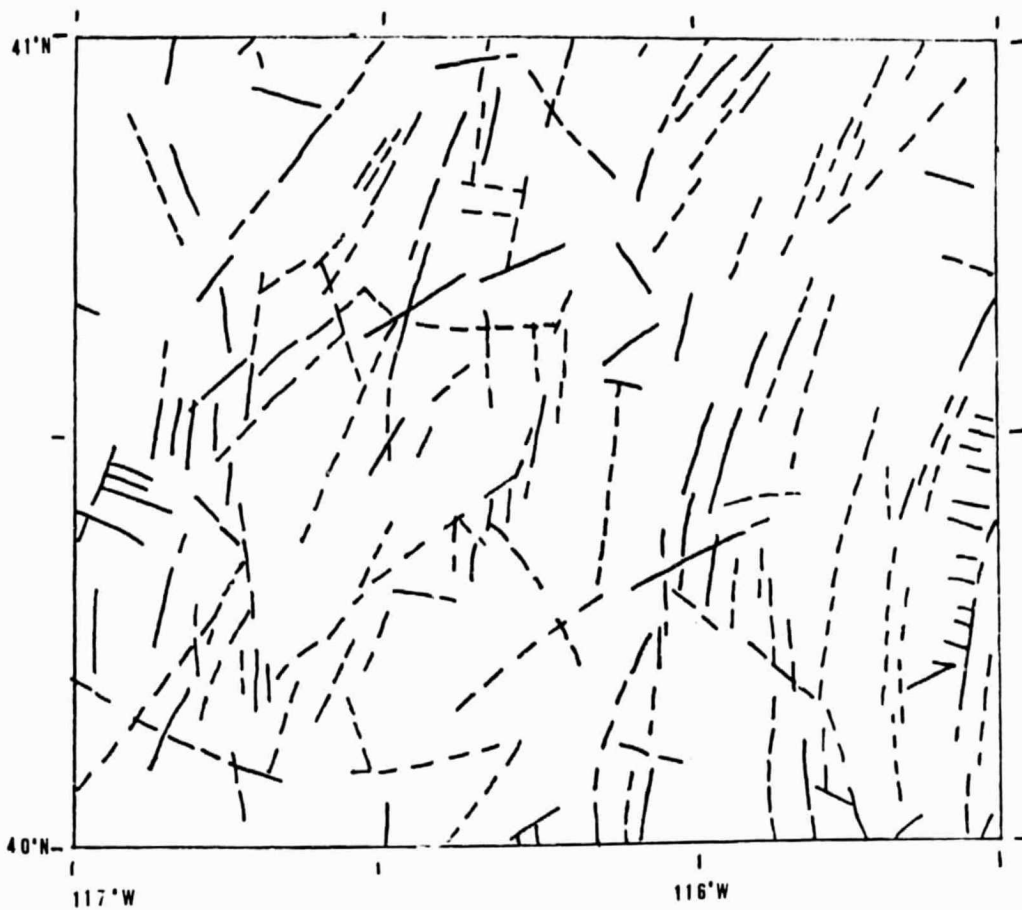
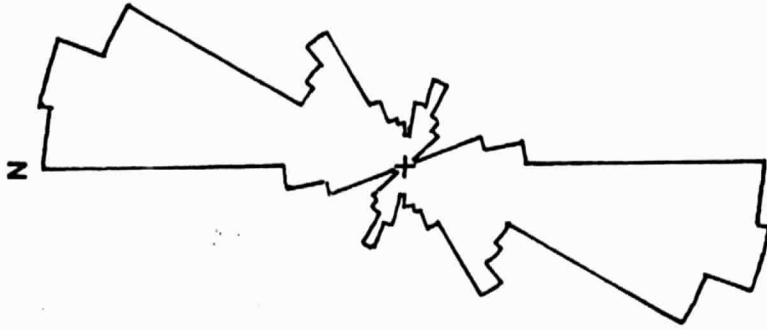
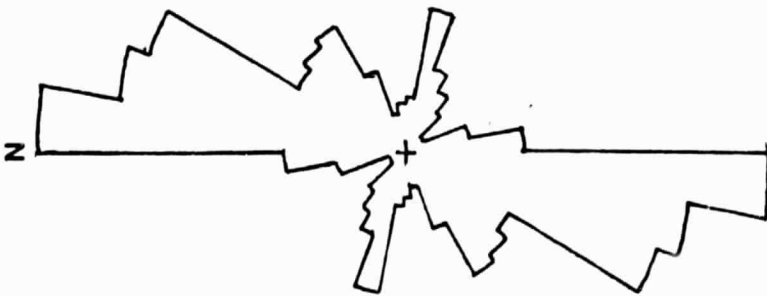


Figure 17. Mapped lineaments in Nevada. The location is indicated on the map to the left. These extended, parallel lineaments are characteristic of dip-slip faulting.  
(scale: 1 cm = 10 km)

ORIGINAL PAGE IS  
OF POOR QUALITY



(b)



(a)

Figure 18. Rose diagrams of lineaments mapped in Nevada. (a) frequency (1"=29.5 line-  
aments), (b) length (1"=4165 km)



There are many lineaments in this region but few intersections.

The lineaments and seismicity of the area near Los Angeles where the left-lateral Garlock fault and the right-lateral San Andreas fault intersect are shown in Figures 19a-19c. Rose diagrams indicating the directions of orientation of the mapped lineaments southeast and northwest of the San Andreas fault are shown in Figures 20 and 21. Using a  $\frac{1}{4}^\circ$  latitude by  $\frac{1}{4}^\circ$  longitude grid, the areas where dip-slip faulting, strike-slip faulting, and more stable areas were distinguished. The variables used in the analysis were the number of past earthquakes (at least one within  $1^\circ$  distance), the number of lineaments ( $>10$  for earthquake prone areas), parallel lineaments ( $>5$  for dip-slip events,  $<5$  for strike-slip events), and lineament intersections ( $>10$  for strike-slip events,  $<10$  for dip-slip events). The data are presented in Figure 22a and the interpretation is given in Figure 22b. Two recent events are consistent with these results: a magnitude 6.4 earthquake located at  $34.41^\circ\text{N}$  and  $118.40^\circ\text{W}$  in 1971 was associated with dip-slip (thrust) motion and a magnitude 6.0 earthquake located at  $34.90^\circ\text{N}$  and  $118.90^\circ\text{W}$  in 1916 was associated with strike-slip motion.

ORIGINAL PAGE IS  
OF POOR QUALITY

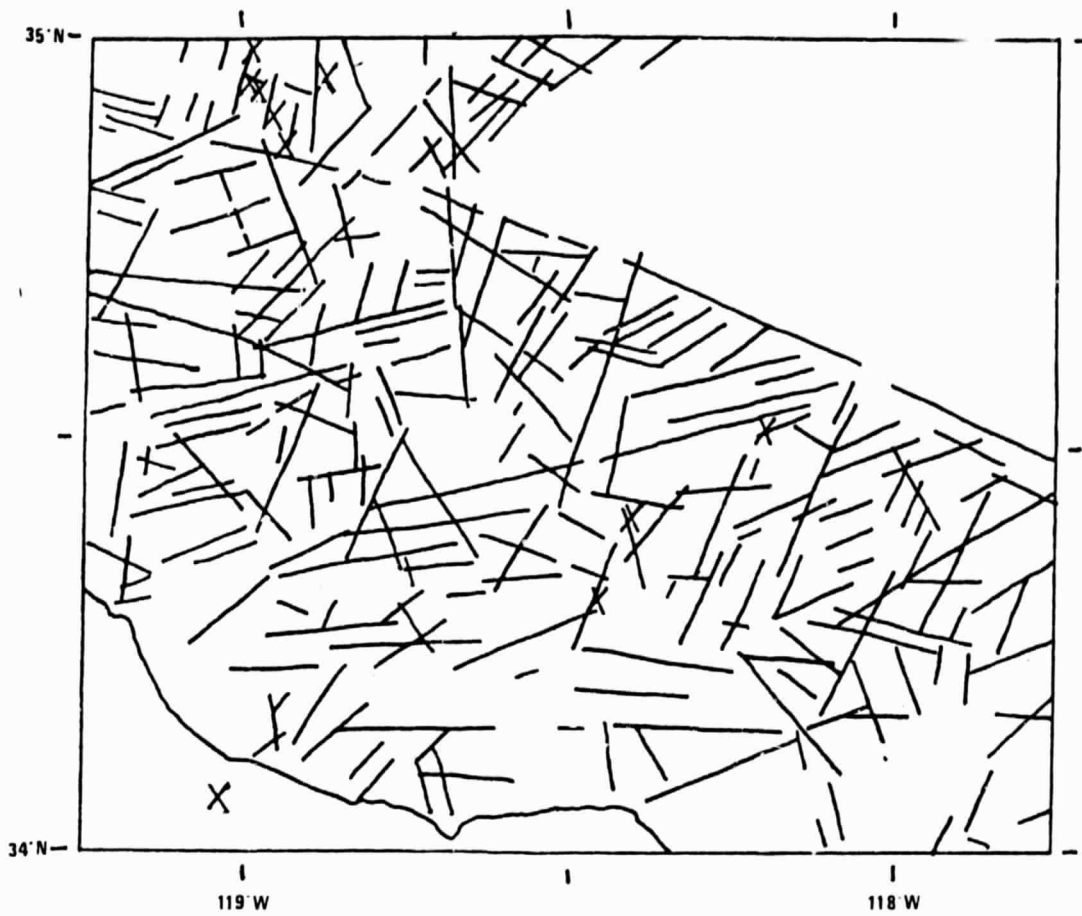


Figure 19a. Mapped lineaments and seismicity near Los Angeles (intersection of Garlock and San Andreas faults). The red X's represent locations of earthquakes of magnitude greater than 5 that occurred from 1932 to 1979. (scale: 1 cm = 10 km)

ORIGINAL PAGE IS  
OF POOR QUALITY

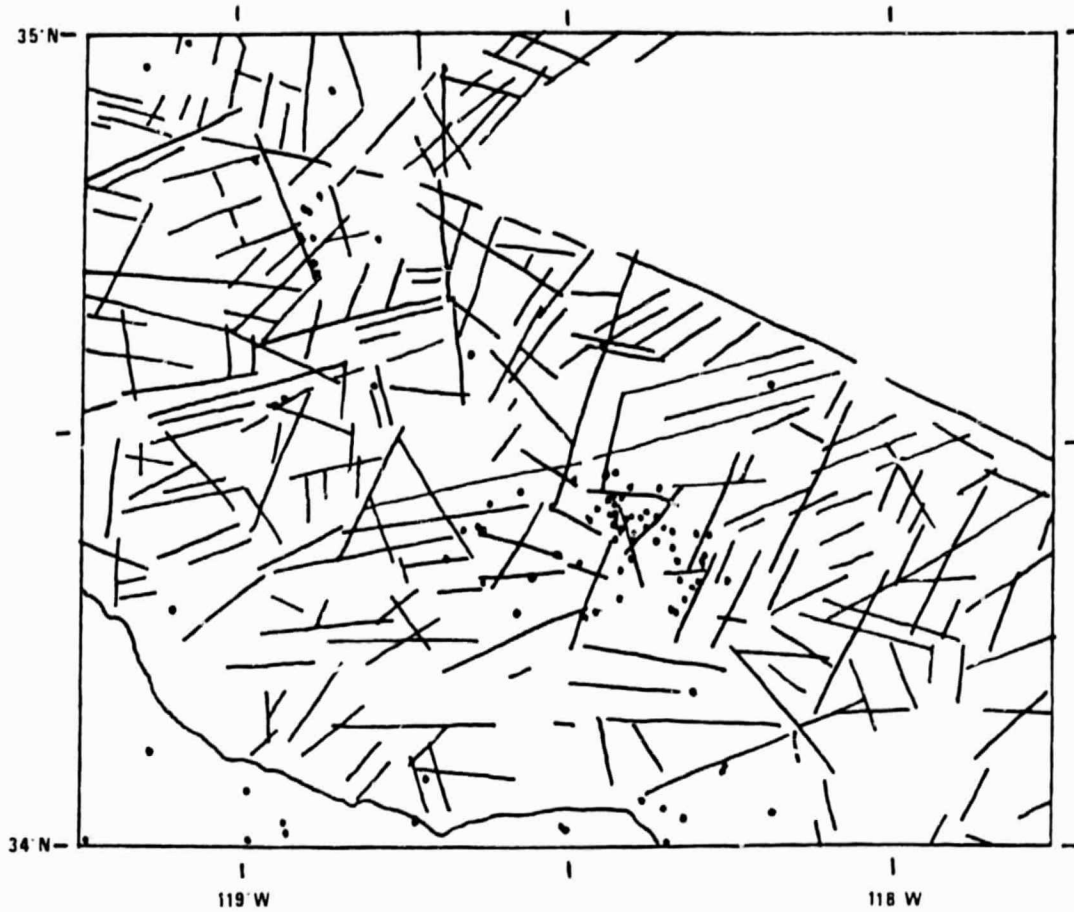


Figure 19b. Mapped lineaments and seismicity near Los Angeles (intersection of Garlock and San Andreas faults). The red dots represent locations of earthquakes of magnitude greater than 2 that occurred in 1972.

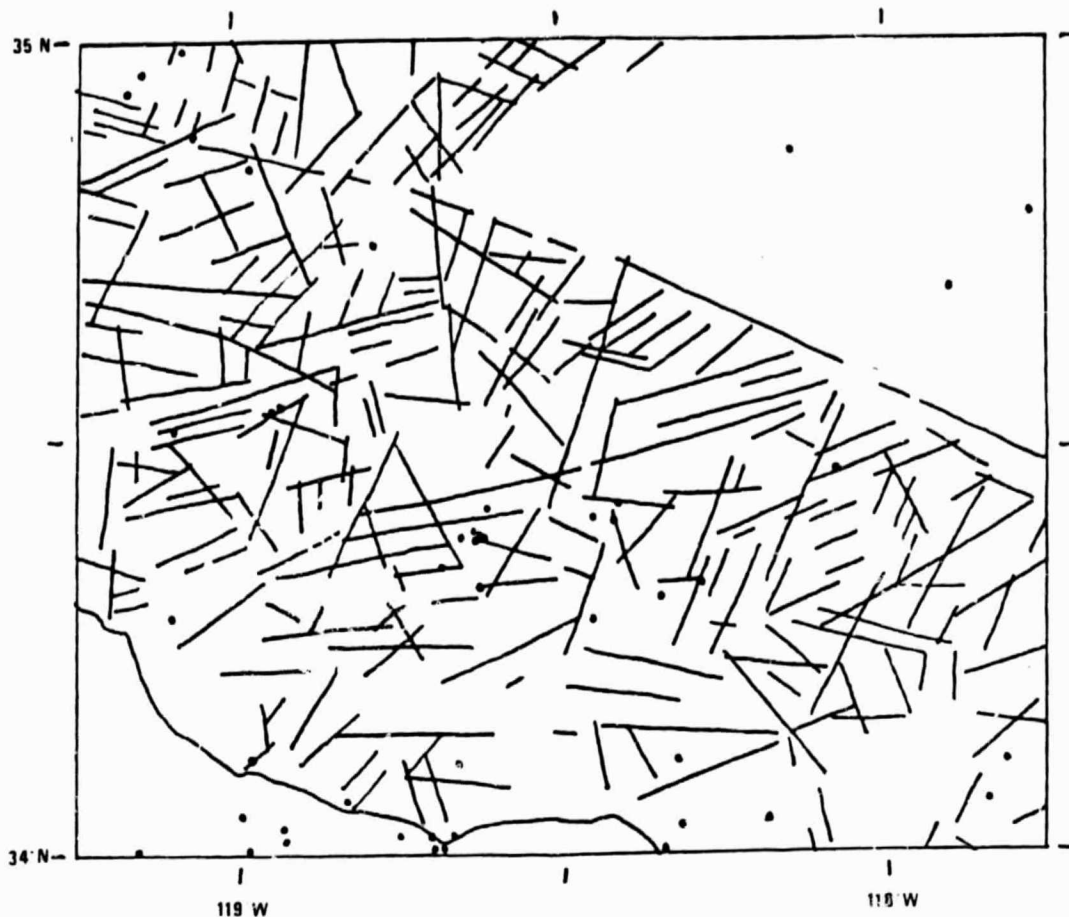
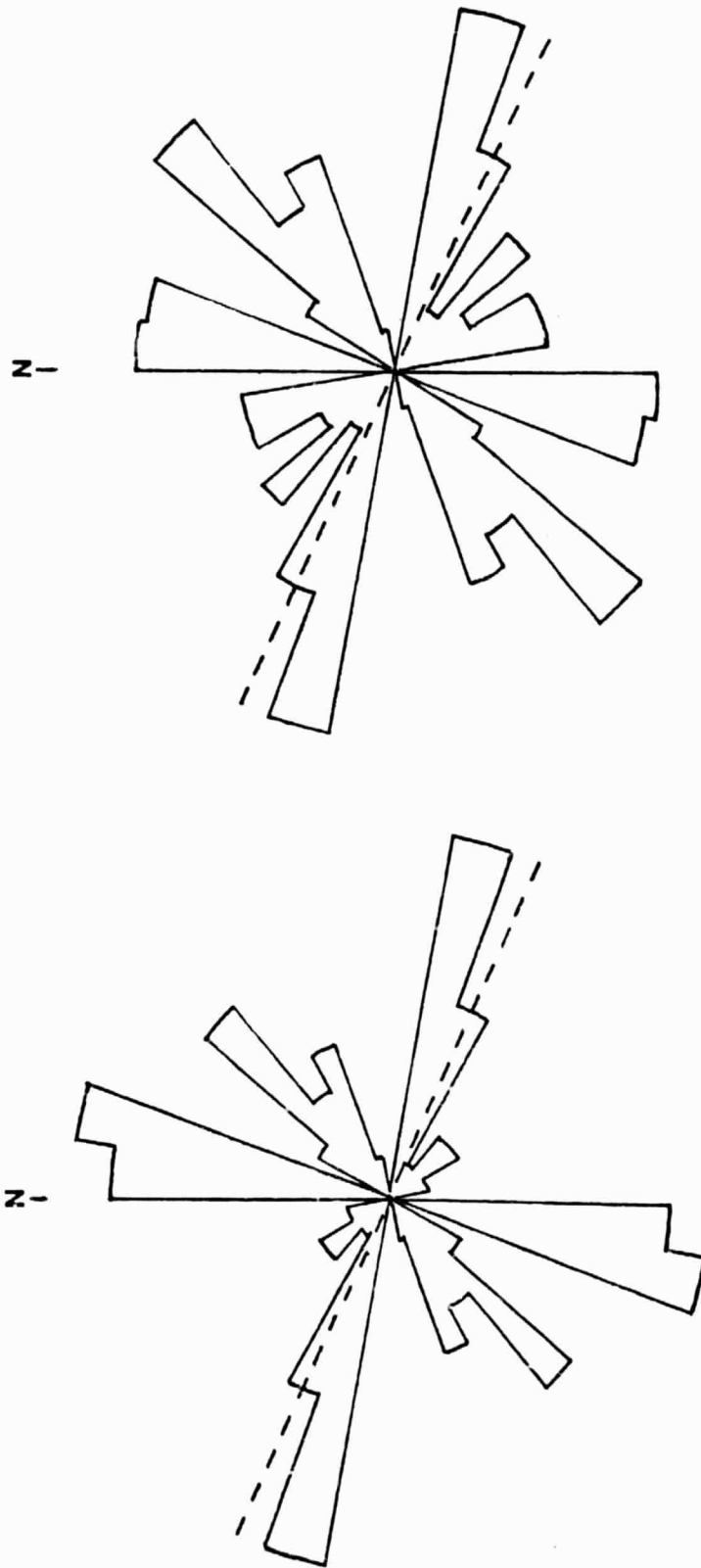


Figure 19c. Mapped lineaments and seismicity near Los Angeles (intersection of Garlock and San Andreas faults). The red dots represent locations of earthquakes of magnitude greater than 2 that occurred in 1979.



(a)

(b)

Figure 20. Rose diagrams of lineaments NE of the San Andreas fault (dashed line) near Los Angeles. (a) frequency (1"=4.5 lineaments), (b) length (1"=398.95 km)

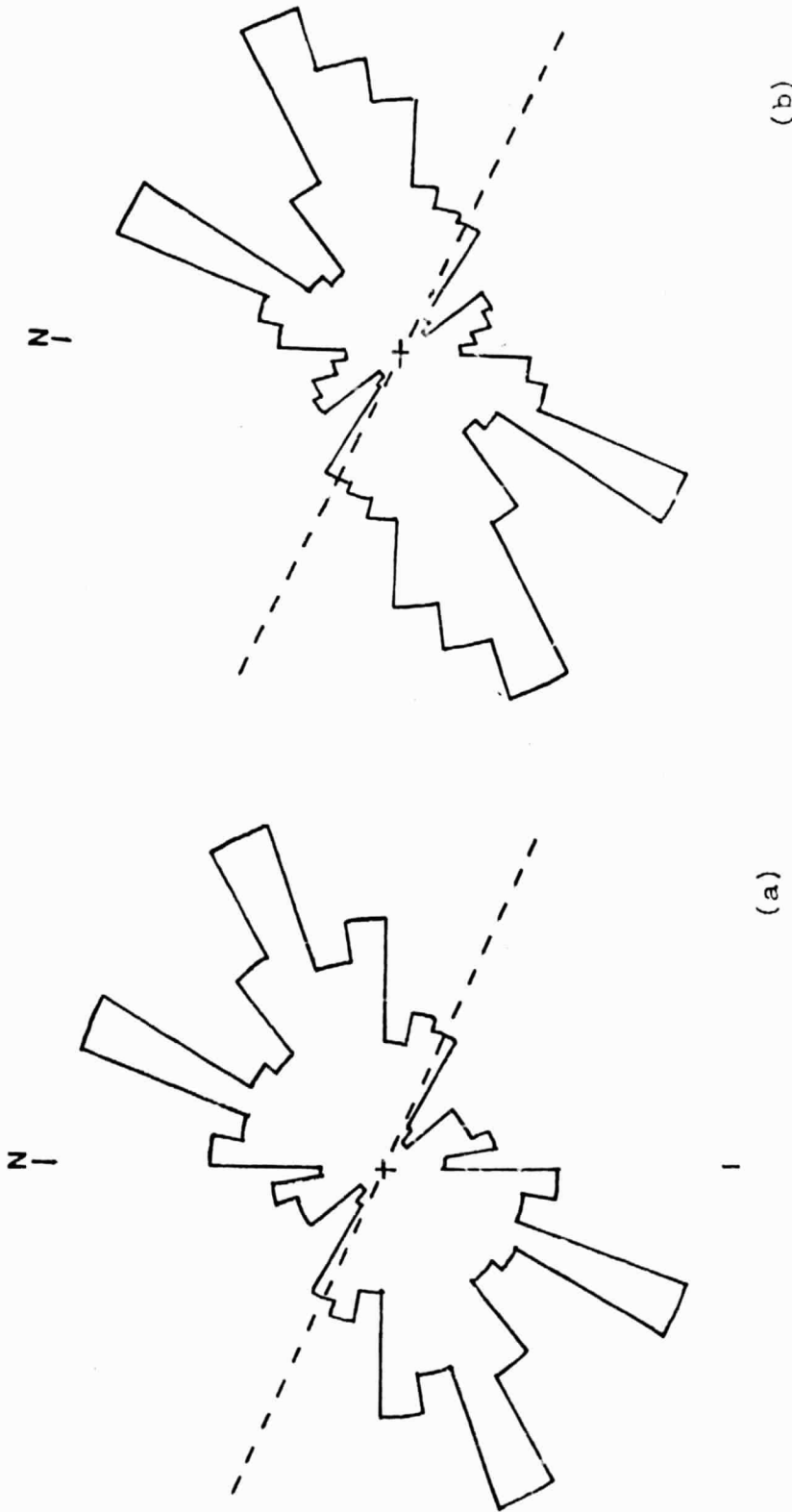
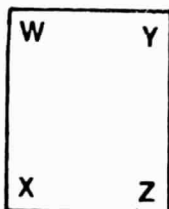
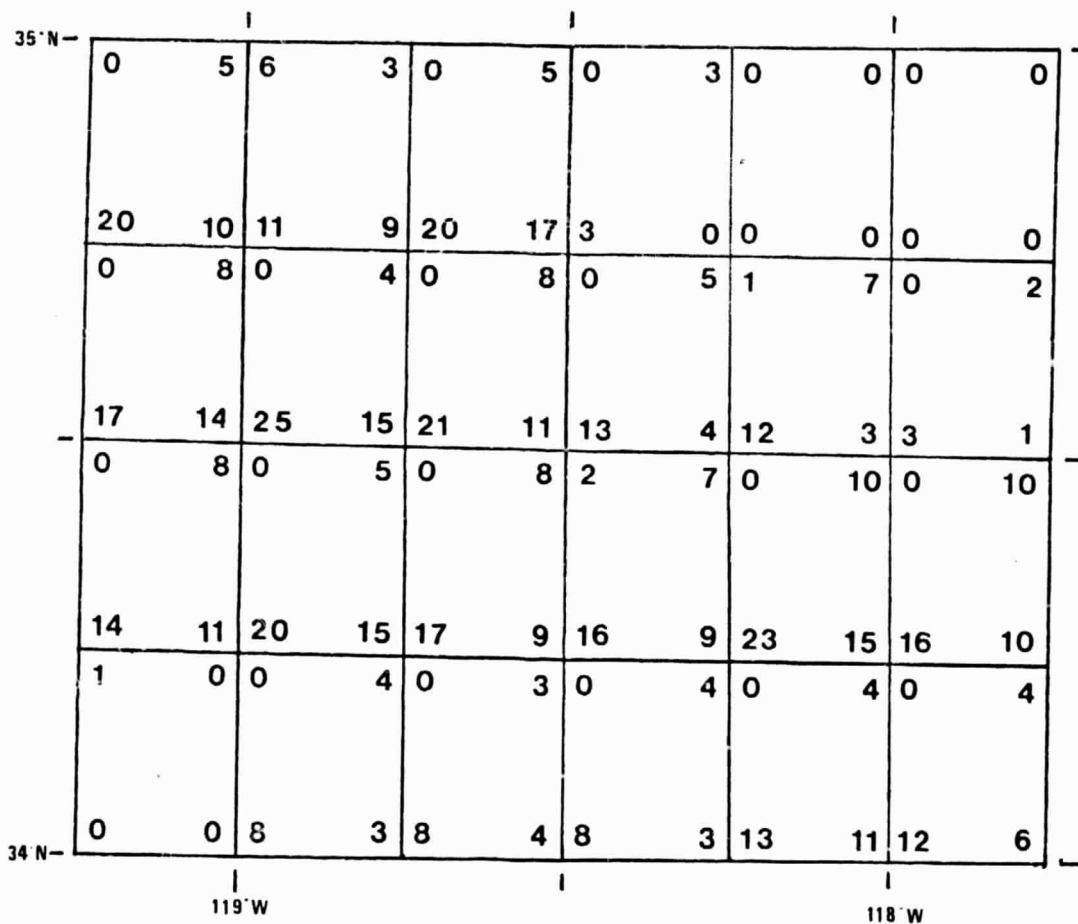


Figure 21. Rose diagrams of lineaments SW of the San Andreas fault (dashed line) near Los Angeles. (a) frequency (1"=17.5 lineaments), (b) length (1"=2171.5 km)



**W** = Number of earthquakes  $m \geq 5$  1932-1979  
**X** = Number of lineaments  
**Y** = Number of parallel lineaments  
**Z** = Number of lineament intersections

Figure 22a. Grid and characteristic traits in the area near Los Angeles.

ORIGINAL PAGE IS  
OF POOR QUALITY

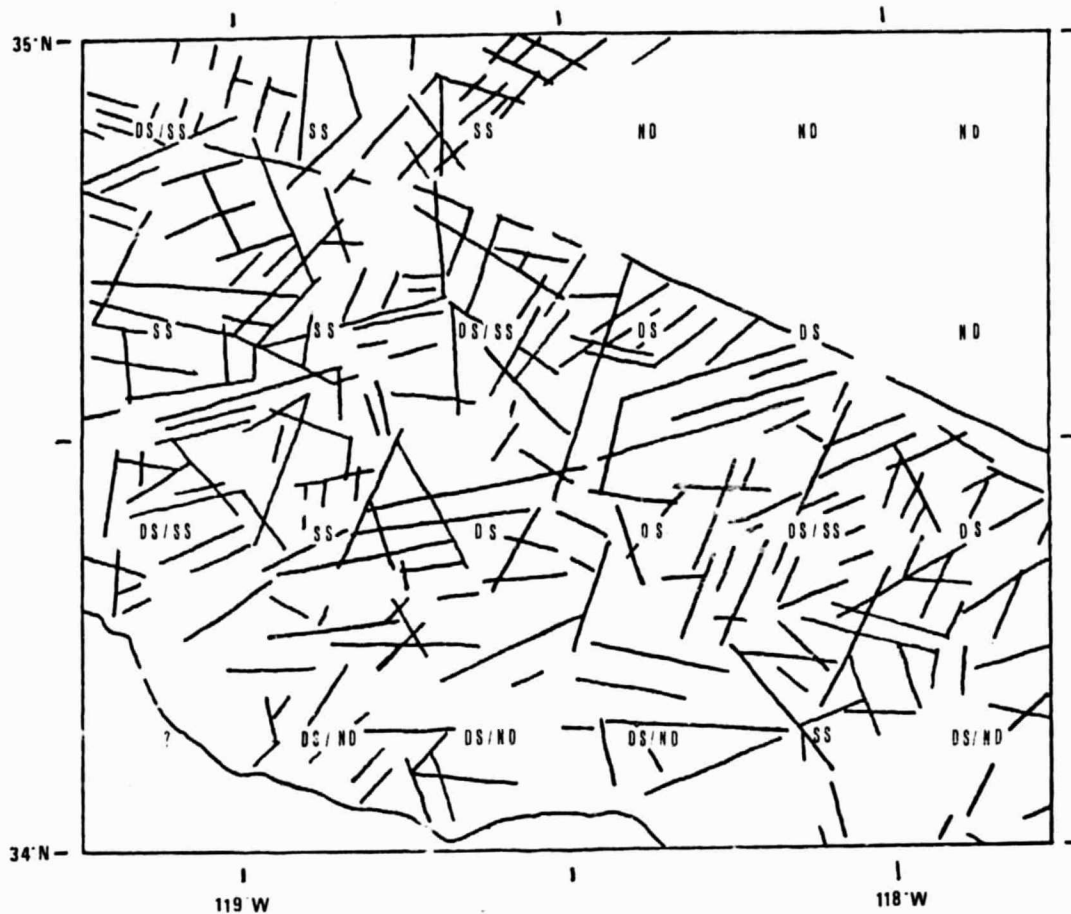


Figure 22b. Interpretation of lineaments and seismicity in the area near Los Angeles. Each set of data in Figure 22a was designated DS (dip-slip characteristics), SS (strike-slip characteristics), or ND (non-dangerous area).



Discussion

The more prominent lineaments on the imagery appear to reflect the more recent fault motions, and therefore, indicate the stresses now present in the region. The other mapped lineaments may represent the stresses that were present in earlier geologic processes. Figure 23 shows several different orientations of the stress ellipsoids and the fault types associated with each stress condition. At present, the intermediate principal stress axis along most of the San Andreas fault is vertical and the least and greatest principal stress axes are horizontal (see Figure 24). The San Andreas fault may be a transform fault associated with a continuation of the East Pacific Rise [Press and Siever, 1974]. Here the North Pacific plate slides past the North American plate in a northwesterly direction. The relative motion of the plates in California is approximately 5.5 cm/yr. Some areas have undergone no movement and in some other areas movement is occurring without earthquake activity [NASA Technical Paper 1464, 1979]. In Central California the rate of movement is only 3-4 cm/yr along the San Andreas fault. In this area the stress appears to be relieved in part by creep. Aseismic plate movement does not usually occur in the areas around Los Angeles and San Francisco. Here the strain is released principally in episodic major earthquakes.

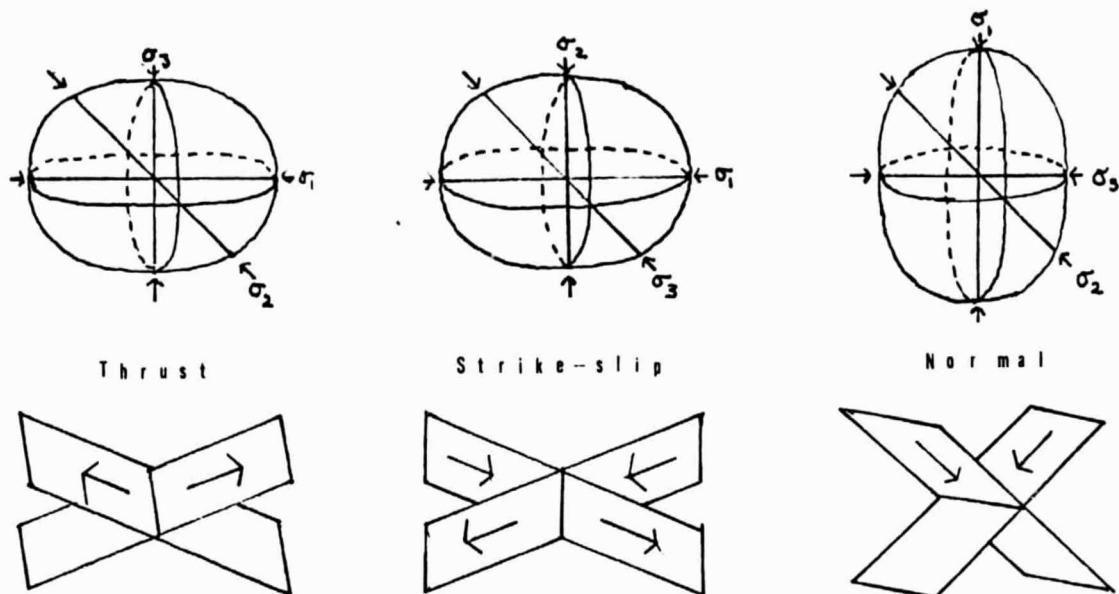


Figure 23. Orientations of stress ellipsoids and the fault motion associated with each stress condition.  $\sigma_1$  is the greatest principal stress axis,  $\sigma_2$  is the intermediate principal stress axis, and  $\sigma_3$  is the least principal stress axis. [Redrawn from Billings (1972), Structural Geology, Fig. 10-14, page 231.]

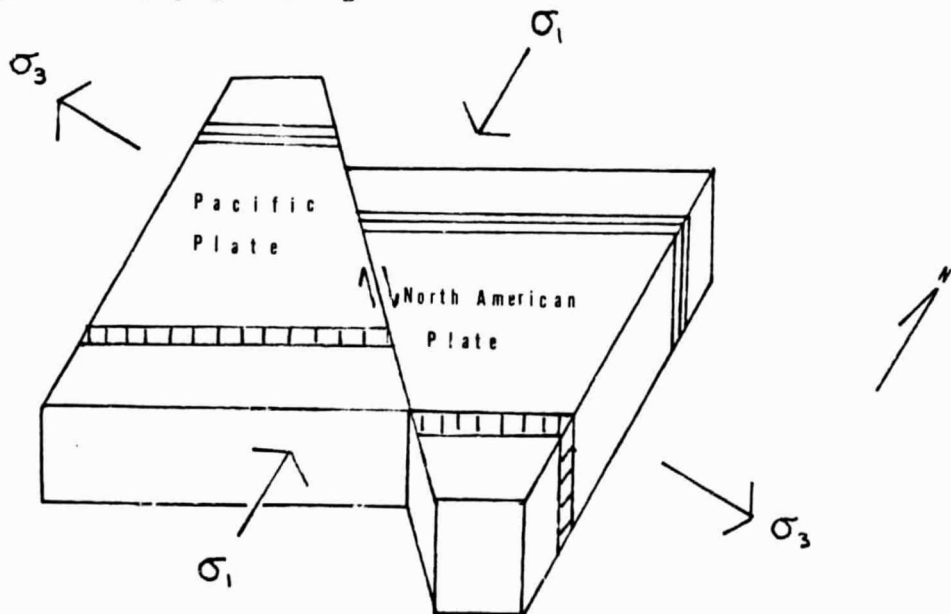


Figure 24. Orientations of stress axes in California. The San Andreas fault is shown separating the Pacific and North American Plates.

A recent study of paleomagnetic data from Miocene rocks by Luyendyk et al, 1980, suggests a rotation of crustal blocks. The crustal blocks are bounded by strike-slip faults. They proposed a model in which the faulting and rotation occurred simultaneously. In this model, rotation began when the Pacific plate collided with the North American plate (late Oligocene) and ended when the San Andreas fault system broke through the crust in Southern California (late Miocene). The rotated blocks include sections near Los Angeles and the Salton Sea that are bounded by the San Andreas fault.

The remotely sensed data from this study also suggest an apparent rotation of lineaments across the San Andreas fault (see Figure 25). The most dominant orientation of lineaments in the Central California region and the Salton Sea region trend in the same direction as the San Andreas fault in these areas. Other prominent orientations are rotated approximately  $10^\circ$  clockwise as one crosses from northeast of the fault to southwest of the fault. These secondary sets of lineaments are oriented at high angles to the San Andreas fault trend.

In the Los Angeles area the major set of lineaments trends northeast-southwest. The San Andreas fault trends  $N25^\circ W$ , a  $20^\circ$  counterclockwise rotation from the orientation of the fault both north and south of the area. Northeast

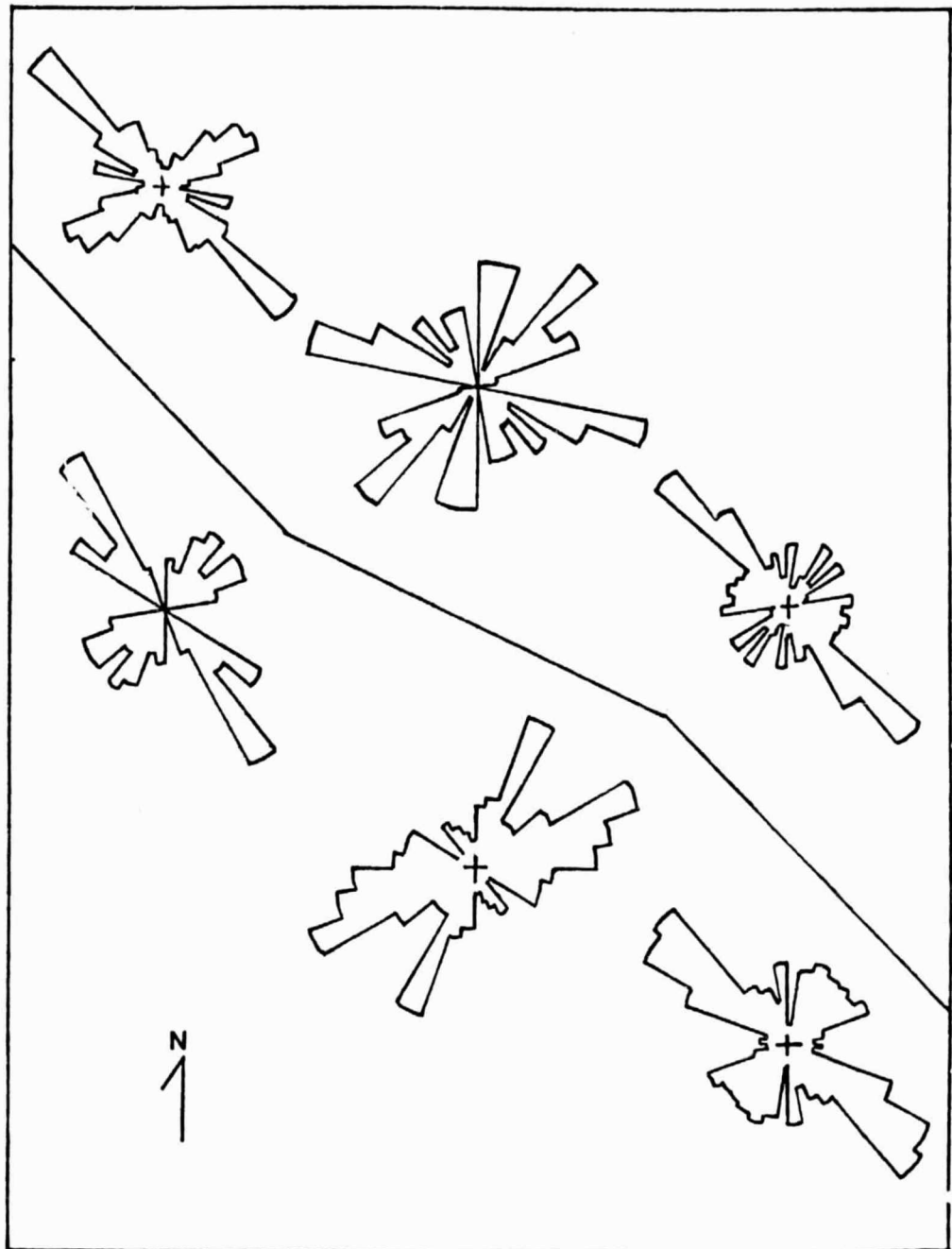


Figure 25. Rose diagrams showing rotation of lineaments across the San Andreas fault. On the left are the lineaments in Central California; the Los Angeles region is shown in the middle; and on the right are the lineaments in the Salton Sea region.

of the San Andreas fault in this area, the orientations of the mapped lineaments are widely dispersed and reflect the complex history of tectonic movement in this region.

Southwest of the fault, the lineament orientations reflect the trend of the Garlock fault. This area is the only region along the San Andreas fault to experience both dip-slip and strike-slip faulting in recent geologic history.

### Summary and Conclusions

In this preliminary investigation, characteristic traits of seismically active areas were recognized on Landsat satellite imagery which correspond to similar traits determined by Briggs et al (1977). Patterns of lineaments including parallel lineaments (characteristic of regions with large dip-slip type earthquakes) and lineament intersections (characteristic of regions with large strike-slip type earthquakes) were the most diagnostic features which were observed. From this study, it is apparent that remotely sensed data may be useful, perhaps as useful as ground-based data, in distinguishing among areas where there is active strike-slip faulting, active dip-slip faulting, and regions of low seismic activity. At a minimum, space imagery can provide important supplementary information to characterize active tectonic regions.

In both the Salton Sea and Central California study areas there were 48 mapped epicentral locations of events of magnitude greater than or equal to 5.0. These epicenters are located in regions predicted in Briggs et al's (1977) study to have large strike-slip earthquakes. All of these epicenters lie within 50 km of the San Andreas fault zone. There are at least 10 mapped lineaments within 25 km of each epicentral location. All of the epicenters lie within 15 km of a mapped lineament and 41 epicenters are within

5 km of a mapped lineament. Of the 7 epicenters that are not within 5 km of a mapped lineament, 3 are in the Salton Sea. Prominent lineament intersections are located within 15 km of 38 of the epicenters. Of these, 24 are located within 5 km of a prominent lineament intersection.

The lineaments on a Landsat image of Nevada were also mapped. This area is in a region predicted by Briggs et al (1977) to have principally dip-slip type earthquakes. There is a strong directionality among the mapped lineaments in this image. The other lineaments are dispersed in azimuth. There are 150 mapped lineaments from  $0^{\circ}\text{N}$  to  $\text{N}30^{\circ}\text{E}$ . In addition to numerous extended, parallel lineaments, Briggs et al (1977) have suggested an association with geothermal activity and sharp relief in areas where there is active dip-slip faulting. The mapped area appeared to have high relief although no measurements were made. Thermal imagery, which might have been useful in identifying geothermal areas, was not available for interpretation.

The areas with the lowest lineament density occur in the Mojave Desert and Great Valley provinces. These areas correspond to areas of low seismic activity according to Briggs et al (1977). In support of this condition, the epicenter maps plotted in this study show no events in part of the Great Valley north of  $36^{\circ}30'\text{N}$  in regions M2 and M3, and only one event of magnitude less than 2 in the eastern

half of Salton Sea region S2.

Previous experience with lineament mapping reveals that among different observers there are wide variations in the number, location, and continuity of individual mapped lineaments; however, the distribution of lineament orientations are remarkably consistent among observers. In this study, lineaments were mapped independently by both the author and another experienced image analyst. The results were consistent with this previous experience in both the Salton Sea area and Central California, although the agreement of the two lineament maps was much better than has been reported previously. Rose diagrams were plotted by both observers and these suggest relative rotations of dominant lineament directions across the San Andreas fault. If their results are correct, the implication is that there has been a relative rotation of crustal blocks associated with the deformation in this area. Independent evidence from paleomagnetic data of such block rotations in this area has been published by Luyendyk et al (1980).

This investigation was based on a visual analysis of Landsat satellite imagery. The agreement of these results with those of the ground-based investigation demonstrates the potential value of remotely sensed data in studying other seismically active regions. More work is needed to develop reliable criteria for inferring the relative ages of



the tectonic features that can be observed from space in different geologic settings. For example, in this study there is some indication that greater spatial sharpness of lineament features is characteristic of the most seismically active regions, while in areas of lower activity the lineaments are less sharp. Data enhancement of digital imagery will also aid in quantifying the observations. This is expected to decrease the subjectivity which often leads to variations among interpretations of satellite imagery by different observers.

### Suggestions for Future Analyses

The experience gained in this study suggests that the following procedure might be used to identify a seismically active continental area:

- (1) Obtain good, cloud-free imagery of the area to be investigated. This could include imagery taken at different times of the year to decrease the effects due to vegetation. Thermal imagery might be used to identify geothermal areas. Relief may be examined stereoscopically on satellite imagery or by radar imagery.
- (2) In a visual analysis, lineaments and other structural features may easily be mapped on a transparent overlay on the imagery. These structural features may be identified by standard geological and geomorphic features as well as by more subtle contrasts due to differences in rock type or texture. Enough imagery should be used to cover a large area so regional structural trends may be observed.
- (3) Digital data could also be acquired. These data might be enhanced through computer methods which offer a means of quantitatively analyzing the data. A few of the available methods are discussed below:
  - (a) Brightness classification maps may be made to show the overall land patterns.

- (b) Maps of local spectral uniformity outline areas which have similar spectral signatures. These might be used to apply the characteristic results of a known area to a new study region.
  - (c) Wave number analysis may be used to determine the orientation and scale of various spatial features in a given scene. By applying a band-pass or band-reject filter, features in any given orientation may be enhanced or removed.
  - (d) Derivative operators may be used to enhance narrow zones which show a rapid change in character. Many of these zones are diagnostic geomorphic and vegetal features.
  - (e) Two images may be merged to maximize the classification categories.
- (4) Seismicity data could be collected and epicenters could be plotted to correspond to the exact scale of each imaged scene. This would aid in identifying the most active areas within a region.
- (5) A list of questions, such as that given in the Appendix, could be used in the analysis. The most important questions appear to be those concerning number of lineaments, lineament intersections, current seismicity, relief, and nearness to major faults. Other characteristics which may be diagnostic should be considered. In

addition, the physical meaning of these traits might be examined. An attempt could be made to identify the most recent geological features. This can be accomplished by locating the most prominent lineaments and by examining the spatial relationships of the mapped lineaments.

- (6) An appropriate grid should be used to assemble these data, so that they may be used in a pattern recognition algorithm to determine characteristic traits. It is suggested that the sample points include epicenters of strong earthquakes. The grid should be small enough to completely sample the entire area. The accuracy of estimating the areas of active faulting will be related to the grid size.

Such studies may prove useful in improving seismic-risk zoning and may add to our understanding of earthquake mechanisms in areas where ground-based data are lacking or inadequate. Remote sensing data offer an inexpensive means of examining large areas in a short amount of time.

References

- Alexander, S. S., 1980, Personal communications.
- Billings, M. P., 1972, Structural geology: New Jersey, Prentice-Hall, Inc., p. 231, Figure 10-14.
- Briggs, P., Press, F., and Guberman, Sh. A., 1977, Pattern recognition applied to earthquake epicenters in California and Nevada: Geol. Soc. America Bull., v. 88, p. 161-173.
- Gelfand, I. M., Guberman, Sh. A., Izvekova, M. L., Keilis-Borok, V. I., and Ranzman, E. Ja., 1972, Criteria of high seismicity determined by pattern recognition: Tectonophysics, v. 13, p. 415-422.
- Gelfand, I. M., Guberman, Sh. A., Keilis-Borok, V. I., Knopoff, L., Press, F., Ranzman, E. Ja., Rotwain, I. M., and Sadovsky, A. M., 1976, Pattern recognition applied to strong earthquakes in California: Physics Earth and Planetary Interiors, v. 11, no. 3, p. 227-283.
- Jahns, R. H., 1954, Investigations and problems of Southern California Geology: California Div. Mines Bull. 170, p. 5-29.
- Johnson, C. E., 1979, I. Cedar--An approach to the computer automation of short-period local seismic networks, II. Seismotectonics of the Imperial Valley of Southern California: PhD. thesis, California Institute of Technology.
- Luyendyk, B. P., Kamerling, M. J., Terres, R., 1980, Geometric model for Neogene crustal rotations in Southern California: Geol. Soc. America Bull., v. 91, p. 211-217.
- NASA Technical Paper 1464, 1979, Application of space technology to crustal dynamics and earthquake research; p. 66-70 and p. 121-126.
- Petrus, C., 1980, Personal communications.
- Press, F., and Siever, R., 1974, Earth: San Francisco, W. H. Freeman and Co., p. 523-526.
- Richter, C. F., 1958, Elementary seismology: San Francisco, W. H. Freeman and Co., p. 441-449.
- Scholz, C. H., Barazangi, B., and Sbar, M. L., 1971, Late Cenozoic evolution of the Great Basin, western United States, as an ensialic interarc basin: Geol. Soc. America Bull., v. 82, p. 2979-2990.

Sharp, R. V., 1972, Tectonic setting of the Salton Trough: U.S.G.S. Prof. Paper 787, p. 3-15.

Sylvester, A. G. and Crowell, J. C., 1979, Tectonics of the juncture between the San Andreas fault system and the Salton Trough, Southeastern California: Univ. of California, p. 1-52.

Taliaferro, N. L., 1941, Geologic history and structure of the Central Coast Ranges of California: California Div. Mines Bull. 118, p. 118-163.

U.S. Geol. Survey and California Div. Mines and Geology, 1966, Geologic map of California: U.S. Geol. Survey Misc. Geol. Inv. Map I-512, scale 1:2,500,000.

APPENDIX

The following list of questions were used to interpret the epicentral regions. This list includes parameters used in previous ground-based investigations [Briggs et al (1977) and Gelfand et al (1976)].

1. In what natural province is the epicenter located?
2. Description of event: magnitude? date(s)? observed surface faulting?
3. Is the relief sharp? moderate to sharp? moderate? low to moderate? low?
4. Within 40 km is there any known dip-slip faulting? thrusting? strike-slip faulting?
5. Are there indications of geothermal activity within 50 km?
6. What is the distance to the nearest spreading center? [lat 40.5°N, long 126.6°W or lat 33.2°N, long 115.6°W]
7. How far is the nearest body of water?
8. What is the focal mechanism?
9. What are the preferred orientations for the main shock fault plane solution?
10. How many earthquakes with magnitude greater than 5 have occurred within 50 km from 1932-1979?
11. How many faults are there within 25 km?
12. How many subparallel (intersection angle less than 20°) faults are there within 25 km?
13. How many fault intersections are there within 50 km?
14. How far is the closest branch of the San Andreas fault system?
15. What are the trends of the major faults within 50 km?
16. How far is the nearest fault?
17. How far is the nearest fault intersection?
18. What features were used to identify the lineaments on the imagery?

19. What are the trends of the lineaments mapped within 50 km?
20. How many lineaments are there within 25 km?
21. How many parallel lineaments are there within 25 km?
22. How many lineament intersections are there within 25 km?
23. How far is the nearest lineament?
24. How far is the nearest lineament intersection?
25. Are the lineaments well-defined within 25 km?
26. Is the area within 25 km seismically active?
27. Does the seismicity occur at the same locations as the lineaments? lineament intersections?



SECTION III

UTILITY OF DIGITALLY MERGED SEASAT-A SAR, LANDSAT MSS, AND  
MAGNETIC FIELD DATA SETS FOR MAPPING LITHOLOGY  
AND STRUCTURE IN A VEGETATED TERRAIN

The Pennsylvania State University  
The Graduate School  
Department of Geosciences

Utility of Digitally Merged Seasat-A SAR,  
Landsat MSS, and Magnetic Field Data Sets  
for Mapping Lithology and Structure  
in a Vegetated Terrain

A Thesis in  
Geophysics

by

Casey Edward Ravenhurst

Submitted in Partial Fulfillment  
of the Requirements  
for the Degree of

Master of Science

November 1980

I grant the Pennsylvania State University the nonexclusive right to use this work for the University's own purposes and to make single copies of the work available to the public on a not-for-profit basis if copies are not otherwise available.

  
Casey Edward Ravenhurst

ORIGINAL PAGE IS  
OF POOR QUALITY

We approve the thesis of Casey Edward Ravenhurst.

Date of Signature:

8 October 1980

Shelton S. Alexander

Shelton S. Alexander, Professor of  
Geophysics, Chairman of the  
Geophysics Program, Thesis Advisor

7 October 1980

Earl K. Graham

Earl K. Graham, Professor of  
Geophysics

Oct. 7, 1980

Peter M. Lavin

Peter M. Lavin, Associate Professor  
of Geophysics

October 7 1980

David P. Gold

David P. Gold, Professor of Geology

ABSTRACT

Remotely sensed data from each part of the electromagnetic spectrum contains potentially different and independent information about the earth's surface and subsurface. Interpretation of these different data sets, together with conventional geophysical and geological information, is greatly facilitated by merging all the data sets such that each (spatial) resolution element has associated with it an n-dimensional vector composed of information from each of the n data sets. In this study, Landsat MSS, Seasat-A Synthetic Aperture Radar (SAR), and magnetic field data from the South Mountain area west of Gettysburg, Pennsylvania, were registered to match each other in spatial position, and merged. Pattern recognition techniques were then applied to the composite data set to determine its utility in recognizing different rock types and structures in vegetated terrain around South Mountain. The SAR imagery was filtered in order to reduce its directional dependence. Principal components analysis was used to decrease the dimensionality of the entire data set. A texture algorithm was then applied to the first two principal axes, and later to the third axis, in order to enhance various geologic features. Next, the contribution of each data set and texture measure to the separability of rock type classes in the training area was evaluated.

A classification of the entire study area was then done using the enhanced data that contributed the most to the separability of classes.

The texture measures were found to emphasize the geologic information in the data and thus increase the separability of the rock type classes. The best classification was obtained when texture measures from each of the first three principal component axes were merged with the magnetic field data. About 40% of the area was classified as having the same rock types as the geologic map showed. The confusion of rock type classes was due to the large amount of variance within each class when compared to the between-group variance. The variance is thought to originate from three sources; registration errors, the heavy vegetation cover, and systematic noise in the SAR data.

A test of the correlation between SAR tone and texture, Landsat tone and texture, and magnetic field data, revealed no tone or texture measures linking any two of these original data sets.

The magnetic field data showed a 60% correlation with the surface geology of the area, and about 20% was correlatable with the known subsurface geology. In contrast, the satellite data was related only to the surface characteristics. Thus, the merged data set contained mainly surface information, but had a small component of subsurface information.

ORIGINAL PARTIAL  
OF POOR QUALITY      TABLE OF CONTENTS

	<u>Page</u>
LIST OF TABLES.....	vii
LIST OF FIGURES.....	viii
ACKNOWLEDGEMENTS.....	xi
 CHAPTER	
I. INTRODUCTION.....	1
Sensor Capabilities.....	1
Statement of Problem.....	6
II. STUDY AREA.....	8
III. METHOD.....	14
Data Collection.....	14
Relationship of magnetic field data and geologic features.....	17
Preprocessing.....	18
Reformatting and rotating the Seasat SAR data set.....	18
Filtering SEASAT SAR data.....	19
Processing the magnetic field data.....	20
Registration of all the data sets.....	24
Principal components analysis.....	28
Feature Extraction.....	35
Choosing training areas.....	35
Spectral signatures.....	39
Textural signature algorithm.....	39
Correlations between data sets.....	42
Discrimination.....	42
Classification.....	44
IV. RESULTS.....	46
Registration.....	46
Relationship of magnetic field data and geologic features.....	46
Correlations between SAR, Landsat, and magnetic field data.....	50
Classification using texture measures from principal component axes 1 and 2.....	52
Classification using texture measures from principal component axes 1 and 2 plus magnetic field data.....	82
Classification using texture measures from principal component axes 1,2 and 3 plus magnetic field data.....	84

ORIGINAL PAGE IS  
OF POOR QUALITY

TABLE OF CONTENTS

	<u>Page</u>
V. DISCUSSION AND CONCLUSIONS.....	86
Discussion.....	86
Conclusions.....	92
VI. APPENDIX A.....	94
VII. REFERENCES.....	123

## LIST OF TABLES

ORIGINAL PAGE 19  
OF POOR QUALITY

<u>Table</u>		<u>Page</u>
1	Registration of merged data to topographic maps..	28
2	Correlation of channels with principal component axes.....	33
3	Correlation matrix for initial given channels....	33
4	Correlation matrix for principal component axes..	34
5	Rock type classes in Catoctin metavolcanics.....	37
6	Rock type classes in Chilhowee metasediments.....	38
7	The texture-tone variables of Hsu's algorithm....	41
8	Correlation of SAR tone with principal component axes 2 and 3 texture measures.....	51
9	Correlation matrix for texture measures from principal component axes 1,2, and 3.....	53
10	Correlation of magnetic field with principal component axes 1,2, and 3 texture measures.....	54
11	Confusion matrices for magnetic field survey area	56
12	Significance of data sets or variables in the magnetic field survey area.....	60
13	Confusion matrices for entire study area.....	62
14	Confusion matrices for principal components of entire study area.....	67
15	Significance of the variables in the entire study area.....	73
16	Confusion matrices for texture measures.....	74
17	Significance of the texture variables.....	79
18	Seasat-A Synthetic Aperture Radar (SAR) specifications.....	95
19	Seasat-A Satellite specifications.....	96



LIST OF FIGURES

<u>Figure</u>		<u>Page</u>
1	Generalized atmospheric transmission spectrum and sensor bands.....	2
2	Index map of southeastern Pennsylvania.....	9
3	Seasat SAR scene.....	10
4	Regional geology of study area.....	11
5	Hypothetical configurations of basement in the South Mountain area.....	13
6	Landsat MSS scene (band 7).....	15
7	Magnetic field survey grid.....	16
8	NMAP digital printout of magnetic field data (not corrected for line printer).....	23
9	NMAP of Landsat MSS data rotated to zero azimuth..	25
10	NMAP of Seasat SAR data rotated to zero azimuth..	25
11	NMAP of rubbersheet-stretched Seasat SAR data....	26
12	NMAP of merged Landsat MSS - Seasat SAR data....	26
13	NMAP of principal component axis 1.....	30
14	NMAP of principal component axis 2.....	30
15	NMAP of principal component axis 3.....	31
16	NMAP of principal component axis 4.....	31
17	Linear features and major structural and geologic units of the study area.....	32
18	Detailed geology of magnetic field survey area...	47
19	Contoured total magnetic field.....	48
20	Magnetic field profile and geologic cross section.....	49
21	Landsat spectral signatures scattergram for magnetic field survey area.....	57

LIST OF FIGURES

<u>Figure</u>		<u>Page</u>
22	Landsat + SAR spectral signatures scattergram for magnetic field survey area.....	58
23	Landsat + SAR + magnetic field spectral signatures scattergram for magnetic field survey area.....	59
24	Landsat spectral signatures scattergram for entire study area.....	63
25	Landsat + SAR spectral signatures scattergram for entire study area.....	64
26	Landsat + SAR textural signatures scattergram for entire study area.....	65
27	Principal components signatures scattergram for entire study area.....	68
28	Principal component axis 1 textural signatures scattergram for entire study area.....	69
29	Principal component axis 2 textural signatures scattergram for entire study area.....	70
30	Principal component axes 1 and 2 textural signatures scattergram for the entire study area..	71
31	Principal component axes 1 and 2 scattergram for the 5 most important texture measures in the entire study area.....	75
32	Principal component axes 1 and 2 scattergram for the 5 most important texture measures in the magnetic field survey area.....	76
33	Principal component axes 1 and 2 scattergram for 5 most important texture measures plus magnetic field data.....	77
34	Principal component axes 1,2, and 3 scattergram for 7 most important texture measures plus magnetic field data.....	78
35	Classification map of the entire study area.....	81
36	Classification map showing only the areas classified as Harpers formation.....	81

## LIST OF FIGURES

<u>Figure</u>		<u>Page</u>
37	Digital classification map (6 variables) for magnetic field survey area (not corrected for line printer).....	83
38	Digital classification map (8 variables) for magnetic field survey area.....	85
39	Letter code and frequency wavelength bands.....	99
40	Types of reflection.....	100
41	Variations in skin depth for various soil types..	103
42	Resolution.....	104
43	Typical input-output transfer function.....	108
44	Typical target confusion on Seasat-A SAR resulting from four looks.....	109
45	Spatial integration to Landsat resolution (80 m) on SAR (40 looks).....	110
46	Layover and foreshortening in SLAR imagery.....	116
47	Target altitude effects.....	118

## ACKNOWLEDGMENTS

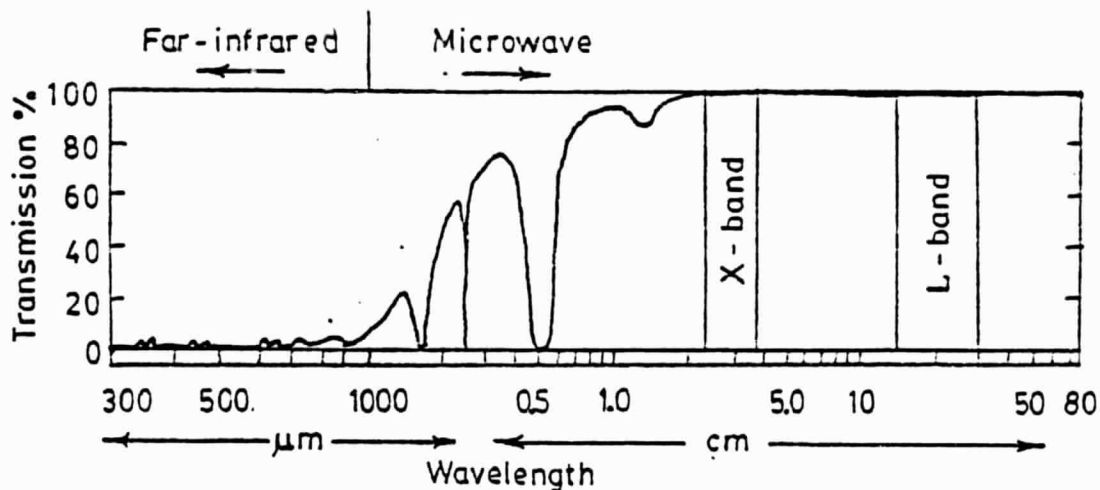
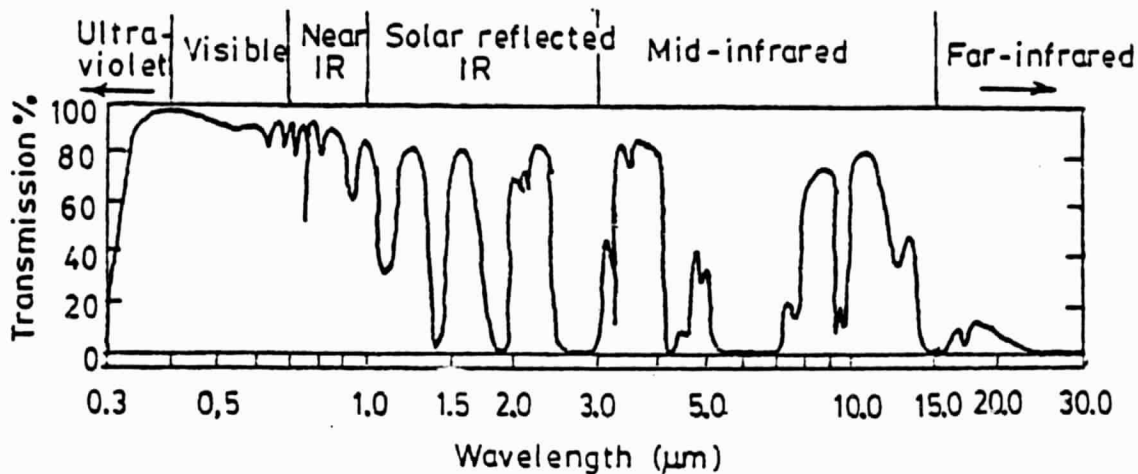
I wish to thank Mr. S. W. McCandless Jr. at User Systems Engineering in Washington D.C., for providing the Seasat-A SAR data tape. I also thank Dr. Shelton S. Alexander, my thesis advisor, for his suggestions concerning the thesis project, and Greg Pavlin for his advice during various stages of the thesis. My stay here was funded primarily by a postgraduate scholarship from the National Research Council of Canada, and the research was supported by National Aeronautics and Space Administration Cooperative Agreement NAG-5-49 and Advanced Research Projects Agency Grant AFOSR 77-3340.

## INTRODUCTION

Sensor Capabilities

The mapping of geologic features from space is still in its infancy. We are still experimenting with various sensors which record potentially useful geologic information from different parts of the electromagnetic spectrum. Each new sensor provides a wealth of information about this planet, some in spectral bands beyond our visible range. As shown in Figure 1, the wavelengths of interest for remote sensing extend from the ultraviolet, around 0.4 micrometers to microwaves at 50 centimeters, a range of  $10^6$  in wavelength. This spectrum can be divided into several segments each of which has special characteristics useful for remote sensing of surface features. The ultraviolet wavelengths shorter than 0.4 micrometers are generally not exploited for remote sensing because of high atmospheric absorption and Rayleigh scattering.

The information recorded by the Landsat Multi-Spectral Scanners (MSS) in the visible and near-infrared spectral ranges from 0.5 micrometers to 1.1 micrometers, has been the subject of considerable research and exploitation for almost a decade now. Foresters have used it to map vegetation distribution, while geologists have used it in arid regions to map regional rock type and structural geology.



<u>Landsat MSS</u>		<u>Seasat-A SAR</u>
Band 4	0.5 - 0.6 $\mu\text{m}$	23 cm
Band 5	0.6 - 0.7 $\mu\text{m}$	
Band 6	0.7 - 0.8 $\mu\text{m}$	
Band 7	0.8 - 1.1 $\mu\text{m}$	

Figure 1. Generalized atmospheric transmission spectrum and sensor bands (after Goetz and Rowan, 1980).

Ferrous iron-ion transition bands occur in the visible range, and although not ideal, the ratio of Landsat spectral band 5 to Landsat spectral band 4, can be used to discriminate hematite, goethite, and limonite as a group from practically all other minerals (Vincent, 1977). In vegetated areas though, Landsat MSS data offers little direct information about the soil or rock types. The spectral reflectance of vegetation in the visible to near-infrared differs markedly from that of rocks and soils, so that even a small amount of vegetation will alter the apparent spectral signatures of rocks and soils (Goetz and Rowan, 1980).

The solar-reflected infrared region, 1-3 micrometers, shows strong atmospheric water absorption bands; thus, information about bound and unbound water contained in surface materials is not transmitted. The 2-2.5 micrometer region though, does contain sharp, highly diagnostic spectral absorption bands for layered silicates and carbonates. The Thematic Mapper instrument planned for Landsat D will have two spectral bands centered at 1.6 and 2.2 micrometers and will increase significantly the lithologic mapping capability from space (Goetz and Rowan, 1980).

In the reflected portion of the spectrum, from the visible region to the solar-reflected infrared region, the spectrum of the stressed vegetation can be used to outline

mineralized areas or map lithologies and soil types. The geobotanical variations which cause the spectral changes range from slightly stressed vegetation, to completely barren areas. These variations are specifically related to anomalous concentrations of metals or to regional lithologic variations. Much more research is needed to establish the uniqueness of this shift in vegetation spectra; its change with the seasons, sun angle, and precipitation (Goetz and Rowan, 1980).

In the 3-5 micrometer range of the mid-infrared portion of the spectrum, the crossover occurs between solar-reflected and surface-emitted energy. This region has not been thoroughly investigated. In the 8-15 micrometer region, emittance variations provide a basis for distinguishing silicate and non-silicate rocks and for discriminating between silicate rocks. Moreover, thermal inertia information from this region can provide significant lithologic information. Aircraft systems for this region have operated successfully, but systems with sufficient spatial resolution for spectral imaging from orbit require the development of better detector arrays.

The Seasat Synthetic Aperture Radar (SAR) is an imaging radar system in the L-band that does not depend on either solar-reflected or surface-emitted energy. It is an active system that provides its own source of illumination at any specified angle, penetrates most weather conditions, and can



operate day or night. The price paid for these advantages compared to passive sensors operating in the visible to infrared spectral range, is that a much larger power output is required and extensive preprocessing is required to generate images. Appendix A contains a detailed discussion of the Seasat SAR characteristics.

The large incidence angles used with SAR and SLAR (Side-Looking Airborne Radar) cause terrain characteristics to be emphasized; however, shadow zones are created in which terrain details are lost. The SAR return is a function of various characteristics of the signal, such as incident angle, polarization, and frequency, as well as dielectric properties and roughness of the surface. The surface properties influencing the SAR return are different from those influencing the return in the visible spectral region, because each part of the electromagnetic spectrum reflected from the earth contains independent information about the earth's surface.

Other types of remotely sensed data, such as magnetic field and gravity field intensities give subsurface information. By merging the data sets, such that each digital picture element (pixel) or spatial resolution element is a multidimensional vector, a classification map according to vegetation/soil/rock/structural units should be possible. The texture associated with one or more data sets may also be used as additional independent information.

Texture measures defined by Hsu (1979) have been implemented on Penn State's IBM 370/3033 computer by Pavlin (1979). Parker (1980) then applied them to Landsat data of the Nevada test site, Degelen area of the USSR, and the Tourtan Alfella area in North Africa. Results of this study indicate that some texture measures are much better discriminators of rock types than are spectral tones. Texture measures are simply added to other data for each pixel to create a larger-dimension data set.

The merged data set used in the study contained four channels of Landsat MSS data, one channel of Seasat SAR data, and a channel of magnetic field data covering part of the area investigated. The digital computer processing and classification of the merged digital data set was then undertaken using the package of programs developed at the Office for Remote Sensing of Earth Resources (ORSER) at the Pennsylvania State University (Turner et al, 1978).

#### Statement of Problem

The main purpose of this study was to apply data enhancement techniques to different remotely sensed digital data sets in an attempt to map rock types and structure in a heavily vegetated terrain. The data sets available included Landsat MSS, Seasat SAR, and in part of the region, closely

sampled magnetic field data obtained by a surface survey. To facilitate the joint use of these data sets, computer programs had to be altered or written which filtered the Seasat SAR data and cast it in a format compatible with the ORSER package of programs, which were developed for multispectral image data. Also, a program had to be written which determined 17 texture measures in every pixel neighborhood in the data set and then stored them as extra channels. The texture measures in each pixel neighborhood were expected to add additional geologic information to the data sets. The magnetic field data had to be resampled such that one data value existed for every satellite picture element (pixel). Then the magnetic field data could be cast in ORSER format and merged with the other data sets. By merging all the data sets, including the derived texture measures, the significance of each one to the separability of rock type classes could be determined and the best ones used in the final classification.

## STUDY AREA

A magnetic tape containing digital Seasat SAR data was obtained from Samuel W. McCandless Jr. at User Systems Engineering in Washington, D.C. The data on this tape had been radiometrically and geometrically corrected, but was not in the usual NASA Landsat format. The tape contained a 100 x 70 kilometer scene of an area in Pennsylvania, from South Mountain to McAlevy's Fort to Mifflinburg to York (Figures 2 and 3). The area of study chosen was 18 x 18 kilometers in the South Mountain area just west of Gettysburg, as indicated in Figure 2. It is part of the Blue Ridge Province of the Appalachians and contains Precambrian metavolcanics of the Catoclin formation as well as Cambrian metasediments of the Chilhowee Group (Figure 4). This area consists of linear ridges trending approximately N 30° E. The mountains are rugged with a maximum relief of 1100 feet. Approximately 80 percent of the area is represented by slopes. Generally, breaks in the slope are controlled by lithology (Farlekas, 1961). Although folding has been shown to be the dominant method of deformation in most of the South Mountain region of Pennsylvania and Maryland, faulting is prominent in the study area (Fauth, 1962). The Carbaugh-Marsh Creek fault which passes through the center of the study area, is a strike-slip fault with right-lateral displacement of 3.2 kilometers. This fault is

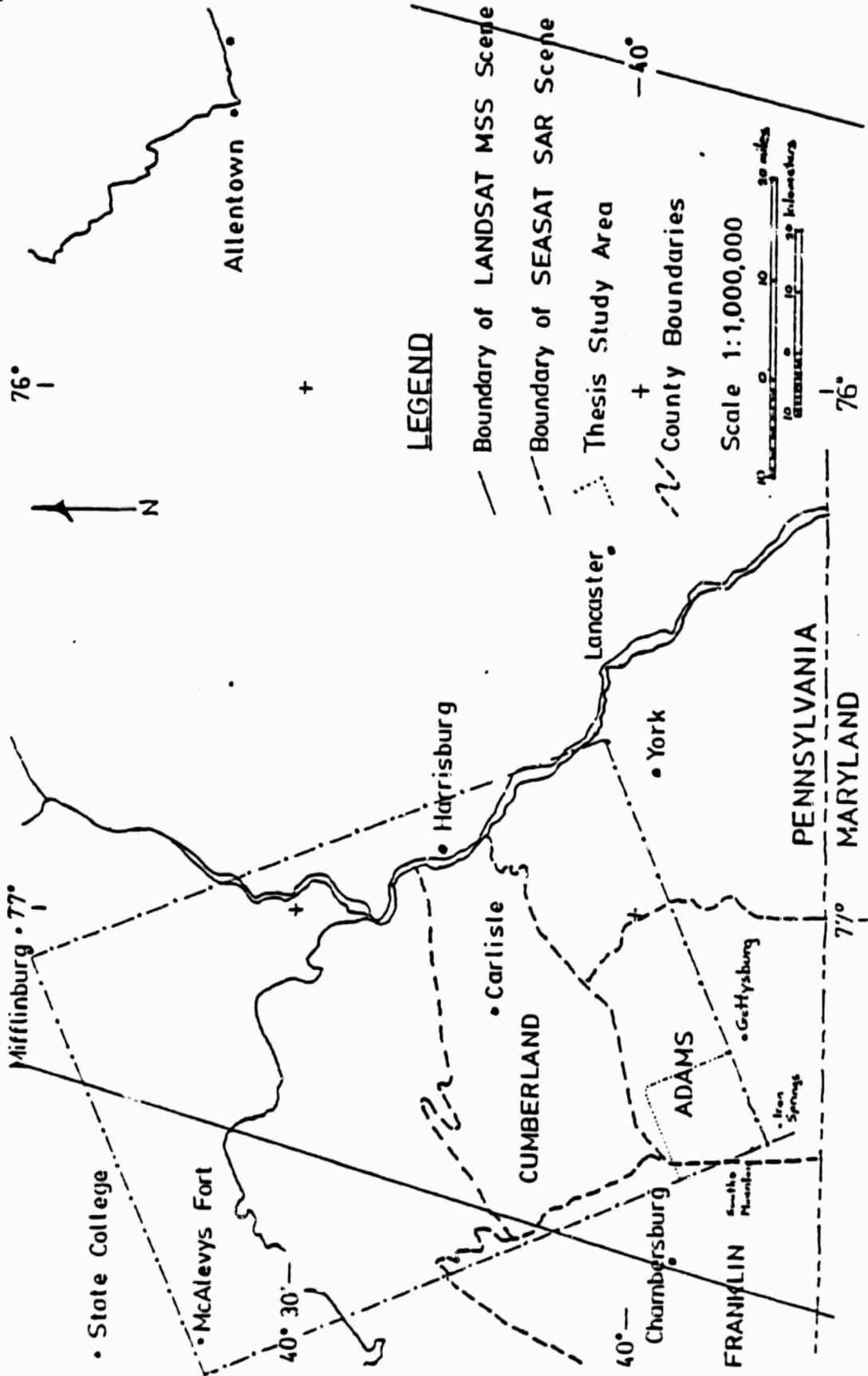
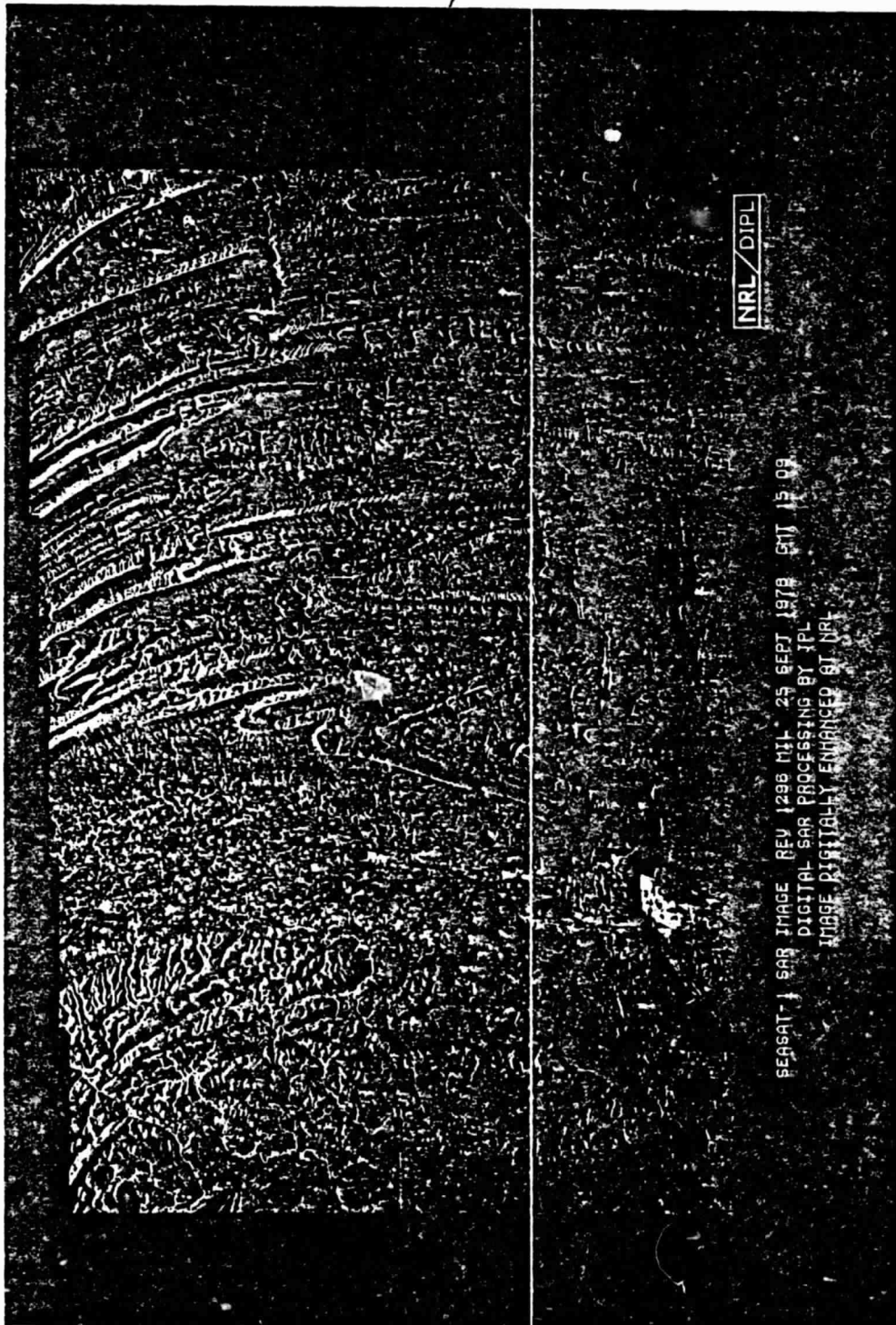


Figure 2. Index map of southeastern Pennsylvania.

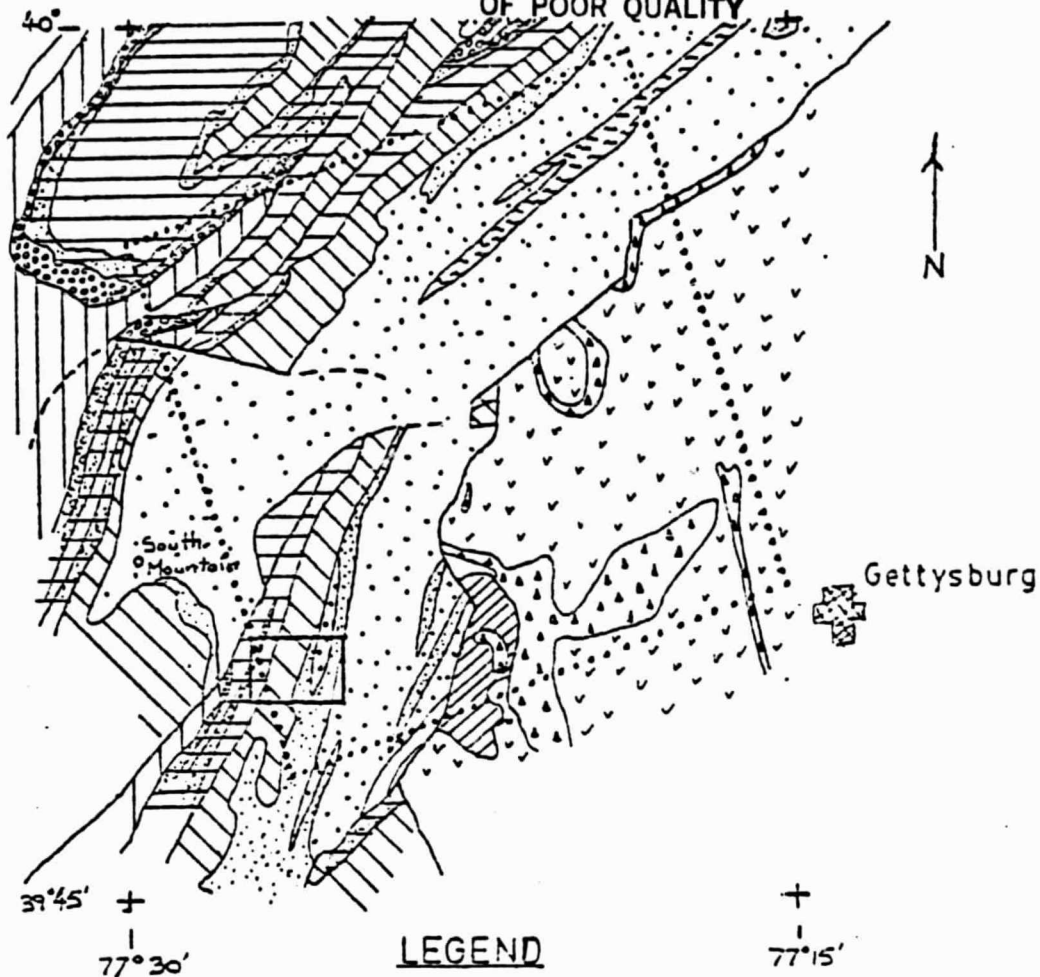
ORIGINAL PAGE IS  
OF POOR QUALITY



NRL/DIPL



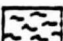



SEASAT SAR IMAGE REV 1296 MFL 25 SEPT 1978 GMT 15 09  
DIGITAL SAR PROCESSING BY JPL  
IMAGE DIGITALLY ENHANCED AT NRL

Figure 3. Seasat SAR scene



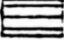
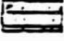
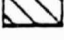




LEGEND

Catoctin formation

-  Metabasalt
-  Metarhyolite
-  Greenstone schist
-  Ordovician limestone and dolomite
-  Triassic sandstone and shale
-  Triassic diabase

Chilhowee group

-  Tomstown formation -shale with dolomite
-  Antietam formation -quartzite
-  Harpers formation -Montalto member-quartzite
-  Harpers formation -graywacke and siltstone
-  Weverton formation-quartzite, phyllite, graywacke
-  Magnetic Survey Area
-  Thesis Study Area

Scale 1:250,000

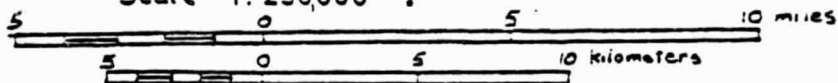


Figure 4. Regional geology of study area (after Socolow, 1960).

aligned with the Everett lineament to the west (Kowalik and Gold, 1974).

The area has been actively mined in the past due to numerous deposits of native copper and copper sulfides in metabasalts and Cornwall-type magnetite-copper deposits (Rose, 1970). Greenstone deposits are being actively mined at present. The volcanic rocks are thought to be subaerial (Fauth, 1978), and thus volcanogenic massive sulfides are not present. For this study a geologic map was compiled from maps by Stose (1932) and Fauth (1962, 1978). To the west the area is flanked by the Great Valley of the Valley and Ridge province, whereas on the east it terminates against the fault-bounded Triassic lowlands. Traditionally, the basic structure of South Mountain was thought to be a rooted anticlinorium with an overturned western limb (Epenshade, 1970). There is now mounting geophysical evidence that the entire Blue Ridge is actually a thrust sheet above a major decollement (King, 1964; Cook et al, 1979). Gwinn (1970) outlines three possible basement configurations in the South Mountain area (Figure 5). This study does not present any new evidence to resolve this controversy. The presence of such a range of different rock types and a complexity of structure makes it an interesting area to develop and test techniques for interpreting combinations of remotely sensed and conventional geophysical observations, in a vegetated terrain with considerable topographic relief.



ORIGINAL PAGE IS  
OF POOR QUALITY

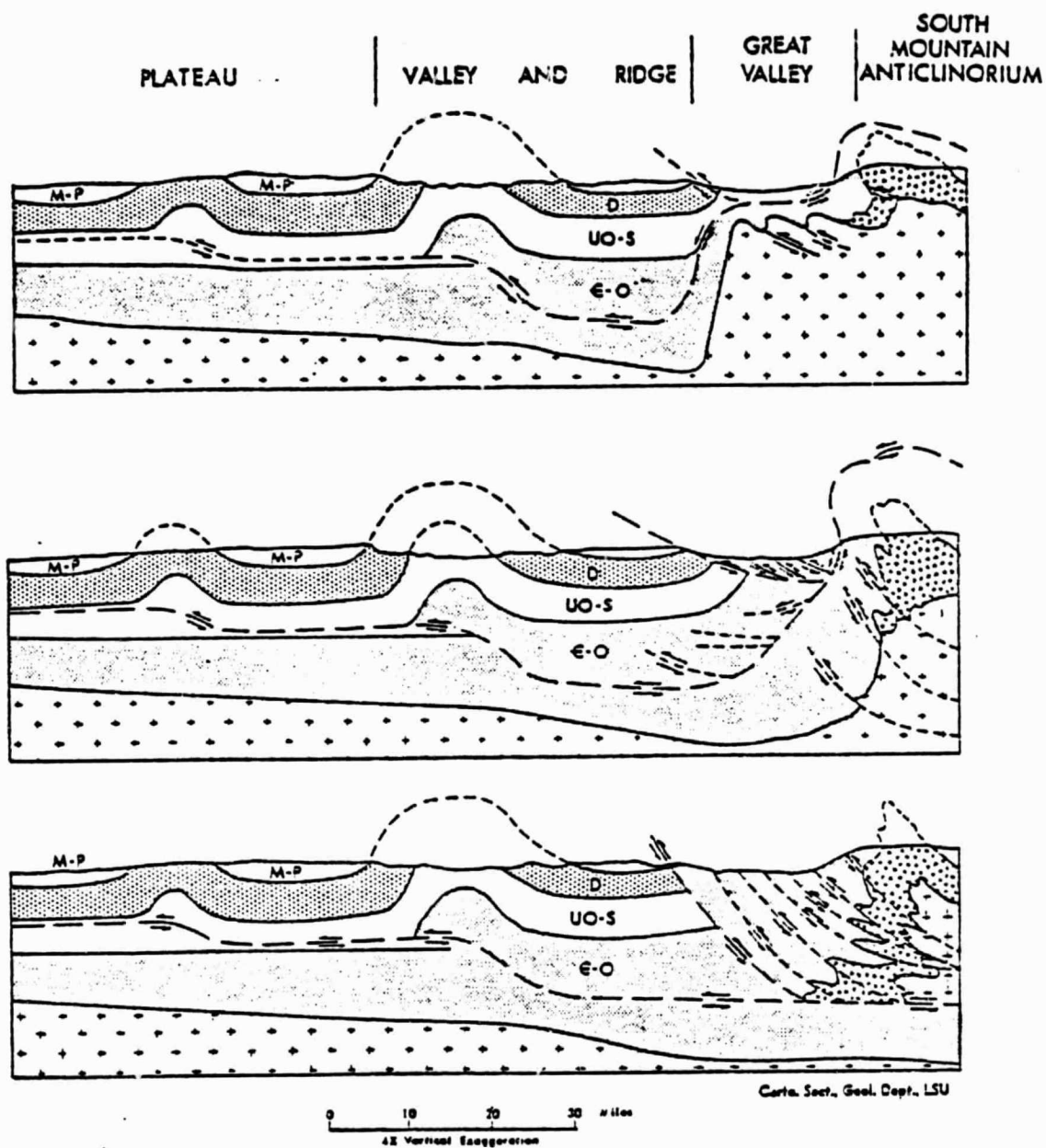


Figure 5. Hypothetical configurations of basement in the South Mountain area (after Gwinn, 1970).

## METHOD

Data Collection

Much of the work in this study was involved with preprocessing of the data, especially the Seasat SAR data. Because the SAR data was collected on September 25, 1978, a Landsat tape from the Fall season was chosen. A tape from the same year was not readily available and was not considered essential. The Landsat tape selected was NA0160, NASA ERTS E-1440-15172, October 6, 1973 (Figure 6).

The idea that a data set representing an entirely different rock property might aid in distinguishing rock types in a vegetated area, prompted the investigation of the aeromagnetic coverage in the South Mountain area. Through consultation with Dr. P.M. Lavin (1980), it was discovered that although one-quarter mile flightline coverage existed in the Triassic basin near Gettysburg, the area of interest was covered by flightlines four miles apart. This was much too coarse a sampling interval to be of any use in this study; therefore, a field magnetic survey was undertaken.

Grid lines were laid out by pace and compass, perpendicular to the regional geological trend (Figure 7). It was hoped that by this orientation of grid lines, a large line spacing could be used without causing aliasing of the data. The lines were spaced 400 meters apart and readings

ORIGINAL PAGE IS  
OF POOR QUALITY



14877-38 14877-001 14875-38 448-15172-7 01  
06OCT73 C N48-19/14876-25 N N48-17/14876-19 MSS 7 D SUN EL39 92148 131.5 24-N-1-N-D



Figure 6. Landsat MSS scene (band 7)

ORIGINAL PAGE 19  
OF POOR QUALITY

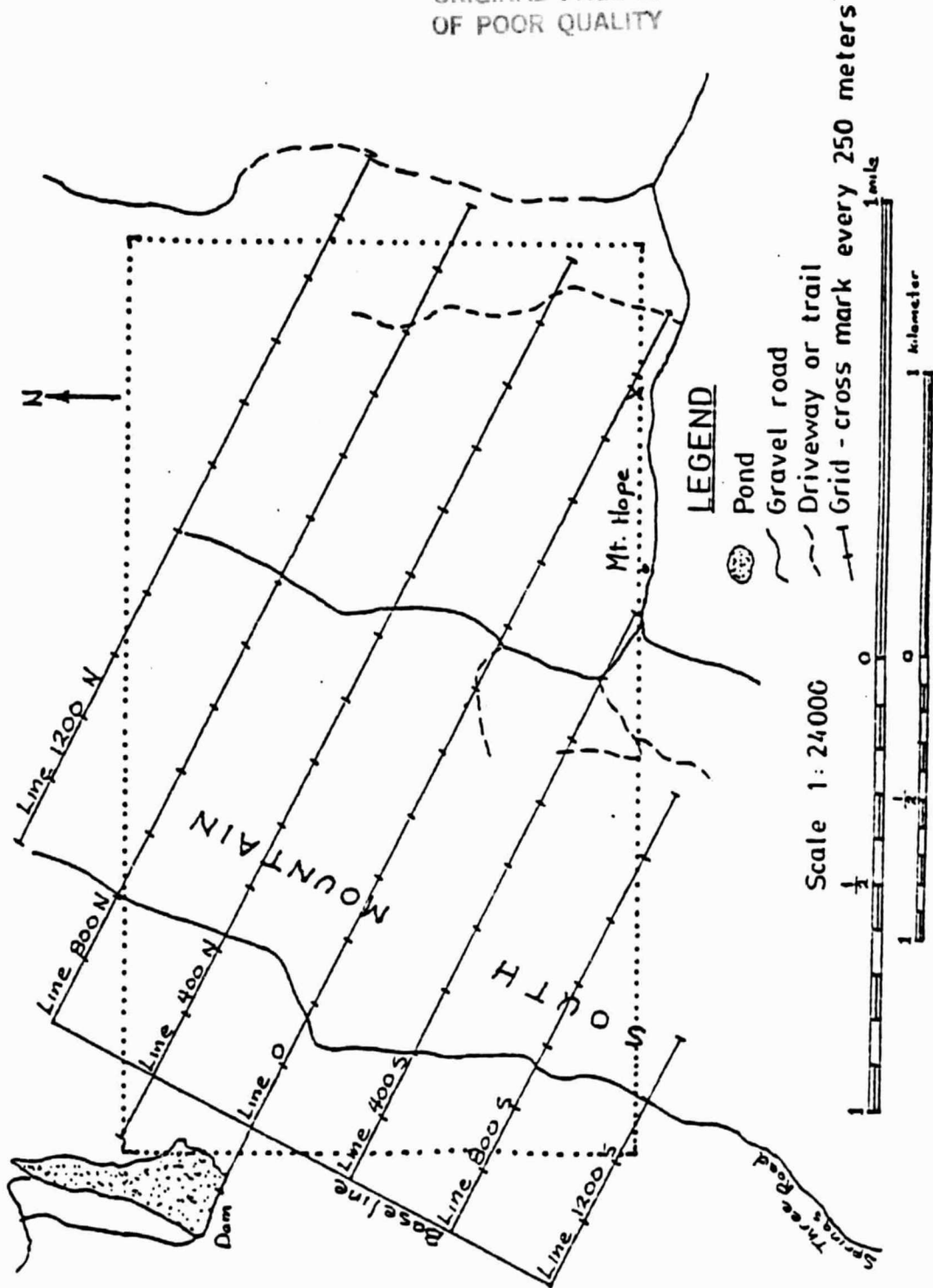


Figure 7. Magnetic field survey grid. Location shown in Figure 4.

Adams Co.  
Franklin Co.

were taken every 25 meters along the lines. The area chosen lay five kilometers directly southeast of the town of South Mountain. The area contained both a large diversity of rock types and a sparse population. One small copper prospect near Mt. Hope, which was mined at the turn of the century, was included in the survey area. The survey was conducted using the proton precession magnetometer belonging to the Geophysics Program, Geosciences Department of the Pennsylvania State University. The actual dimensions of the area were 3.2 kilometers east-west by 2.0 kilometers north-south (Figure 4).

#### Relationship of magnetic field data and geologic features

The magnetic field data was used both as an aid to surface rock type classification, and in determining the relationship between subsurface geologic structure and the total magnetic field. In the magnetic field survey area, a geologic cross-section was compared to a magnetic field profile. Also, the contoured total magnetic field map was compared to the detailed ground-mapped geology.

## Preprocessing

Reformatting and rotating the Seasat SAR data set. The first step in the processing of the Seasat SAR data set was to make it compatible with the Office for Remote Sensing of Earth Resources (ORSER) system of programs (Turner et al, 1978); references in this section and elsewhere are made to specific programs in that system, and a description of each is available in their manual. This entailed translating the tape from ASCII to EBCDIC format using the PSUDEBE magnetic tape utility program, and then rewriting the ORSER SUBSET program so that it produced a labelled tape in the ORSER format. The original SAR tape also had a LRECL=6144 and a BLKSIZE=6144. This had to be changed to the ORSER specifications of LRECL=3692 and BLKSIZE=3700. This meant that an entire line of data from the SAR tape could not be subset onto the ORSER tape all at one time.

A further complication to the eventual spatial registration of the Seasat SAR scene to a Landsat scene was that the azimuth of the SAR scene (perpendicular to the scan line orientation) was 246 degrees. This was 125 degrees off from the azimuth of the Landsat scene (11 degrees azimuth). The ORSER SUBGM program will not allow more than 36 lines of data in memory; thus, only rotations of less than 10 degrees will usually be allowed each time (depending on the size of the data set, of course). This problem was alleviated by

subsetting a small area of interest (size limited by computer storage capability) and incorporating in the rewritten SUBSET program (SUBRAD), a section that switched lines and elements, thus implementing a 90 degree rotation.

The resolution of the SAR is 25 meters but the sampling rate is finer. Thus the SAR data after rotation had a pixel spacing of 18 meters between elements and 16 meters between lines. The NMAP digital image scale of the SAR data (1:6299), was much larger than that of the Landsat digital image (1:31102.4). The desired scale was 1:24000, but the SUBGM program could not handle such a drastic scale reduction, except by a series of iterative reductions. Thus the SUBRAD program sampled every third element of every third line, giving a scale of 1:18898.

Filtering Seasat SAR data. The second step was to remove the look direction dependency of the SAR data (Appendix 1) by applying a filter in the wavenumber domain of the form:

$$(1/(1 - 0.5 \cos 2\phi))^{1/2} \quad (1)$$

where  $\phi$  = the azimuthal angle or viewing angle.

The filter had values from 0.8 to 1.4 and thus did not change the average values in the space domain very much. The 0-255 dynamic range was preserved. The filter values were simply multiplied by the data wavenumber values in the

wavenumber domain. The filter was also multiplied by a Hamming window to minimize spectral leakage in the space domain. A major problem was the limited core space available for the large arrays involved in the 2-D fast Fourier transform. This problem is somewhat alleviated now, with the new MVS system for the IBM 370/3033 computer at Penn State. Another possibility for decreasing the core space needed, would be to apply a truncated version of the filter in the space (or image) domain and use a convolution technique.

Processing the magnetic field data. The third step was to cast the magnetic field data into a form compatible (same sampling interval and dynamic range) with the other two data sets. The data set had to be resampled and interpolated. The Nyquist wavenumber (Brigham, 1974) of the magnetic field data, at a 25 meter sampling interval, was about  $0.0082 \text{ meters}^{-1}$ , thus a sampling interval greater than 61 meters along the lines could lead to aliasing. Across the lines it was assumed that the 400 meter sampling interval was adequate, because the rock units were striking in that direction.

In order to use the ORSER program SUBGM, the data had to be extrapolated to form a square grid. The lines were extended by adding data from adjacent lines (Figure 7). Lines 400 North and Zero spanned the entire length of the



grid; thus, data values at the ends of these lines were used to extend all the other data lines in the grid. Line 400 North was used to extend lines in the northern part of the grid, while line Zero was used to extend lines in the southern part of the grid. The data were then resampled at a 50 meter interval along the lines and linearly interpolated to a 50 meter sampling interval across the lines. The resulting rectangular data set had to be reduced to a 0-255 range and then written to tape in ORSER format. A program (SUBMAG) was written which accomplished that step. The data set could then be rotated to zero azimuth and rescaled to a 1:24000 scale using the ORSER program SUBGM. An attempt was made to use cubic convolution resampling during the data set rotation, but when that failed (for an unknown reason), a nearest neighbor resampling was used. The resulting density slice map (NMAP) is shown in Figure 8. The blank areas represent the highest magnetic field readings, while the darkest symbols represent the lowest readings. The final scale of the NMAP was 1:24000 which meant that a sampling interval of 61 meters was used and some aliasing may have occurred.

This type of ground survey magnetic field data is referred to as "draped" data, because the elevation at which each point was read was constantly changing due to the rugged topography. Filtering the data would have first required reducing it to a single datum plane. The Fourier

Figure 8. NMAP digital printout of magnetic field data (not corrected for line printer ). The line printer outputs 10 symbols per inch but only 6 lines per inch. The figure has also been reduced during copying. The solid line outlines the actual magnetic field survey area before extrapolation, as shown in Figures 4 and 7. Each symbol represents a level of intensity of the total magnetic field, with blank areas containing the highest magnetic field values, and each symbol (. , - + X N \*) representing areas of progressively lower total magnetic field values.

ORIGINAL PAGE IS  
OF POOR QUALITY

37XI 879I 883I 888I 893I 898I 903I 908I 913I 918I 923I 928I 933I 938I 943I  
I I I I I I I I I I I I I I I I I  
1 I IX I 1  
2 I IXN I 2  
3 I IXNN I 3  
4 I IXNNN I 4  
5 I IXNNNN I 5  
6 I IXNNNNN I 6  
7 I IXNNNNNN I 7  
8 I IXNNNNNNN I 8  
9 I IXNNNNNNNN I 9  
10 I IXNNNNNNNNN I 10  
11 I IXNNNNNNNNNN I 11  
12 I IXNNNNNNNNNNN I 12  
13 I IXNNNNNNNNNNNN I 13  
14 I IXNNNNNNNNNNNNN I 14  
15 I IXNNNNNNNNNNNNNN I 15  
16 I IXNNNNNNNNNNNNNNN I 16  
17 I IXNNNNNNNNNNNNNNNN I 17  
18 I IXNNNNNNNNNNNNNNNNN I 18  
19 I IXNNNNNNNNNNNNNNNNNN I 19  
20 I IXNNNNNNNNNNNNNNNNNNN I 20  
21 I IXNNNNNNNNNNNNNNNNNNNN I 21  
22 I IXNNNNNNNNNNNNNNNNNNNNN I 22  
23 I IXNNNNNNNNNNNNNNNNNNNNNN I 23  
24 I IXNNNNNNNNNNNNNNNNNNNNNNN I 24  
25 I IXNNNNNNNNNNNNNNNNNNNNNNNN I 25  
26 I IXNNNNNNNNNNNNNNNNNNNNNNNNN I 26  
27 I IXNNNNNNNNNNNNNNNNNNNNNNNNNN I 27  
28 I IXNNNNNNNNNNNNNNNNNNNNNNNNNNN I 28  
29 I IXNNNNNNNNNNNNNNNNNNNNNNNNNNNN I 29  
30 I IXNNNNNNNNNNNNNNNNNNNNNNNNNNNNN I 30  
31 I IXNNNNNNNNNNNNNNNNNNNNNNNNNNNNNN I 31  
32 I IXNNNNNNNNNNNNNNNNNNNNNNNNNNNNNNN I 32  
33 I IXNNNNNNNNNNNNNNNNNNNNNNNNNNNNNNNN I 33  
34 I IXNNNNNNNNNNNNNNNNNNNNNNNNNNNNNNNNN I 34  
35 I IXNNNNNNNNNNNNNNNNNNNNNNNNNNNNNNNNNN I 35  
36 I IXNNNNNNNNNNNNNNNNNNNNNNNNNNNNNNNNNNN I 36  
37 I IXNNNNNNNNNNNNNNNNNNNNNNNNNNNNNNNNNNNN I 37  
38 I IXNNNNNNNNNNNNNNNNNNNNNNNNNNNNNNNNNNNNN I 38  
39 I IXNNNNNNNNNNNNNNNNNNNNNNNNNNNNNNNNNNNNNN I 39  
40 I IXNNNNNNNNNNNNNNNNNNNNNNNNNNNNNNNNNNNNNNN I 40  
41 I IXNN I 41  
42 I IXNNN I 42  
43 I IXNN I 43  
44 I IXNNN I 44  
45 I IXNN I 45  
46 I IXNNN I 46  
47 I IXNN I 47  
48 I IXNNN I 48  
49 I IXNN I 49  
50 I IXNNN I 50  
51 I IXNN I 51  
52 I IXNNN I 52  
53 I IXNN I 53  
54 I IXNNN I 54  
55 I IXNN I 55  
56 I IXNNN I 56  
57 I IXNN I 57  
58 I IXNNN I 58  
59 I IXNN I 59  
60 I IXNNN I 60  
61 I IXNNN I 61  
62 I IXNN I 62  
63 I IXNNN I 63  
64 I IXNNN I 64  
65 I IXNNN I 65  
66 I IXNNN I 66  
67 I IXNNN I 67  
68 I IXNNN I 68  
69 I IXNNN I 69  
973I 878I 883I 888I 893I 898I 903I 908I 913I 918I 923I 928I 933I 938I 943I

methods used in more simple continuation problems from one linear surface to another would not be applicable (Henderson and Cordell, 1971; Syberg, 1972). Instead, a finite harmonic series approximation would have to be used. Because topography did not seem to have a significant effect on the data set, no filtering was attempted.

Registration of all the data sets. The fourth step was the rotation of both the Landsat data and the filtered SAR data to zero degree azimuth (Figures 9 and 10) using SUBGM. The area shown in Figures 9 to 12 is the entire thesis study area as outlined in Figures 2 and 4. Some changes in array size specifications in SUBGM were made in order to allow larger rotations. Scale changes and the interpolation of the data to form square pixels were accomplished at the same time. Then, registration points were picked on the NMAP digital images of each scene. This step was very difficult due to the intrinsic differences in the information recorded by each sensor. By choosing 20 well-distributed registration points, a set of fourth degree polynomial functions could be used to rubbersheet-stretch the SAR data using the ORSER programs RUBRFUN and SUBGM. These polynomials were arrived at by a step-up, linear, multiple regression procedure as explained in the ORSER manual (Turner et al, 1978). The rubbersheet stretched SAR data (Figure 11) was matched to the Landsat data by minimizing

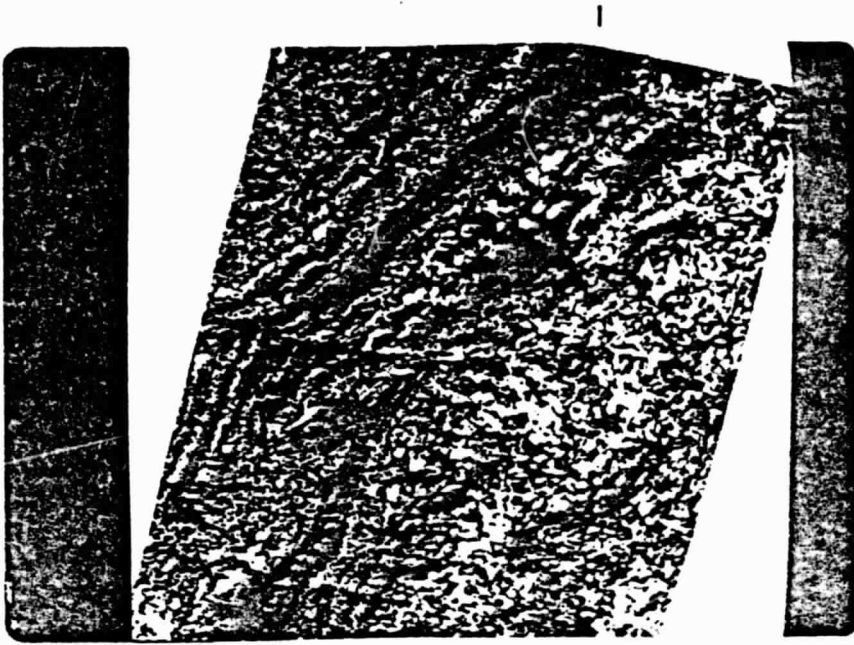


Figure 9. NMAP of Landsat MSS data rotated to zero azimuth.

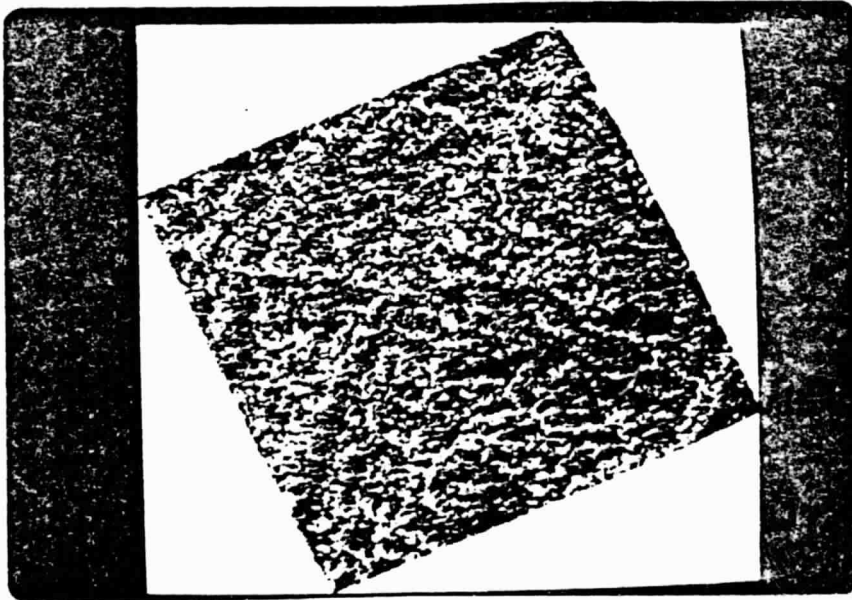


Figure 10. NMAP of Seasat SAR data rotated to zero azimuth.



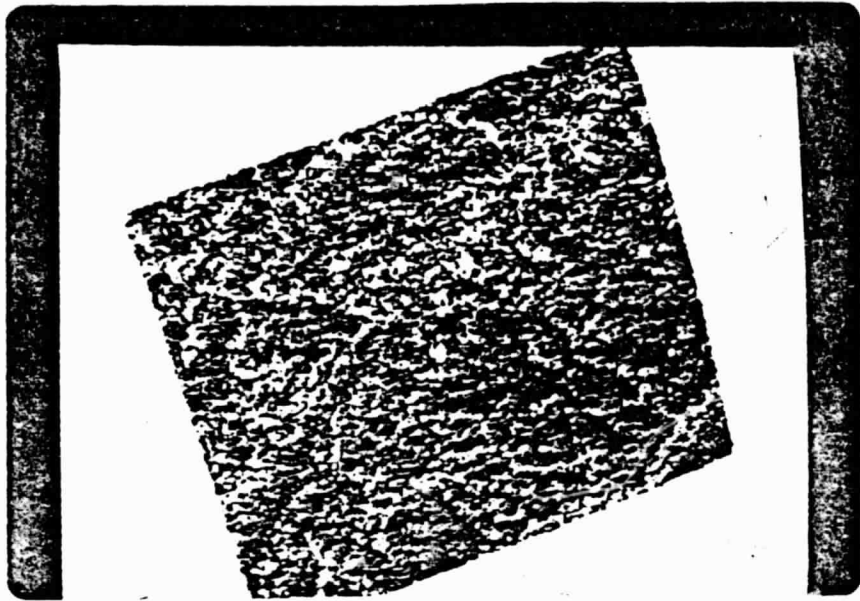


Figure 11. NMAP of rubbersheet-stretched Seasat SAR data.

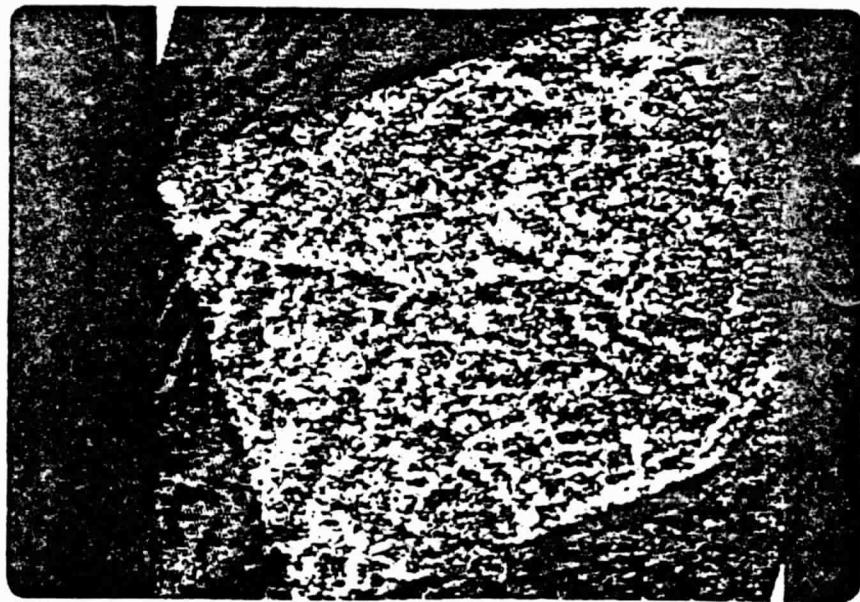


Figure 12. NMAP of merged Landsat MSS - Seasat SAR data.

the error between all the paired registration points. This data set was then merged with the Landsat data and stored on tape as a fifth channel (Figure 12). Before merging, the Landsat data was contrast-stretched by 2.5 times in all 4 channels so that it covered more of the 0-255 range and thus was more compatible with the SAR data.

The small area of magnetic field data was then merged with the Landsat-SAR data. No rubbersheet stretching of the magnetic data was undertaken. After a close comparison of the corrected Landsat digital image with a set of USGS 1:24000 scale topographic maps of the area (Iron Springs, Fairfield, Caledonia Park, and Arendtsville quadrangles) (USGS, 1953), it was concluded that rubbersheet stretching was not required. This conclusion held for the entire study area. The registration of the combined image was accomplished through a simple overlaying and recording of matching pixel coordinates and latitude-longitude coordinates (Table 1). The magnetic field data set was used as a sixth channel in a small section of the area of interest (Figure 4) to test its usefulness in distinguishing rock types.

Principal components analysis. The final step in the preprocessing of the data was the principal component transformation of the entire merged Landsat-SAR data set. The starting point of principal component analysis is the

Table 1. Registration of merged data to topographic maps.

Latitude	Longitude	Line Number	Element Number
39°55'00" N	77°27'30" W	2521	401
39°55'00" N	77°22'30" W	2522	516
39°50'00" N	77°27'30" W	2672	400
39°50'00" N	77°22'30" W	2673	516

USGS  
Topographic Map  
(1:24,000)

Combined Landsat-SAR-  
Magnetics Image  
(1:24,000)



assumption that conservation of variance corresponds to conservation of information. The method employs a rotational transformation of the original data set such that each new axis accounts for progressively less and less of the total variance (Borden et al, 1976). The transformation is useful because it requires no prior information and can be used to reduce the dimensionality of the data set if there is redundancy among channels. The NMAP density slice displays of four of the resulting five axes are shown in Figures 13,14,15, and 16. The first principal axis contained 86.9 percent of the total variance, the second axis contained 11.0 percent, and the higher numbered axes contained the rest of the variance. Table 2 illustrates the fact that axis 1 had a high negative correlation with channel 5, the SAR channel, and that axis 2 had a high negative correlation with both channels 3 and 4. Thus the first principal axis was essentially the SAR data, whereas the second and third axes were the first and second principal components of the four Landsat channels. Table 3 shows that the Seasat SAR channel was not highly correlated with any of the Landsat channels and thus was a very unique set of data. This also illustrates why registration of the SAR to the Landsat data was very difficult. After the principal component transformation, the resulting axes showed very little correlation with each other as shown in Table 4. The principal component axes are by definition, those axes that minimize this correlation.

ORIGINAL PAGE IS  
OF POOR QUALITY

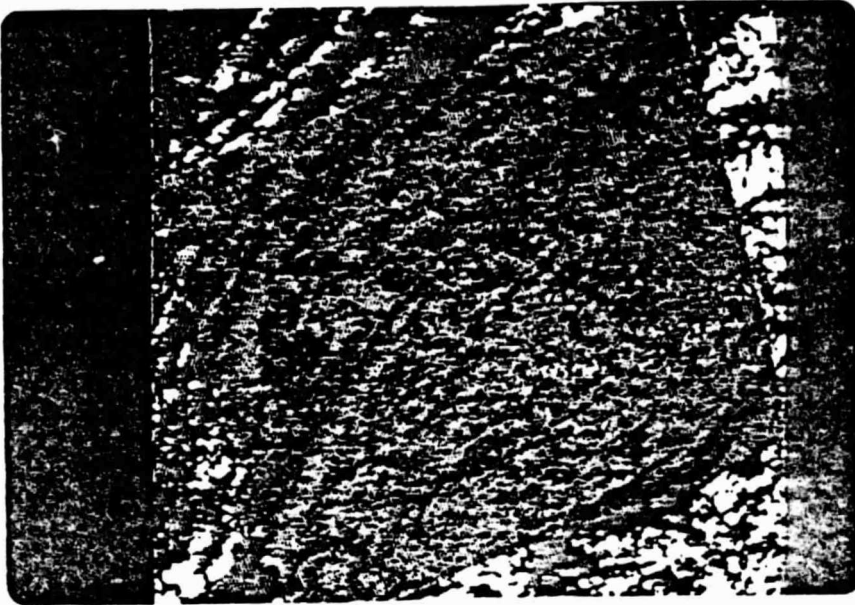


Figure 13. NMAP of principal component axis 1.



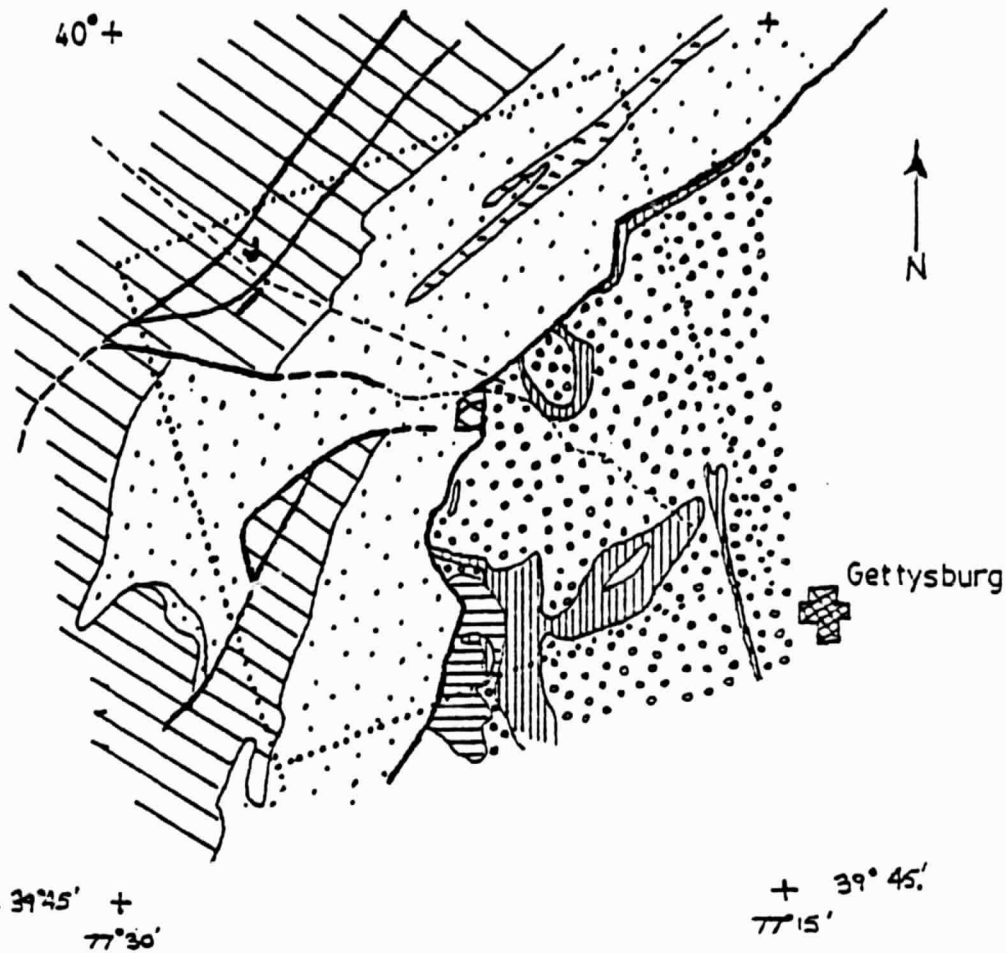
Figure 14. NMAP of principal component axis 2.














Figure 15. NMAP of principal component axis 3.



Figure 16. NMAP of principal component axis 4.



LEGEND

- |   |                                      |   |                   |
|---|--------------------------------------|---|-------------------|
|  | Precambrian schist                   |  | Thesis study area |
|  | Precambrian metavolcanic             |  | Faults            |
|  | Cambrian metasediment                |  | Power line        |
|  | Ordovician limestone<br>and dolomite |  | Marsh Creek       |
|  | Triassic sandstone<br>and shale      |  | Reservoir         |
|  | Triassic diabase                     |   |                   |

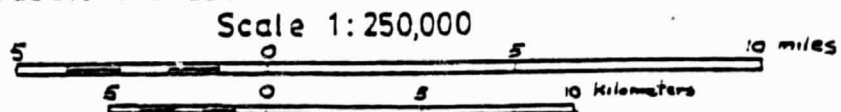


Figure 17. Linear features and major structural and geologic units of the study area (after Socolow, 1960).

Table 2. Correlation of channels with principal component axes.

Axis:	1	2	3	4	5
Channel					
1	0.12	-0.45	-0.80	0.01	-0.37
2	0.09	-0.34	-0.91	0.11	0.20
3	0.14	-0.98	0.00	-0.10	0.02
4	0.13	-0.95	0.19	0.20	-0.02
5	-1.00	-0.02	-0.00	-0.00	-0.00

Table 3. Correlation matrix for initial given channels.

Channel:	1	2	3	4	5
Channel					
1	1.00				
2	0.82	1.00			
3	0.45	0.33	1.00		
4	0.30	0.18	0.94	1.00	
5	-0.11	-0.08	-0.12	-0.11	1.00

Table 4. Correlation matrix for principal component axes

Axis:	1	2	3	4	5
Axis					
1	1.00				
2	0.19	1.00			
3	-0.06	-0.17	1.00		
4	-0.06	-0.14	0.01	1.00	
5	0.04	-0.11	-0.04	-0.03	1.00

## Feature Extraction

Choosing training areas. Training areas were chosen within the area of the image that was geologically mapped most recently (Fauth, 1978); the testing area was that area mapped earlier by Fauth (1962), while the rest of the area of interest was classified and compared to the mapping done by Stose (1932). An NMAP digital image of the merged Landsat-SAR data set (corrected for the line printer) was overlain manually on the geology map of Fauth (1978). The rock type boundaries were then traced and transferred to an NMAP not corrected for the line printer, because this was the data set on which the final classification had to be done. Training areas were chosen on the basis of this NMAP and a uniformity map (UMAP), also not corrected for the line printer. Three criteria were followed in establishing training areas:

- (1) Sites within the area of the magnetic field survey were chosen first.
  
- (2) Sites used in the texture analysis (including all those outside the area of the magnetic survey and some inside) had to contain a minimum of 51 pixels. This criterion is based on the work of Foley (1971). His principle states that for a valid analysis the minimum number of pixels sampled must be three times as large

as the number of variables used. Because the texture algorithm calculates 17 measures of texture, 51 pixels were needed.

- (3) Because texture was one of the measures used in discriminating between classes, the training areas were chosen by using both the NMAP and UMAP digital outputs. The predominant intensity level and degree of uniformity within a given rock type area were considered to be characteristic of that rock type. Training areas were chosen on that basis.

There were 14 training areas chosen inside the magnetic field survey area (Figure 37), and 26 more were chosen outside that area. Areas that were too small to use for the texture measure analysis were input together as one training area, or else the statistics from them were combined afterwards so that they essentially represented one larger area. The characteristics of each rock type class are listed in Tables 5 and 6. All the training areas were chosen either within the Precambrian Catoclin formation of metavolcanics (rock type classes A, B, and C) or in the Cambrian Chilhowee group of metasediments (rock type classes D, E, F, and C).



Table 5. Rock type classes in Catocctin metavolcanics  
(after Fauth, 1978).

Rock type class	Characteristics
Rock type A	Phyllites which were originally a rhyolite tuff. A thin bed outcrops in the eastern part of the magnetic survey area. One training area was chosen in the magnetic field survey area; none outside.
Rock type B	Metarhyolites which were originally glassy lava flows or welded tuffs. Many outcrops occur. Three training area were chosen in the magnetic field survey area, seven outside.
Rock type C	Metabasalts which were the initial lava flows, were followed by thick sequences of rhyolite and then a final intrusion of basalt. Poor exposure exists. Three training areas were chosen in the magnetic field survey area, seven outside.

Table 6. Rock type classes in Chilhowee metasediments  
(after Fauth, 1978).

Rock type class	Characteristics
Rock type D	Loudoun formation composed of phyllites and graywackes. It occurs along lower slopes of ridges. Outcrops are rare. Two training areas were chosen in the magnetic field survey area, five outside.
Rock type E	Weverton formation composed of quartz phyllites, quartzose graywackes, and quartzites. It is a major ridge former. Two training areas were chosen in the magnetic field survey area, five outside.
Rock type F	Harpers formation composed of greywacke siltstone and greywacke. It forms shallow longitudinal valleys. Two training areas were chosen in the magnetic field survey area, one outside.
Rock type G	Harpers formation - Montalto member composed of medium-grained quartzite. It forms the upper slopes and crests of ridges. One training area was chosen in the magnetic field survey area, six outside.

Spectral signatures. Once all the training areas were chosen, they were input to the ORSER program STATS, which computed the mean vector and the variance-covariance matrix for each training area. The training areas within the magnetic survey area were each characterized by a six-component mean vector or spectral signature. These mean vectors were then input to a multivariate stepwise discriminate analysis program (BMD07M) developed at UCLA (Jennrich and Sampson, 1979). This program tests the separability of rock types, as will be explained later. The first four Landsat components were input first, then the Seasat SAR component was added, and finally the magnetic survey component was added. In this way, the contribution of each component to the separability of rock types could be tested. The five-component mean vectors of the training areas outside the magnetic survey area, plus some inside the area, were tested in the same way. Each training area was then input to the texture algorithm.

Textural signature algorithm. Most classification decision rules in use at present depend on the assumption of normally distributed data for their implementation. The minimum-distance decision rule assumes equal within-group variances as well as normality of the data, while the Mahalanobis distance classifier takes account of different within-group variance-covariance matrices, thus resulting in

higher classification accuracy. Hsu (1979) states that it has been well-documented that spectral response data, in most cases, are not normally distributed. This non-normality causes substantial errors in final decision maps produced by most classifiers. To solve the problem, as well as to improve the feature extraction capability, he proposed a textural algorithm that in effect creates a more normally distributed data set (Hsu, 1979). A (3x3) pixel window design was applied to the data to extract 17 texture measures which were assigned to the center pixel of the (3x3) pixel box. These measures of texture tone (Table 7) were implemented by the computer program written by Pavlin (1979).

This texture algorithm was applied to the Seasat SAR channel of each of the training areas. The algorithm computed the average of each texture measure within each training area and output this measure as the textural signature of that training area. These signatures could then be input to the BMD07M program to test the separability of rock types. By adding the spectral tone signatures from the Landsat channels as four more variables, the separability due to texture measures could be compared to that due to spectral signature alone. The texture algorithm was also applied to the first three axes of the principal component transformed data to test the effect on separability using this transformation.

Table 7. The texture-tone variables of Hsu's algorithm  
(after Hsu, 1979).

Code	Description or computational formula
1. MEAN	Average
2. STD	Standard deviation
3. SKEW	Skewness
4. KURT	Kurtosis
	} the four central moments
5. MDEVN	$[x_i - \bar{x}]/n$ , where $x_i$ =tone value of individual pixel $\bar{x}$ =mean
6. MPTCON	$[x_i - x_c]/n$ , where $x_c$ =tone value of center point
7. MPTREL	$(x_c - x_i)/n$
8. MINCON	$[x_i - x_j]/n$ , $i$ and $j$ are adjacent pixels
9. MINSQR	$(x_i - x_j) / n$
10. M2NCON	$[x_i - x_k]/n$ , $i$ and $k$ are second neighbors
11. M2NSQR	$(x_i - x_k) / n$
12. MADAT1	Mean area above datum 1 (50)
13. MADAT2	Mean area above datum 2 (100)
14. MADAT3	Mean area above datum 3 (150)
15. MBDAT1	Mean area below datum 1 (50)
16. MBDAT2	Mean area below datum 2 (100)
17. MBDAT3	Mean area below datum 3 (150)

The texture measures that best separated the categories were then extracted for each pixel neighborhood and written to tape, using a modified version of the previously implemented texture program of Pavlin (1979).

Correlations between data sets. The first principal component axis essentially represented the SAR data, while the second and third axes represented the first and second principal components of the four Landsat channels respectively. Thus, a test could be made (over the entire study area), of the correlation between the Landsat textures and either the SAR tone or the SAR texture. The correlation between the SAR tone and each of the 17 texture measures of both principal component axes 2 and 3 was first tested. Then, a test was made of the correlation between the texture measures (from all three principal component axes) that best separated the rock type categories. Four texture measures from principal component axis 1 were used, five from axis 2, and one from axis 3. In the magnetic field survey area, the correlation between 17 texture measures from all three principal component axes and the magnetic field data, was tested. Eight texture measures from each of the principal component axes 1 and 2, plus one from axis 3, were used in the test.

Discrimination. A useful supplement to the ORSER set of programs was the UCLA BMD07M program which performed a multiple group discriminant analysis on the mean signatures of the training areas. The variables were entered one at a time depending on their F-statistic (which measures that variable's contribution to the between-group variance). The variable with the largest F-statistic was the one that contributed the most to the between group variance and the least to the within group variance. This variable was entered first. If, as more variables were entered, a variable's F-statistic dropped below a certain level, that variable was deleted from the analysis. In this manner, the variables that contributed the most to the discrimination of rock types could be identified. Once all the variables with a large enough F-statistic were entered, a canonical analysis, developed by Merembeck et al (1976), was done, which fitted a new set of mutually orthogonal axes to the data by rotation, translation, and scaling, such that the first axis accounted for the greatest amount of variance with succeeding axes accounting for less and less. Mathematically the process created a set of transformed variables by maximizing the between-class covariance and minimizing the within-class covariance. The first two canonical axes were plotted on a scattergram to give an optimal two-dimensional picture of the separation of groups. These scattergrams were used in each step of the analysis,

to determine the contribution of each data set and/or texture measure to the separability of rock types (Figures 21 to 34). Each rock type symbol on the scattergrams represents a training area for that rock type. If two training areas of one rock type class are very close together, only one symbol is printed. The asterisks (\*) indicate the location of the mean values of each rock type class in canonical space. The characteristics of the rock type classes are tabulated in Tables 5 and 6. The abscissa or horizontal axis is the first canonical axis, and the ordinate or vertical axis is the second canonical axis.

### Classification

The data classification was first performed on five channels of texture measures computed from the principal component transformed data. Texture measures 7, 8, and 14 (Table 7), extracted from principal component axis 1, and texture measures 3 and 5, extracted from principal component axis 2, were merged forming a new data set used in the classification. Using the ORSER program CANAL, the signature from each of the training areas was used to construct canonical axes that best separated the data classes. The data pixels were then transformed into canonical space and classified using a minimum distance



rule. The 5-channel data set was reduced to 4 canonical axes. Classification was performed on the entire study area and then on the magnetic field survey area after the addition of the magnetic field data. The 6-channel data set in the magnetic field survey area was also reduced to 4 canonical axes.

A comparison of principal component axis 3 (Figure 15) with a map of the linear features and major structural and geologic units (Figure 17), reveals the close similarities and thus the importance of the third principal component. The Carbaugh-Marsh Creek fault shows up well, cutting horizontally across the Figure. The powerline right-of-way is also clearly visible. The most interesting feature of Figure 15 though, is the significant contrast across the faults separating the Triassic Basin on the east from the Blue Ridge province on the west. In the Blue Ridge, the metavolcanic rocks seem to be displayed as lighter colored, and the metasediments are a darker green. In the Triassic Basin, all units appear much darker.

An attempt was made to improve the classification accuracy in the magnetic field survey area by using more texture measures including one from principal component axis 3. Eight channels were used initially, and reduced to 5 canonical axes.

## RESULTS

Each data set was tested for its geologic information content. The magnetic field data alone could be correlated very well with the geology of the study area. With the merged data set, a steady progression was made towards better and better automatic computer classification of the study area. Isolating the causes of classification errors was difficult, but one of the principal causes was probably registration errors.

Registration

Registration of the SAR data to the Landsat data resulted in a 15 pixel or better accuracy between matching registration points. This is about a 1 kilometer or better relative accuracy. No measure of absolute accuracy could be obtained.

Relationship of magnetic field data and geologic features

A comparison of the total magnetic field to the geology and geologic structure in the survey area (Figures 18, 19, and 20), yielded some interesting correlations.

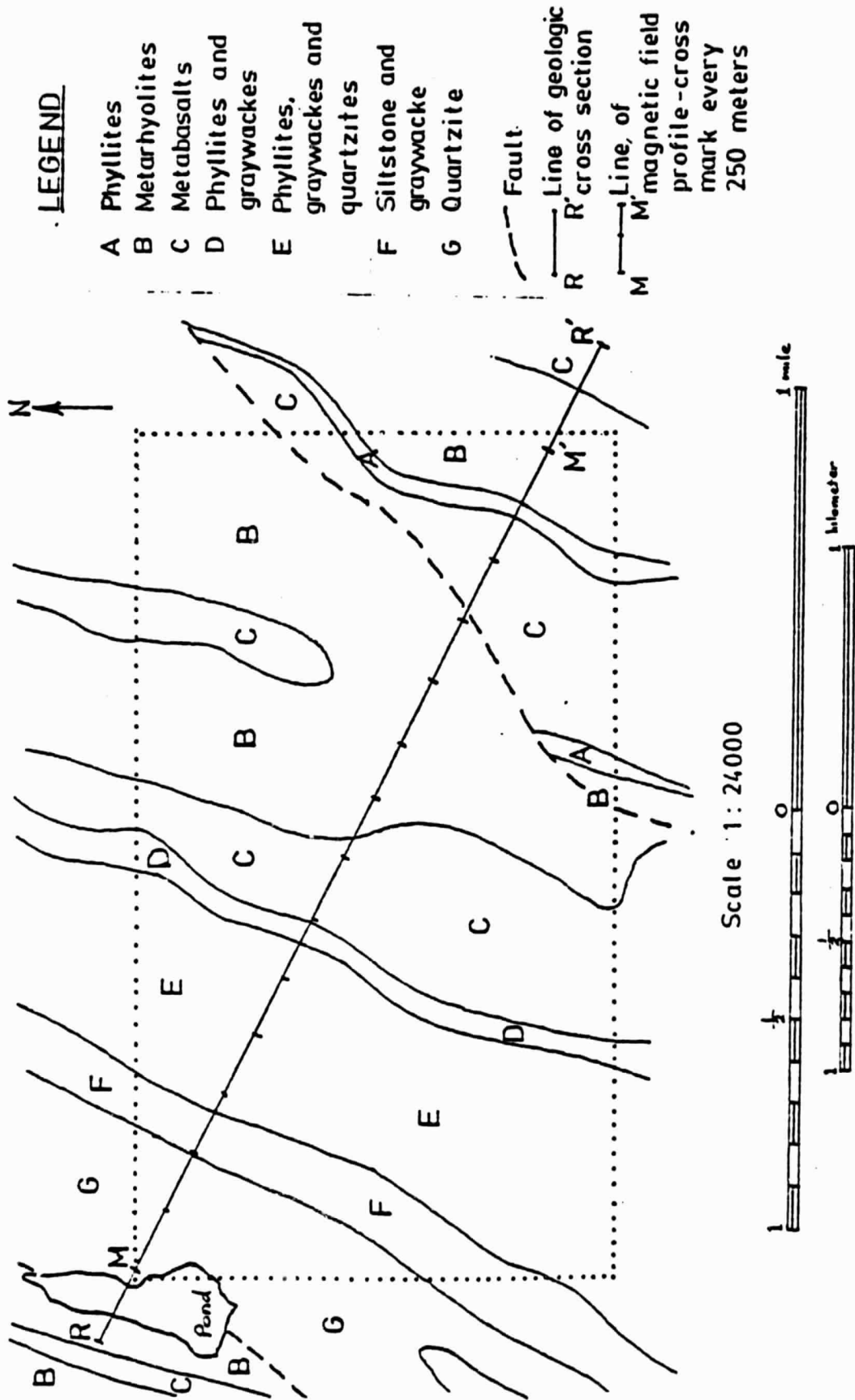


Figure 18. Detailed geology of magnetic field survey area (after Socolow, 1960).

ORIGINAL PAGE IS  
OF POOR QUALITY

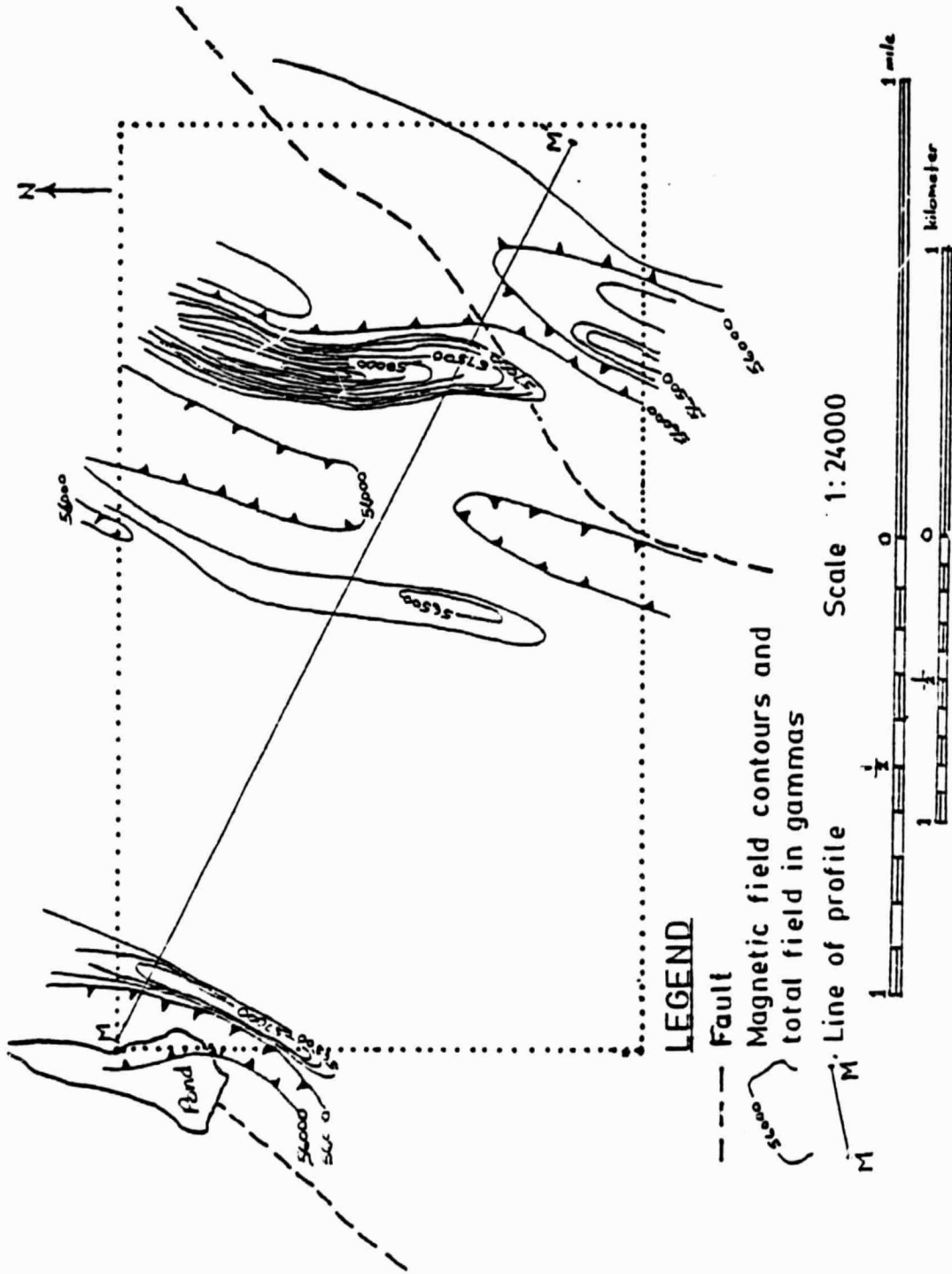


Figure 19. Contoured total magnetic field.

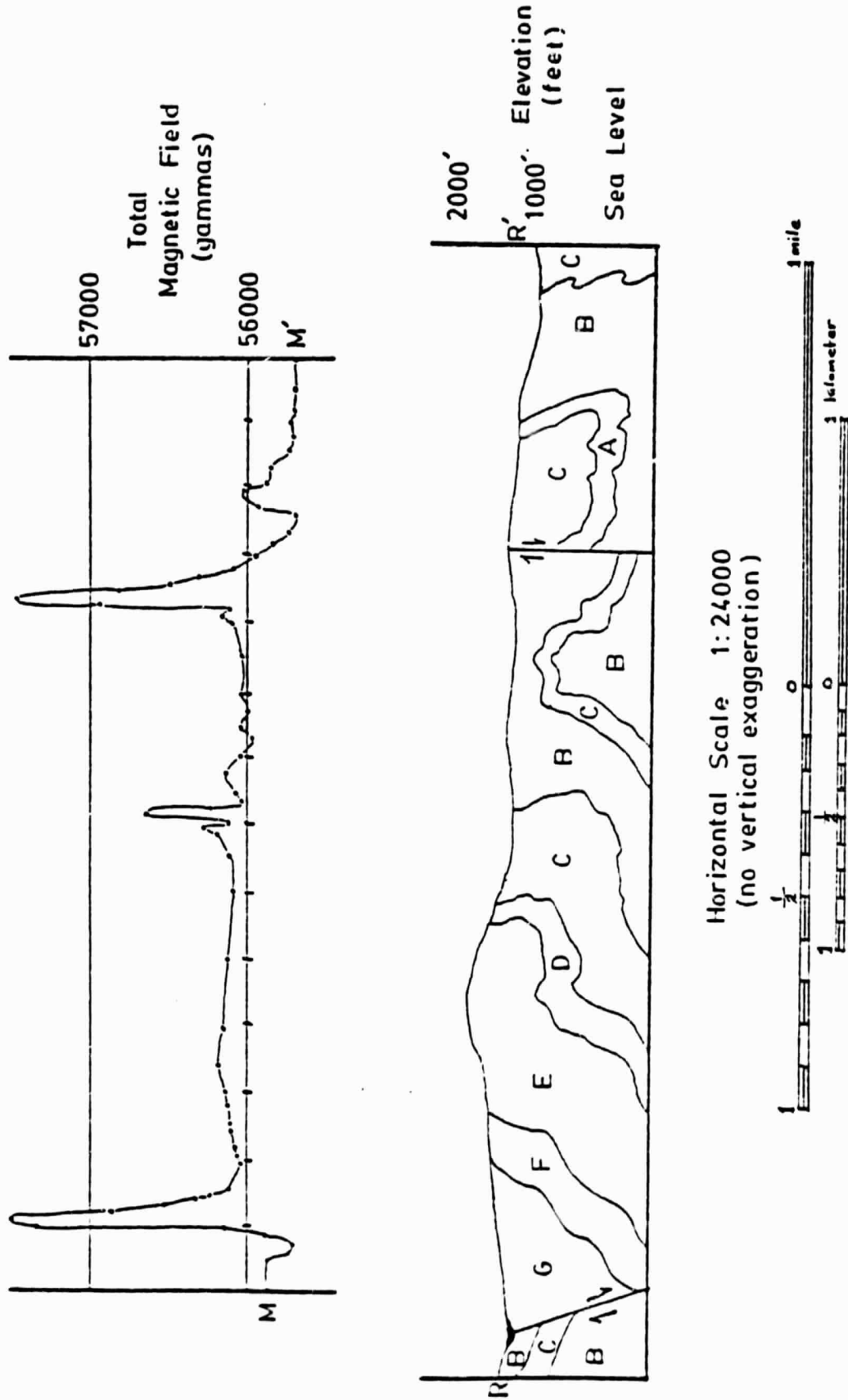


Figure 20. Magnetic field profile and geologic cross section (after Socolow, 1960)

The magnetic field highs correlated in general with the occurrence of the metabasalts either at the surface (Figures 18 and 19), or at depth (Figure 20), except in the northwest corner of the survey area. There, a substantial magnetic high occurred in an area mapped as quartzites. This suggests that either metabasalts outcrop there, or occur at fairly shallow depths, similar to the cross-section (Figure 20) in the eastern part of the survey area. The metarhyolites had, in general, a low magnetic expression especially in the eastern part of the survey area where the profile shows they were not underlain at depth by metabasalts. The metasediments had an intermediate magnetic expression. Thus, the total magnetic field was with some exceptions, well correlated with the surface rock types.

#### Correlations between SAR, Landsat, and magnetic field data

The texture measures of principal component axes 2 and 3 were tested for their correlation with the SAR tone and texture. If a strong correlation existed, the approximate equivalent of the SAR data could be derived from the Landsat data in future studies. Table 8 shows the correlation between the SAR data and the 17 texture measures from principal component axes 2 and 3. No strong correlation exists (a perfect correlation would be 1.00); thus the SAR data is indeed a unique data set.

Table 8. Correlation of SAR tone with principal component axes 2 and 3 texture measures.

Texture measure	SAR and principal component axis 2 correlations	SAR and principal component axis 3 correlations
1	0.19	-0.06
2	-0.07	-0.07
3	0.04	0.01
4	-0.02	-0.01
5	-0.07	-0.07
6	-0.05	-0.07
7	-0.17	-0.03
8	-0.06	-0.08
9	-0.07	-0.07
10	-0.07	-0.07
11	-0.07	-0.07
12	0.04	0.02
13	0.04	-0.09
14	-0.05	-0.10
15	-0.02	0.0
16	-0.07	-0.02
17	-0.05	-0.02

A further test was made of the correlation between the texture measures (from principal component axes 1,2, and 3), which contributed the most to the separability of the rock type classes. Ten measures of texture were used, and the results are shown in Table 9. In the magnetic field survey area, the magnetic field data was included, and 18 channels were used in the correlation (Table 10). The highest correlation between texture measures was found to be 0.94 between texture measures 5 and 9 of principal component axis 2. There was essentially no correlation between texture measures from different principal component axes. The magnetic field data showed about a 0.20 correlation with texture measures 5,9 and 14 from principal component axis 2 and texture measure 12 from principal component axis 1. These correlations are relatively low and would not be discernable by a visual inspection of the data.

Classification using texture measures from principal component axes 1 and 2

The training areas chosen were used to test the contribution of each data set to the separability of rock type classes. The evaluation of these results was done by comparing, between each step, the confusion matrices and the canonical scattergrams output by the stepwise discriminant



Table 9. Correlation matrix for texture measures from principal component axes 1,2, and 3.

Texture measure:	2P3	2P4	2P5	2P9	2P14	3P14	1P6	1P7	1P8	1P14
Texture measure										
2P3	1.00									
2P4	-0.09	1.00								
2P5	-0.03	-0.20	1.00							
2P9	-0.04	-0.07	0.94	1.00						
2P14	-0.02	-0.00	0.22	0.24	1.00					
3P14	0.01	-0.01	-0.02	-0.03	-0.04	1.00				
1P6	-0.01	-0.02	0.01	0.01	-0.02	-0.06	1.00			
1P7	-0.04	0.01	0.00	-0.00	0.01	0.01	-0.24	1.00		
1P8	-0.01	-0.01	-0.01	-0.01	-0.03	-0.04	0.51	-0.02	1.00	
1P14	-0.02	0.01	0.07	0.08	0.03	0.11	-0.26	0.16	-0.22	1.00

Table 10. Correlation of magnetic field with principal component axes 1, 2, and 3 texture measures.

Texture measure	Magnetic field correlation
2P3	-0.04
2P4	0.03
2P5	-0.18
2P8	-0.15
2P9	-0.18
2P11	-0.16
2P14	-0.20
2P16	0.08
3P14	0.09
1P6	0.07
1P7	-0.02
1P8	0.06
1P9	0.07
1P11	0.02
1P12	-0.21
1P14	-0.11
1P15	0.09

Variables 1P1 - 1P17 = Principal component axis 1 texture measures

Variables 2P1 - 2P17 = Principal component axis 2 texture measures

Variable 3P14 = Principal component axis 3 texture measure

analysis program BMD07M. Table 11 shows the confusion matrices in the magnetic field survey area. These matrices show the accuracy of classification of the mean values from each training area. The training area (after canonical transformation) is classified into that group to which it is most similar. Because the rock type of each training area is known, the accuracy of the classification can be tested and expressed as a confusion percentage. The effect on the confusion percentage by the addition or deletion of a data set or variable, can thus be used as a measure of the contribution of that variable to the separability of rock type classes.

The contribution of the four Landsat variables to the separability of rock type classes was tested first. The matrices show a 14% confusion among the training areas in this first case; 7% confusion with the addition of the SAR channel and 0% confusion after the addition of the magnetic field channel. The canonical scattergrams (Figures 21, 22, and 23) show some improvement with each step, but not as clearly as the confusion matrices, due principally to the limitation of only being able to display two canonical axes. However, the canonical axes displayed are always those that contain most of the variance. The most significant variables chosen by the program BMD07M for each case, are shown in Table 12. Landsat channel 4 was the most significant, and the magnetic field data was more significant than the SAR data.

Table 11. Confusion matrices for magnetic field survey area.  
Rock type classes are defined in Tables 5 and 6.

(a) Landsat channels only (1,2,3,4).

True rock class	Number of cases classified into rock class						
	A	B	C	D	E	F	G
A	1	0	0	0	0	0	0
B	0	3	0	0	0	0	0
C	0	1	1	1	0	0	0
D	0	0	0	2	0	0	0
E	0	0	0	0	2	0	0
F	0	0	0	0	0	2	0
G	0	0	0	0	0	0	1

(b) Landsat + SAR channels (1,2,3,4,5)

True rock class	Number of cases classified into rock class						
	A	B	C	D	E	F	G
A	1	0	0	0	0	0	0
B	0	3	0	0	0	0	0
C	0	1	2	0	0	0	0
D	0	0	0	2	0	0	0
E	0	0	0	0	2	0	0
F	0	0	0	0	0	2	0
G	0	0	0	0	0	0	1

(c) Landsat + SAR + magnetic field channels (1,2,3,4,5,6)

True rock class	Number of cases classified into rock class						
	A	B	C	D	E	F	G
A	1	0	0	0	0	0	0
B	0	3	0	0	0	0	0
C	0	0	3	0	0	0	0
D	0	0	0	2	0	0	0
E	0	0	0	0	2	0	0
F	0	0	0	0	0	2	0
G	0	0	0	0	0	0	1

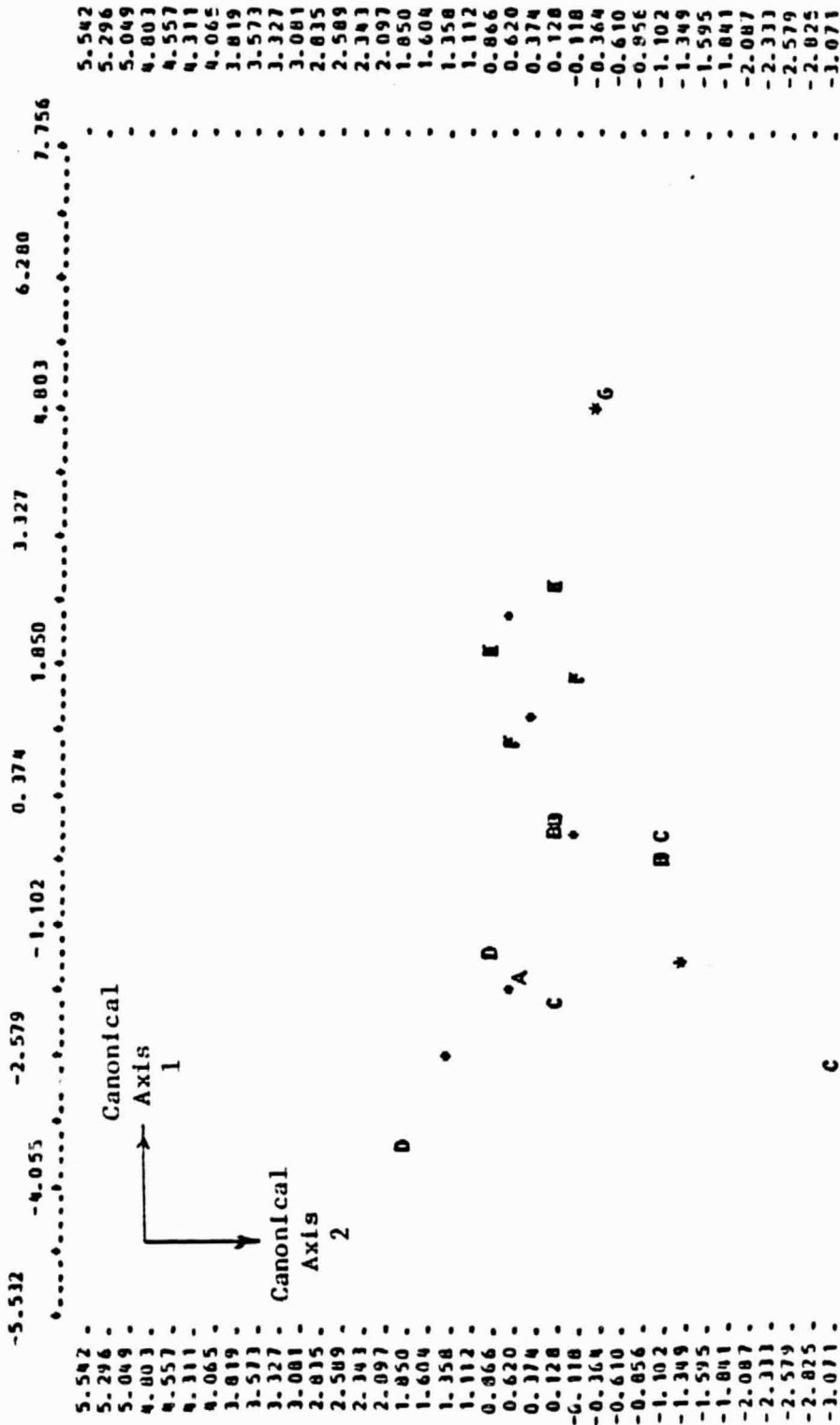


Figure 21. Landsat spectral signatures scattergram  
for magnetic field survey area.

ORIGINAL PAGE IS  
OF POOR QUALITY

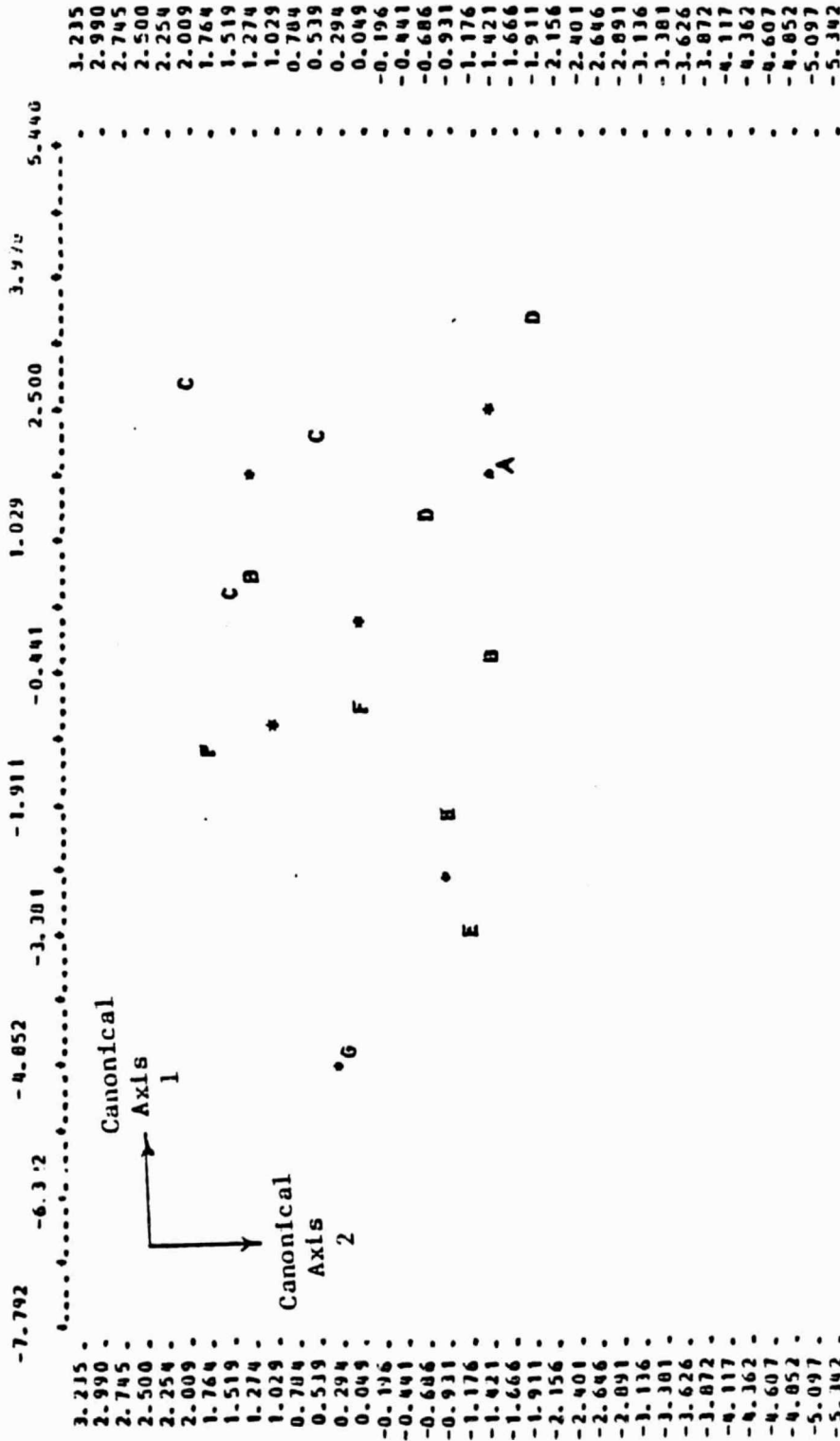


Figure 22. Landsat + SAR spectral signatures scattergram  
for magnetic field survey area.

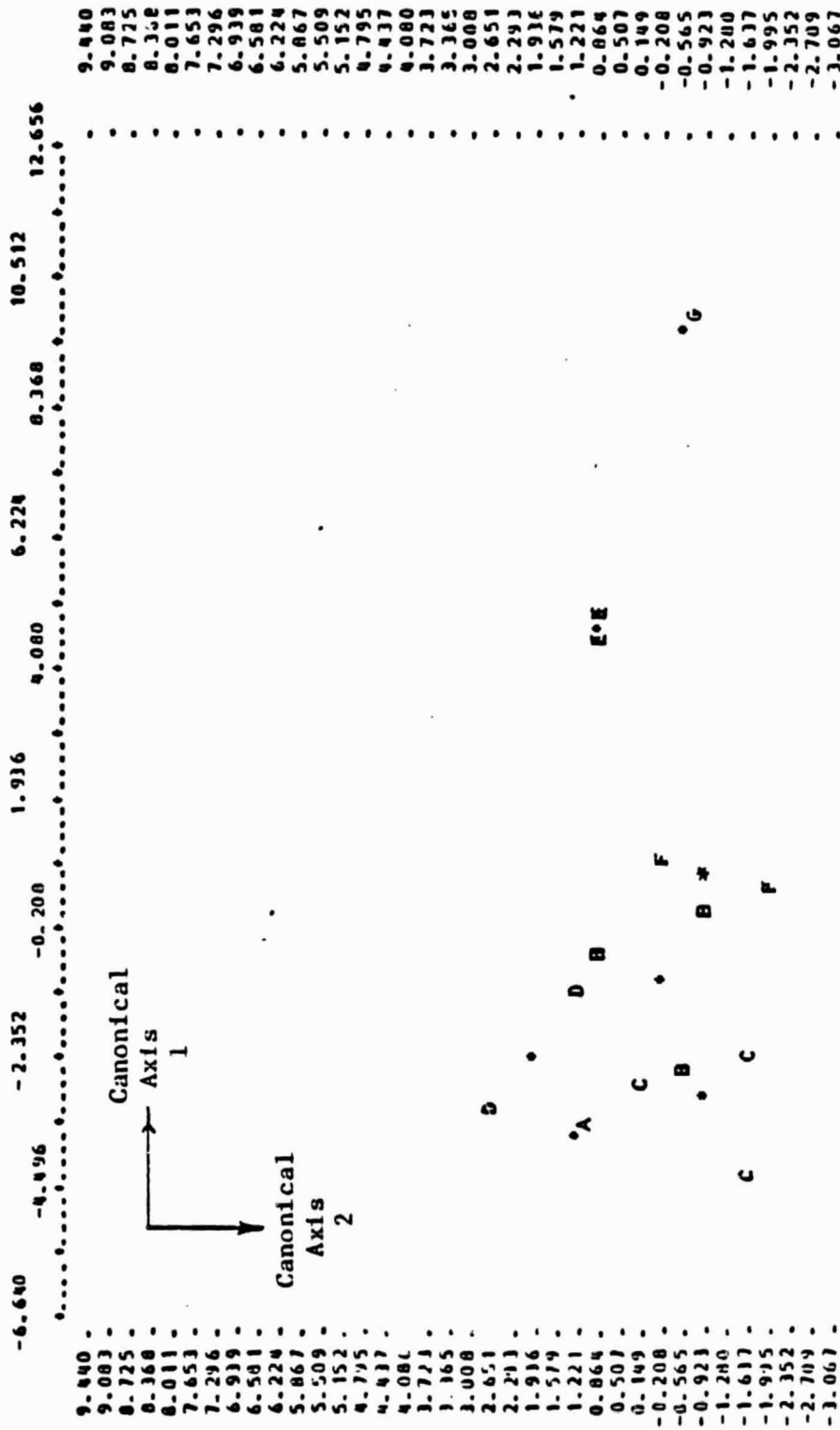


Figure 23. Landsat + SAR + magnetic field spectral signatures scattergram for magnetic field survey area.

ORIGINAL PAGE IS  
OF POOR QUALITY

Table 12. Significance of data sets or variables in the magnetic field survey area.

	Landsat only	Landsat + SAR	Landsat + SAR + magnetic field
Most significant variable	4	4	4
	3	3	6
↓	2	2	3
	1	5	5
↓		1	2
Least significant variable			1

Variable 1 = Landsat channel 1 (0.5-0.6  $\mu\text{m}$ )

Variable 2 = Landsat channel 2 (0.6-0.7  $\mu\text{m}$ )

Variable 3 = Landsat channel 3 (0.7-0.8  $\mu\text{m}$ )

Variable 4 = Landsat channel 4 (0.8-1.1  $\mu\text{m}$ )

Variable 5 = SAR channel

Variable 6 = Total magnetic field



In the larger area, more training sets were used and no magnetic field data were available. First, the contribution of the Landsat data to the separability of the classes was tested, then the SAR data was added, and finally the effect of 17 SAR texture measures was tested. Table 13 shows the confusion matrices. The matrices show a 29% confusion in the first case; a much more reasonable number than the 14% confusion that resulted in the magnetic survey case with only the Landsat channels, because more training areas were used. The SAR data reduced the confusion to 7%, and the 17 SAR texture measures reduced the confusion to 0%. The same improvement is evident to a lesser degree in the canonical scattergrams (Figures 24, 25, and 26). Figure 26 shows good clustering of the rock type classes. Rock type E which is the Weverton formation composed of phyllite, graywacke and quartzite, and rock type F which is the Harpers formation composed of siltstone and graywacke, are well separated from each other and from the other rock type clusters. Rock type B which is metarhyolite is well clustered and is fairly well separated from the other clusters. Rock type C (metabasalt) and G (quartzite) are confused.

The next step was to apply a principal components transformation to the data and then apply the texture algorithm to the first three principal axes. The principal component transformation did not change the distributions of the data. The data still showed a near-normal, or skewed

Table 13. Confusion matrices for entire study area.  
 Rock type classes are defined in Tables 5 and 6.

(a) Landsat channels only (1,2,3,4)

True rock class	Number of cases classified into rock class				
	B	C	E	F	G
B	4	2	0	1	2
C	1	7	0	0	0
E	0	0	4	2	0
F	0	0	0	2	0
G	0	0	1	0	5

(b) Landsat + SAR channels (1,2,3,4,5)

True rock class	Number of cases classified into rock class				
	B	C	E	F	G
B	7	1	1	0	1
C	0	7	0	0	0
E	1	0	5	0	0
F	0	0	0	2	0
G	0	0	1	0	5

(c) Landsat + SAR texture (1,2,3,4, + 17 textures)

True rock class	Number of cases classified into rock class				
	B	C	E	F	G
B	9	0	0	0	0
C	0	8	0	0	0
E	0	0	6	0	0
F	0	0	0	2	0
G	0	0	0	0	6

ORIGINAL WORK IS  
OF POOR QUALITY

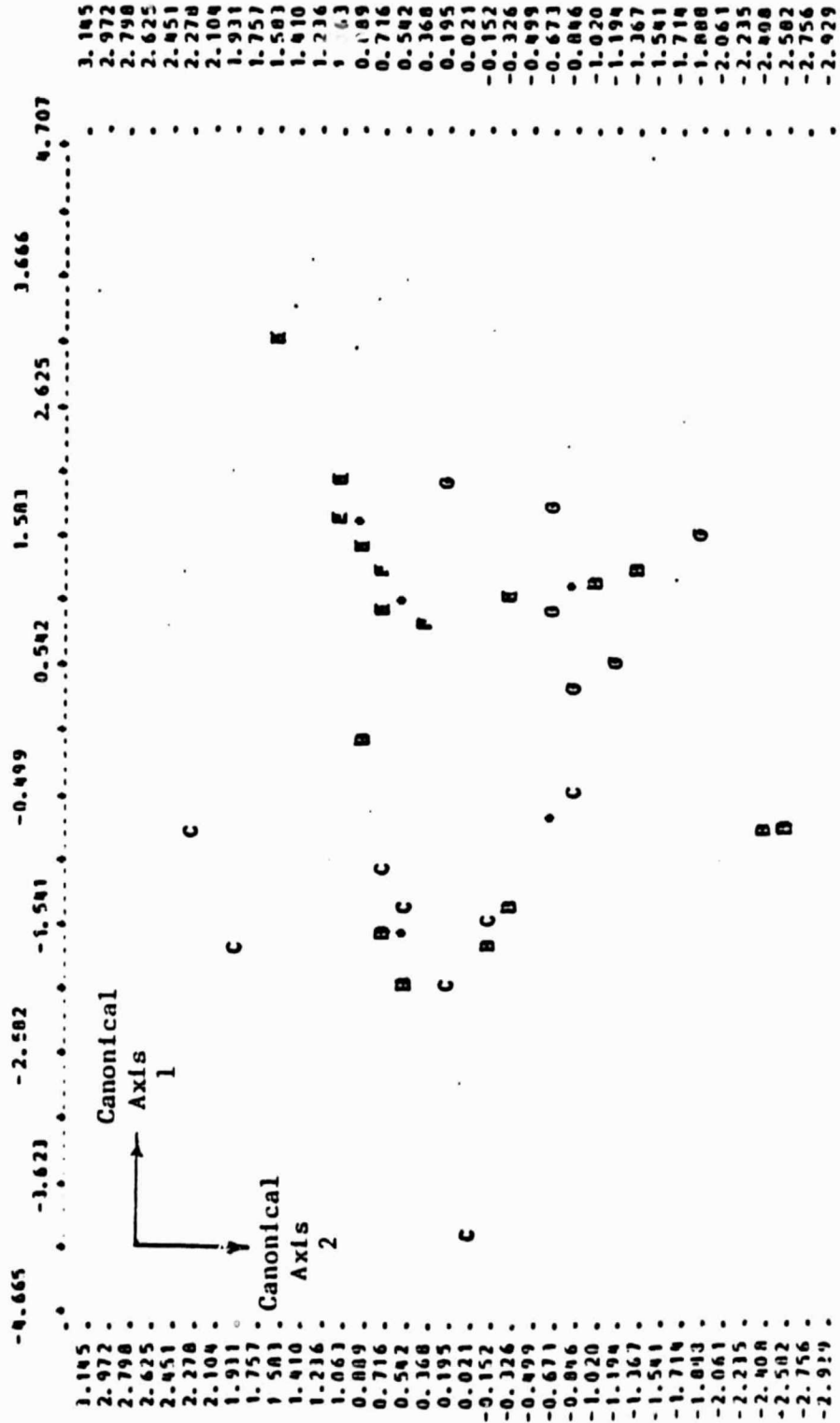


Figure 24. Landsat spectral signatures scattergram  
for entire study area.

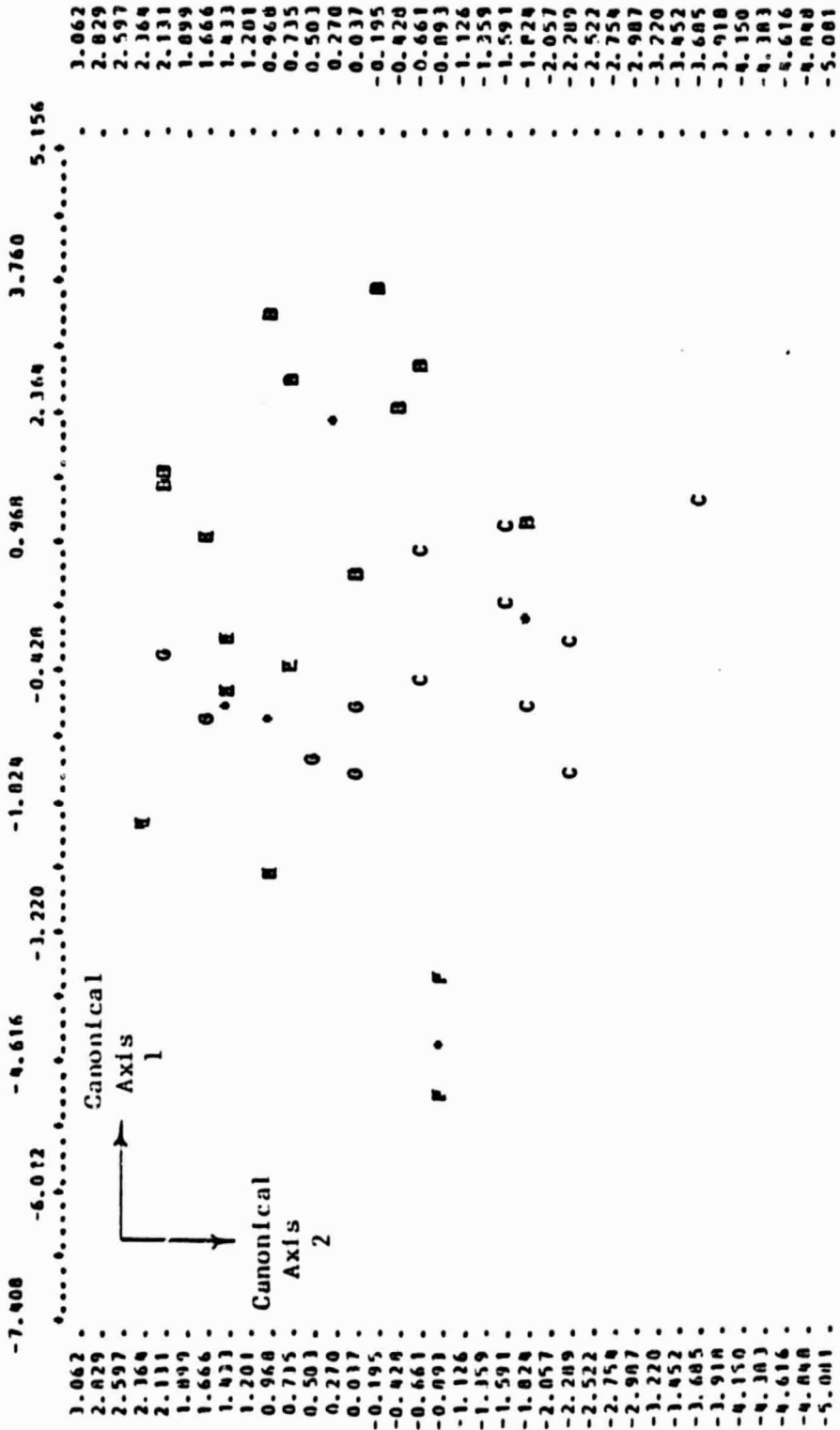


Figure 25. Landsat + SAR spectral signatures scattergram  
for entire study area.

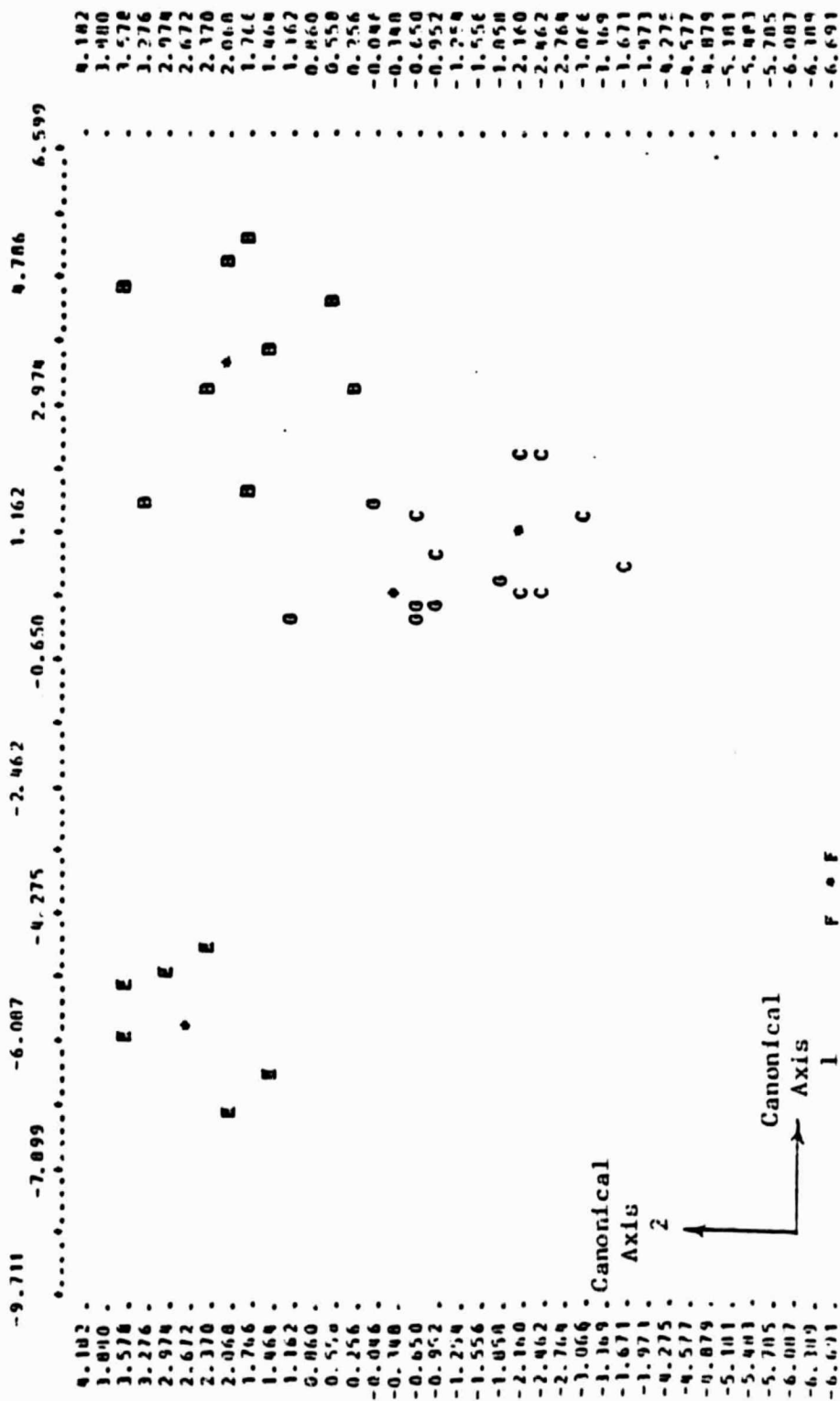


Figure 26. Landsat + SAR textural signatures scattergram for entire study area.

distribution. The texture measures 7 and 8 (Table 7), obtained from principal component 1, had skewed distributions, and texture measure 14 had a spike at zero containing 7% of the data. Because texture measure 14 represents the mean area above a tonal value of 150, the spike represents the large number of pixel neighborhoods in which all the pixels are below 150. Texture measures 3 and 5 obtained from principal component axis 2 showed normal and skewed distributions, respectively. Table 14 shows the resulting confusion matrices. With the transformed principal component axes alone, a confusion of 10% resulted among the training areas, which is an improvement over the 10% confusion obtained before the principal components transformation. Texture measures obtained from principal component axis 1, showed an increase in confusion to 12%, and the texture measures obtained from principal components axis 2, showed a further increase in confusion to 16%. By combining the texture measures from both principal axes, 34 channels resulted, and the confusion among training areas was reduced to zero. The scattergrams do not show the change in confusion, except for the 34 variable case, in which a significant improvement was noted (Figures 27,28,29,30). The texture measures derived from principal component axis 1 show a good separation of rock type classes E,F and B, while C and G are confused. The same results were obtained when the SAR texture measures were combined with the Landsat channels (Figure 26).

Table 14. Confusion matrices for the principal components of entire study area. Rock type classes are defined in Tables 5 and 6.

(a) Principal components channels only (5 channels)

True rock class	Number of cases classified into rock class				
	B	C	E	F	G
B	8	1	0	0	0
C	0	8	0	0	0
E	1	0	5	0	0
F	0	0	0	2	0
G	0	0	1	0	5

(b) Texture measures from principal component axis 1 (17 channels).

True rock class	Number of cases classified into rock class				
	B	C	E	F	G
B	7	0	0	0	2
C	0	6	0	0	2
E	0	0	6	0	0
F	0	0	0	2	0
G	0	0	0	0	6

(c) Texture measures from principal component axis 2 (17 channels).

True rock class	Number of cases classified into rock class				
	B	C	E	F	G
B	8	0	0	0	1
C	1	6	1	0	0
E	0	0	5	0	1
F	0	0	0	2	0
G	0	0	1	0	5

(d) Texture measures from p.c. 1 and p.c. 2 (34 channels).

True rock class	Number of cases classified into rock class				
	B	C	E	F	G
B	9	0	0	0	0
C	0	8	0	0	0
E	0	0	6	0	0
F	0	0	0	2	0
G	0	0	0	0	6

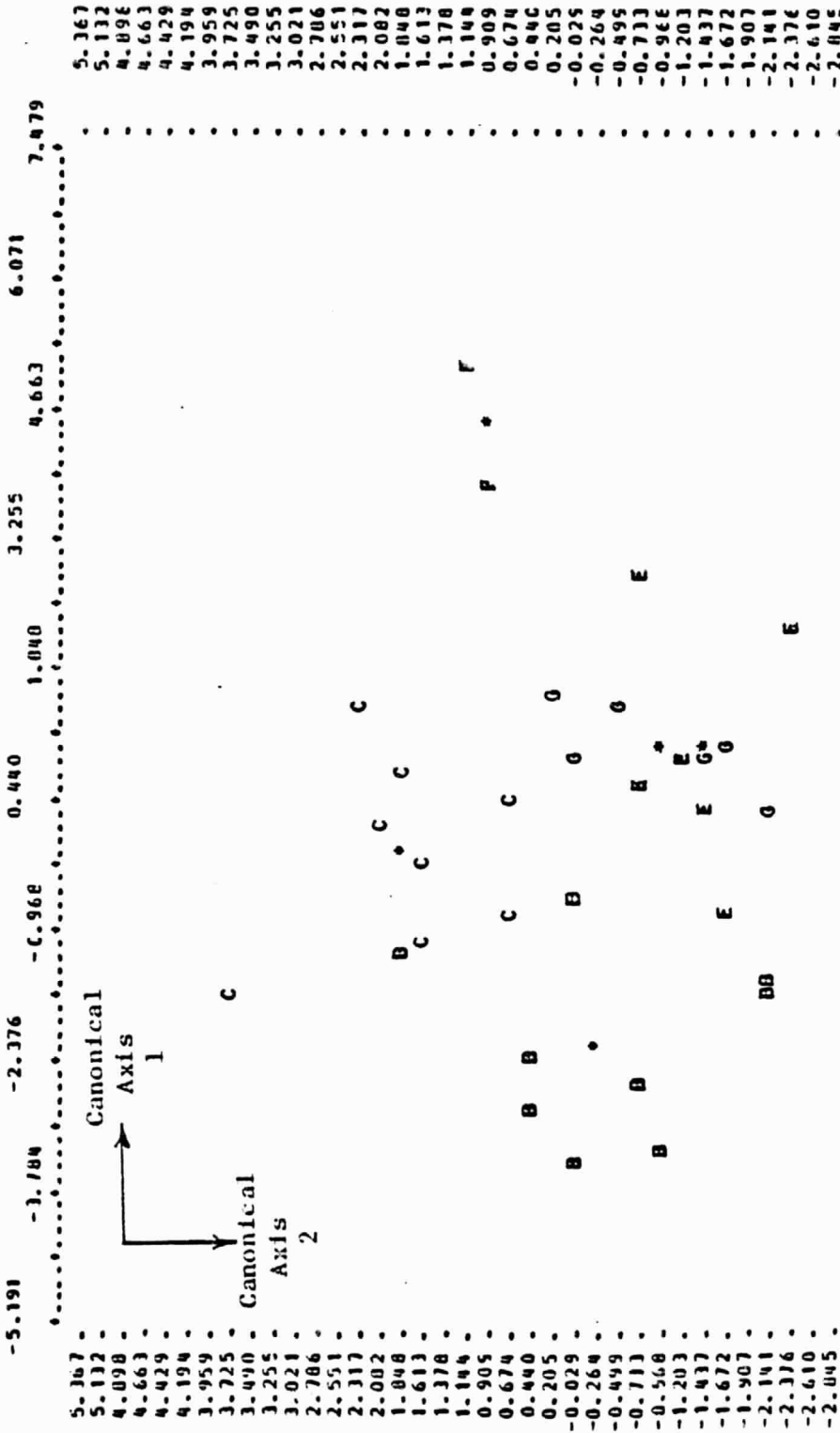


Figure 27. Principal components signatures scattergram  
for entire study area.



ORIGINAL PAGE IS  
OF POOR QUALITY

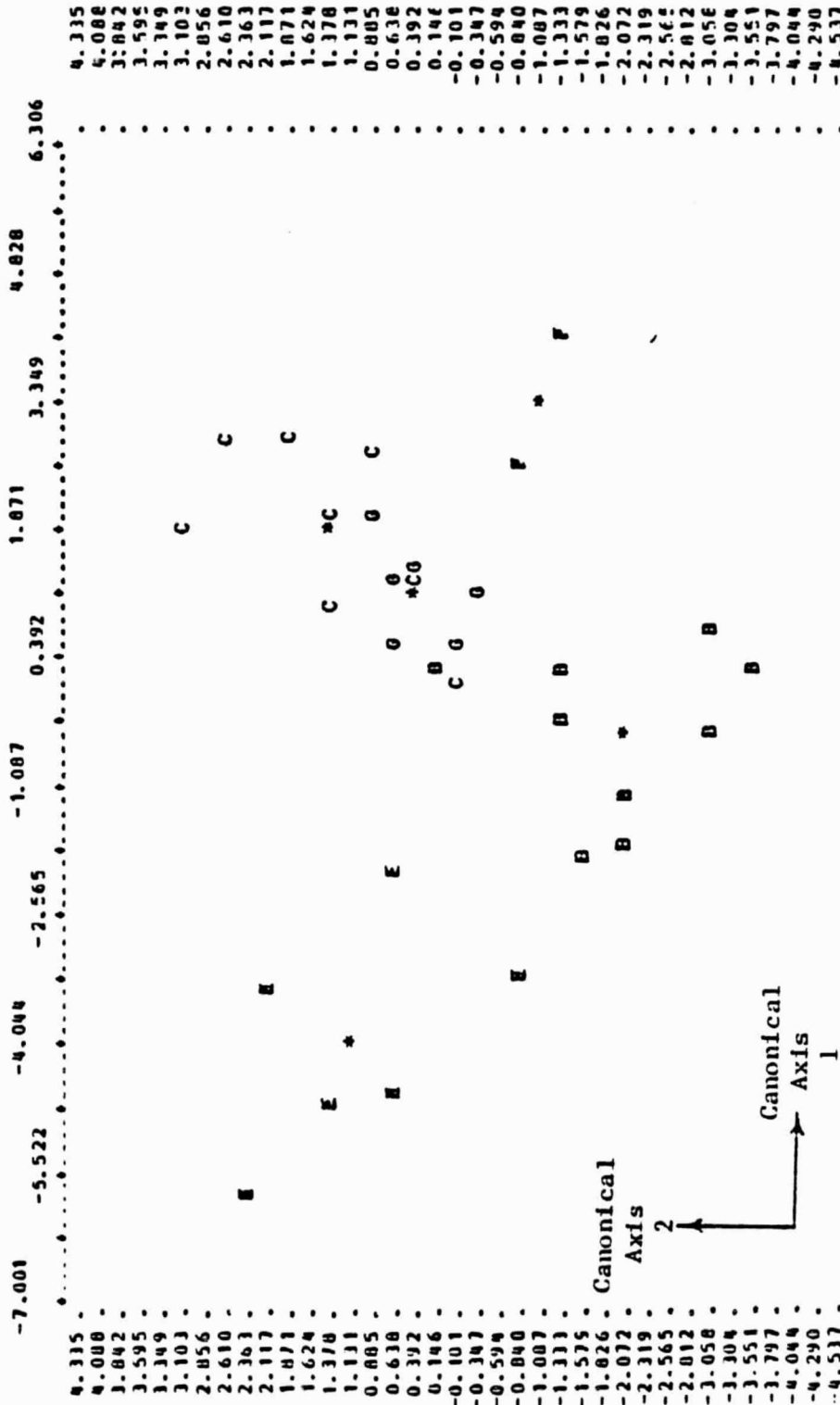


Figure 28. Principal component axis 1 textural signatures scattergram for entire study area.

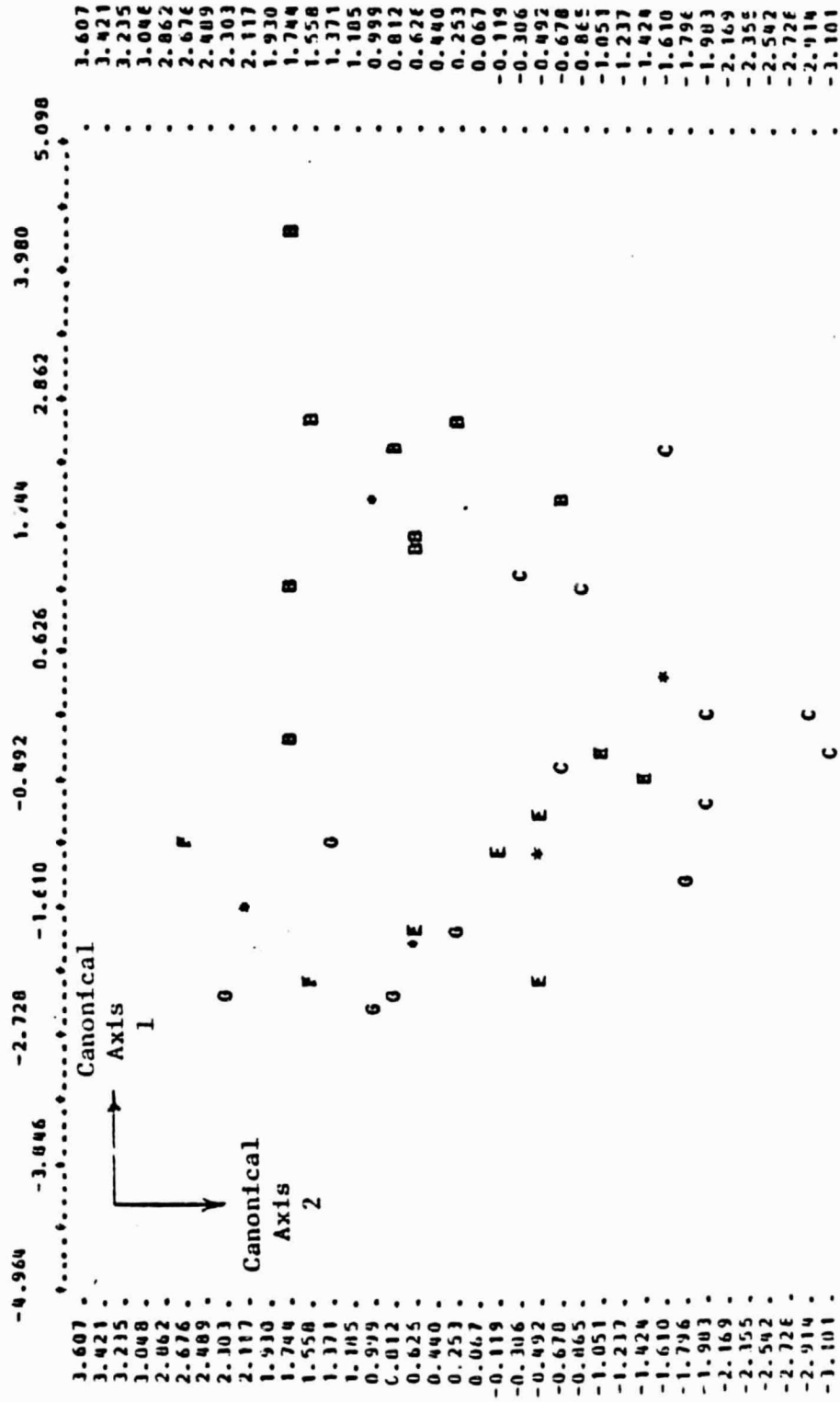


Figure 29. Principal component axis 2 textural signatures scattergram for entire study area.

ORIGINAL PAGE IS  
OF POOR QUALITY

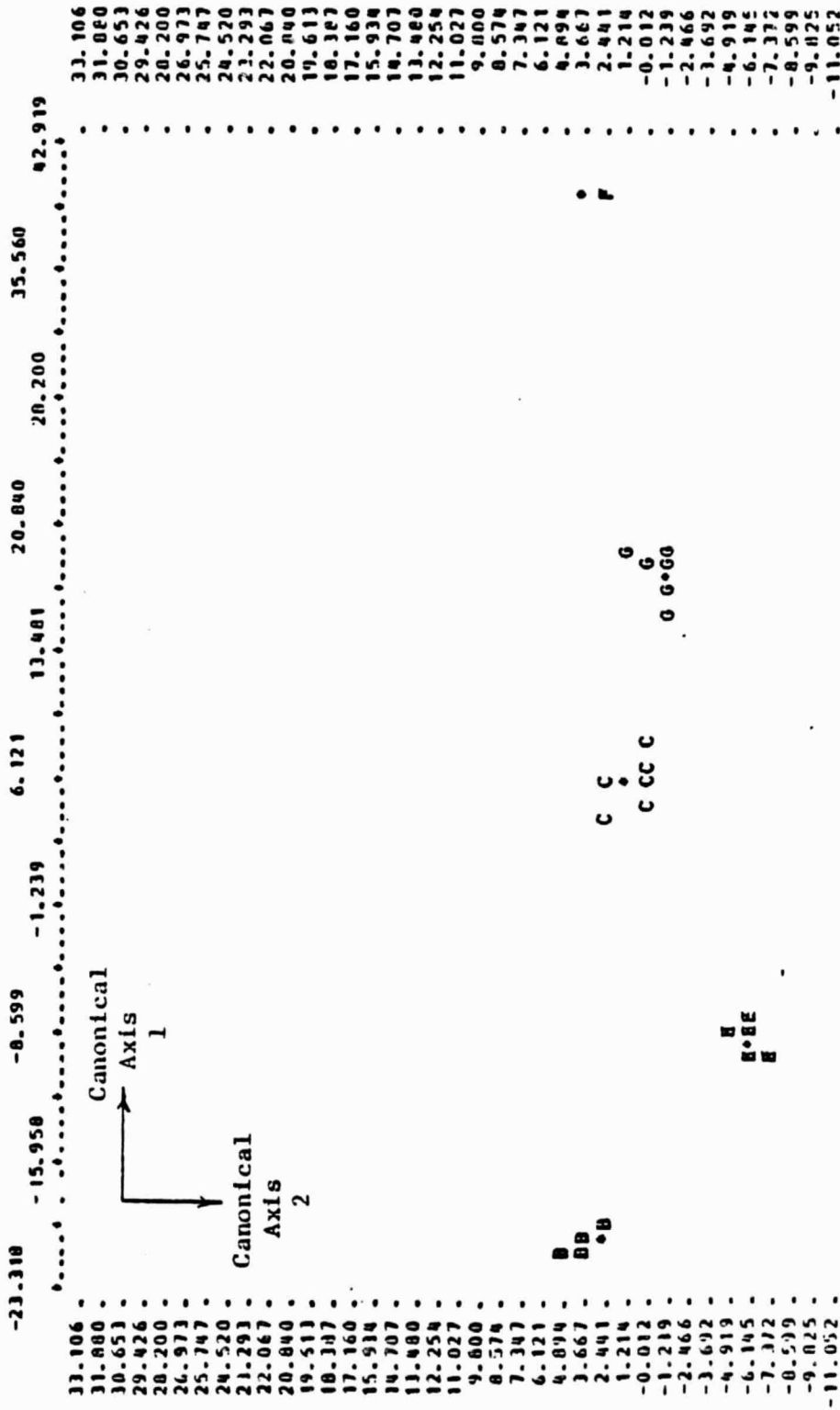


Figure 30. Principal component axes 1 and 2 textural signatures scattergram for entire study area.

This illustrates the fact that principal component axis 1 is equivalent to the SAR channel. For principal component axis 2 the texture measures show a much poorer separability, with only B (metarhyolite) being completely separable. It must be remembered though that only the first two canonical axes are represented. The significance of the variables to the separability of the rock type classes was determined by the program BMD07M and is shown in Table 15.

For the combined texture measures of principal component axes 1 and 2, the best five texture measures were chosen, written to tape, and used in the final classification. Before classification, a test of separability was made using only these five texture measures over the entire study area, and including the magnetic field data in the magnetic field survey area. The results are shown in the confusion matrices of Table 16 and the scattergrams of Figures 31, 32, and 33. Using the 5 texture channels as variables, a 6% confusion between training areas occurred in the entire study area and a 14% confusion occurred using only those training areas in the magnetic field survey area. When the magnetic field survey data was added as a sixth channel, the confusion was reduced to 0%. The scattergrams show less separability than the confusion matrices indicate, and they do not show the decrease in confusion with the addition of the magnetic field data. Table 17 shows the significance of each variable to the separability of rock type classes.

Table 15. Significance of the variables in the entire study area.

	Landsat only	Landsat + SAR	Landsat + SAR texture	P.C. tone	P.C. 1 texture	P.C. 2 texture	P.C. 1&2 textures
Most significant variable  ↓  Least significant variable	4	5	T4	P1	1P8	2P5	1P8
	3	4	T12	P4	1P14	2P13	2P5
	2	3	T11	P5	1P6	2P7	1P14
	1	2	T2	P2	1P7	2P4	2P3
		1	T17	P3	1P4	2P3	1P7
			T15		1P5	2P10	2P14
			T14				2P16
			T16				2P8
			T1				2P11
			T5				2P9
							2P4
							1P6

Variables 1 - 4 = Landsat channels

Variable 5 = SAR channel

Variables T1 - T17 = SAR texture measures

Variables P1 - P5 = Principal component axes

Variables 1P1 - 1P17 = Principal component axis 1  
texture measures

Variables 2P1 - 2P17 = Principal component axis 2  
texture measures

Table 16. Confusion matrices for texture measures.  
 Rock type classes are defined in Tables 5 and 6.

(a) Texture channels for entire study area (5 channels).

True rock class	Number of cases classified into rock class				
	B	C	E	F	G
B	8	0	1	0	0
C	1	7	0	0	0
E	0	0	6	0	0
F	0	0	0	2	0
G	0	0	0	0	6

(b) Texture channels for magnetic field survey area  
 (5 channels).

True rock class	Number of cases classified into rock class						
	A	B	C	D	E	F	G
A	1	0	0	0	0	0	0
B	0	1	2	0	0	0	0
C	0	0	3	0	0	0	0
D	0	0	0	2	0	0	0
E	0	0	0	0	2	0	0
F	0	0	0	0	0	2	0
G	0	0	0	0	0	0	1

(c) Texture and magnetic field data channels in magnetic  
 field survey area (6 channels).

True rock class	Number of cases classified into rock class						
	A	B	C	D	E	F	G
A	1	0	0	0	0	0	0
B	0	3	0	0	0	0	0
C	0	0	3	0	0	0	0
D	0	0	0	2	0	0	0
E	0	0	0	0	2	0	0
F	0	0	0	0	0	2	0
G	0	0	0	0	0	0	1

ORIGINAL PAGE IS  
OF POOR QUALITY

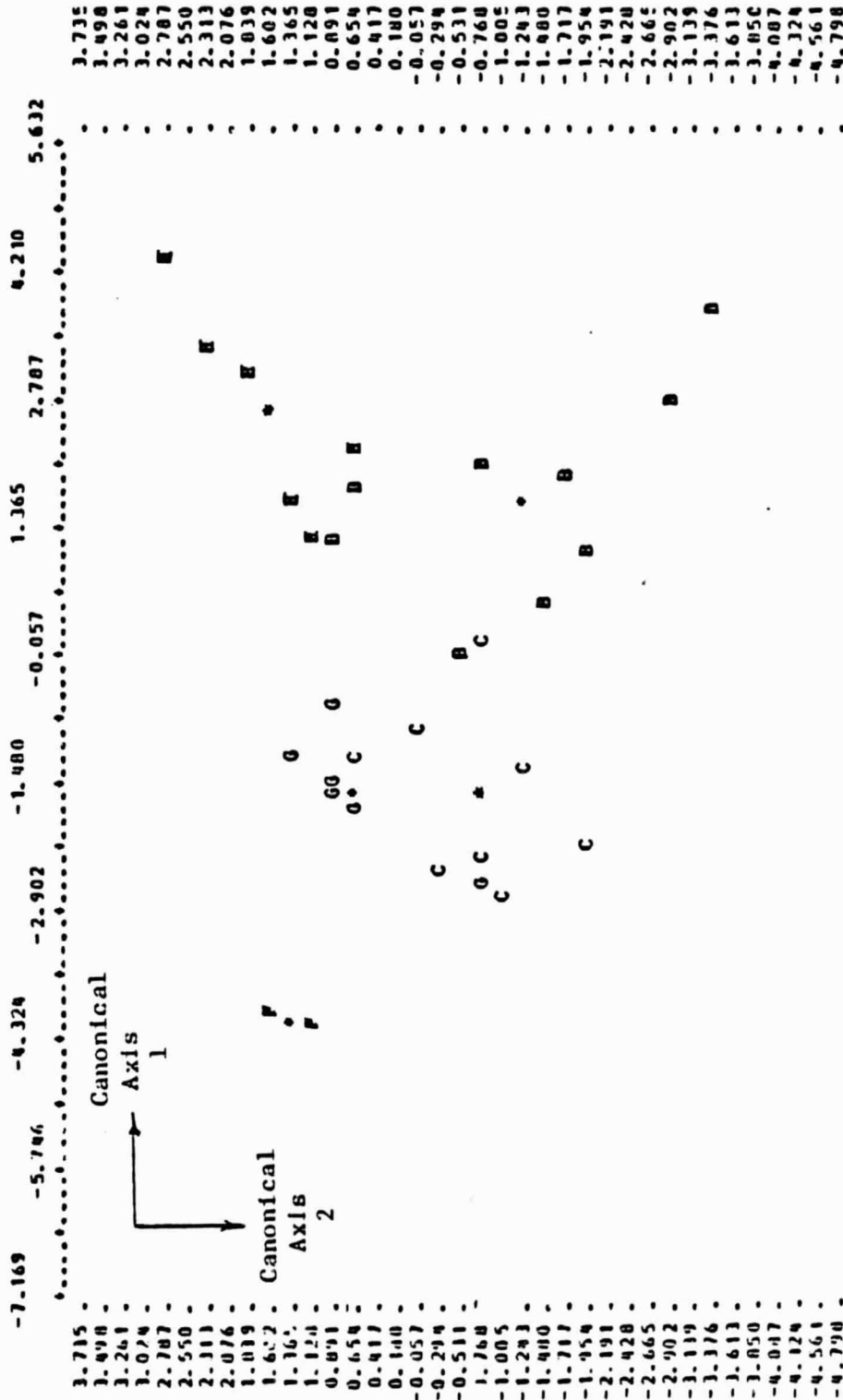


Figure 31. Principal component axes 1 and 2 scattergram for the 5 most important texture measures in the entire study area.

ORIGINAL PAGE IS  
OF POOR QUALITY



Figure 32. Principal component axes 1 and 2 scattergrams for the 5 most important texture measures in the magnetic field survey area.



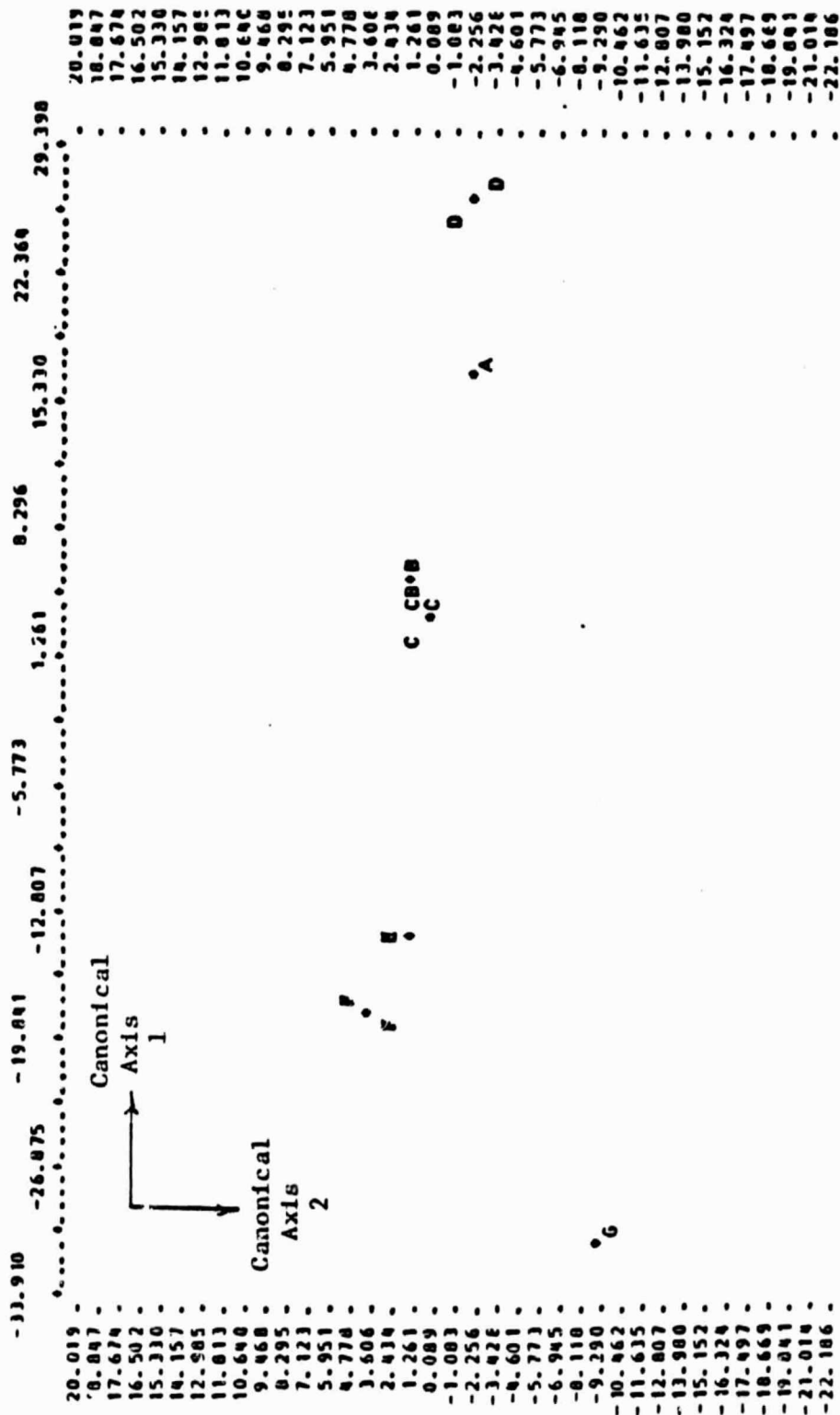


Figure 33. Principal component axes 1 and 2 scattergram for  
5 most important texture measures plus  
magnetic field data.

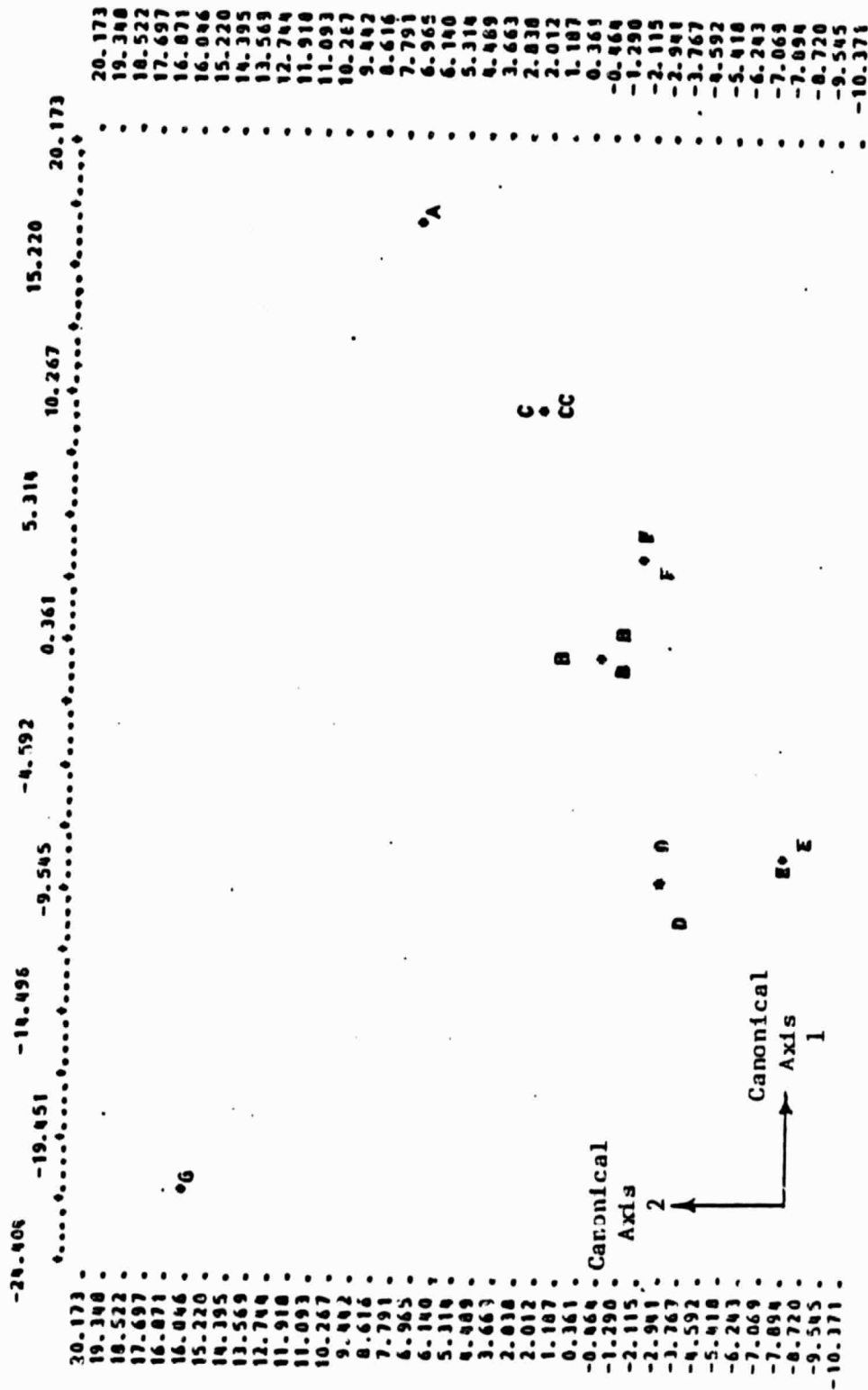


Figure 34. Principal component axes 1,2, and 3 scattergram for 7 most important texture measures plus magnetic field data.

ORIGINAL PAGE IS  
OF POOR QUALITY

Table 17. Significance of the texture variables.

	Entire survey area	Magnetic field survey area (texture only)	Magnetic field survey area (texture plus magnetic field) (6 channels)	Magnetic field survey area (texture plus magnetic field) (8 channels)
Most significant variable	1P8	2P5	2P5	2P5
	2P5	1P8	6	3P14
↓	1P14	1P14	1P8	1P8
Least significant variable	2P3	1P7	2P3	1P6
	1P7	2P3	1P14	2P4
			1P7	2P9
				6

Variable 6 = Total magnetic field

Variables 1P1 - 1P17 = Principal component axis 1  
texture measures

Variables 2P1 - 2P17 = Principal component axis 2  
texture measures

Variable 3P14 = Principal component axis 3  
texture measure

The significance of each variable changes with the addition of the magnetic field data.

Despite the encouraging results obtained in discriminating between training areas, the final classified data set compared rather poorly with the the ground-mapped geology in the training area and in the testing area (Figure 35). The reasons for this are considered in Chapter V. In the training area, the Harpers formation (F) was outlined relatively well (figure 36), but the other rock type classes were commonly confused. No definite area of concentration of the G symbols, representing the Harpers formation - Montalto member, could be found. Limiting distances (the distance from the mean beyond which a pixel is no longer considered a member of that class) were chosen on the basis of both the confidence intervals, and the distances of separation between classes. Varying the limiting distances did not change the classification accuracy. A final limiting distance was decided on by a visual analysis of the classification map. The degree of confusion was decreased as much as possible while limiting the amount of blank space or unclassified area. In the testing area, no areas of concentration of certain symbols could be outlined and thus the classification accuracy could not be tested. However, certain regional structural and lithologic features are recognizable on Figure 35. The fault structure separating the Blue Ridge from the Triassic Basin is discernable as a

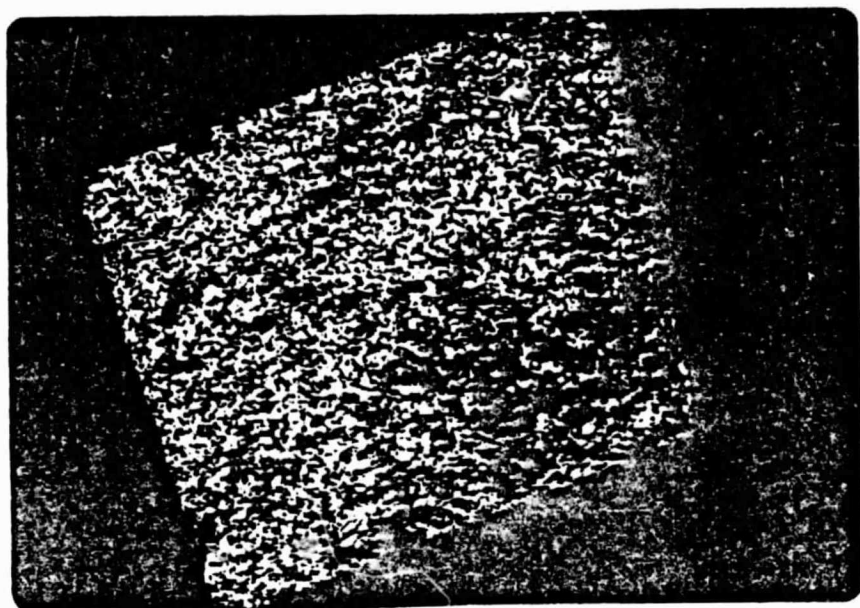


Figure 35. Classification map of the entire study area.

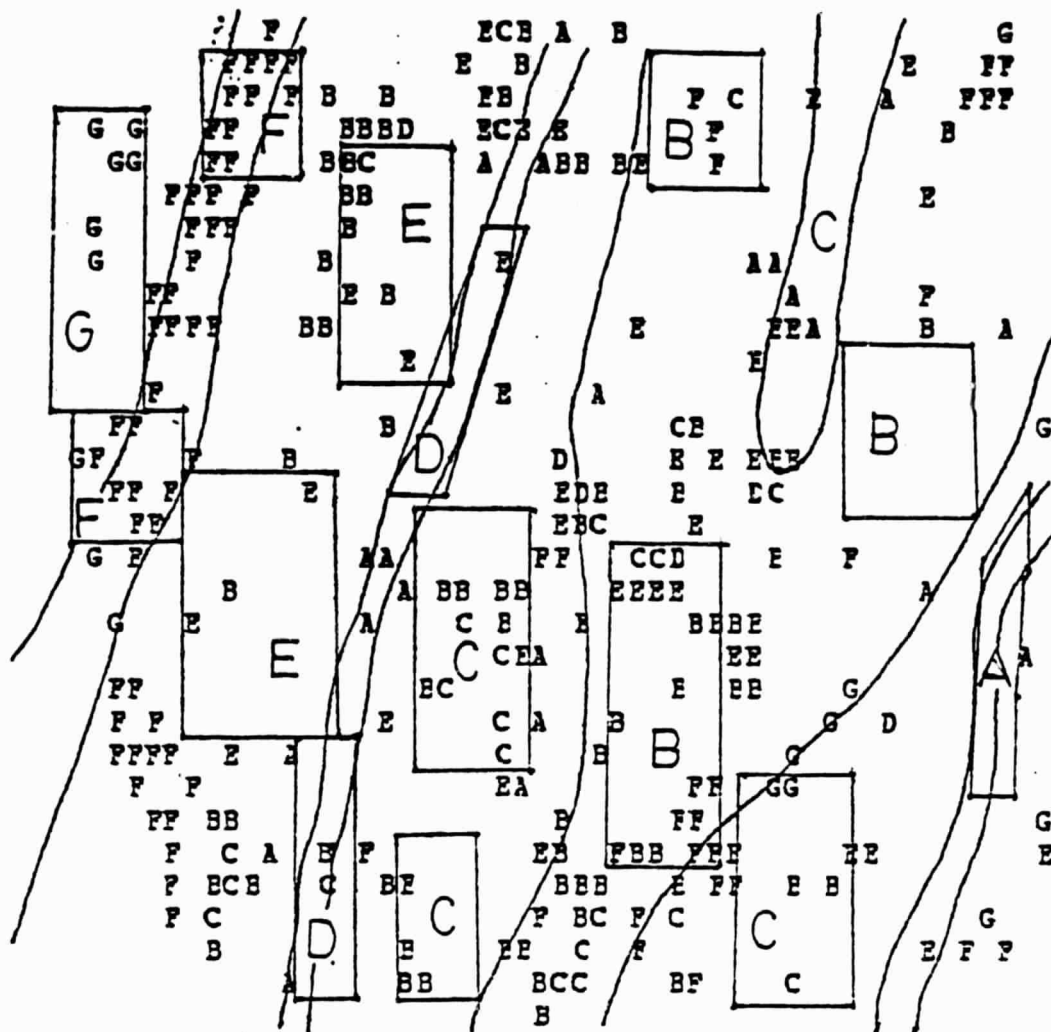


Figure 36. Classification map showing only the areas  
classified as Harpers formation.

transition zone separating darker areas to the east from the lighter colored Blue Ridge. The Everett lineament and Carbaugh-Marsh Creek fault zone is also discernable cutting horizontally across the figure.

Classification using texture measures from principal component axes 1 and 2 plus magnetic field data

As a test of the contribution of the magnetic field data to the classification accuracy, a digital map was produced for the magnetic field survey area (Figure 37). The original training areas chosen are shown, and the ground-mapped geological boundaries are outlined. The results show that even in those areas used for training, the pixels (as represented by the small letters and blank spaces), were often not classified as the rock type characteristic of that training area. Rock types F (siltstone and graywacke) and G (quartzite) were the only ones classified with any reasonable accuracy. The appearance of the F symbols to the southeast of the boundary between F and E indicates that there may have been an error in the ground-mapped geology. Other concentrations of the symbols F and G throughout the map indicate that either those rock types appear there and the ground-mapped geology is wrong, or that the vegetation/soil/structure expression at that location is much the same as in the training area.



**LEGEND**

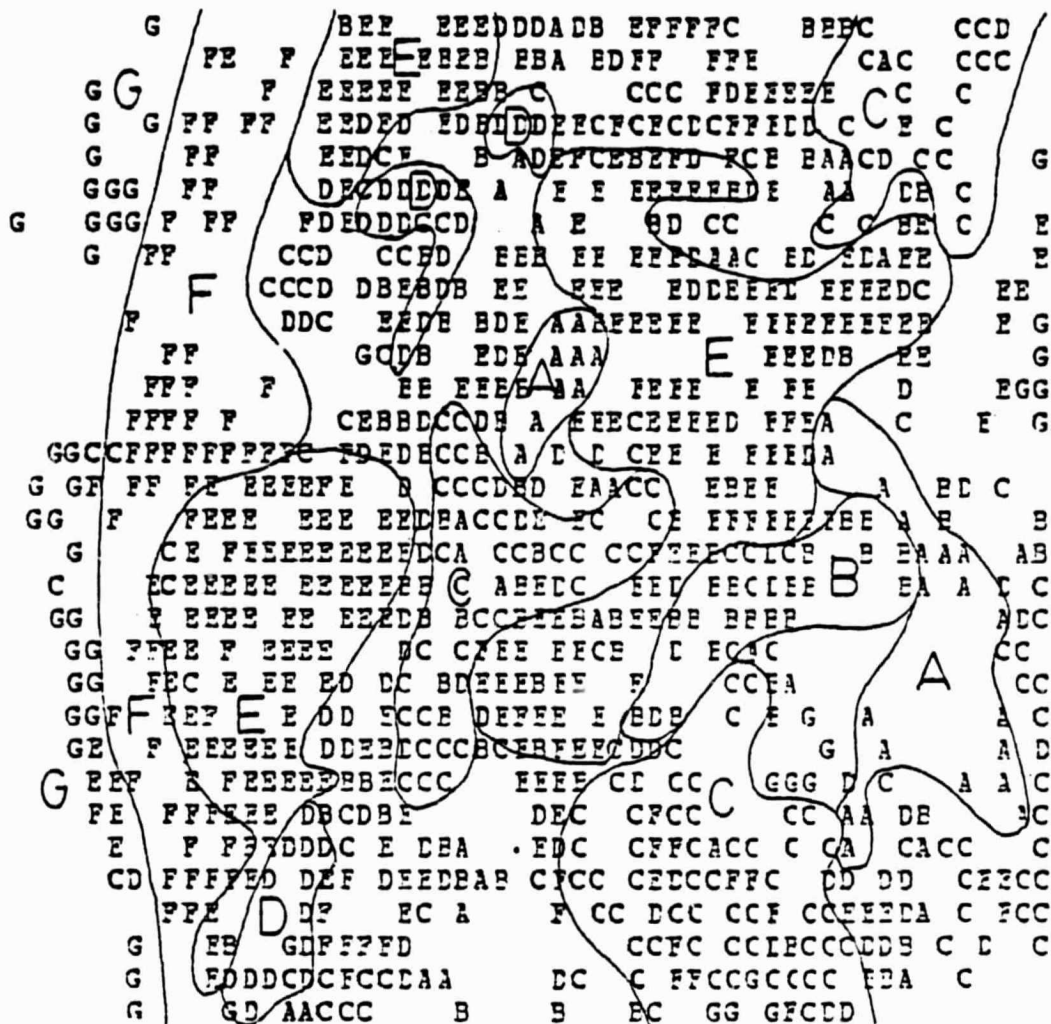
- A Phyllites
- B Metarhyolites
- C Metabasalts
- D Phyllites and graywackes
- E Phyllites, graywackes and quartzites
- F Siltstone and graywacke
- G Quartzite
- D Training area with symbol for rock type
- Ground mapped geologic boundaries
- Horizontal scale 1:24000
- Vertical scale 1:14400

Figure 37. Digital classification map (6 variables) for magnetic field survey area (not corrected for line printer).

Classification using texture measures from principal component axes 1,2, and 3 plus magnetic field data

The classification map using 7 measures of texture from principal component axes 1,2, and 3, plus magnetic field data (8 channels in all), shows an improvement in classification (Figure 38). The data was reduced to 5 canonical axes. The importance of each initial variable to the final classification is shown in Table 17. The magnetic field data was much less important in this case than in the 6 variable case. The scattergram (Figure 34) shows some improvement over that for the 6 variable case (Figure 33). The classification digital map (Figure 38) for this case shows enough grouping of rock type symbols, that areas of concentration can be outlined. A comparison of the outlined area to the geological boundaries of Figure 37, show that a lot of error and confusion still exists, especially between rock type E (phyllite, graywacke and quartzite) and rock type B (metarhyolite). However, there is a definite improvement over the 6 variable case. When the discrimination of rock types in the training area is this marginal, there is no point in testing the accuracy of the algorithm in another area.





LEGEND

- A Phyllites
- B Metarhyolites
- C Metabasalts
- D Phyllites and graywackes
- E Phyllites, graywackes and quartzites
- F Siltstone and graywacke
- G Quartzites

Boundary drawn around area of symbol concentration

Horizontal scale 1:24000 , Vertical scale 1:14400

Figure 38. Digital classification map (8 variables) for magnetic field survey area (not corrected for line printer).

## DISCUSSION AND CONCLUSIONS

Discussion

Seasat SAR records information about the earth's surface that is very different from that recorded by Landsat and by other sensors (Figure 1). The SAR representation of the surface is strongly effected by layover and foreshortening, which can be corrected for with an independent data source, such as the topography of the surface. Even with topographic data, the registration of the SAR data to the true surface location must be accomplished before appropriate corrections can be made. In this study, registration of the SAR data to the Landsat data was done without applying a topographic correction to the SAR data. A relative registration accuracy of 1 kilometer or better was obtained, which is rather poor and more work needs to be done to increase the registration accuracy. An absolute measure of accuracy was not possible. The effects of layover and foreshortening contributed significantly to the registration inaccuracies (see Appendix A). In the South Mountain area, the total elevation difference is 1100 feet, resulting in a geometric error, due to foreshortening, of 1 kilometer (Appendix A, Figure 47). Because this elevation difference does not occur at one location, a registration

accuracy much better than 1 kilometer should be possible. The rubbersheet stretch of the SAR data (to fit the registration points), is the best average correction of layover and foreshortening that is possible.

The effect of the subsurface rock types on the magnetic field at the surface was found to be substantial. Filtering to remove the effect of deep sources was not attempted due to the similarity of deep strong sources and shallow wide sources. Thus, great care must be exercised in using magnetic field data to determine surface lithology. Once the surface lithology has been determined though, the magnetic field data may provide great insight into the structure of the subsurface.

A comparison of the information content of each of the data sources was made by testing the correlations among them. It was found that the SAR data is unique and cannot be derived from Landsat MSS data. The texture measures most significant in separating the rock type classes may be correlated when they are derived from the same principal component axis, but they are not correlated when derived from different axes. The magnetic field data is not strongly correlated with any of these texture measures. Each principal component and magnetic field represents a unique data set describing a different aspect of the surface and/or subsurface of the earth.

The addition of the SAR and magnetic field data sets to the four Landsat channels, greatly increased the separability of rock type classes in the training area. These two extra data sets provided unique information about the geology that was not available from the Landsat channels alone. The Seasat SAR appears to penetrate the vegetation canopy and interact with the surface material. However, the vegetation affects the SAR signal to some extent. The magnetic field data definitely contains subsurface information. But, even the addition of these two independent data sets could not completely solve the difficulty inherent in identifying lithologic units in vegetated terrain. The large variance within each class (especially of the SAR data) due to the masking effect of the vegetation, resulted in a within-category standard deviation that, in the final classification, was at least of the same order of magnitude as the separation between categories.

Principal component transformation and then generation of texture measures from the principal axes were used in an attempt to increase the classification accuracy. The 5 texture measures that accounted for essentially 100% of the variance in the data sets were written to tape and used in the final classification. The texture measures showed slightly more normal distributions as predicted by Hsu (1979), in all but one of the channels and thus were more

suites to the minimum distance classifier used. Even after all these attempts at increasing the separability of the classes, a very poor classification accuracy was obtained (Figures 35 and 37).

The stepwise discriminate analysis program BMD07M found a good separability between the mean values of the training areas, as indicated by the encouraging results obtained by comparing the confusion matrices and scattergrams during each step of the feature extraction. An explanation for this must include the fact that the BMD07M program used only the mean signatures within each training area. The large variance must occur not between the mean values of the training areas belonging to each class, but within each training area itself. The main source of this variance was probably the SAR data set due to its large "noise equivalent difference in the scattering coefficient ( $NE\Delta\sigma_0$ )" and coherent speckle (see Appendix A). Registration errors may also have contributed significantly. A solution would be to classify the average of a small area and assign a rock type symbol to the center pixel. This would tend to decrease both the noise within the SAR data and the effect of registration errors.

The SAR data at 25 meter resolution has a very large "noise equivalent  $\Delta\sigma_0$  ( $NE\Delta\sigma_0$ )", which is the least detectable difference in the scattering coefficient (see Appendix A). This limits the number of gray levels that can

be resolved to about seven. Closer spaced gray scale levels are lost in the noise. Spatial averaging increases the number of resolvable gray levels as well as decreasing the  $NE\Delta\sigma$ , such that a more accurate representation of the surface is obtained.

Another major source of variance in the SAR data could be coherent speckle (see Appendix A). Speckle introduces false texture into the SAR image so that only texture coarser than this systematic component is real surface texture. Spatial averaging will decrease, but not eliminate, the effects of speckle. Because the final classification used a data set created from texture measures, coherent speckle was undoubtedly a contributor to classification inaccuracies.

The variance in a data set in which training areas have been chosen can be separated into two types; between-group variance and within-group variance. The usefulness of a data set is determined by the ratio of the two variances -- the F-statistic. For the SAR data, conflicting results were obtained. In the magnetic field area, where small training areas were used, the average SAR variable within each area was less significant than the magnetic field variable and most of the Landsat variables (Table 12). In the larger survey area though, where larger training areas were used, the SAR variable was the most significant. This illustrates the effect of spatial averaging on the usefulness of the SAR data set. In this study, spatial averaging was not carried

out as one of the initial steps. Instead, every third data value was used and some information was thus lost. However, spatial averaging was achieved to some extent during the filtering process which removed the directional dependence of the SAR data.

The first attempt at classification of rock type classes did not utilize principal component axis 3 in any way. This component does nevertheless outline the linear features, as well as the structural and major geologic units of the area (Figures 15 and 17).

The striking differences between the Blue Ridge province and the Triassic Basin to the east (Figure 15) may be due to different landuse practices. Topographic maps show a transition from mainly forested land in the Blue Ridge to predominantly agricultural land in the Triassic Basin.

A comparison of the texture measures derived from axis 3 with the texture measures from the other two principal component axes, revealed that texture measure 14 would be significant in increasing the separability of the rock type classes. By using this texture measure as well as 3 texture measures from each of principal component axes 1 and 2, plus the magnetic field data, a much better classification was achieved (Figure 38).

## Conclusions

This study includes an extensive amount of software development to introduce SAR data processing capabilities at the Pennsylvania State University. Computer programs were written or modified to filter the SAR data and put it in the ORSER format (used in the processing of Landsat MSS data). Programs were also written to cast the magnetic field data into this format. The SAR data could then be merged with Landsat MSS and magnetic field data. The texture measures of Hsu (1979) were tested on the merged data set and were found to contribute significantly to a reasonably good (40%) rock type classification.

By merging all the data sets, the significance of each variable to the separation of rock type classes could be easily tested and compared. The most significant variables were used in the final classification. In future analyses, other geophysical data such as gravity, resistivity, electromagnetic, and seismic velocity observations, could be included in the data set in a manner analogous to that used for the magnetic field intensity data in this study. Remote mapping of lithology and structure in heavily vegetated terrain may be improved with better registration of the SAR data to Landsat MSS data, spatial averaging of the SAR data to reduce its noise content, and inclusion of as many independent data sets as are available. By including the



surface-mapped geology of an area as one of the data sets, an analysis of the relationship(s) between surface and subsurface geology and structure could be undertaken.

## SEASAT-A SAR CHARACTERISTICS

Seasat SAR compared to Landsat MSS and aerial photographs

The Seasat SAR is an active imaging system. It provides its own source of illumination, unlike a passive system such as Landsat. Its specifications are tabulated in Table 18. The Seasat-A Satellite specifications are tabulated in Table 19. The main difference between the SAR and Landsat MSS or aerial photographs is that it is a range measuring device while they are angle measuring devices. The position of an object in a photograph is determined by its angular direction from the nadir. Where an object is imaged by the SAR is determined by its ground range distance. The advantages of SAR are that it penetrates most weather conditions and provides its own source of illumination at any specified angle. The radar return is a function of incidence angle, polarization, frequency (all characteristics of the signal), dielectric properties and roughness of the surface. The incidence angle used in SLAR and SAR causes terrain characteristics to be emphasized although some detail is lost in the shadows. This is also true for low sun-angle aerial photographs. Variations in the ground slope give rise to continuous changes in the effective angle of incidence, which determines the amount of

Table 18. Seasat-A Synthetic Aperture Radar (SAR) specifications.

Purpose:	Obtain images of sea surface and sea ice Detect and measure ocean wavelength and direction. Detect slicks, current patterns, ice bergs, ice leads, ice coverage, ice type.
Actual coverage:	Swaths starting or ending at sea, with extensive land coverage.
Frequency:	1340 Mhz. (L-band)
Wavelength:	23 cm.
Polarization:	HH (Horizontal transmit and receive).
Antenna:	14 m x 2 m
Antenna beam:	1° x 6°, pointed 20° off vertical
Coverage:	100 km swath, 250-350 km off nadir
Resolution:	25 m at 4 looks
Pixel spacing:	18 m in range, 16 m in azimuth
Dynamic range:	-25 dB to +5 dB.
Transmit pulse width:	31 usec
PRF:	approx. 1000 Hz.
Power:	250 watts
Weight:	80 Kg
Operation:	Line-of-sight only
Aircraft heritage:	JPL X-L band radar, numerous military radars
Experiment team leader:	Dr. John Apel - NOAA

Table 19. Seasat-A Satellite specifications.

Launch date:	June 26, 1978.
Altitude:	790.17 km. $\pm$ 50 m.
Coverage:	72° North to 72° South
Period:	100.75 minutes
Orbits per day:	14.3
Orbit repeat (exact):	152 days
Inclination:	108° nominal, 104° - 108° range
Lifetime:	3 months

backscatter and thus the tone of the image. Unlike the shadows on aerial photographs which contain a certain amount of information within the shadow area, radar shadows are total, because there is no illumination and consequently no reradiation from the shadow zone. Another big difference is the fact that the length of the shadow of an object varies depending on the depression angle (angle above the horizontal) of the radar beam at that point. In low relief areas, the oblique illumination and resultant shadowing by imaging radar can generally provide enhancement of topographically expressed geological features; however, in mountainous terrain, radar shadowing can deter geological interpretation. For most operational side-looking radar systems, the interpretive data loss increases as terrain slopes exceed  $35^{\circ}$  and the local relief surpasses 1000 meters (Matthews, 1975). The local relief is a measure of the height difference encountered locally between the summits and valley floors. It is a useful parameter because it provides an index to the topographic irregularity of an area. There is an obvious link between the local relief and the terrain texture (large-scale texture) of an area, and it may be hypothesized that because of the geometric relationship between topography and radar shadow, there should be an empirical relationship between the radar shadow pattern and the terrain macro-roughness (Parry, 1973). There have been some attempts to arrive at this empirical

relationship (Parry, 1973; Lewis and Waite, 1972), with limited success.

The word RADAR is an acronym derived from Radio Detection And Ranging. Electromagnetic energy is transmitted, and the part of it scattered back to the receiver from the target, is detected. With imaging radar, the ground can be considered as an array of scatterers. Frequencies in the range of 250 to 40,000 mhz. are used (Figure 39), with a letter code of frequency-wavelength bands; K,X,L etc. that have been arbitrarily selected by the military. Longer wavelengths have greater penetration but require better sensors to achieve the same resolution. The nature of the reflected wave is influenced by the dielectric constant of the surface and by whether it is smooth or rough. Smooth surfaces are those with reflecting facets (surface height deviation from a mean plane) less than  $\lambda/10$ . They are characterized by specularlike reflection at incident angles between  $10^\circ$  and  $30^\circ$ . Rough surfaces are those with reflecting facets between  $\lambda/2$  and  $2\lambda$  and are called diffuse reflectors (Figure 40). Some surfaces are neither diffuse nor specular. This results when the surface roughness is near the wavelength of the illuminating energy or when parts of the surface are smooth while other parts are rough.

Incident radar waves are either horizontally or vertically polarized, a definition which is based on the orientation of the electric field vector. The reflecting surface can have

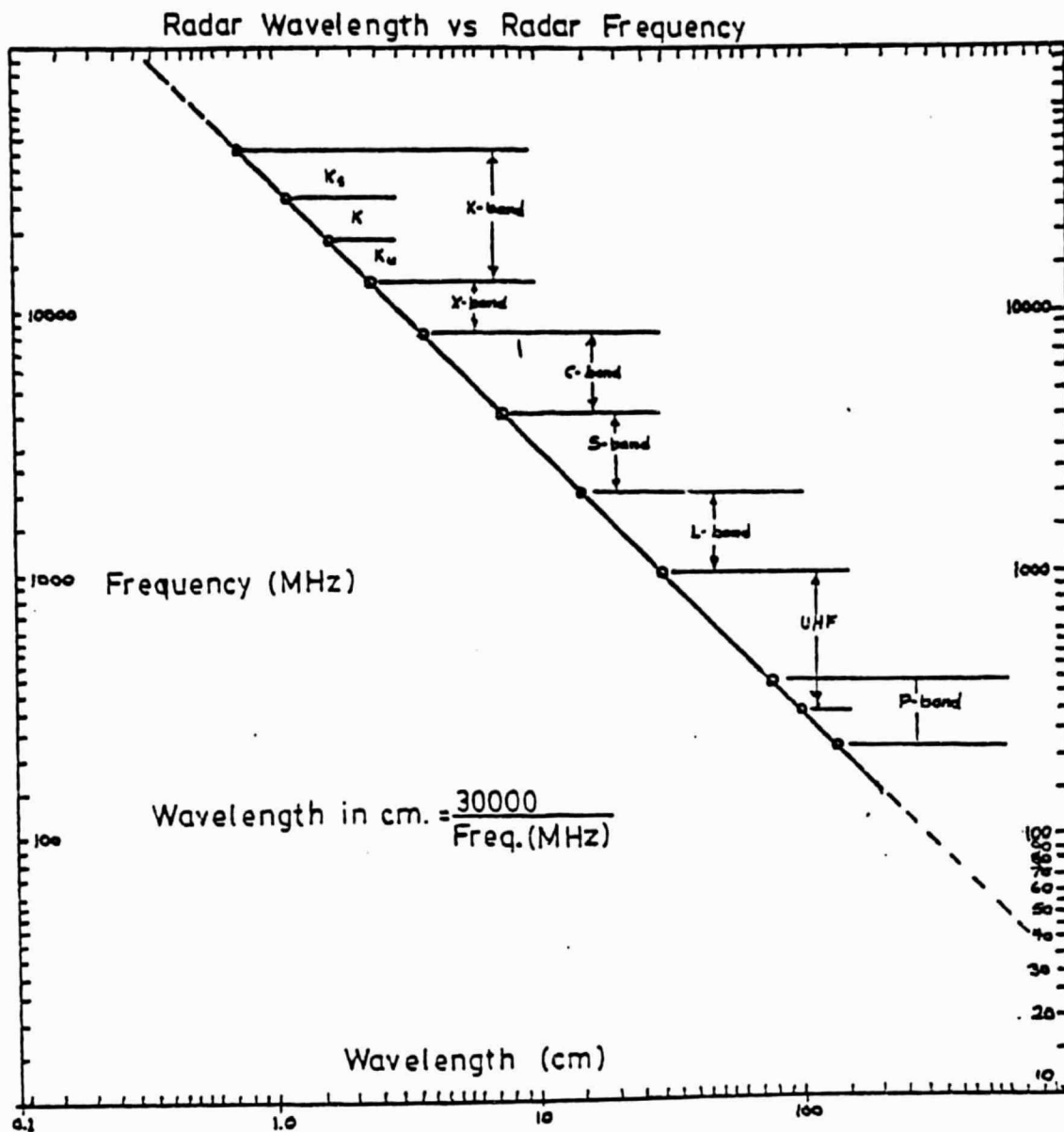
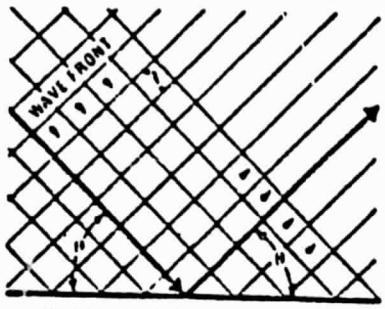


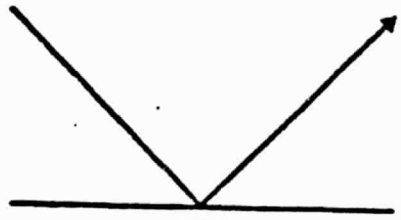
TABLE OF RADAR BANDS AND FREQUENCIES

Radar Frequency Band	Wavelength ( $\lambda$ )	Frequency Range
P	136 - 77 cm	220 - 390 MHz
UHF	100 - 30 cm	300 - 1000 MHz
L	30 - 15 cm	1000 - 2000 MHz
S	15 - 7.5 cm	2000 - 4000 MHz
C	7.5 - 3.75 cm	4000 - 8000 MHz
X	3.75 - 2.40 cm	8000 - 12500 MHz
Ku	2.40 - 1.67 cm	12500 - 18000 MHz
K	1.67 - 1.18 cm	18000 - 26500 MHz
Ka	1.18 - 0.75 cm	26500 - 40000 MHz

Figure 39. Letter code and frequency-wavelength bands (after Macdonald, 1969).

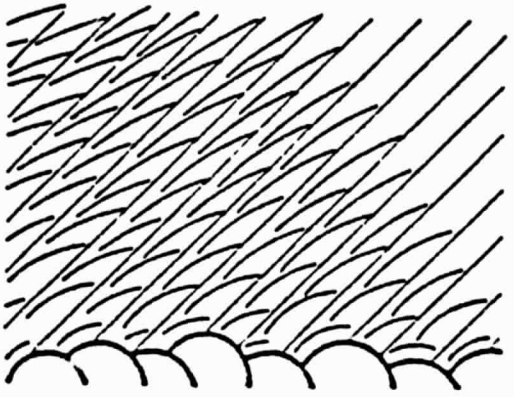


WAVE FRONT SMOOTH

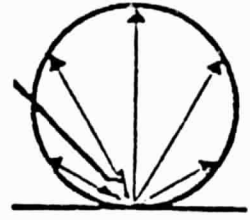


RAY

SPECULAR REFLECTION



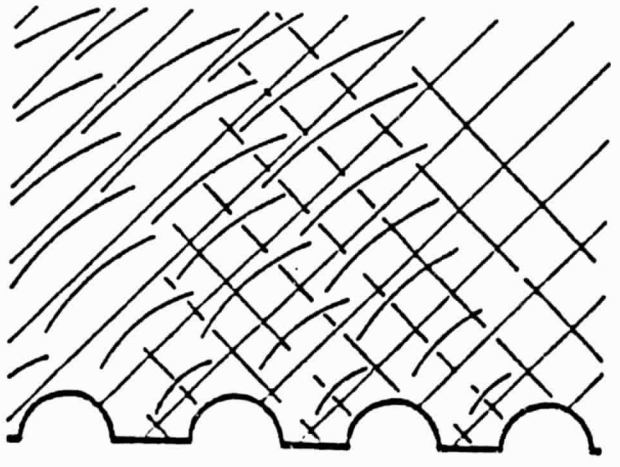
WAVE FRONT ROUGH



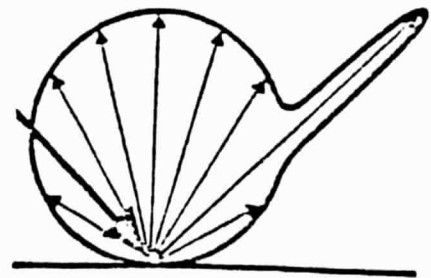
RAY

DIFFUSE REFLECTION

6031-5



WAVE FRONT



RAY

DIFFUSE AND SPECULAR REFLECTION

Figure 40. Types of reflection (after Goodyear Aerospace, 1977).



depolarization effects on the radiation such that a horizontally polarized wave can return with either the same polarization (HH) or a vertical polarization (HV). The same applies for an initially vertically polarized beam.

Surface roughness determines the tone and texture of an image. This is complicated by the vegetal canopy. Where vegetation covers the ground surface, the radar return may be influenced by the combination of vegetation and terrain surface below the vegetation (MacDonald and Waite, 1973). In a given area, how much the vegetation influences the radar return is determined by the wavelength; the radar return for longer wavelengths is influenced less by the vegetation. The Seasat SAR at a 23 centimeter wavelength is relatively little affected by vegetation. Polarization of the electric vector of the radar signal is also a variable. A measure of surface roughness may be obtained by comparing the direct and cross polarized components of the signal return (Ellermeir et al, 1966). The Seasat SAR transmits and receives in the HH mode.

The dielectric constant or permittivity of a material is a function of frequency; it is almost constant over the radar portion of the spectrum for most natural materials, but does decrease with decreasing frequency (increasing wavelength) (Parry, 1973). It is proportional to the moisture content and porosity of the surface material and affects both the reflectivity and conductivity of this

surface material. Reflectivity is directly proportional to the dielectric constant - moist areas give a higher return. Surface material conductivity inversely affects the depth of radar penetration and is directly proportional to the dielectric constant. Thus the radar penetration is greater in dry materials than in wet, and is greater for long wavelengths as shown in Figure 41, taken from Parry (1977). The skin depth of the Seasat SAR L-band is about 1.0 meters in average moist loams and can penetrate to 10 meters in dry sand.

### Resolution

While the ultimate resolution attained by the system is a function of many parameters, the single criterion most commonly used to judge it is the pulse packet size projected on the ground (Leighty, 1968). The system parameters that determine the pulse packet size are the antenna beamwidth and pulse length as measured at the half power points. The range resolution is determined by the pulse length - objects separated by a slant range distance less than half of the pulse length are unresolvable (Figure 42). The two reflected signals from the objects are received as one continuous echo, and the two targets cannot be differentiated. The range resolution (RR) on the ground varies with the depression angle and is given by:

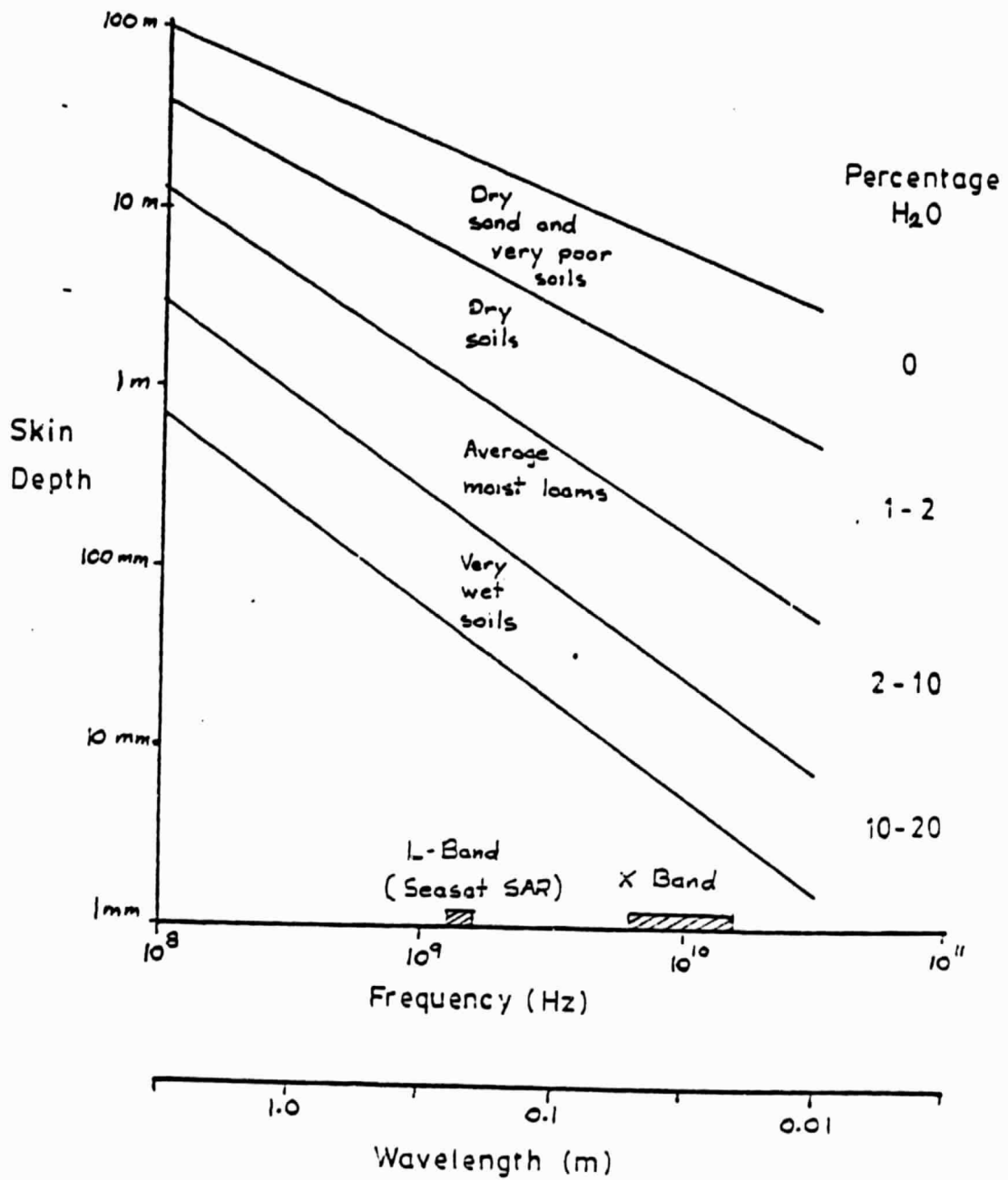


Figure 41. Variations in skin depth for various soil types (after Parry, 1977).

ORIGINAL PAGE IS  
OF POOR QUALITY

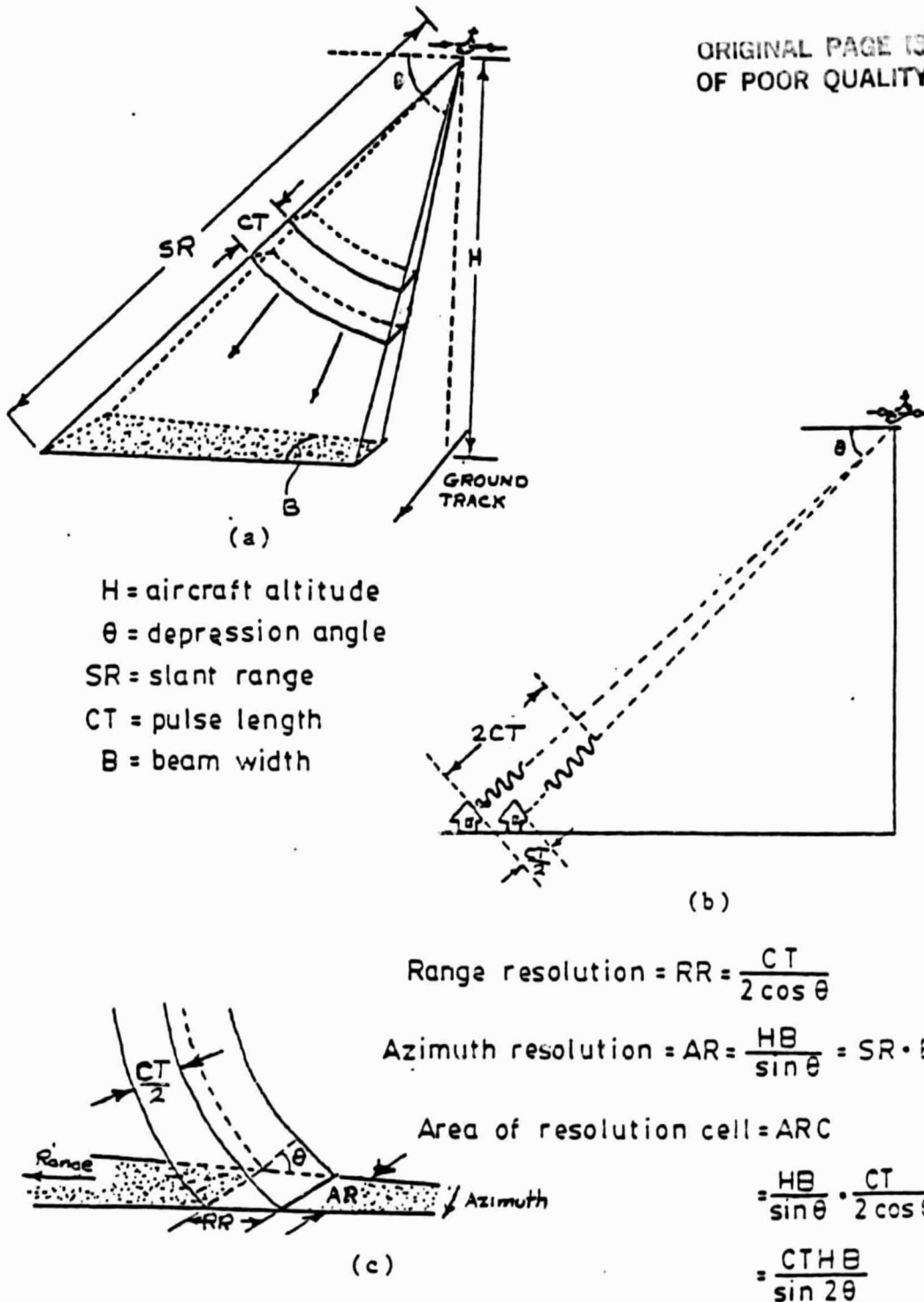


Figure 42. Range resolution

(a) Radar configuration

(b) Relation between pulse length and range resolution

(c) Range resolution and depression angle

(after Parry, 1973).

$$RR = \frac{c\tau}{2 \cos\theta} \quad (2)$$

where  $c = 3 \times 10^8$  m/sec

$\tau$  = pulse duration (sec)

$\theta$  = depression angle

RR = range resolution (Parry, 1973)

Range resolution is worst at large depression angles close to the ground track, which is why side-looking radar is used. It can be improved by decreasing the pulse length, but a minimum limit exists because the average power transmitted is a direct function of the pulse length. Also, if the transmitter pulse width is decreased, the bandwidth of the receiver must be increased because the bandwidth of a pulse is inversely proportional to its time duration. For most types of receivers, an increase in bandwidth results in an increase in noise level, so the amplitude of the transmitted pulses must be increased to maintain the signal-to-noise ratio. Further complications can be introduced to range resolution calculations by using other than constant amplitude rectangular pulses (Goodyear Aerospace, 1977)

Azimuth (along-track) resolution (AR) is also a variable quantity if a real-aperture system is used. It is a function of transmitted wavelength and dimensions of the antenna and is given by:

$$AR = \frac{H\theta}{\sin \theta} \quad (3)$$

where  $\Theta = 1.2\lambda/D$

$\Theta$  = half-power beamwidth in radians

$\lambda$  = radiation wavelength

D = antenna aperture size

H = aircraft altitude

$\Theta$  = depression angle

AR = azimuth resolution (Parry, 1973)

thus the area of the resolution cell (ARC) is

$$ARC = \frac{c\tau}{2 \cos \Theta} \cdot \frac{H\Theta}{\sin \Theta} = \frac{c\tau H\Theta}{\sin 2\Theta} \quad (4)$$

(Parry, 1973)

which is the basic factor controlling the resolution capabilities of a radar system.

A considerable improvement can be achieved by use of synthetic aperture techniques so that the effective size of the antenna is greatly increased over that physically realizable. The resolution limit of synthetic aperture radar is one-half the physical antenna length. The increased resolution is achieved by generating a phase history for a given target by moving the target through the pulsed radar beam. What is actually happening is that the transmitter moves relative to the target. Resolution differs from detectability in that a small fence post with dimensions below the resolution limit will be detected if it is resonant to the wavelength of the radar and if it is

illuminated at the right angle. The size and shape of the object however, will not be determinable.

Signal-to-noise ratio, dynamic range, and contrast

These three characteristics are best discussed together because of their close functional relationship. The signal-to-noise ratio was found not to be a good measure of the noisy aspect of the image. Instead, the "noise equivalent  $\sigma_0$  (scattering coefficient)" which is a measure of the lowest detectable  $\sigma_0$  of the system and the "noise equivalent  $\Delta\sigma_0$ " which is the least detectable difference in  $\sigma_0$  of the system, were found to be much better measures (Figure 43) as illustrated by Beal et al (1977). The "noise equivalent  $\sigma_0$ " ( $NE\sigma_0$ ) represents the lower bound of the dynamic range, while the saturation of the system represents the upper bound. For the Seasat SAR at 25 meter resolution, the  $NE\Delta\sigma_0$  is about 3 dB while the dynamic range is about 20 dB. This means that only 7 gray levels can be expected to be resolved. Spatial averaging will increase the dynamic range and decrease the  $NE\Delta\sigma_0$ . Seasat SAR measures 4 independent looks to construct a 25-meter resolution cell but further averaging, maybe to the resolution of Landsat is necessary to discriminate a reasonable number of gray levels (Figure 44 and 45) as illustrated by Beal et al (1977).

ORIGINAL PAGE IS  
OF POOR QUALITY

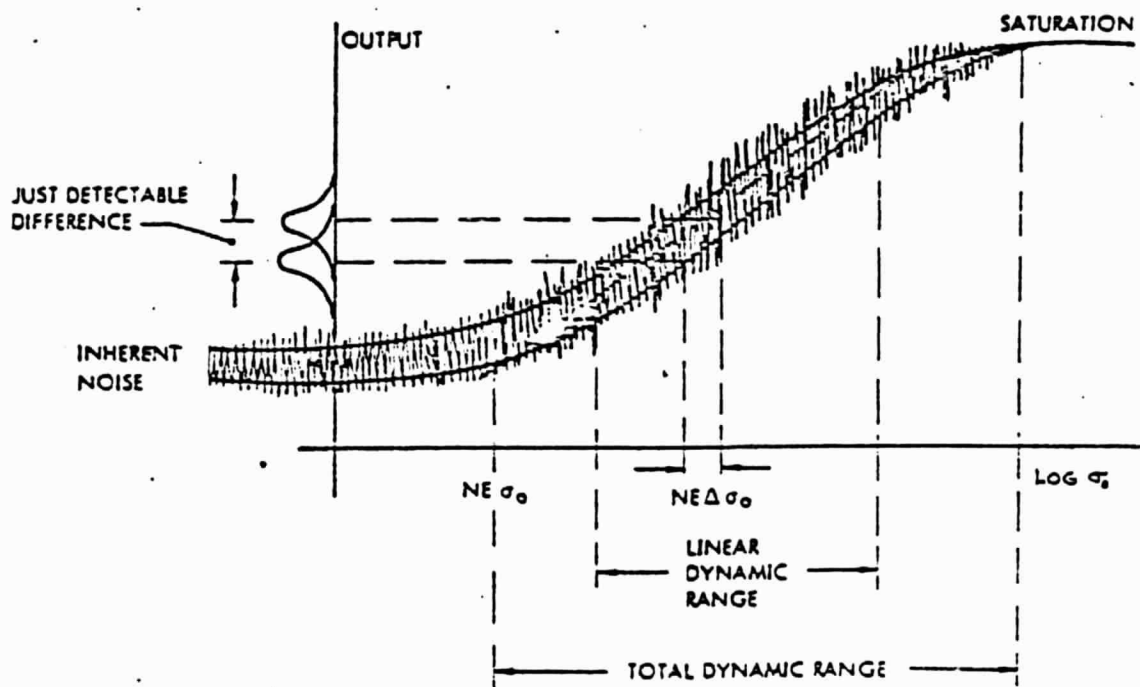


Figure 43. Typical input-output transfer function (after Beal et al, 1977).



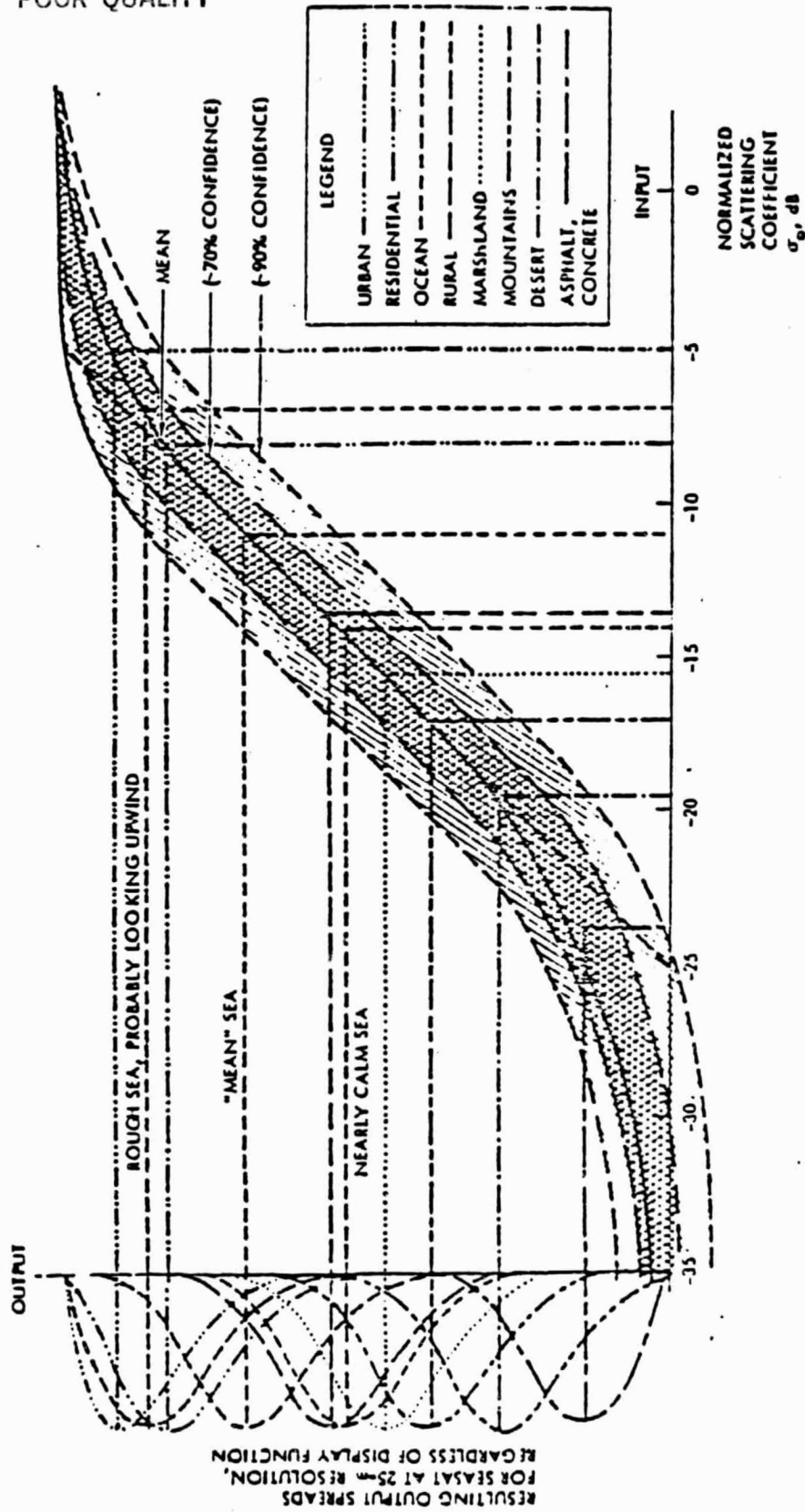


Figure 44. Typical target confusion on Seasat-A SAR resulting from four looks (after Beal et al, 1977).

ORIGINAL PAGE IS  
OF POOR QUALITY

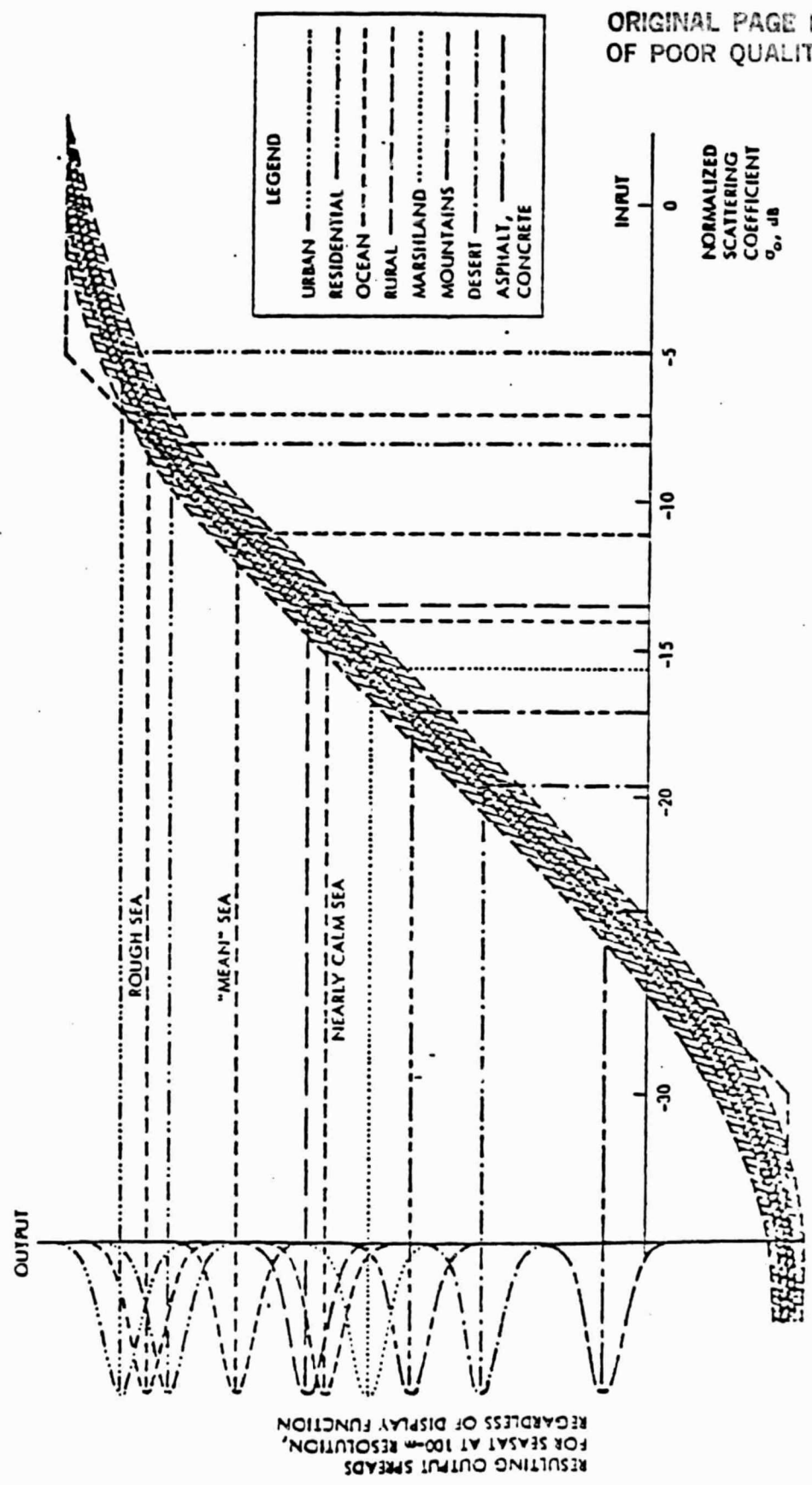


Figure 45. Spatial integration to Landsat resolution (80 m) on SAR (40 looks)  
(after Beal et al, 1977).

RESULTING OUTPUT SPREADS  
FOR SEASAT AT 100-m RESOLUTION,  
REGARDLESS OF DISPLAY FUNCTION,

Contrast is the most critical image descriptor. If spatial resolution degrades, the gray scale resolution usually improves, and the overall quality remains about the same. If the signal-to-noise ratio  $NE\sigma_0$  degrades, one can still obtain good imagery from the brighter targets. If contrast is low however, both weak and strong targets are affected. A low-contrast system would continue to detect strong point sources, but they would be surrounded by a uniform, non-informative gray (Beal et al, 1977). For the Seasat SAR, the chief contamination sources resulting in low contrast are high frequency amplitude, phase, and timing errors. If ten such contamination sources are postulated, which would be close to the worst case, the resulting ratio of useful energy to total energy would be 90%. The dynamic range of the Seasat SAR is -25 dB to +5 dB but this range will not be accommodated simultaneously. For any particular image, the contrast ratio will limit the "local" dynamic range to about 20 dB (Beal et al, 1977).

#### Radiometric accuracy

Imaging radar return is a function of the surface configuration described by  $\sigma_0$ , which is the differential scattering cross section per unit area, and a function of systematic effects. If the instrument were "perfect", and

the mapping function were unique and known, a calibrated map of radar backscatter would be produced. Such is not the case, but the resulting image can still be used mostly in the category of pattern recognition or detection in which a knowledge of absolute backscatter is not required (Beal et al, 1977).

There are two main systematic effects that can be easily removed and these are range loss and antenna gain pattern. In real-aperture systems radar return is reduced by a factor of range to the fourth power while in synthetic aperture systems the factor is range to the third power. The pixels can be corrected for this range loss by a simple coefficient multiplication to remove the effect of changing slant range. (Lowry et al, 1978). Imaging radar mounted on a satellite has additional effects which are much more difficult to remove. Both the rotation of the planet and the antenna pointing errors cause a slant-range displacement of a fixed point on the planetary surface. This effect is sometimes called range walk. In addition, at satellite altitudes the curvature of both the signal wavefronts and the planetary surface give rise to significant slant-range displacements called range curvature. The combined effect of the two types of displacement is called range migration (Vant et al, 1979).

A major cause of uncertainty in backscatter values in all imaging radar systems is due to coherent speckle (Rayleigh

fading). It is caused by the fine diffraction pattern created by each reflecting element in the scene when illuminated by a monochromatic, spatially coherent source. In effect, the ground surface can be considered as a source containing a number of randomly phased oscillators at slightly different frequencies. The signals add in phase at some time and out of phase at others, which results in coherent fading or interference. When treated at a coarser level, speckle patterns introduce texture into the radar image (Parry, 1977). Only textures coarser than this system component are real surface textures. In the Seasat SAR for example, fields of identical scatterers, in the absence of other contamination sources, produce backscatter variances of 3 dB at the scale of a single resolution element. There is no effective way to reduce this variance except by spatial averaging. The variance will decrease proportionally to the square root of the number of cells which are spatially integrated (Beal et al, 1977).

Many investigators have found that the number of linear features found on an image varies markedly with the direction of illumination. The generally excepted remedy is to obtain multiple look-direction imagery over the terrain, but this is expensive. However it is evident that the detectability factor of features off-normal can be improved by spatial filtering in the Fourier plane of a single look-direction image by using a filter which has an angular power variation of the form of equation 5.

$$D = K(1 - \cos 2\phi) \quad (5)$$

where D = an empirical detectability factor

$\phi$  = the azimuthal angle or viewing angle

and K = a function of the incidence angle

The filtered spectrum upon reconversion to an image would have a relatively uniform detectability factor for almost all azimuth angles (Eppes and Rouse, 1974).

#### Geometric accuracy

Imaging radar is a range measuring device. Data are digitally recorded by sampling the returning signal with a constant delay interval. As a result, the ground resolution cell in the near range is much bigger than in the far range. The first step is to convert slant range to ground range using the formula:

$$GR = (SR^2 - H^2)^{1/2} \quad (6)$$

where H = aircraft altitude above the terrain

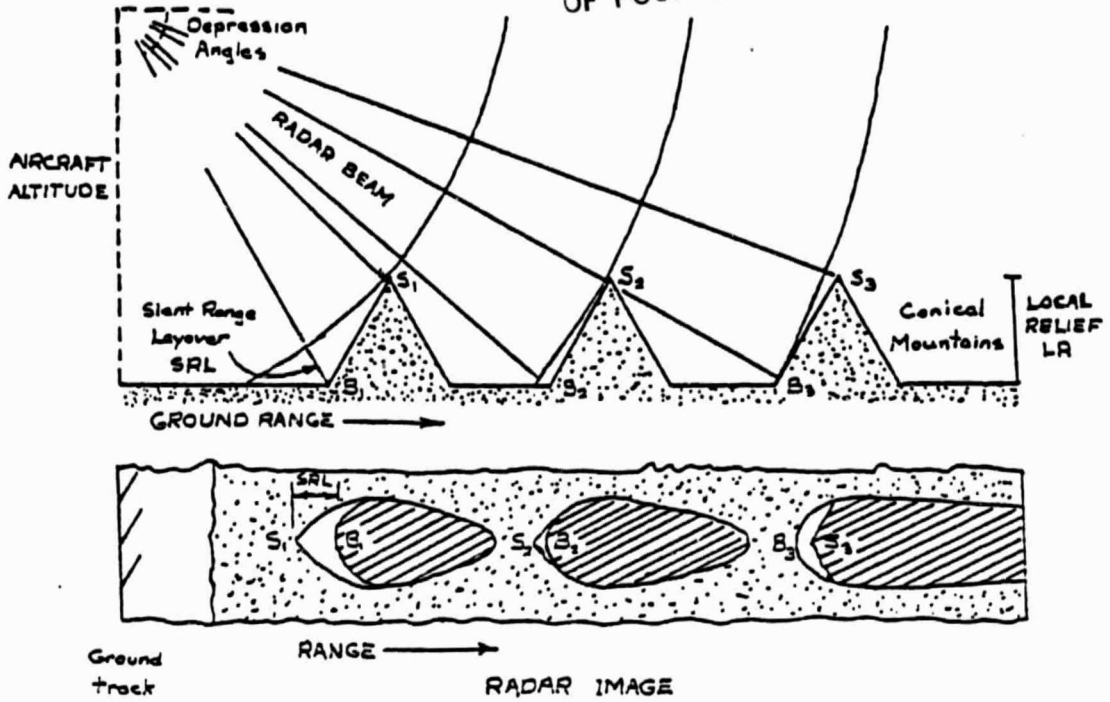
SR = slant range

GR = ground range

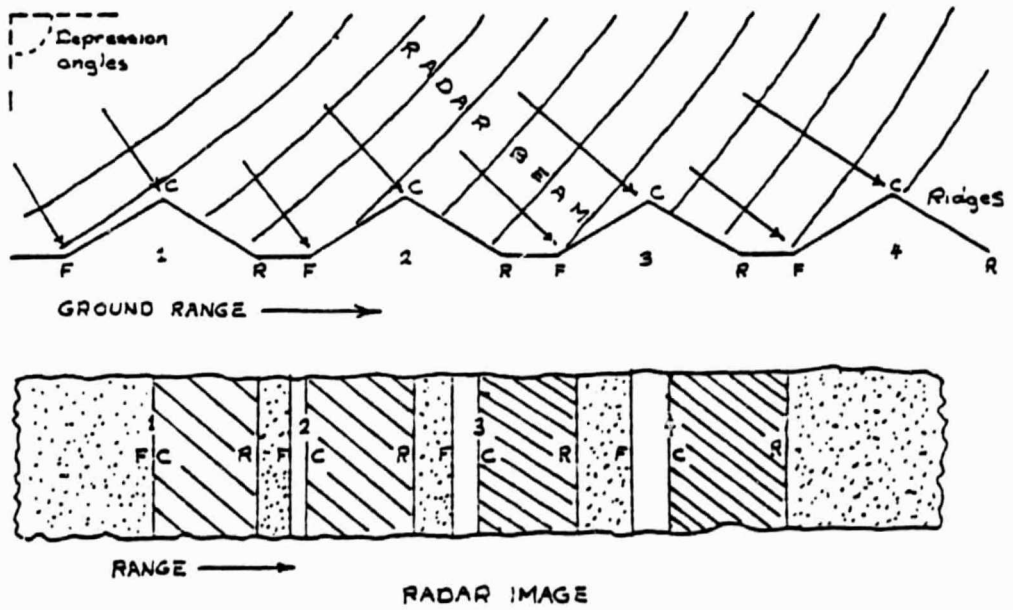
In this formula the earth is assumed to be flat. For satellite data this assumption cannot be made and corrections are complicated by range migration (Vant et al,1979). Next, the image must be resampled to generate square pixels. Due to the changing resolution with ground range or slant range, there are two options for resampling. These are a linear interpolating oversampling, and a boxcar filter or running mean averaging. In either case the resampling must be done with care to avoid aliasing errors (Lowry et al,1977). The difference between the two methods is that either a pixel size near to the smallest resolution cell is chosen as a standard (oversampling), or one near to the largest resolution cell is chosen (averaging). For applications where the small amount of high frequency noise introduced by the boxcar filter is important, a different filter may have to be used (Lowry et al,1978).

Geometric problems that are inherent in all radar systems imaging irregular terrain surfaces and which cannot be corrected, are foreshortening and layover. Foreshortening is the compression in the length of equal slope elements when viewed at different incidence angles. It is at a maximum at zero incidence and is completely eliminated at grazing incidence (Figure 46). Layover results because radar is a time dependent ranging system and the location of an object on a radargram is based on the time required for the transmitted energy to complete the round trip back to

ORIGINAL PAGE IS  
OF POOR QUALITY



(a)



(b)

Figure 46. Layover and foreshortening

(a) Slant-range layover

(b) Foreshortening

(after Parry, 1973).



the receiver. In the case of SLAR systems, where the radar pulse is obliquely incident at the surface, mountain summits and ridge crests lie at shorter slant ranges than their foot slopes, with the result that the summit is imaged closer to the ground track on the radar image (Figure 46). This situation, which arises whenever the slope angle of the terrain feature exceeds the complement of the depression angle, is more likely to occur at large depression angles (in the near range) (Parry, 1973). Foreshortening occurs at all incidence angles. Figure 47 illustrates the effect of target altitude upon the location of the target in the SAR image. In the figure,  $A$  is the altitude of the target,  $T$ , and  $(a)$  is the altitude of the satellite,  $S$ , with respect to the image datum plane. In the SAR image,  $T$  would appear at  $T_s$ , and would have a ground displacement of  $R_s$ . This displacement is opposite from that of the optical perspective in which  $T$  would be imaged at  $T_o$ . Values of the displacement at the near edge and far edge of the SAR image are tabulated, along with the difference in their displacements (Beal et al, 1977). In the case of the thesis study area where the maximum elevation difference is 1100 feet, the displacement of the highest point relative to its true location on the image datum plane through the lowest point is about 1 kilometer. This substantial displacement would of course be spread over many pixels. The values of  $R_s$  listed in Figure 47 do not include the effects of the

ORIGINAL PAGE IS  
OF POOR QUALITY

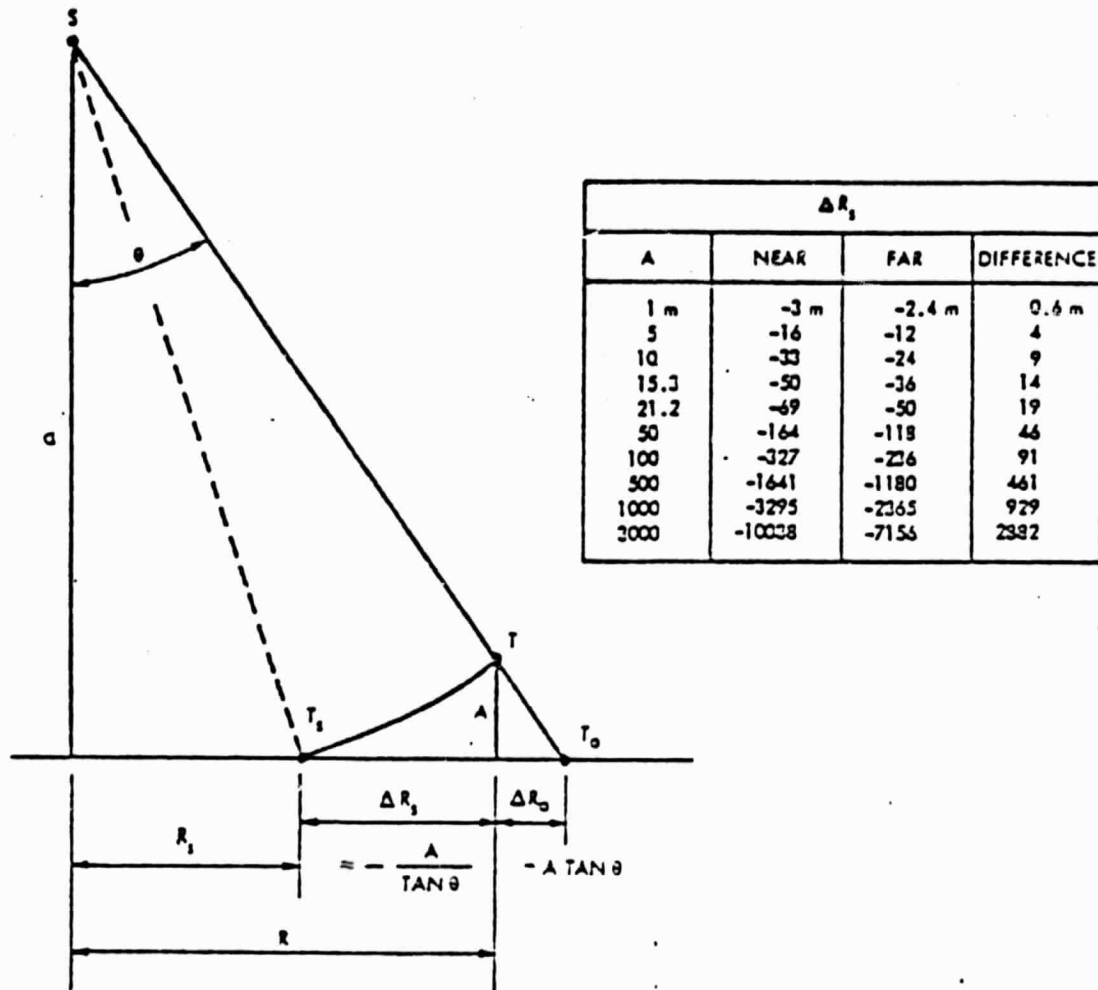


Figure 47. Target altitude effects  
(after Beal et al, 1977).

curved earth surface which are significant (Beal et al, 1977).

#### Landsat MSS - Seasat SAR Synergism

Combining these two types of data retains all the information available from each sensor system and additional detailed data resulting from their superposition. The Landsat imagery is sensitive to water and vegetation type and condition, while radar imagery is affected to a degree by vegetation moisture content, but principally by terrain parameters and general type of vegetation (Harris and Graham, 1976).

Radar and Landsat imagery may be combined in a number of different ways. The two basic choices are digitally or photographically. Most combinations thus far have been done photographically. Registering the Landsat image photographically to the radar image is very time consuming and inaccurate. It is done through enlargements and reductions and thus it is only possible to get a good average scale adjustment, with some areas of misregistration in the final composite. Four methods of photographically combining this imagery are described in Harris and Graham (1976). These methods are additive as well as multiplicative techniques accomplished through the use of many

internegatives exposed through different color filters. The method with the most promise, they conclude, is an additive process involving the use of six negatives; three from Landsat MSS bands 4,5, and 7 and three of the radar image. It appears that they used an X-band radar in the HH mode.

The method of digital image registration involves the selection of tiepoints or ground control points (GCP's) in both images and then the radar image is manipulated to fit the Landsat image. The relationship between the tiepoints in the two images is assumed to be a polynomial with the coefficients determined by a least squares fitting of the polynomial to the tiepoints. The method is generally much more accurate than the photographic techniques, but both methods are complicated by the high noise content of SLR which makes the choice of tiepoints difficult (Murphrey, 1978). Once the data registration is complete, many different methods of combining the data exist.

The Landsat images can be transformed from red-green-blue (RGB) color coordinates to hue-saturation-intensity (HSI) color coordinates. Then the digitally registered radar data can be inserted as the intensity component and the resulting data transformed back to RGB coordinate space (Daily et al, 1978). The ORSER facility at the Pennsylvania State University does not have this capability.

Other methods involve using a Landsat channel as one color coordinate and for example VH and VV polarization L-band as the other two color coordinates (Daily et al, 1978).

A rather obvious combination that no one seems to have tried, is to evaluate the principal components of the four Landsat bands and then combine them with the radar channels (polarizations and wavelengths), or combine all the data first and then obtain principal components.

Once the data are registered and combined, they may be converted to image form for visual interpretation (Daily et al, 1978), or be subjected to "automatic" pattern recognition techniques. Areas of interest where ground truth information is available, are used to "train" automated classifiers. This is where a problem may arise with the large dimensionality of the combined data. When the number of training samples is small, the classification accuracy in an eight-dimensional space (for example) may be less accurate than that achieved with fewer dimensions (Ahern et al, 1978). This restriction will then dictate either how many training samples have to be obtained, or how many principal components can be used.

#### Summary and Problems

Imaging radar provides unique information which when combined with information from other sensors, potentially can increase the classification accuracy greatly. The price for this unique information is dealing with problems in data

quality due to sensor characteristics and imaging system geometry and the extensive processing required to generate an image from the raw data. Foreshortening and layover errors will always be present in the imagery due to inherent characteristics of the radar system. Coherent speckle now creates many problems, but in the future may become less severe as improvements in the electronics are made; spatial averaging helps to overcome this problem. Registration of radar data to other data is still not very accurate especially for satellite radar which is complicated by range migration. Extensive work still needs to be done to improve radar data analysis and interpretation. There is no mathematical technique which explains the terrain response to radar, so interpretations have to rely on empirical relationships. Visual inspection of radar imagery suggests that surface texture is a prominent controlling factor in the radar response. Also, boundaries where significant changes occur tend to be emphasized suggesting that the response is in some sense equivalent to an edge enhancement (spatial derivative) of visible-band channels. With further work will come greater understanding of the surface characteristics and interactions with radar that determine the observed radar return.

- A' n, F. G., D. G. Goodenough, A. L. Grey, R. A. Ryerson, R. J. Vilbikaitus, and M. Goldberg, Simultaneous microwave and optical wavelength observations of agricultural targets, Canadian Journal of Remote Sensing, 3, 127-142, 1978.
- Beal, R., J. Springett, R. Lipes, C. Wu, and N. Evans, Seasat-A SAR Design Verification Report, Jet Propulsion Laboratory, 622-31, California Institute of Technology, Pasadena, California, 1977.
- Borden, F. Y., D. M. Barr, and D. N. Applegate, Skylab S-192 channel evaluation by analysis of digital data, in Interdisciplinary Applications and Interpretations of EREP Data within the Susquehanna River Basin, pp. 5-13, Office for Remote Sensing of Earth Resources, The Pennsylvania State University, tech. Rpt. 2-76, 1976.
- Brigham, E. O., The Fast Fourier Transform, Prentice-Hall Inc., New Jersey, 1974.

Cook, F. A., D. S. Albaugh, L. D. Brown, S. Kaufman, J. E. Oliver, Thin-skinned tectonics in the crystalline southern Appalachians; COCORP seismic-reflection profiling of the Blue Ridge and Piedmont, Geology, 7, 563-567, 1979.

Daily, M., C. Elachi, T. Farr, and G. Schaber, Discrimination of geologic units in Death Valley using dual frequency and polarization imaging radar data, Geophysical Research Letters, 5, 889-892, 1978.

Ellermeir, R. D., A. K. Fung, and D. S. Simonett, Some empirical and theoretical interpretations of multiple polarization radar data, in Proc. Symp. Remote Sensing of Environment, 4th, pp. 657-670, 1966.

Epenshade, G. H., Geology of the northern part of the Blue Ridge anticlinorium, in Studies of Appalachian Geology, Central and Southern, edited by W. Fisher, F. J. Pettijohn, J. C. Reed, and K. H. Weaver, pp. 199-211, Wiley Interscience, 1970.



Eppes, T. A., and J. W. Rouse, Jr., Viewing angle effects on radar images, Photogrammetric Engineering, 40, 169-173, 1974.

Farlekas, G. M., The Geology of Part of South Mountain of the Blue Ridge Province north of the Pennsylvania-Maryland Border, M.S. thesis, 64 pp., Dept. of Geology, Penn State Univ., 1961.

Fauth, J. L., Geology of South Mountain Northwestern Adams County, Pennsylvania, M.S. thesis, 103 pp., Dept. of Geology, Penn State Univ., 1962.

Fauth, J. L., Geology and mineral resources of the Iron Springs area, Adams and Franklin Counties PA., Pennsylvania Geological Survey, 4th series, 1978.

Foley, D., The probability of error in the design set as a function of the sample size and dimensionality, Technical Report RADC-TR-71-171, 1971.

Goetz, A. F. H., and L. C. Rowan, Geologic remote sensing, Science, preprint, submitted April 18, 1980.

Goodyear Aerospace, SAR - Fundamentals of synthetic aperture radar system employing optical correlation, GIB-9399A, 1977.

Gwinn V. E., Kinematic patterns and estimates of lateral shortening, Valley and Ridge and Great Valley provinces, central Appalachians, south-central Pennsylvania, in Studies of Appalachian Geology, Central and Southern, edited by W. Fisher, F. J. Pettijohn, J. C. Reed and K. H. Weaver, pp. 127-146, Wiley Interscience, 1970.

Harris, G. Jr., and L. C. Graham, Landsar-radar synergism, Congress of the International Society of Photogrammetry, 13th, Commission 7, 1976.

Henderson, R. G., and L. Cordell, Reduction of unevenly spaced potential field data to a horizontal plane by means of a finite harmonic series, Geophysics, 36, 856-866, 1971.

Hsu, S. Y., Texture-tone analysis for automated landuse mapping, panchromatic images, Photogrammetric Engineering and Remote Sensing, 44, 1393-1404, 1978.

Hsu, S. Y., The Mahalanobis classifier with the generalized inverse approach for automated analysis of imagery texture data, Computer Graphics and Image Processing, 9, 117-134, 1979.

Jennrich, R., and P. Sampson, P7M and BMD07M - Stepwise discriminate analysis, Biomedical Computer Programs, U.C.L.A. Dept. of Biomathematics, 1979.

King, P. B., Further thoughts on tectonic framework of the southeastern United States, in Tectonics of the Southern Appalachians, edited by W. D. Lowry, pp. 5-31, Va. Polytech. Inst., Department of Geol. Sci., Mem. 1, 1964.

Kowalik, W. S., and D. P. Gold, The use of Landsat-1 imagery in mapping lineaments in Pennsylvania, Proc. First International Conference on the New Basement Tectonics, Utah Geol. Assoc. Pub. No. 5, 236-249, 1974.

Lavin P. M., Personal communication, 1980.

Leighty, R. D., Remote sensing for engineering investigation of terrain: Radar systems. Proc. Symp. Remote Sensing of Environment, 5th, 669-682, 1968.

Lewis, A. J., and W. Waite, Cumulative frequency curves of the Darien Province, Panama, Proc. Symp. of the E.M. Wave Propagation Panel of AGARD, 17th, Colorado Springs, CO., 1972.

Lowry, R. T., D. G. Goodenough, J. S. Zelenka, and R. A. Shuchman, On the analysis of airborne synthetic aperture radar imagery of the ocean, Proc. Canadian Symp. on Remote Sensing, 4th, 480-505, 1977.

Lowry, R. T., S. Shlien, and D. G. Goodenough, A CCRS system for synthetic aperture radar imagery analysis, Proc. Canadian Symp. on Remote Sensing, 5th, 363-372, 1978.

MacDonald, H. C., Geologic evaluation of radar imagery from Darien Province, Panama, Modern Geology, 1, 1-63, 1969.

MacDonald, H. C., and W. P. Waite, Imaging radars provide terrain texture and roughness parameters in semi-arid environments, Modern Geology, 4, 145-158, 1973.

Matthews, R. E. (editor), Active Microwave Workshop Report, NASA SP-376, NTIS N76-11811, 1975.

Merembeck, B. F., F. Y. Borden, M. H. Podwysocki, and D. N. Applegate, Application of canonical analysis to multispectral scanner data, Proc. Annual Symp. on Computer Application in the Mineral Industries, 14th, University Park, Pennsylvania, 1976.

Murphrey, S. W., SAR-Landsat Image Registration Study, NASA-CR-156847, International Business Machines Corp., Gathersburg, 1978.

Parker, R., Application of Texture-Tone Analysis of Landsat Data to Geologic Exploration, Senior thesis at Allegheny College, Pennsylvania, 1980.

Parry, J. T., The role of AN/APS-94D X-band SLAR in terrain analysis, Defense research board of Canada, contract SP2-7090163, us serial 2SP3-0024, 1973.

Parry, J. T., Interpretation techniques for X-band SLAR, Proc. Canadian Symp. on Remote Sensing, 4th, 376-394, 1977.

Pavlin, G., Computer programs; HSUDRIVE, TEX13, TEX2, implementing the Hsu texture measures, 1979.

Rose, A. W., Metal mines and occurrences in Pennsylvania, in Atlas of Pennsylvania's Mineral Resources, part 3, Pennsylvania Geological Survey, 4th series, 1970.

Socolow, A. A., Geologic Map of Pennsylvania (1:250,000), Pennsylvania Geological Survey, 4th series, 1960.

Stose, G. W., Geology and Mineral Resources of Adams County, PA., Pennsylvania Geological Survey, 4th series, 1932.

Syberg, F. J. R., Potential field continuation between general surfaces, Geophysical Prospecting, 20, 267-282, 1972.

Turner, B. J., D. N. Applegate, and B. F. Merembeck, Satellite and aircraft multispectral scanner digital data user manual, Office for Remote Sensing of Earth Resources, The Pennsylvania State University, 1978.

United States Department of the Interior, Topographic Maps, 7.5 Minute Series, 1953.

Vant, M. R., R. W. Herring, and E. Shaw, Digital processing techniques for satellite-borne synthetic-aperture radars, Canadian Journal of Remote Sensing, 5, 67-73, 1979.

Vincent, R. K., Geochemical mapping by spectral ratioing methods, in, Remote Sensing Applications for Mineral Exploration, edited by W. L. Smith, pp. 73-98, 1977.